



# Synthesis of metal oxide-based catalysts by microwave-assisted solution combustion method

Kawthar Frikha

## ► To cite this version:

Kawthar Frikha. Synthesis of metal oxide-based catalysts by microwave-assisted solution combustion method. Theoretical and/or physical chemistry. Université de Haute Alsace - Mulhouse; Ecole Nationale d'Ingénieurs de Sfax (Tunisie). Laboratoire de Génie des Matériaux et Environnement, 2020. English. NNT : 2020MULH4686 . tel-03010014v2

**HAL Id: tel-03010014**

**<https://hal.science/tel-03010014v2>**

Submitted on 30 Mar 2022

**HAL** is a multi-disciplinary open access archive for the deposit and dissemination of scientific research documents, whether they are published or not. The documents may come from teaching and research institutions in France or abroad, or from public or private research centers.

L'archive ouverte pluridisciplinaire **HAL**, est destinée au dépôt et à la diffusion de documents scientifiques de niveau recherche, publiés ou non, émanant des établissements d'enseignement et de recherche français ou étrangers, des laboratoires publics ou privés.

UNIVERSITÉ DE HAUTE-ALSACE–UNIVERSITÉ DE STRASBOURG  
ÉCOLE NATIONALE D'INGÉNIEURS DE SFAX–UNIVERSITÉ DE SFAX

# THESE

**En cotutelle internationale**

Pour l'obtention du grade de

**DOCTEUR DE L'UNIVERSITÉ DE HAUTE-ALSACE**

**ÉCOLE DOCTORALE : Physique et Chimie-Physique (ED 182)**

Discipline : Chimie-Physique

ET

**DOCTEUR DE L'ÉCOLE NATIONALE D'INGÉNIEURS DE SFAX**

**ÉCOLE DOCTORALE : Sciences et Technologies**

Discipline : Matériaux et Environnement

Présentée et soutenue publiquement

par

**Kawthar FRIKHA**

Le 27 Mai 2020

---

## **SYNTHÈSE DE CATALYSEURS D'OXYDES MÉTALLIQUES PAR LA MÉTHODE DE COMBUSTION EN SOLUTION ASSISTÉE PAR MICRO- ONDES**

---

### **Jury :**

*M. Patrick FIEVET, Professeur des Universités, UTINAM, France (Président)*

*M. Jean-Luc ROUSSET, Directeur de Recherche, IRCELyon, France (Rapporteur)*

*Mme. Hanene AKROUT, Maître de Conférences HDR, CERTE, Tunisie (Rapporteur)*

*Mme. Simona BENNICI, Chargée de Recherche HDR, IS2M, France (Examinatrice)*

*M. Lionel LIMOUSY, Professeur des Universités, IS2M, France (Co-Directeur de thèse)*

*M. Jamel BOUAZIZ, Professeur des Universités, LAMA, Tunisie (Co-Directeur de thèse)*

## Acknowledgments

*I would like to thank Prof. Vincent ROUCOULES, director of the Institute of Materials Science of Mulhouse (IS2M), and Prof. Jamel BOUAZIZ, director of the Laboratory of Advanced Materials (LAMA) for welcoming me during the last three years of the PhD study.*

*I would like to thank my thesis committee members: Prof. Patrick FIEVET, Dr. Jean-Luc ROUSSET, Dr. Hanene AKROUT, and Dr. Simona BENNICI for their insightful comments and valuable suggestions on this thesis work.*

*I would like to take this opportunity to thank Prof. Dominique ADOLPHE, the head of the doctoral school in exact science at the University of Haute Alsace (UHA), who was able, despite the extraordinary circumstances, to negotiate the best deal for making possible the PhD defense.*

*I would like to express my sincere gratitude to my supervisors Prof. Lionel LIMOUSY and Prof. Jamel BOUAZIZ for giving me the opportunity to work under their guidance. I greatly appreciate the commitment, the continuous support, and the encouragement throughout the years of the PhD study.*

*My sincere gratitude also goes to Dr. Simona BENNICCI, who provided me an opportunity to join her team—Transfers, Reactivity, Materials for Clean Processes (TRM2P)—, and who gave me access to the laboratory and research facilities. I especially want to thank her for her willingness to give her time so generously. Her constructive suggestions, during the planning and development of this research work, have been very much appreciated.*

*I wish to thank many people; Ms. Laure MICHELIN, Ms. Habiba NOUALI, Ms. Samar HAJJARGARREAU, Mr. Ludovic JOSIEN, and Mr. Loic VIDAL, staff of the IS2M institute, for their contribution to this project and for allowing me to learn from them as much as I could; Dr. Kamel CHAARI, who was involved in the implementation of this research project. I also wish to thank my fellow doctoral students and my labmates at IS2M for all the fun we have had. It was great sharing laboratory with all of you!*

*A very special gratitude goes to the Tunisian Ministry of Higher Education and Scientific Research (MESRS), as well as, to the French National Centre for Scientific Research (CNRS) organization for providing financial support, during my stay in France.*

*Last, but not the least, I want to say “thank you” to my family: my parents, my brother and my sister for believing in me and supporting me along the way.*

*I place on record, my sense of gratitude to one and all, who directly or indirectly, have contributed to the accomplishment of this thesis work.*

## Table of Contents

Acknowledgments .....	i
Table of Contents .....	ii
List of Figures .....	vii
List of Tables.....	xii
List of Abbreviations .....	xiv
<b>GENERAL INTRODUCTION .....</b>	<b>1</b>
Résumé en Français de l'introduction générale .....	5
<b>CHAPTER 1. REVIEW OF THE LITERATURE .....</b>	<b>7</b>
Introduction .....	10
1.1 The potential of metal oxides for heterogeneous catalysis.....	10
1.1.1 Characteristics of Ni, Co and Cu oxide-based catalytic materials .....	11
1.1.1.1 Bulk structure .....	12
1.1.1.2 Surface structure.....	13
1.1.2 Multifunctional catalysts containing Ni, Co or Cu .....	14
1.1.2.1 Ni containing catalysts.....	14
1.1.2.2 Co containing catalysts .....	15
1.1.2.3 Cu containing catalysts .....	15
1.1.3 Characteristics of alumina and its application in catalysis .....	16
1.1.4 Alumina-Ni/Co/Cu chemical interaction.....	18
1.1.5 Applications in heterogeneous catalysis: oxidation of carbon monoxide .....	20
1.1.5.1 Cobalt oxide ( $\text{Co}_x\text{O}_y$ ).....	21
1.1.5.2 Nickel oxide ( $\text{Ni}_x\text{O}_y$ ) .....	24
1.1.5.3 Copper oxide ( $\text{Cu}_x\text{O}_y$ ).....	24
1.1.6 Methods for metal oxides catalytic materials elaboration.....	27
1.1.6.1 Ceramic method (solid-state reaction).....	27
1.1.6.2 Co-precipitation.....	27
1.1.6.3 Sol-gel.....	28
1.1.6.4 Impregnation .....	28
1.2 Microwave chemistry for metal oxide catalysts synthesis .....	29
1.2.1 Introduction to microwave chemistry .....	29
1.2.2 Microwave assisted solution combustion synthesis .....	34

---

1.2.2.1	Theory of combustion reaction .....	35
1.2.2.2	Solution combustion parameters .....	36
1.2.2.2.1	Chemical composition of precursors.....	37
1.2.2.2.2	Stoichiometry of the reactants (RV/OV ratio).....	39
1.2.2.2.3	Heating method.....	39
1.2.2.3	Mechanism of oxide forming .....	40
1.2.2.4	Metal oxides prepared by SCS .....	41
1.2.2.4.1	Al <sub>2</sub> O <sub>3</sub> .....	41
1.2.2.4.2	NiO .....	41
1.2.2.4.3	Co <sub>3</sub> O <sub>4</sub> .....	42
1.2.2.4.4	CuO .....	42
1.2.2.4.5	Ni/Al <sub>2</sub> O <sub>3</sub> .....	43
1.2.2.4.6	Co/Al <sub>2</sub> O <sub>3</sub> .....	44
1.2.2.4.7	Cu/Al <sub>2</sub> O <sub>3</sub> .....	44
1.2.3	Advantages and disadvantages .....	48
	Conclusions .....	49
	Résumé en Français du chapitre 1 .....	51
<b>CHAPTER 2.</b>	<b>MATERIALS AND METHODS.....</b>	<b>53</b>
	Introduction .....	55
2.1	Catalysts preparation.....	55
2.1.1	Catalyst samples.....	55
2.1.2	Chemical reagents .....	56
2.1.3	Synthesis procedures .....	56
2.1.4	Theoretical calculations.....	57
2.2	Catalysts characterization.....	61
2.2.1	X-ray fluorescence spectroscopy (XRF) .....	62
2.2.2	X-ray diffraction (XRD).....	62
2.2.3	N <sub>2</sub> adsorption-desorption analysis .....	62
2.2.4	Scanning electron microscopy (SEM) coupled with energy dispersive X-ray spectrometry (SEM-EDX) .....	63
2.2.5	Transmission electron microscopy (TEM) .....	63
2.2.6	X-ray photoelectron spectroscopy (XPS) .....	63
2.3	Catalytic testing .....	64
2.3.1	Experimental setup.....	64

2.3.2 Operating conditions .....	65
Conclusions .....	67
Résumé en Français du chapitre 2 .....	68
<b>CHAPTER 3. CATALYST CHARACTERIZATION.....</b>	<b>70</b>
Introduction .....	73
3.1 Binary oxide catalysts .....	73
3.1.1 Effect of stoichiometry (RV/OV ratio) .....	73
3.1.1.1 Effect of stoichiometry (RV/OV ratio) - metal loading = 10 wt% .....	73
3.1.1.1.1 XRF .....	73
3.1.1.1.2 XRD .....	74
3.1.1.1.2.1 Nickel based catalysts.....	74
3.1.1.1.2.2 Cobalt based catalysts.....	75
3.1.1.1.2.3 Copper based catalysts.....	76
3.1.1.1.3 N <sub>2</sub> adsorption-desorption isotherms.....	78
3.1.1.1.3.1 Nickel based catalysts.....	79
3.1.1.1.3.2 Cobalt based catalysts.....	80
3.1.1.1.3.3 Copper based catalysts.....	81
3.1.1.1.4 SEM.....	83
3.1.1.1.4.1 Nickel based catalysts.....	83
3.1.1.1.4.2 Cobalt based catalysts.....	84
3.1.1.1.4.3 Copper based catalysts.....	85
3.1.1.1.5 XPS .....	87
3.1.1.1.5.1 Nickel based catalysts.....	87
3.1.1.1.5.2 Cobalt based catalysts.....	88
3.1.1.1.5.3 Copper based catalysts.....	89
3.1.1.1.6 TEM .....	91
3.1.1.1.6.1 Nickel based catalysts.....	91
3.1.1.1.6.2 Cobalt based catalysts.....	92
3.1.1.1.6.3 Copper based catalysts.....	94
3.1.1.2 Effect of stoichiometry (RV/OV ratio) - metal loading = 2 wt% .....	96
3.1.1.2.1 XRD .....	96
3.1.1.2.2 N <sub>2</sub> adsorption-desorption isotherms.....	99
3.1.1.2.3 SEM.....	101
3.1.2 Effect of metal loading .....	104

3.1.2.1	XRF .....	104
3.1.2.2	XRD.....	104
3.1.2.2.1	Nickel based catalysts .....	104
3.1.2.2.2	Cobalt based catalysts .....	107
3.1.2.2.3	Copper based catalysts .....	109
3.1.2.3	N <sub>2</sub> adsorption-desorption isotherms .....	110
3.1.2.3.1	Nickel based catalysts .....	110
3.1.2.3.2	Cobalt based catalysts .....	110
3.1.2.3.3	Copper based catalysts .....	111
3.1.2.4	SEM.....	112
3.1.2.4.1	Nickel based catalysts .....	112
3.1.2.4.2	Cobalt based catalysts .....	114
3.1.2.4.3	Copper based catalysts .....	115
3.1.2.5	SEM-EDX.....	116
3.1.2.5.1	Nickel based catalysts .....	116
3.1.2.5.2	Cobalt based catalysts .....	117
3.1.2.5.3	Copper based catalysts .....	117
3.2	Ternary oxide catalysts.....	118
3.2.1	XRD .....	118
3.2.2	N <sub>2</sub> adsorption-desorption isotherms .....	120
3.2.3	SEM.....	121
3.2.4	XPS.....	122
3.2.5	TEM .....	124
	Conclusions .....	130
	Résumé en Français du chapitre 3 .....	132
	<b>CHAPTER 4. CATALYST ACTIVITY EVALUATION.....</b>	<b>135</b>
	Introduction .....	137
4.1	Catalysts efficiency: Catalytic oxidation of CO over binary oxide catalysts .....	137
4.1.1	Effect of RV/OV ratio on the catalytic performance .....	137
4.1.1.1	Effect of RV/OV ratio on CO oxidation activity over 10MAI-x calcined catalysts	137
4.1.1.1.1	Nickel-based catalysts .....	137
4.1.1.1.2	Cobalt-based catalysts .....	139
4.1.1.1.3	Copper-based catalysts .....	140

---

4.1.1.1.4	Comparison study of the different 10MAI-x calcined catalysts .....	141
4.1.1.2	Effect of RV/OV ratio on CO oxidation activity over 2MAI-x calcined catalysts	145
4.1.1.2.1	Nickel-based catalysts .....	145
4.1.1.2.2	Cobalt-based catalysts .....	146
4.1.1.2.3	Copper-based catalysts .....	147
4.1.2	Effect of metal loading on the catalytic performance .....	148
4.1.2.1	Nickel-based catalysts .....	148
4.1.2.2	Cobalt-based catalysts .....	149
4.1.2.3	Copper-based catalysts .....	151
4.2	Catalysts efficiency: Catalytic oxidation of CO over ternary oxides catalysts .....	155
4.3	Comparison with the literature .....	159
	Conclusions .....	160
	Résumé en Français du chapitre 4 .....	162
	<b>CONCLUSIONS AND PERSPECTIVES .....</b>	<b>164</b>
	Résumé en Français de la conclusion générale .....	170
	<b>REFERENCES .....</b>	<b>172</b>
	<b>ANNEX A .....</b>	<b>185</b>
	<b>ANNEX B .....</b>	<b>191</b>

## List of Figures

<b>Figure 1. 1.</b> Sequence of structure transformation of alumina and aluminum hydroxides [53].	17
<b>Figure 1. 2.</b> Crystal structure of spinel (shaded circles: M atoms; hollow circles: O atoms) [77].	19
<b>Figure 1. 3.</b> Schematic presentation of the electromagnetic spectrum [110].	30
<b>Figure 1. 4.</b> (a) Microwave heating and (b) conventional heating [110]	31
<b>Figure 1. 5.</b> Water molecule rotations in an alternating electrical field under microwave irradiation.	32
<b>Figure 1. 6.</b> Possible combinations of microwave chemistry with common synthesis routes.	33
<b>Figure 1. 7.</b> Fire triangle.	34
<b>Figure 1. 8.</b> Number of published articles on SC chemistry between 1998 and 2016 [125].	35
<b>Figure 1. 9.</b> SCS of metal oxide from aqueous solution [126].	35
<b>Figure 1. 10.</b> (a) Flaming type and (b) smoldering type combustion reactions [130, 131].	38
<b>Figure 1. 11.</b> Mechanism of aluminum nitrate–urea combustion reaction.	41
<b>Figure 2.1.</b> Steps involved in microwave assisted solution combustion synthesis.	57
<b>Figure 2.2.</b> Variations of the mole of urea involved in the system as a function of RV/OV ratio.	61
<b>Figure 2.3.</b> Scheme of installation used for the catalytic tests.	65
<b>Figure 2.4.</b> Catalytic procedures used to determine the light-off temperature, $T_{100}$ and the isothermal CO conversion at specific temperatures.	66
<b>Figure 3. 1.</b> XRD patterns of 10NiAl–x calcined catalysts.	75
<b>Figure 3. 2.</b> XRD patterns of 10CoAl–x calcined catalysts.	76
<b>Figure 3. 3.</b> XRD patterns of 10CuAl–x calcined catalysts.	77
<b>Figure 3. 4.</b> $N_2$ adsorption-desorption isotherm of 10NiAl–x calcined catalysts.	80
<b>Figure 3. 5.</b> $N_2$ adsorption-desorption isotherm of 10CoAl–x calcined catalysts.	81
<b>Figure 3. 6.</b> $N_2$ adsorption-desorption isotherm of 10CuAl–x calcined catalysts.	82
<b>Figure 3. 7.</b> SEM images of (a) 10NiAl–0.9, (b) 10NiAl–1.0 and (c) 10NiAl–1.1 calcined samples.	84

<b>Figure 3. 8.</b> SEM images of (a) 10CoAl-0.9, (b) 10CoAl-1.0 and (c) 10CoAl-1.1 calcined samples. ....	85
<b>Figure 3. 9.</b> SEM images of (a) 10CuAl-0.9, (b) 10CuAl-1.0 and (c) 10CuAl-1.1 calcined samples. ....	86
<b>Figure 3. 10.</b> (a) Ni 2p <sub>3/2</sub> , (b) Al 2p and (c) O 1s XP spectra for 10NiAl-x calcined samples. ....	88
<b>Figure 3. 11.</b> (a) Co 2p <sub>3/2</sub> , (b) Al 2p and (c) O 1s XP spectra for 10CoAl-x calcined samples. ....	89
<b>Figure 3. 12.</b> (a) Cu 2p <sub>3/2</sub> , (b) Al 2p and (c) O 1s XP spectra for 10CuAl-x calcined samples. ....	90
<b>Figure 3. 13.</b> TEM images (inset, nanoparticle size distribution) of 10NiAl-1.1 calcined sample. ....	92
<b>Figure 3. 14.</b> TEM-EDX and dot mapping analyses of 10NiAl-1.1 calcined sample. ....	92
<b>Figure 3. 15.</b> TEM images (inset, nanoparticle size distribution) of 10CoAl-1.1 calcined sample. ....	93
<b>Figure 3. 16.</b> TEM-EDX and dot mapping analyses of 10CoAl-1.1 calcined sample. ....	94
<b>Figure 3. 17.</b> SAED patterns of 10CoAl-1.1 calcined sample. ....	94
<b>Figure 3. 18.</b> TEM images (inset, nanoparticle size distribution) of 10CuAl-1.1 calcined sample. ....	95
<b>Figure 3. 19.</b> TEM-EDX and dot mapping analyses of 10CuAl-1.1 calcined sample. ....	95
<b>Figure 3. 20.</b> SAED patterns of 10CuAl-1.1 calcined sample. ....	95
<b>Figure 3. 21.</b> XRD patterns of 2MAI-x calcined catalysts. ....	99
<b>Figure 3. 22.</b> N <sub>2</sub> adsorption-desorption isotherm of MAI-x calcined catalysts. ....	101
<b>Figure 3. 23.</b> SEM images of (a) 2NiAl-0.9, (b) 2NiAl-1.0 and (c) 2NiAl-1.1 calcined samples. ....	102
<b>Figure 3. 24.</b> SEM images of (a) 2CoAl-0.9, (b) 2CoAl-1.0 and (c) 2CoAl-1.1 calcined samples. ....	103
<b>Figure 3. 25.</b> SEM images of (a) 2CuAl-0.9, (b) 2CuAl-1.0 and (c) 2CuAl-1.1 calcined samples. ....	103
<b>Figure 3. 26.</b> XRD patterns of XNiAl calcined catalysts. ....	106
<b>Figure 3. 27.</b> Effect of nickel content on the $\alpha/\gamma$ phase ratio. ....	107
<b>Figure 3. 28.</b> XRD patterns of XCoAl calcined catalysts. ....	108
<b>Figure 3. 29.</b> Effect of cobalt content on the $\alpha/\gamma$ phase ratio. ....	108
<b>Figure 3. 30.</b> XRD patterns of XCuAl calcined catalysts. ....	109
<b>Figure 3. 31.</b> N <sub>2</sub> adsorption-desorption isotherms of XNiAl calcined samples. ....	110

<b>Figure 3. 32.</b> N <sub>2</sub> adsorption-desorption isotherms of XCoAl calcined samples. ....	111
<b>Figure 3. 33.</b> N <sub>2</sub> adsorption-desorption isotherms of XCuAl calcined samples .....	112
<b>Figure 3. 34.</b> SEM images of (a) 5NiAl, (b) 10NiAl, (c) 15NiAl and (d) 20NiAl calcined samples. ....	113
<b>Figure 3. 35.</b> SEM images of (a) 5CoAl, (b) 10CoAl, (c) 15CoAl and (d) 20CoAl calcined samples. ....	114
<b>Figure 3. 36.</b> SEM images of (a) 5CuAl, (b) 10CuAl, (c) 15CuAl and (d) 20CuAl calcined samples. ....	116
<b>Figure 3. 37.</b> SEM-EDX elemental distribution maps of (a) 10NiAl, (b) 15NiAl and (c) 20NiAl calcined samples. ....	116
<b>Figure 3. 38.</b> SEM-EDX elemental distribution maps of (a) 10CoAl, (b) 15CoAl and (c) 20CoAl calcined samples.....	117
<b>Figure 3. 39.</b> SEM-EDX elemental distribution maps of (a) 10CuAl, (b) 15CuAl and (c) 20CuAl calcined samples.....	118
<b>Figure 3. 40.</b> XRD patterns of 5M5MAI calcined catalysts.....	120
<b>Figure 3. 41.</b> N <sub>2</sub> adsorption-desorption isotherm of 5M5MAI calcined catalysts.....	121
<b>Figure 3. 42.</b> SEM images of (a) 5Ni5CoAl, (b) 5Ni5CuAl and (c) 5Co5CuAl calcined samples. ....	122
<b>Figure 3. 43.</b> XP spectra of (a) 5Ni5CoAl, (b) 5Ni5CuAl and (c) 5Co5CuAl calcined samples. ....	124
<b>Figure 3. 44.</b> TEM images of 5Ni5CoAl calcined sample.....	126
<b>Figure 3. 45.</b> TEM images of 5Ni5CuAl calcined sample.....	127
<b>Figure 3. 46.</b> TEM images of 5Co5CuAl calcined sample. ....	127
<b>Figure 3. 47.</b> TEM-EDX elemental analyses of (a) 5Ni5CoAl (b) 5Ni5CuAl and (c) 5Co5CuAl calcined samples. ....	128
<b>Figure 3. 48.</b> TEM-EDX dot-mapping analyses of (a) 5Ni5CuAl and (b) 5Co5CuAl calcined samples. ....	129
<b>Figure 3. 49.</b> SAED patterns of (a) 5Ni5CoAl (b) 5Ni5CuAl and (c) 5Co5CuAl calcined samples. ....	130
 <b>Figure 4. 1.</b> (a) CO conversion under transient and (b) steady state conditions over the 10NiAl-x calcined catalysts. ....	138
<b>Figure 4. 2.</b> (a) CO conversion under transient and (b) steady state conditions over the 10CoAl-x calcined catalysts.....	139

<b>Figure 4. 3.</b> (a) CO conversion under transient and (b) steady state conditions over the 10CuAl-x calcined catalysts.....	140
<b>Figure 4. 4.</b> CO conversion over Al <sub>2</sub> O <sub>3</sub> . ....	141
<b>Figure 4. 5.</b> Comparison of the catalytic performances of the different 10MAI-x calcined catalysts for CO oxidation under transient and steady state conditions. ....	143
<b>Figure 4. 6.</b> (a) CO conversion under transient and (b) steady state conditions over the 2NiAl-x calcined catalysts. ....	145
<b>Figure 4. 7.</b> (a) CO conversion under transient and (b) steady state conditions over the 2CoAl-x calcined catalysts.....	147
<b>Figure 4. 8.</b> (a) CO conversion under transient and (b) steady state conditions over the 2CuAl-x calcined catalysts.....	148
<b>Figure 4. 9.</b> (a) CO conversion under transient and (b) steady state conditions over the XNiAl calcined catalysts.....	149
<b>Figure 4. 10.</b> (a) CO conversion under transient and (b) steady state over the XCoAl calcined catalysts.....	150
<b>Figure 4. 11.</b> (a) CO conversion under transient and (b) steady state conditions over the XCoAl calcined catalysts.....	151
<b>Figure 4. 12.</b> (a) CO conversion under transient and (b) steady state conditions over the 5M5MAI calcined catalysts. ....	156
<b>Figure A. 1.</b> XRD patterns of 10MAI-x calcined catalysts obtained with different RV/OV ratios. ....	186
<b>Figure A. 2.</b> Nitrogen adsorption/desorption isotherms of Al-x calcined samples obtained with different RV/OV ratios. ....	187
<b>Figure A. 3.</b> SEM images of Al-1.0 calcined sample. ....	187
<b>Figure A. 4.</b> SEM images of 10NiAl-0.8 calcined sample. ....	187
<b>Figure A. 5.</b> SEM images of 10NiAl-1.2 calcined sample. ....	188
<b>Figure A. 6.</b> SEM images of 10CoAl-0.8 calcined sample.....	188
<b>Figure A. 7.</b> SEM images of 10CoAl-1.2 calcined sample.....	188
<b>Figure A. 8.</b> SEM images of 10CuAl-0.8 calcined sample.....	188
<b>Figure A. 9.</b> SEM images of 10CuAl-1.2 calcined sample.....	189
<b>Figure A. 10.</b> XRD patterns of XNiAl calcined catalysts obtained with different metal loadings.....	189

<b>Figure A. 11.</b> XRD patterns of XCoAl calcined catalysts obtained with different metal loadings.....	190
<b>Figure B. 1.</b> XRD patterns of (a)10NiAl-x, (b) 10CoAl-x and (c) 10CuAl-x catalyst samples before and after their use in CO oxidation.....	193
<b>Figure B. 2.</b> XRD patterns of (a) XNiAl and (b) XCuAl catalyst samples before and after their use in CO oxidation. ....	194

## List of Tables

<b>Table 1. 1.</b> Properties of 3d Series of transition elements (Co–Cu) [18].....	12
<b>Table 1. 2.</b> Structural properties of Ni, Co and Cu oxides [19-24].....	13
<b>Table 1. 3.</b> <i>Structural properties of <math>\alpha</math>-Al<sub>2</sub>O<sub>3</sub> and <math>\gamma</math>-Al<sub>2</sub>O<sub>3</sub></i> [55, 56]. ....	17
<b>Table 1. 4.</b> Carbone monoxide oxidation activities of unsupported catalysts [85]. ....	20
<b>Table 1. 5.</b> Activity of unsupported cobalt oxide catalysts in CO oxidation [86]. ....	21
<b>Table 1. 6.</b> Light-off temperatures for Co <sub>3</sub> O <sub>4</sub> catalysts on various supports [92]. ....	22
<b>Table 1. 7.</b> Survey of catalytic studies over Co containing catalysts.....	23
<b>Table 1. 8.</b> Survey of catalytic studies over Cu containing catalysts.....	26
<b>Table 1. 9.</b> Most common precursors and solvents used for SCS [121, 129]. ....	39
<b>Table 1. 10.</b> Survey of different metal oxides prepared by SCS. ....	46
<b>Table 2.1.</b> Specifications of chemical reagents. ....	56
<b>Table 2.2.</b> Oxidizing and reducing valences of different chemical reagents. ....	58
<b>Table 2. 3.</b> Main techniques used for catalysts characterization. ....	61
<b>Table 2.4.</b> Operating conditions for catalytic testing.....	66
<b>Table 3. 1.</b> Elemental analysis of the 10MAI–x calcined catalysts. ....	74
<b>Table 3. 2.</b> Structural properties of 10MAI–x calcined catalysts. ....	77
<b>Table 3. 3.</b> Textural properties of 10MAI–x calcined catalysts. ....	82
<b>Table 3. 4.</b> BEs of the Ni 2p <sub>3/2</sub> , Al 2p and O 1s XP spectra for 10NiAl–x calcined samples. ....	88
<b>Table 3. 5.</b> BEs of the Co 2p <sub>3/2</sub> , Al 2p and O 1s XP spectra for 10CoAl–x calcined samples. ....	89
<b>Table 3. 6.</b> BEs of the Cu 2p <sub>3/2</sub> , Al 2p and O 1s XP spectra for 10CuAl–x calcined samples. ....	90
<b>Table 3. 7.</b> Physico-chemical properties of 2MAI–x calcined catalysts.....	101
<b>Table 3. 8.</b> Elemental analysis of the XMAI calcined catalysts. ....	104
<b>Table 3. 9.</b> Structural properties of $\gamma$ -Al <sub>2.67</sub> O <sub>4</sub> and NiAl <sub>2</sub> O <sub>4</sub> .....	105
<b>Table 3. 10.</b> <i>Structural properties of <math>\gamma</math>-Al<sub>2.67</sub>O<sub>4</sub>, Co<sub>3</sub>O<sub>4</sub> and CoAl<sub>2</sub>O<sub>4</sub></i> .....	107
<b>Table 3. 11.</b> CuO crystallite size of XCuAl calcined catalysts. ....	109
<b>Table 3. 12.</b> Textural properties of XMAI calcined catalysts. ....	112
<b>Table 3. 13.</b> XRF elemental analysis and textural properties of 5M5MAI calcined catalysts. ....	121

<b>Table 3. 14.</b> Surface M/Al atomic ratios determined by XPS for 5M5MAI calcined samples. ....	124
<b>Table 4. 1.</b> Effect of RV/OV ratio on the light-off temperatures of 10NiAl-x catalyst samples. ....	138
<b>Table 4. 2.</b> Effect of RV/OV ratio on the light-off and T <sub>50</sub> temperatures of 10CoAl-x catalyst samples. ....	139
<b>Table 4. 3.</b> Effect of RV/OV ratio on the light-off, T <sub>50</sub> and T <sub>100</sub> temperatures of 10CuAl-x catalyst samples. ....	141
<b>Table 4. 4.</b> Effect of RV/OV ratio on the light-off temperatures of 2NiAl-x catalyst samples. ....	146
<b>Table 4. 5.</b> Effect of RV/OV ratio on the light-off and T <sub>50</sub> temperatures of 2CoAl-x catalyst samples. ....	147
<b>Table 4. 6.</b> Effect of RV/OV ratio on the light-off, T <sub>50</sub> and T <sub>100</sub> temperatures of 2CuAl-x catalyst samples. ....	148
<b>Table 4. 7.</b> Effect of metal loading on the light-off, T <sub>50</sub> and T <sub>100</sub> temperatures of XNiAl calcined catalysts. ....	149
<b>Table 4. 8.</b> Effect of metal loading on the light-off, T <sub>50</sub> and T <sub>100</sub> temperatures of XCoAl calcined catalysts. ....	151
<b>Table 4. 9.</b> Effect of metal loading on the light-off, T <sub>50</sub> and T <sub>100</sub> temperatures of XCuAl calcined catalysts. ....	152
<b>Table 4. 10.</b> Main data of the characterization and catalytic activity tests over XMAI calcined catalysts. ....	154
<b>Table 4. 11.</b> The light-off, T <sub>50</sub> and T <sub>100</sub> temperatures of 5M5MAI calcined catalysts. ....	156
<b>Table 4. 12.</b> Main data of the characterization and catalytic activity tests over 5M5MAI calcined catalysts. ....	158
<b>Table A. 1.</b> Textural properties of Al-x calcined samples. ....	187

## List of Abbreviations

Abbreviation	Definition
VOCs	Volatile Organic Compounds
MACS	Microwave Assisted Combustion Synthesis
IUPAC	International Union of Pure and Applied Chemistry
BET	Brunauer-Emmett-Teller method
GHSV	Gas Hourly Space Velocity
HC	Hydrocarbon
NM	Not Mentioned
MW	Microwave
CS	Combustion Synthesis
SHS	Self-propagating High-temperature Synthesis
SCS	Solution Combustion Synthesis
RV	Reducing Valence
OV	Oxidizing Valence
C–H	Carbon-Hydrogen bond
TGA	ThermoGravimetric Analysis
DTA	Differential Thermal Analysis
DSC	Differential Scanning Calorimetry analysis
PEG	Polyethylene Glycol
SP	Stoichiometric Proportions
XRF	X-Ray Fluorescence spectrometry
WDXRF	Wavelength Dispersive X-Ray Fluorescence
XRD	X-Ray Diffraction
SEM	Scanning Electron Microscopy
TEM	Transmission Electron Microscopy
XPS	X-ray Photoelectron Spectroscopy
EDX	Energy Dispersive X-ray spectrometry
SAED	Selected Area Electron Diffraction
JCPDS	Joint Committee on Powder Diffraction Standards
ICDD	International Centre for Diffraction Data
FWHM	Full Width at Half Maximum
BJH	Barrett-Joyner-Halenda method
VVH	Space Velocity
BE	Binding Energy
T <sub>1</sub>	Light-off temperature of the oxidation of CO into CO <sub>2</sub>
T <sub>50</sub>	Temperature for the half conversion of CO into CO <sub>2</sub>
T <sub>100</sub>	Temperature for the full conversion of CO into CO <sub>2</sub>
XMAI–x, XMAI and 5M5MAI	Catalyst samples designation

## GENERAL INTRODUCTION

---

Metal oxides represent a large class of inorganic compounds possessing a broad range of physico-chemical properties. Metal oxides have found potential application in various areas including materials science, chemical sensors, microelectronics, nanotechnology, environmental remediation, analytical chemistry, solid-state chemistry, fuel cells, and catalysis. Due to their enhanced redox, acid-base and structural properties, metal oxides constitute one of the most important and widely used categories of solid catalysts, either as active phases or as supports for highly dispersed metal/metal oxides catalysts. Among the various metal oxides, transition metal based oxides are the most present in the preparation of catalytic materials and constitute the largest family of catalysts in heterogeneous catalysis. Transition metal oxides have been currently used by energy, chemical, and environmental industries, and their uses in environmental applications significantly expanded since the mid of the 20th century. In this field, the catalytic applications involve several important reactions such as dehydrogenation, selective oxidations, selective reductions, volatile organic compounds (VOCs) removal, photocatalysis and electrocatalysis. The understanding of the chemical compositions, crystal and electronic structure (oxidation state) at the surface of oxides catalytic materials is mandatory to establish correlation between their catalytic (chemical reactivity) and physicochemical properties.

As with most materials, metal oxides catalysts performances are strongly dependent on their preparation procedures and conditions. The catalysts' preparation significantly affects the chemical and structural features of the catalysts' surface thus directing their surface reactivity. Metal oxide catalysts can be prepared by different preparation routes, such as co-precipitation, impregnation, ion exchange, and deposition-precipitation. Although well established, these conventional methods still present considerable drawbacks as they need a high number of synthetic steps, they are highly energy- and time-consuming, and they require special equipment. Some novel preparation routes, such as microwave assisted combustion synthesis (MACS), allow overcoming the disadvantages of the conventional methods. It has been recently demonstrated that microwaves are a very effective technology in applied chemistry and can be employed as an attractive alternative for the development of new-technology materials. The advantages of MACS over conventional methods include the very short time duration, the set-up simplicity, the high reaction rates, the low operating temperatures, and the controlled volumetric heating. The introduction of microwave energy in oxides-based catalysts production has showed very good results on the chemical homogeneity of the obtained solids, a high purity, a high sinterability, and the possibility to obtain

homogeneous catalysts with enhanced specific surface area. The solution combustion route is a well-established method of preparing both simple and mixed metal oxides catalysts.

Heterogeneous oxidation catalytic reactions are very interesting in environment protection processes and the reaction of the oxidation of carbon monoxide (CO) into carbon dioxide (CO<sub>2</sub>) has been considered as an effective pathway to reduce CO emissions and as an ideal reaction to study the catalytic performance of the catalysts. Abatement of CO has attracted the attention of researchers for a long time during the last decades, and the development of the “three-way” catalytic converter is an example of an effective practice. Supported precious metals such as Pt, Pd or Rh deposited on alumina and/or ceria-doped oxides are the most efficient CO oxidation catalysts in automotive exhaust gas catalysis. Due to the high price and scarcity of precious metals, and to the remarkable progresses in oxide syntheses, catalytic oxidation of CO over oxide catalysts has gained significant interest. Simple oxides of transition metals, mainly Co, Ni, and Cu have been extensively studied and they have shown an interesting activity for CO oxidation; however, most of these oxides are generally sensitive to deactivation or poisoning phenomena. CO oxidation performances over these transition metal oxides are considered to be enhanced by loading/mixing on/with other oxides, such as alumina, zirconium oxide or ceria.

The main objective of this project is to prepare mixed binary and ternary transition metal oxides based catalysts by microwave assisted solution combustion method for carbon monoxide removal. It aims to develop an original synthesis for the preparation of active and stable catalysts. Ni, Co and Cu oxides based-catalysts were chosen as active phases due to their relatively low cost, availability and enhance activity in oxidation reactions.

One of the most challenging tasks in catalysis studies is to deeply understand the origin of their properties and to figure out how to modulate them by modifying the composition and/or the synthesis parameters. In order to answer to this challenge, a research strategy was put in place and the thesis manuscript follows the same logic. The first part of this thesis project was dedicated to the synthesis and deep characterization of the catalytic materials by a multi technique approach. The second part was devoted to the study of the catalytic activity of the obtained materials in the reaction of oxidation of carbon monoxide, used as test reaction. In a third, the catalytic properties were analyzed and correlated to their physicochemical properties. Several factors such as the initial chemical precursor's composition, the nature of the metal precursor and the metal loading were explored.

The present thesis report is presented in four chapters; each chapter begins with a brief –introduction– of the developed task and closes with –conclusions– to remind the readers of the key findings.

**Chapter 1 –REVIEW OF THE LITERATURE–** highlights the importance of transition metal oxides materials, their properties, their applications in heterogeneous catalysis, and their method of elaboration. A brief overview on microwave chemistry's theory is reported before to focus on the solution combustion synthesis route specifically used for making oxide materials. The concept of combustion reaction, the solution combustion parameters, and the possible mechanism involved in the synthesis of alumina are discussed. At last, details on metal oxides based catalysts synthesized by solution combustion are presented, along with a summary of their specific properties and applications.

**Chapter 2 –MATERIALS AND METHODS–** describes the chemicals used in the various preparation experiments, reports the theoretical equations used for samples' elaboration, and the experimental protocols and instruments used, during this thesis work.

**Chapter 3 –CATALYST CHARACTERIZATION–** provides a thorough discussion of the characterization results of the various metal oxide catalysts. In this chapter, the correlation between synthesis parameters and physicochemical properties was described. Moreover, this chapter reports a comparative study of the catalysts presenting various compositions and metal contents.

**Chapter 4 –CATALYST ACTIVITY EVALUATION–** is devoted to the study of the catalytic activity, with a particular emphasis on the effect of the factors stated in chapter 3. The correlation between physicochemical properties of the catalysts and their CO oxidation activity was also described.

Finally, this thesis report closes with –CONCLUSIONS AND PERSPECTIVES– regarding the work described in this thesis.

## Résumé en Français de l'introduction générale

Les oxydes métalliques représentent une famille de composés inorganiques disposant d'une large gamme de propriétés physico-chimiques, qui sont par conséquent adaptés pour différentes applications. En raison de leurs propriétés acido-basiques particulières, de leur caractère redox et de leurs propriétés structurales, les oxydes métalliques constituent une des catégories de catalyseurs solides les plus utilisées, aussi bien en tant que phase active ou comme support pour des catalyseurs à base de métaux dispersés sur des supports ou des oxydes métalliques seuls. Parmi les différents oxydes métalliques, les métaux de transition sont les plus utilisés pour la préparation de matériaux catalytiques.

Les catalyseurs d'oxydes métalliques peuvent être préparés de différentes façons, telles que par co-précipitation, imprégnation, échange ionique ou par dépôt et précipitation. Bien que bien établies, ces méthodes conventionnelles présentent des inconvénients majeurs car elles nécessitent des nombreuses étapes de synthèse, des temps de synthèse longs, des protocoles de préparation fortement énergivores et elles nécessitent des équipements dédiés et des traitements post-synthèse. De nouvelles méthodes de préparation, telle que la synthèse par combustion assistée par micro-ondes (MACS), permettent de se débarrasser de ces inconvénients majeurs. L'introduction de l'énergie par micro-ondes pour la production de catalyseurs d'oxydes métalliques a conduit à de très bons résultats en termes d'homogénéité chimique, pureté et la possibilité d'obtenir des catalyseurs avec des propriétés texturales et structurales améliorées.

L'objectif principal de ces travaux de thèse était de développer de nouveaux catalyseurs d'oxydes mixtes binaires ou ternaires de métaux de transition par la méthode de combustion en solution assistée par micro-ondes. La stratégie adoptée dans le cadre de ces travaux de thèse a été la suivante: pendant la première partie de ces travaux les activités ont essentiellement concerné à la synthèse et à la caractérisation fine des matériaux par une approche multi techniques. La seconde partie des travaux a porté sur l'évaluation des performances catalytiques physico-chimiques des catalyseurs élaborés pour la réaction test choisie: l'oxydation du monoxyde de carbone. Ce document entend retracer la méthodologie présentée ci-dessus, et présenter les principaux résultats obtenus suite aux travaux menés au cours de ces trois années de recherche.

Ce manuscrit de thèse est composé de quatre chapitres, une introduction et une conclusion. Il décrit l'ensemble des travaux accomplis sur la synthèse des catalyseurs d'oxydes métalliques et l'étude de leurs propriétés physico-chimiques et de leurs activités catalytiques.

Le **chapitre 1** –REVUE DE LA LITTÉRATURE– met en avant l'importance des oxydes de métaux de transition en catalyse hétérogène. Il reprend également leurs caractéristiques physico-chimiques et leurs propriétés particulières en catalyse, leurs méthodes d'élaboration, avec une attention particulière portée sur la méthode de combustion en solution assistée par micro-ondes.

Le **chapitre 2** –MATERIAUX ET METHODES– présente les matériaux et les méthodes utilisées pour la synthèse, la caractérisation physico-chimique, et la mise en œuvre des tests catalytiques. La théorie, permettant de calculer et de bien maîtriser les conditions de synthèse des catalyseurs d'oxydes métalliques, est également exposée.

Le **chapitre 3** –CARACTÉRISATION DES CATALYSEURS– reprend les principaux résultats obtenus lors de la caractérisation multi-échelle des catalyseurs d'oxydes métalliques (oxydes mixtes bi ou tri métalliques).

Le **chapitre 4** –ÉVALUATION DE L'ACTIVITÉ CATALYTIQUE– regroupe les principaux résultats des tests d'oxydation catalytiques. Les performances catalytiques des catalyseurs sont comparées et interprétées en fonction de leurs propriétés physico-chimiques.

## CHAPTER 1. REVIEW OF THE LITERATURE

## Table of contents

Introduction .....	10
1.1 The potential of metal oxides for heterogeneous catalysis.....	10
1.1.1 Characteristics of Ni, Co and Cu oxide-based catalytic materials .....	11
1.1.1.1 Bulk structure .....	12
1.1.1.2 Surface structure.....	13
1.1.2 Multifunctional catalysts containing Ni, Co or Cu .....	14
1.1.2.1 Ni containing catalysts.....	14
1.1.2.2 Co containing catalysts .....	15
1.1.2.3 Cu containing catalysts .....	15
1.1.3 Characteristics of alumina and its application in catalysis .....	16
1.1.4 Alumina-Ni/Co/Cu chemical interaction.....	18
1.1.5 Applications in heterogeneous catalysis: oxidation of carbon monoxide .....	20
1.1.5.1 Cobalt oxide ( $\text{Co}_x\text{O}_y$ ).....	21
1.1.5.2 Nickel oxide ( $\text{Ni}_x\text{O}_y$ ) .....	24
1.1.5.3 Copper oxide ( $\text{Cu}_x\text{O}_y$ ).....	24
1.1.6 Methods for metal oxides catalytic materials elaboration.....	27
1.1.6.1 Ceramic method (solid-state reaction).....	27
1.1.6.2 Co-precipitation.....	27
1.1.6.3 Sol-gel.....	28
1.1.6.4 Impregnation .....	28
1.2 Microwave chemistry for metal oxide catalysts synthesis .....	29
1.2.1 Introduction to microwave chemistry .....	29
1.2.2 Microwave assisted solution combustion synthesis .....	34
1.2.2.1 Theory of combustion reaction .....	35
1.2.2.2 Solution combustion parameters .....	36
1.2.2.2.1 Chemical composition of precursors.....	37
1.2.2.2.2 Stoichiometry of the reactants (RV/OV ratio).....	39
1.2.2.2.3 Heating method.....	39
1.2.2.3 Mechanism of oxide forming .....	40
1.2.2.4 Metal oxides prepared by SCS .....	41
1.2.2.4.1 $\text{Al}_2\text{O}_3$ .....	41

1.2.2.4.2	NiO .....	41
1.2.2.4.3	Co <sub>3</sub> O <sub>4</sub> .....	42
1.2.2.4.4	CuO .....	42
1.2.2.4.5	Ni/Al <sub>2</sub> O <sub>3</sub> .....	43
1.2.2.4.6	Co/Al <sub>2</sub> O <sub>3</sub> .....	44
1.2.2.4.7	Cu/Al <sub>2</sub> O <sub>3</sub> .....	44
1.2.3	Advantages and disadvantages .....	48
Conclusions .....		49
Résumé en Français du chapitre 1 .....		51

## Introduction

This chapter includes a thorough literature survey and provides background information on the subject of interest. An account of the characteristics, applications and method of elaboration of Ni, Co and Cu-based oxide catalysts can be found in the first Section. Subsequent section of this chapter provides a general overview of the microwave-assisted solution combustion method. In this section, the theory of combustion reaction and the method's parameters are discussed. Possible mechanism involved in the synthesis of alumina is given. A list of metal oxides prepared by solution combustion method is presented, along with their preparation procedures, properties and applications. At the end, advantages and drawbacks of the solution combustion method are summarized.

### 1.1 The potential of metal oxides for heterogeneous catalysis

The first introduction of the concept of “catalysis” was by Berzelius in 1836, in order to normalize some earlier findings on chemical transformations, such as starch transformation into sugar by acids, the decomposition of hydrogen peroxide into water and molecular oxygen by metals, the conversion of alcohol to acetic acid over platinum wire, and the conversion of alcohol to acetic aldehyde over platinum wire, etc [1-5]. In his report released in 1836, Berzelius proposed the existence of a new force, called “*catalytic power*”, and described the catalytic concept as the decomposition of chemical compounds by the “*catalytic power*” [2]. Sixty years later, Oswald set up the kinetic model of this phenomenon and provided the definition: “*A catalyst is a substance that changes the rate of a chemical reaction without itself appearing in the products*” [6]. By definition and according to the IUPAC (1996), “*a catalyst is a substance that increases the rate of a reaction without modifying the overall standard Gibbs energy of the reaction*” [7].

Catalytic reactions are classified into two broad categories based on whether the catalyst is soluble in the reaction (homogeneous catalysis) or not (heterogeneous catalysis). Heterogeneous catalysis is widely used in the petrol industry and the production of base chemicals. In fact, nearly 85%–90% of all products in chemical industry rely on heterogeneous catalysis [8]. The key benefit of a heterogeneous catalyst is that it remains in a solid state during the reaction, allowing its recovery and reuse.

Heterogeneous catalysis is a multidisciplinary field that requires strong knowledge on solid catalysts, ranging from their preparation to their characterization (of the surface mainly), but also on the reaction kinetics and mechanisms.

Metal oxides belong to the most useful catalytic materials in heterogeneous redox catalysis [8], in which the active phase consists of single metal oxides, metal oxide mixtures, or complex metal oxides. Applications of metal oxide catalysts reach out various catalytic reactions including acid-base reactions, selective reduction reactions, selective oxidation reactions, total oxidation reactions, etc. Three key criteria of metal oxides are of importance:

- The redox properties of the oxide
- The oxidation state of the surface
- The coordination environment of atoms in the surface [9].

These properties might arise from the fact that metal oxides are made-up of metallic cations and oxygen anions. The ionicity of metallic cations and oxygen anions in the surface layer results in the dissociative adsorption of adsorbed molecules and the presence of surface-adsorbate species interactions [9]. Metallic cations and oxygen anions exposed on the surface form acidic and basic sites, as well as acid-base pair sites that can eventually introduce acid-base properties. The fact that metallic cations can exist in various oxidation states confers the ability to undergo oxidation and reduction [9]. The acid-base and redox properties are a matter of choice of the metallic cations and they have determining effects on the interaction of adsorbed molecules with the oxide surfaces [10-13]. A variety of other contributing factors are: the presence of defect structures, the presence of crystalline and amorphous phases, the structure of a crystalline phase, the crystallite size, the bulk and surface composition, the surface structure and the kinetics and thermodynamics of phase formation and transformation [14].

### **1.1.1 Characteristics of Ni, Co and Cu oxide-based catalytic materials**

Transition metal oxides are potential catalysts in heterogeneous catalysis. These metal oxides possess interesting surface properties, which are supposed to be beneficial for their application in catalysis. Some aspects of the surface chemistry of transition metal oxides are listed as follows:

- Presence of cations and anions in a well-defined spatial structure
- Possibility of covalent and ionic bonding

- Presence of surface adsorbed species
- Ability of cations to undergo oxidation and reduction
- Presence of cationic and anionic vacancies
- Presence of surface acidity and basicity
- High mobility of lattice oxygen and their capability to react [15].

Ni, Co and Cu oxide-based catalysts are among the most commonly used metal oxide catalysts. Such metal oxides have several advantages, including their availability and their low price that make them a good alternative to expensive noble-metal based catalysts. 3d transition metal oxides such as, Ni, Co and Cu oxides (**Table 1.1**) exhibit non-stoichiometric composition giving rise to the presence of structural defects. Such defects, when present at the surface of the oxide, ameliorate the electrons transport connected to enhanced electrical conductivity [14, 16]. Additionally, transition metal oxide based catalysts are more resistant to deactivation by poisoning compared to noble metal based catalysts [17].

**Table 1. 1.** *Properties of 3d Series of transition elements (Co–Cu) [18].*

Group	3	...	9	10	11	12
Period 4	Sc	...	$_{27}\text{Co}$	$_{28}\text{Ni}$	$_{29}\text{Cu}$	Zn
Electron configuration	–	–	$[\text{Ar}] 4s^2 3d^7$	$[\text{Ar}] 4s^2 3d^8$ $[\text{Ar}] 4s^1 3d^9(*)$	$[\text{Ar}] 4s^2 3d^9$ $[\text{Ar}] 4s^1 3d^{10}(*)$	–
Atomic radii (Å)	–	–	1.88–2.14	1.94–2.16	1.9–2.16	–

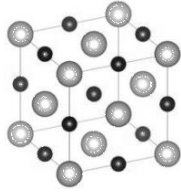
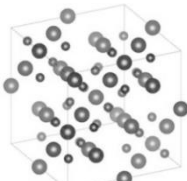
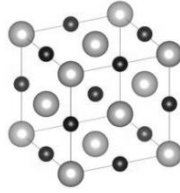
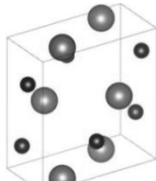
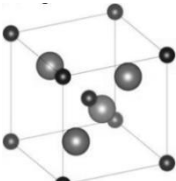
(\*): Exceptions related to Klechkowski's rule

#### 1.1.1.1 Bulk structure

The composition, structure, and properties of transition metal oxides are so variable that only a generalization can be stated: the ionic radius of a transition metal is usually smaller than that of  $\text{O}^{2-}$ . Thus, most of oxide structures exhibit cubic close packing of anions, with metal cations occupying the octahedral and tetrahedral holes (sites) of the oxide network [15]. Transition metal oxides exist in several crystal structures. Certain oxide could present more than one crystal structure at ambient temperature due to their high activation energy in the process of transformation from a less thermodynamically stable to a more stable structure [15].

The known structures of Ni, Co and Cu oxides, studied as catalytic materials, are summarized and drawn in **Table 1.2**.

**Table 1. 2.** *Structural properties of Ni, Co and Cu oxides [19-24].*

Oxides	CoO <sup>1</sup>	Co <sub>3</sub> O <sub>4</sub> <sup>1</sup>	NiO <sup>1</sup>	CuO <sup>1</sup>	Cu <sub>2</sub> O <sup>1</sup>
Unit cell of the crystal structure	 Rock-salt (NaCl)	 Spinel	 Rock salt (NaCl)	 PtS structure	 Cristobalite
Crystal system	Cubic	Cubic	Cubic	Monoclinic	Cubic
Crystal Lattice	—	—	Bunsenite	Tenorite	Cuprite
Lattice Parameters [Å, °]	a=b=c=4.2667 $\alpha=\beta=\gamma=90.0$	a=b=c=8.0821 $\alpha=\beta=\gamma=90.0$	a=b=c=4.1684 $\alpha=\beta=\gamma=90.0$	a=4.6837 b=3.4226 c=5.1288 $\alpha=\gamma=90.0$ $\beta=99.54$	a=b=c=4.258 $\alpha=\beta=\gamma=90.0$
Unit cell volume[Å <sup>3</sup> ]	77.67	527.92	72.43	81.08	77.20

● Oxygen atoms; ● Metal atoms

<sup>1</sup>Unit cell projected along the normal vector of facet (121) with c axis pointing upward

### 1.1.1.2 Surface structure

Surface reconstruction is achieved through thermodynamically driven atomic ordering, which takes place in an oriented manner to minimize the surface Gibbs energy per unit surface area. The reduction of the surface Gibbs energy results in thermodynamically more stable oxides. However, metastable surface structure can exist if the energy barrier for reconstruction is not reached.

When a metastable surface acquires enough thermal energy, upon heating, to reach the barriers for atomic migration, reconstruction by rearrangement of surface atoms takes place to lower the surface Gibbs energy and the structure of the reconstructed surface is no longer a simple extension of the bulk. Otherwise, adsorption of molecules can substantially change the stability of a certain surface structure. It often increases the stability of unstable surface. Some surfaces lose oxygen atoms to lower the Gibbs energy of the system. In this case, the anion vacancies form a sub-structure [15].

### 1.1.2 Multifunctional catalysts containing Ni, Co or Cu

#### 1.1.2.1 Ni containing catalysts

Nickel belongs to the same subgroup of palladium in the period table and it can be considered as its “poor younger sibling” in the field of transition metal catalysis. Indeed, the use of nickel as a catalyst, particularly in hydrogenation reactions, has been established, in 1897, by the investigations of Sabatier and Senderens [25, 26]. In the periodic table, nickel is among the group 10 elements next to palladium (Pd) and platinum (Pt), which means that it can perform many of the same elementary reactions [27].

Moving back into the history of nickel as a catalyst, the activity of reduced nickel phase, in hydrogenation reactions, is connected to that of nickel oxide and especially of nickel suboxide ( $\text{Ni}_4\text{O}$ ), which results from the incomplete reduction of the monoxide. According to the analysis of Sabatier and Espil, it has been established that the process of nickel monoxide reduction ( $\text{NiO}$ ), during hydrogenations reactions, passes through the formation of a suboxide, apparently  $\text{Ni}_4\text{O}$ , which is also partially reduced to metallic nickel [28]. Afterwards, the use of Nickel, supported or combined with another compound, has expanded and grown significantly in many interesting catalytic reactions related to both the academic and industrial areas of material science.

Over the years, nickel based catalysts have been identified to be among the most efficient transition metal based catalysts in catalytic biomass gasification for steam reforming and tar cracking [29-34]. Compared to reduced nickel, the use of nickel oxide might seem less spectacular, as its application is limited to some oxidation reactions including the catalytic combustion reactions and the oxidation of volatile organic compounds (VOCs) [17]. The catalytic properties of nickel oxide compounds strongly depend from the preparation methods and the temperature of the oxide formation.

Some of the key features of nickel-based catalysts that have to be considered are: (1) the high reactive organo-metallic species, (2) the high carbon-carbon bond rupture capability (3) the easy accessibility of  $\text{Ni}^0/\text{Ni}^{\text{I}}/\text{Ni}^{\text{II}}/\text{Ni}^{\text{III}}$  oxidation states and (4) the strong affinity to unsaturated systems and coordination (activation) of multiple bonds [35]. However, one major issue in using nickel catalyst is the rapid loss of activity due to sensitivity to poisoning, especially coke deposition and progressive formation of sulphate, which are well known to lead to irreversible deactivation [29].

### 1.1.2.2 Co containing catalysts

Co containing catalysts are also one of the most active low-cost catalysts, which have been used for various heterogeneous catalytic oxidation reactions, including the oxidation of VOCs, methane, toluene, propane and ethanol [37-44]. The high activity of Co containing catalysts in oxidation reactions is associated to the presence of mobile oxygen in their spinel structure [44]. These catalysts exhibit excellent reduction ability and oxygen vacancies as well as a high concentration of electrophilic oxide species [44]. The activity of Co containing catalysts depends on the preparation method, treatment conditions, oxidation state and the nature of the selected supports and promoters. For the supported Co containing catalysts, the activity depends mainly on the nature of the support and the direct Co-support interactions. Studies on cobalt based catalysts supported on different supports ( $\text{Al}_2\text{O}_3$ ,  $\text{SiO}_2$ ,  $\text{ZrO}_2$ ,  $\text{TiO}_2$ , etc) showed that the varied cobalt-support interactions give rise to differences in reducibility and dispersion of the active phase on different supports, consequently affecting the activity of cobalt oxide catalysts [40-43]. Promotion of Co containing catalysts with noble metals such as Ru, Pt and Pd can modify significantly the cobalt catalyst structure and subsequently the catalytic performance.

### 1.1.2.3 Cu containing catalysts

Copper containing catalysts have received a great deal of attention, with respect to Ni-based catalyst, for their outstanding catalytic properties as well as low cost. Copper-based catalysts are active in wide range of catalytic oxidation reactions, including the total oxidation of carbon monoxide, hydrocarbons, chlorinated hydrocarbons, and alcohols and nitrogen oxides. Sulphur dioxide reduction reactions can be also catalyzed by copper oxide [44-48]. This catalyst is considered as well as an ideal model to understand the mechanism of many catalytic reactions. Other advantages include long lifetime and possibility of regeneration [17, 45].

It is worth noting that Ni, Co and Cu oxides-based catalytic materials are not widely used solely as heterogeneous catalysts for many reasons, including:

- The hydrothermal stability is one important limitation for single oxides
- The reactivity per mass unit of oxides is much lower than that of noble metals
- The sensitivity to poisons such as  $\text{SO}_x$ , CO, and  $\text{NO}_x$  is high [17]

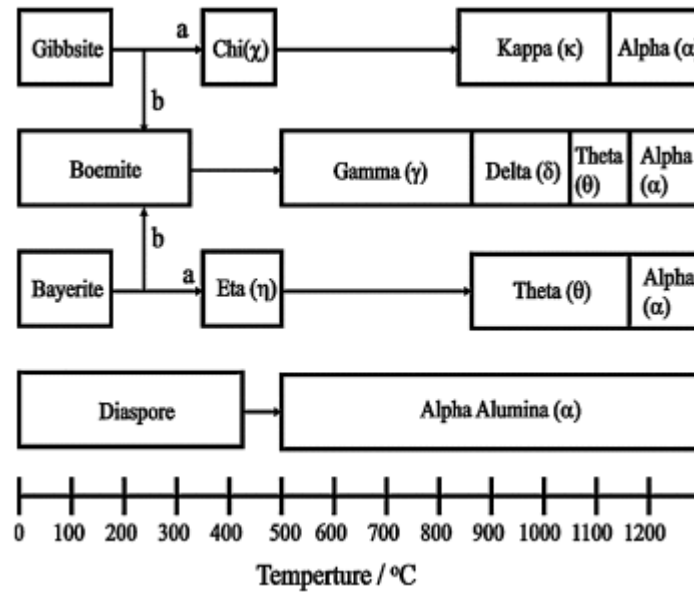
Several research studies were carried out to deal with those limitations and to establish strategies for improving the stability and activity of single metal-oxide catalysts, although the

reactivity per mass unit cannot obviously compete with that obtained over noble metals. To overcome these limitations, various preparation solutions have been tested as dispersing the oxides on various catalyst supports, doping with metal additives, producing porous structures with enhanced specific surface, by putting in place new synthesis routes, in order to form solid solutions and produce mixed-oxide structures.

The use of mixed oxides materials seems to promote the catalytic activity and stability of the catalysts. Indeed, transition metal elements with mixed valences are beneficial to enhance the electronic, structural, and chemical properties and to obtain high catalytic performances [14]. In this respect, some mixed oxide catalysts have shown a clear improvement over single oxides, such as higher thermal stability and better sintering resistance under different reaction conditions.

### 1.1.3 Characteristics of alumina and its application in catalysis

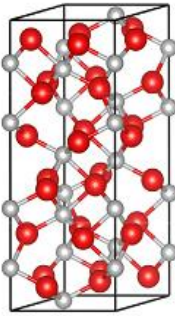
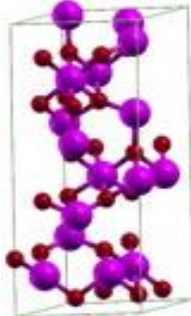
Aluminum oxide ( $\text{Al}_2\text{O}_3$ ) or alumina exists both in amorphous-hydrated forms ( $\text{Al}_2\text{O}_3 \cdot x\text{H}_2\text{O}$ : diaspor =  $\text{Al}_2\text{O}_3 \cdot \text{H}_2\text{O}$ ; gibbsite =  $\text{Al}_2\text{O}_3 \cdot 3\text{H}_2\text{O}$  and bauxite = impure form of gibbsite) and crystalline forms such as  $\chi$ - $\text{Al}_2\text{O}_3$ ,  $\eta$ - $\text{Al}_2\text{O}_3$ ,  $\gamma$ - $\text{Al}_2\text{O}_3$ ,  $\kappa$ - $\text{Al}_2\text{O}_3$ ,  $\delta$ - $\text{Al}_2\text{O}_3$ ,  $\beta$ - $\text{Al}_2\text{O}_3$ ,  $\theta$ - $\text{Al}_2\text{O}_3$  and  $\alpha$ - $\text{Al}_2\text{O}_3$ . Dehydrating amorphous-hydrated alumina by thermal or hydroxylation treatments leads to transition aluminas ( $\chi$ - $\text{Al}_2\text{O}_3$ ,  $\eta$ - $\text{Al}_2\text{O}_3$ ,  $\gamma$ - $\text{Al}_2\text{O}_3$ ,  $\kappa$ - $\text{Al}_2\text{O}_3$ ,  $\delta$ - $\text{Al}_2\text{O}_3$ ,  $\beta$ - $\text{Al}_2\text{O}_3$ ,  $\theta$ - $\text{Al}_2\text{O}_3$ ). These phases are thermally unstable and undergo an irreversible phase transformation when a defined temperature limit is over passed. On the other hand, the evolution kinetics of the transition aluminas depend on the treatment conditions (duration and temperature). Several studies have shown that transition aluminas start to convert into the most thermally stable form  $\alpha$ - $\text{Al}_2\text{O}_3$  (or corundum) at around 500 °C, whereas a well crystalline form is only formed under heat treatments at elevated temperatures above  $\approx 1100$  °C [49-52]. **Figure 1.1** displays the pathways of  $\text{Al}_2\text{O}_3$  transition during heat treatment.



**Figure 1. 1.** Sequence of structure transformation of alumina and aluminum hydroxides [53].

Transition aluminas, especially  $\gamma$ - $\text{Al}_2\text{O}_3$ , are widely used in catalysis and can be applied either as a catalytic support or as a catalyst. They have a high degree of porosity and large surface area (about  $100$ – $250 \text{ m}^2\text{g}^{-1}$ ). The surface area decreases dramatically with the formation of  $\alpha$ - $\text{Al}_2\text{O}_3$  ( $1$ – $5 \text{ m}^2\text{g}^{-1}$ ) [54]. The bulk crystal structure of  $\alpha$ - $\text{Al}_2\text{O}_3$  and  $\gamma$ - $\text{Al}_2\text{O}_3$  with the lattice parameters are presented in **Table 1.3**.

**Table 1. 3.** Structural properties of  $\alpha$ - $\text{Al}_2\text{O}_3$  and  $\gamma$ - $\text{Al}_2\text{O}_3$  [55, 56].

Oxide	$\alpha$ - $\text{Al}_2\text{O}_3$	$\gamma$ - $\text{Al}_2\text{O}_3$
Unit cell of the crystal structure	 <p>Corundum</p>	 <p>Spinel-like</p>
Crystal system	Hexagonal	Triclinic close to hexagonal
Lattice parameters [Å, °]	$a = b = 4.754$ $c = 12.990$ $\alpha = \beta = 90.0$ $\gamma = 120.0$	$a = 5.606$ $b = 5.570$ $c = 13.482$ $\alpha = 89.4$ $\beta = 90.0$ $\gamma = 120.2$

●● Oxygen atoms; ●● Metal atoms

Aluminum oxide possesses strong ionic inter-atomic bonding, making it an extremely stable material. Other interesting properties include excellent mechanical strength, a high melting point, and most importantly, chemical inertness under severe conditions of temperature and corrosion [55]. Such properties combined with its low cost and availability made alumina an attractive choice in many applications. In particular, alumina is widely used in soft abrasive, wear-resistant coating, catalyst support, adsorbent, electrical component, and a large variety of other industrial applications. In catalysts field, alumina is used due to its ideal cost-efficiency, adhesive properties, structural and thermal stability over the temperature range of interest for most catalytic reactions in both oxidizing and reducing atmospheres. In addition, it exhibits acidic/basic properties, which make it appropriate system to be used as a support for highly dispersed metal catalysts [57]. Mesoporous alumina, with high surface area and enhanced textural properties (high surface area and pore volume, narrow pore size distribution) is of great interest, allowing a better dispersion of active sites [58-60]. Alumina-supported precious metal catalysts (Pt, Pd or Rh) have been used, since the 1980's, in automotive and industrial catalytic converters for VOCs removal [61-63]. Alumina supported/mixed with transition metal oxides has shown also an excellent catalytic activity on total oxidation of CO and hydrocarbons [17].

#### **1.1.4 Alumina-Ni/Co/Cu chemical interaction**

Supported oxide catalysts that do not interact with the support develop three dimensional crystallites, whose properties are similar to those of large bulk crystals. However, some oxides interact strongly with the supports and form well-dispersed or monolayer structures, which properties are different from the three-dimensional crystallites.

The formation of well-dispersed or monolayer phases is actually quite common among transition metal oxides and the existence of this interaction appears to be a general characteristic of the most part of  $\gamma$ -Al<sub>2</sub>O<sub>3</sub>-supported/mixed oxide catalysts, since the  $\gamma$ -Al<sub>2</sub>O<sub>3</sub> crystal structure corresponds to that of the spinel characterized by a deficit of cations (about 11 % of the cation sites missing to achieve stoichiometry) [55, 56, 64]. This interaction is expressed in terms of incorporation of metal ions into the alumina lattice sites of octahedral or tetrahedral symmetry. The incorporation of metal ions into tetrahedral sites (strong interaction) produces a metal “surface spinel”, which is probably similar to metal aluminate. Incorporation of metal ions into octahedral sites (weak interaction) leads to the formation of dispersed metal oxide species close to the surface. When the saturation of all available lattice

sites is reached (monolayer coverage), the “bulk-like” metal oxide phases segregate on the surface. A greater proportion of the metal ions diffuse into the lattice sites of alumina when the temperature increases, and eventually gives rise to the formation of a solid solution of bulk aluminate.

Nickel oxide forms a well-dispersed phase on  $\gamma$ - $\text{Al}_2\text{O}_3$  instead of crystallites of NiO. This well-dispersed two-dimensional phase is actually constituted of Ni ions occupying the tetrahedral holes at the surface of the alumina to form a layer of spinel-like  $\text{NiAl}_2\text{O}_4$ . It seems that the addition of another phase (metals/metal oxides) to Ni- $\gamma$ - $\text{Al}_2\text{O}_3$  systems affects the interaction between alumina and Ni ions [65-70]. Similar incorporation into the alumina structure has also been observed for Co, and Cu in Co- $\gamma$ - $\text{Al}_2\text{O}_3$  [71-74] and Cu- $\gamma$ - $\text{Al}_2\text{O}_3$  [75] systems, respectively.

As mentioned earlier, some mixed oxides with alumina could form aluminates  $\text{MAl}_2\text{O}_4$ , where M is a divalent cationic metal, resulted from the solid-solid chemical interaction. Aluminate adopts spinel structures with interesting physical and electronic properties. The structure of spinel  $\text{MAl}_2\text{O}_4$  is cubic with tetrahedral sites occupied by cation M (**Figure 1.2 (a)**) and octahedral sites occupied by cation Al (**Figure 1.2 (b)**) [76, 77]. Mixed oxides with spinel structure can be used as catalysts or catalytic support. They present undisputable advantages, such as high thermal stability, high mechanical resistance, low surface acidity and hydrophobicity.

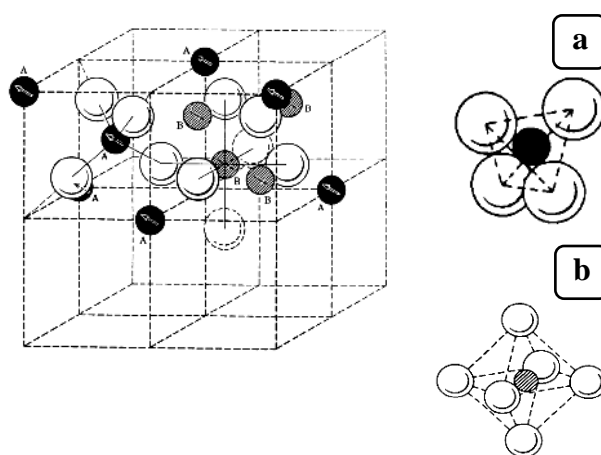


**Figure 1. 2.** *Crystal structure of spinel (shaded circles: M atoms; hollow circles: O atoms) [77].*

### 1.1.5 Applications in heterogeneous catalysis: oxidation of carbon monoxide

Carbon monoxide (CO) is an integral component of atmospheric pollution, produced largely from vehicle emissions, industrial activities and residential sector. CO is considered as a precursor of ground-level ozone formation, it also contributes to the acidification of air, soil and groundwater, which affects the balance of the earth's ecosystems and the human well-being [78, 79].

In automotive exhaust emission control, the catalytic oxidation of carbon monoxide ( $2\text{CO} + \text{O}_2 \rightarrow 2\text{CO}_2$ ) is a major solution for CO abatement [80-84]. CO oxidation on supported noble metal catalysts has attracted great interest during the past half-century. The reaction was studied on model catalysts based on noble metals (platinum, palladium, rhodium, and gold) deposited on alumina and/or ceria. Three-way automotive catalysts were developed in the same model to achieve an efficient emission control by simultaneously catalyzing three types of reactions: CO oxidation, hydrocarbon (HC) oxidation, and  $\text{NO}_x$  reduction [61-63].

Supported or unsupported transition metal oxides have shown also a good activity in the oxidation of CO. The most commonly used catalysts include chromium oxide, manganese dioxide, iron oxide, cobalt oxide, nickel oxide and copper oxide [44]. **Table 1.4** shows the activities of unsupported noble metals and transition metal oxide catalysts for CO oxidation at 300°C (Gas mixture = 1 % CO in  $\text{O}_2$  excess).

**Table 1. 4.** *Carbone monoxide oxidation activities of unsupported catalysts [85].*

Active phase	Reaction rate at 300 °C
Pd	500
Pt	100
Au	15
$\text{Co}_3\text{O}_4$	80
CuO	45
$\text{MnO}_2$	3.4
$\text{Fe}_2\text{O}_3$	0.4
$\text{Cr}_2\text{O}_3$	0.03
NiO	0.013

It is obvious that noble metals are more active than transition metal oxide based catalysts. However, some oxides, especially those of Co and Cu, present an interesting activity for CO oxidation. Transition metal oxide based catalysts were widely used for the oxidation of VOCs, due to their low cost and ready availability. Other benefits include the following: long

lifetime, regeneration capability and resistance to poisoning [44]. All these advantages have allowed transition metal oxides to be reconsidered for practical applications. A very important point is the presence of an oxide (the support), which may have a crucial effect on the activity and performance of active transition metal oxide in the oxidation of CO.

### 1.1.5.1 Cobalt oxide ( $\text{Co}_x\text{O}_y$ )

As there are different forms of cobalt oxides, the most active form for total oxidation is  $\text{Co}_3\text{O}_4$  in which cobalt is present in two valence states (+2 and +3). This form is also the most stable oxide between 350 °C and 900 °C. Above 900 °C,  $\text{Co}_3\text{O}_4$  loses oxygen to give CoO [17]. High activity of  $\text{Co}_3\text{O}_4$  is due to the presence of mobile oxygen inside their spinel structure. This oxide has excellent reduction ability and oxygen vacancies as well as a high concentration of electrophilic oxide species [44]. Activities of different unsupported  $\text{Co}_3\text{O}_4$  catalysts in CO or hydrocarbon total oxidation have been extensively studied [86-91]. **Table 1.5** provides some insights into the main results for CO oxidation (Gas mixture (vol%) = 1 % CO + 1 %  $\text{O}_2$ ).

**Table 1. 5.** Activity of unsupported cobalt oxide catalysts in CO oxidation [86].

Catalyst	Catalyst preparation	Treatment (°C)	BET ( $\text{m}^2\text{g}^{-1}$ )	Activity (200 °C) ( $\mu\text{mol CO}_2 \text{ s}^{-1}\text{m}^{-2}$ )
$\text{Co}_3\text{O}_4$	Commercial (ceramic method)	850	0.44	21
	Calcination of $\text{Co}_2\text{O}_3$ above 400 °C	600	10	13
	Precipitation of $\text{Co}^{2+}$ nitrate in ammonia and calcination above 400 °C	600	5	21
$\text{CoAl}_2\text{O}_4$	Commercial	850	11.3	0.015

Some observations can be drawn from **Table 1.5**:

- Cobalt oxide is a very active catalyst for CO oxidation
- The activity of  $\text{Co}_3\text{O}_4$  samples varies slightly with BET surface area, which suggests that the reaction is not structure sensitive on these materials
- The activity of  $\text{Co}_3\text{O}_4$  catalyst depends on the method of preparation, pre-treatment, and oxidation state
- Cobalt species presented as  $\text{Co}^{2+}$  in  $\text{CoAl}_2\text{O}_4$  is inactive for the CO oxidation reaction (the coexistence of  $\text{Co}^{2+}$  and  $\text{Co}^{3+}$  ions in the same materials seems to be mandatory for the catalytic activity in CO oxidation)

It should be noted, however, that single or unsupported  $\text{Co}_3\text{O}_4$  catalyst is very sensitive to deactivation or poisoning. Also, the pre-treatment prior to reaction and the reaction mixture have a dramatic influence on their activity and stability [87-90].

Supported or doped cobalt catalyst has shown promising performances and they are considered to be less sensitive to pre-treatments and deactivation than single  $\text{Co}_3\text{O}_4$  catalyst.  $\text{Co}_3\text{O}_4$  supported on various supports was investigated for the total oxidation of CO (**Table 1.6**). It has been shown that the activity of supported  $\text{Co}_3\text{O}_4$  catalyst depends on the nature of the support and the metal oxide-support interactions [92].

**Table 1. 6.** *Light-off temperatures for  $\text{Co}_3\text{O}_4$  catalysts on various supports [92].*

Catalyst	% $\text{Co}_3\text{O}_4$	Heat-treatment	Reaction conditions	$T_{50}$ ( $^{\circ}\text{C}$ )
$\text{Co}_3\text{O}_4/\text{SiO}_2$	10 wt%	650 $^{\circ}\text{C}$ , dry air	Gaz mixture = 1 vol% CO + 0.5 vol% $\text{O}_2$ in $\text{N}_2$ ; GHSV = 30000 $\text{h}^{-1}$	172
$\text{Co}_3\text{O}_4/\text{Al}_2\text{O}_3$	10 wt%	650 $^{\circ}\text{C}$ , dry air		172
$\text{Co}_3\text{O}_4/\text{Zeolite Y}$	10 wt%	650 $^{\circ}\text{C}$ , dry air		464
$\text{Co}_3\text{O}_4/\text{TiO}_2$	10 wt%	650 $^{\circ}\text{C}$ , dry air		>500
$\text{Co}_3\text{O}_4/\text{CeO}_2$	10 wt%	650 $^{\circ}\text{C}$ , dry air		135

Zeolite Y or titania supports generate less active cobalt oxide in CO oxidation, whereas ceria confers to cobalt oxide the highest activity, better than alumina or silica and relatively close to that of pure oxides. Alumina and titania give rise to strong interactions with  $\text{Co}_3\text{O}_4$ , with formation of cobalt aluminate ( $\text{CoAl}_2\text{O}_4$ ) or cobalt titanate ( $\text{CoTiO}_3$ ), which are inactive phases in CO oxidation. The formation of cobalt aluminates is always accompanied with a moderate decrease in BET surface area (from 102 to 78  $\text{m}^2\text{g}^{-1}$ ), while cobalt titanate formation induces severe sintering (from 43 to 1.5  $\text{m}^2\text{g}^{-1}$ ) [86, 93, 94].

Activity of supported  $\text{Co}_3\text{O}_4$  catalyst depends also on the preparation method; Yao et al. [95] compared two methods for preparing  $\text{Co}_3\text{O}_4/\text{Al}_2\text{O}_3$  catalysts; mechanical mixing and impregnation process. The catalyst obtained by mechanical mixing showed a higher activity than that prepared by impregnation. Indeed, the impregnation of acidic cobalt salts on alumina can induce a strong interaction, with the formation of cobalt aluminate, and a decrease in activity. A similar experimental method was applied to prepare another type of catalyst, constituted of cobalt oxide deposited on alumina as support [91], which showed high CO conversion at low temperature in a continuous-flow reactor. Representative studies of catalytic activity measurement over different cobalt oxides supported on alumina and other different supports are given in **Table 1.7**.

**Table 1. 7.** *Survey of catalytic studies over Co containing catalysts.*

Ref	Catalyst preparation	Support	Co <sub>3</sub> O <sub>4</sub> (wt%)	Heat-treatment	Pre-treatment <sup>a</sup>	Reaction conditions	T <sub>50</sub> <sup>b</sup> (°C)	T <sub>100</sub> <sup>c</sup> (°C)	R <sub>150</sub> <sup>d</sup>	R <sub>200</sub>
[95]	Mixing of cobalt oxide with colloidal alumina then drying at 150–200 °C	$\gamma$ -Al <sub>2</sub> O <sub>3</sub>	25.2	600 °C, 24 h	Heating in 1–2 vol% O <sub>2</sub> /Heat 500 °C	Gas mixture = 1 vol% CO + 1 vol% O <sub>2</sub> ; T range = 125–200 °C;	–	–	90	900
				850 °C, 24 h			–	–	33	100
			10	600 °C, 24 h			–	–	45	1000
				850 °C, 24 h			–	–	27	90
			45	600 °C, 24 h 850 °C, 24 h			–	–	46	530 20
[95]	Mixing of cobalt oxide with alumina (powder) and 5% of oleic acid then drying at 150–200 °C	$\gamma$ -Al <sub>2</sub> O <sub>3</sub>	15.4	600 °C, 24 h	Heating in 1–2 vol% O <sub>2</sub> /He at 500 °C	Gas mixture = 1 vol% CO + 1 vol% O <sub>2</sub> ; T range = 125–200 °C;	–	–	–	61
		$\alpha$ -Al <sub>2</sub> O <sub>3</sub>	9.2	600 °C, 24 h			–	–	–	1000
		Mullite	9.1	600 °C, 24 h			–	–	–	1
[95]	Impregnation of support with cobalt nitrate solutions then drying at 150–200 °C	$\gamma$ -Al <sub>2</sub> O <sub>3</sub>	17.2	600 °C, 24 h	Heating in 1–2 vol% O <sub>2</sub> /He at 500 °C	Gas mixture = 1 vol% CO + 1 vol% O <sub>2</sub> ; T range = 125–200 °C;	–	–	–	0.3
[91]	Impregnation of support with cobalt nitrate solutions (+NH <sub>3</sub> ) then freeze drying for 24h	$\gamma$ -Al <sub>2</sub> O <sub>3</sub>	20	550 °C, 90 min	Reduction in 5 vol% H <sub>2</sub> or oxidation in 10 vol% O <sub>2</sub>	Gas mixture = 2 vol% CO + 1.17 vol% O <sub>2</sub> ; T range = 21–550 °C;	150	265	–	–
							80	215	–	–
[94]	Impregnation of support with cobalt nitrate solutions then drying at 110 °C	SiO <sub>2</sub>	5 (Co)	400 °C, 4 h	Heating in 10 vol% O <sub>2</sub> /He at 500 °C	Gas mixture = 10 vol% O <sub>2</sub> /He + 4 vol% CO/He; T range = 0–300 °C;		175	–	–
		Al <sub>2</sub> O <sub>3</sub>		400 °C, 4 h			21	200	–	–
		TiO <sub>2</sub>		400 °C, 4 h			240	–	–	–
[93]	Impregnation of support with cobalt nitrate solutions then drying at 110 °C	SiO <sub>2</sub>	5 (Co)	400 °C, 4 h	Heating in 10 vol% O <sub>2</sub> /He at 300 °C	Gas mixture = 10 vol% O <sub>2</sub> /He + 4 vol% CO/He; T range = 0–300 °C;	33	–	–	–
		SiO <sub>2</sub>		700 °C, 4 h			202	–	–	–
		Al <sub>2</sub> O <sub>3</sub>		400 °C, 4 h			12	–	–	–
		Al <sub>2</sub> O <sub>3</sub>		700 °C, 4 h			232	–	–	–
		TiO <sub>2</sub>		400 °C, 4 h			160	–	–	–
		TiO <sub>2</sub>		700 °C, 4 h			300	–	–	–

- <sup>a</sup>: Prior to the first oxidation on a fresh catalyst.
- <sup>b</sup>: Temperatures for the half conversion of CO into CO<sub>2</sub>.
- <sup>c</sup>: Temperatures for the full conversion of CO into CO<sub>2</sub>.
- <sup>d</sup>: The rate of CO<sub>2</sub> produced per unit total surface area at 150 °C.

Rate normalized to 1 vol% O<sub>2</sub>, 1 vol% CO and 0 vol% H<sub>2</sub>O, expressed in mL<sub>CO2</sub> min<sup>-1</sup>g<sup>-1</sup>.

### 1.1.5.2 Nickel oxide (Ni<sub>x</sub>O<sub>y</sub>)

Nickel oxide (NiO) is another active metal oxide in CO oxidation. The activity of the NiO catalyst is linked to its p-type semi-conducting properties with subsequent creation of cationic vacancies. This allows electrons to be easily removed from the metal cations, resulting in the presence of excess active species O<sup>-</sup> in their lattice [44]. However, single or unsupported nickel oxide does not seem to exhibit good performances in CO oxidation, when compared to cobalt and copper oxides. The addition of another metal oxide phase enhances the activity of NiO. Chen et al. [96] tested the catalytic activity of NiO impregnated on Al<sub>2</sub>O<sub>3</sub>, which exhibited a CO conversion of only 50 % at 625 °C. The low activity is attributed to the fact that Ni ions tend to form nickel aluminate, which are inactive phases in CO oxidation.

### 1.1.5.3 Copper oxide (Cu<sub>x</sub>O<sub>y</sub>)

Copper oxide (CuO or Cu<sub>2</sub>O) has been demonstrated to be one of the most active species among the various transition-metal oxides for the total oxidation of CO. Indeed, metallic copper tends to completely oxidize during the reaction to form Cu<sup>+</sup> and Cu<sup>2+</sup> species at the surface [44]. In comparison to Co<sub>3</sub>O<sub>4</sub>, unsupported copper oxides have been less used in CO oxidation. This is primarily related to the coexistence of both Co<sup>2+</sup> and Co<sup>3+</sup> ions in the structure of cobalt oxide, whereas CuO or Cu<sub>2</sub>O have only either Cu<sup>2+</sup> or Cu<sup>+</sup> ions [17]. However, one of the major issues regarding the use of the Cu<sub>x</sub>O<sub>y</sub> catalyst is its low stability. This problem can be managed by appropriate pre-treatments or by using suitable supports. Several factors affect the performance of supported CuO<sub>x</sub> catalyst, such as the catalyst preparation method [97-99], the heat treatment [100, 101] and the reaction conditions (gas reaction mixture and temperature) [102, 103]. The lattice oxygen concentration in Cu<sub>x</sub>O<sub>y</sub> plays also an important role in the CO oxidation. Indeed, oxygen removed from the surface by CO would be substituted by oxygen migrating from subsurface layers and the rate of oxidation becomes limited by subsurface oxygen diffusion [17].

Several studies of copper oxides supported on alumina have focused on the effect of support and catalyst pre-treatment on the catalytic activity in CO oxidation. The main results of these studies are summarized in **Table 1.8**.

On the basis of the considered examples, we can identify several conclusions on the catalytic activity of copper oxides supported on alumina:

- CO oxidation is a structure-sensitive reaction over copper/alumina catalysts
- CO oxidation activity of CuO/Al<sub>2</sub>O<sub>3</sub> catalyst depends on copper contents; at low copper contents, copper is present as a well dispersed surface phase on the alumina surface and the Cu-O bond is basically ionic. Whereas, at high copper loadings, crystalline CuO is formed on the alumina support; the higher metal loadings result in the formation of a more covalent oxide
- The copper surface spinel is induced by the diffusion of copper ions into alumina lattice
- Crystalline copper oxide phases are more active than isolated Cu surface species.

**Table 1. 8.** *Survey of catalytic studies over Cu containing catalysts.*

Ref	Catalyst preparation	Support	CuO (wt%)	Heat-treatment	Pre-treatment	Major findings
[97]	Mechanical mixing of copper oxide with alumina (powder)	$\gamma$ -Al <sub>2</sub> O <sub>3</sub> $\alpha$ -Al <sub>2</sub> O <sub>3</sub> ZrO <sub>2</sub> $\alpha$ -Al <sub>2</sub> O <sub>3</sub>	8.82 3.36 3.3 13.2	900 °C, 2 h	N. M <sup>a</sup>	- $\gamma$ -Al <sub>2</sub> O <sub>3</sub> and ZrO <sub>2</sub> give rise to strong interactions with CuO, with formation of cobalt-aluminate or zinc-aluminate spinel structures.
	Impregnation of support with salt solutions then drying at 250 °C	ZrO <sub>2</sub>	7.97	500 °C, 16 h		- Catalyst containing $\gamma$ -Al <sub>2</sub> O <sub>3</sub> was less active (per unit of surface area) than that containing ZrO <sub>2</sub> or $\alpha$ -Al <sub>2</sub> O <sub>3</sub> . - Formation of spinel structures leads to a decrease in the CO oxidation activity.
[98]	Impregnation of support (pellets) with copper nitrate solutions then drying at 120 °C for 20 h	$\gamma$ -Al <sub>2</sub> O <sub>3</sub>	10.5	500 °C, 12 h	- 4.8 vol% CO in air at 270 °C for 1 h - Pure CO at 175 °C for 1h - Pure CO (15 min) then air (15 min) at 250 °C, three cycles	- Catalyst pre-treatment affects the state of Cu in CuO/Al <sub>2</sub> O <sub>3</sub> catalyst, which in turn affects the catalytic activity in CO oxidation.
[99]	Impregnation of support with copper nitrate solutions then drying at 120 °C	$\gamma$ -Al <sub>2</sub> O <sub>3</sub>	1.23	800 °C	N. M	- Bulk CuAl <sub>2</sub> O <sub>4</sub> can be formed after high temperature calcinations (>700 °C). - The structure of CuO/Al <sub>2</sub> O <sub>3</sub> catalyst depends on both the metal loading and calcination temperature.
			2.44			
			5.88			
			11.1			
			20	400 °C 500 °C 600 °C 700 °C 800 °C 900 °C		- CO oxidation activity increases with increasing copper loading. - CO oxidation activity decreases with increasing calcination temperature.
			27.3			
			33.3			

<sup>a</sup>: Not mentioned

### **1.1.6 Methods for metal oxides catalytic materials elaboration**

Different methods have been employed in the synthesis of metal oxide catalysts. The choice of the preparation method is crucial in controlling the structural, textural and surface properties, as well as the thermal, chemical and mechanical stability of the final solid, and therefore the catalytic properties. Metal oxides, both simple and complex (bulk and supported), can be synthesized by different routes [14, 104-108]. The most common methods used are: ceramic method (solid-state reaction), wet chemical methods like co-precipitation, sol-gel and impregnation.

#### **1.1.6.1 Ceramic method (solid-state reaction)**

This method consists of physically mixing finely ground powder of oxides and heating intimately the mixture at high temperatures, to allow inter-diffusion and solid-state reactions. The use of the phase diagram is generally helpful in fixing the desired composition and conditions for synthesis. This method seems not to be very convenient for preparation of oxide catalysts because of the heterogeneity of the resulting powders, as well as the high temperatures needed, that generally lead to the formation of aggregated powders with poor surface area.

#### **1.1.6.2 Co-precipitation**

Co-precipitation is the most common technique used for preparing mixed oxide catalysts. An aqueous solution of the metal cations is mixed with another solution that contains a precipitating agent. The obtained precipitate is separated, dried, and thermally treated. Co-precipitation is a well-established method for preparing bulk catalysts. However, in some cases, supported metal oxide catalysts can be prepared through co-precipitation. In this case, metal precursors to both the support and the metal oxide active materials are induced to form the support material and the supported layer simultaneously. The support and the supported metal oxide are more spatially distributed than materials derived from the various deposition methods, but a fraction of the supported metal oxide may be located below the surface, leading to overall lower metal oxide dispersion [14]. The major drawback of this technique is the high temperature treatments of the co-precipitated materials which affect the solid state reactions that produce the intimately mixed oxide phase that acts as a catalyst.

### **1.1.6.3 Sol-gel**

Sol-gel method is a multi-step process involving both chemical and physical processes. Contrary to the co-precipitation route, which is a discontinuous transformation, sol-gel method is a homogeneous process which results in a continuous transformation of the solution precursors. In sol-gel processing, a clear colloidal solution called sol is formed by hydrolysis and partial condensation of dissolved precursors. This sol is subsequently converted into a gel material, so-called “hydro-gel” and after drying, a porous solid is obtained. The advantages of the sol-gel methods are: better homogeneity compared to the traditional ceramic method, higher purity, lower processing temperature and better textural and morphological control. There are, however, some disadvantages associated with the sol-gel synthesis: applicable to a limited range of metal oxides, do not give access to fine control of the synthesis parameters, requires numerous synthetic steps and leads to strong agglomeration and aggregation.

### **1.1.6.4 Impregnation**

Impregnation is a well-established method for the preparation of supported metal oxide catalysts. In this method, a solid support material is placed in contact with the precursor solution of the supported metal oxide. If the volume of precursor solution is equal to the total pore volume of the support—volume of solution that might fill all the porosity of the support—, the deposition process is called capillary or dry impregnation. The speed of pores filling is fast, but there are potential problems of internal pore collapse. If the volume of the precursor solution is slightly higher than the total pore volume of the support, the deposition process is known as diffusional or wet impregnation. In this method, the pores of the support are first filled with the same solvent as used for preparing the impregnating precursor solution. The wetted support is then treated with the impregnating precursor solution. The solvent is removed by filtration and/or centrifugation and/or drying. In this case, the impregnation time is much longer than for dry impregnation. This method is simple, allowing a wide range of loadings to be possible. However, the metal oxide active species tend generally to form a metal phase after the solvent removing step.

The methods described above have received a considerable attention and have been used to produce a variety of metal oxides. However, the increasing demand for material properties of high-quality has induced the set-up of alternate synthesis routes. Nonetheless, conventional methods remain relevant and applicable on both laboratory and industrial scale.

Some novel approaches, based on physical and chemical routes have been developed for the synthesis of high added-value inorganic materials, with controlled nanostructures. Examples of these approaches include solvo-thermal methods, template-assisted, kinetic growth control, sono-chemical reactions, complexation, solvent-free activated reactive synthesis, and microwave-assisted chemical reactions.

Another challenge faced by material scientists today is to introduce and implement environmentally friendly methods for material synthesis. The development of new chemical routes should comply with the principles of green chemistry or sustainability. The sustainability concept requires, using less hazardous precursors (e.g. metal acetate or nitrate solutions) in recyclable solvents (e.g. water or ethanol), choosing a fast reaction with a high efficiency (one-pot reaction), limiting the number of reagents and synthetic steps, and most importantly reducing energy consumption.

## **1.2 Microwave chemistry for metal oxide catalysts synthesis**

### **1.2.1 Introduction to microwave chemistry**

“Time is precious!” If this maxim is important in everyday-life, it is also valid in science, especially in the field of synthetic chemistry, whenever a large number of time-consuming trial and error-experiments are needed to design a new synthesis approach, or to optimize an existing synthesis protocol. Rapid synthesis will be absolutely beneficial for scientists to carry-out more experiments within the same period of time.

Microwave (MW)-assisted chemistry has emerged as one of the most promising routes that being a fast synthesis approach. Indeed, it is found that dielectric heating could increase the rate of reactions by a factor of 1000, in comparison with conventional heating. Thus, reactions occur in a few minutes or even seconds [109].

The development of microwave technology was stimulated by World War II, when magnetrons were designed to generate microwave radio signals for RADAR devices. The discovery of microwaves heating was in 1945 by Percy LeBaron; while he was experimenting with radar waves, he accidentally found that a chocolate bar melted in his pocket [110]. Few years later, he developed a deep interest in MW processing and designed the first domestic MW oven in 1954. Since then, research interest, in the development of MW radiation as a source of heating, has continued to grow and the use of microwave heating became more common [111].

MW heating does not only success to reduce time-consuming, but also contributes to green chemistry. Several attributes of microwave heating comply with the green chemical syntheses, including shorter reaction time, lower energy consumption, and higher yields. Furthermore, the use of microwaves has reduced the amount of purification and post-reaction treatments required for the synthesis products. The combination of MW-assisted technology with other green synthesis strategies by using solvent-free reactions, ionic liquids or environmentally friendly reagents would definitely lead to cleaner and greener chemistry [112].

Microwave is an electromagnetic radiation situated between radio waves and infrared frequencies in the electromagnetic spectrum (**Figure 1.3**), with wavelengths ranging from about 1 mm to 1 m, and frequencies between approximately  $3 \times 10^2$  and  $3 \times 10^5$  MHz. The majority of MW ovens used for domestic, industrial and scientific applications operate at a frequency of 2.45 GHz.

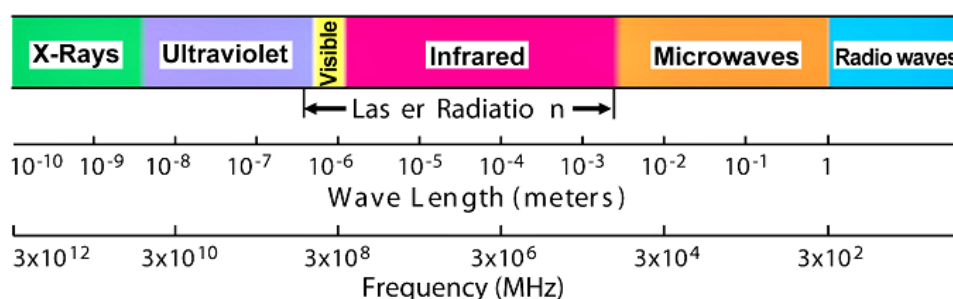


**Figure 1. 3.** *Schematic presentation of the electromagnetic spectrum [110].*

MW radiation can be reflected, transmitted and/or absorbed, when applied on material. Absorbed MW energy provides efficient internal volumetric heating through generation of localized high temperature zones (preferential nucleation sites) in the reaction medium by direct coupling of microwave energy with the molecules present in the solvent (**Figure 1.4 (a)**) [110]. The absorption of MW energy depends on the nature (e.g. polarity) of the solvents that determines their ability to couple with MW irradiation. Water is a polar solvent, a good MW absorber at 2.45 GHz and is considered as the most suitable solvent to carry out chemical reactions under MW irradiation [113-114]. Upon microwave irradiation, polarized water molecules orientate with the oscillating electric field resulting in the molecular rotation. Magnetic field-molecules interactions do not normally occur, though. The intermolecular friction and collision caused by molecular rotation induce selective heating (superheating zones) and a rise in temperature, which is sufficient to nucleus formation and selective crystallization [110]. This should be followed by a heat transfer processes from the

superheated zones (hot spots) to those with the lower temperature. A simplified schematic illustration of the microwave heating of water molecules is shown in **Figure 1.5**.

The presence of dissolved ionic salts in water has an effect on molecular structure of water. Indeed, water molecules tend to bond spontaneously to the ions via intermolecular hydrogen bonding, and those water molecules that are coordinated to the ions are rotationally fixed. Consequently, the efficiency of the conversion of microwave energy into thermal energy would be lower. At higher concentrations, the effects of ionic salts are reversed, due to a greater ordering of the water molecules [112]. In view of the advantages of using water, most of the research activities have been devoted to the microwave-assisted synthesis of inorganic materials in aqueous solution. Nonetheless, it is important to note that using water as a solvent in microwave synthesis allows a further step on the path of green synthesis.

The heating phenomenon are different for conventional and microwave ovens. In conventional heating, the external surface gets heated first via heat flow from the external heat sources, and then the heating front propagates from the hot surface to core via conduction or convection, until finally a uniform temperature is reached in the overall sample (**Figure 1.4 (b)**). In this case, the heating process is long. As a result of this propagated heating, there is always a temperature difference between the external surface and the core, as shown schematically in Figure 1.5.b. Unlike conventional heating, MW processing provides uniform, volumetric and fast heating of the solvent, because the MW energy is directly coupled with the species in the reaction medium at the molecular level [110].

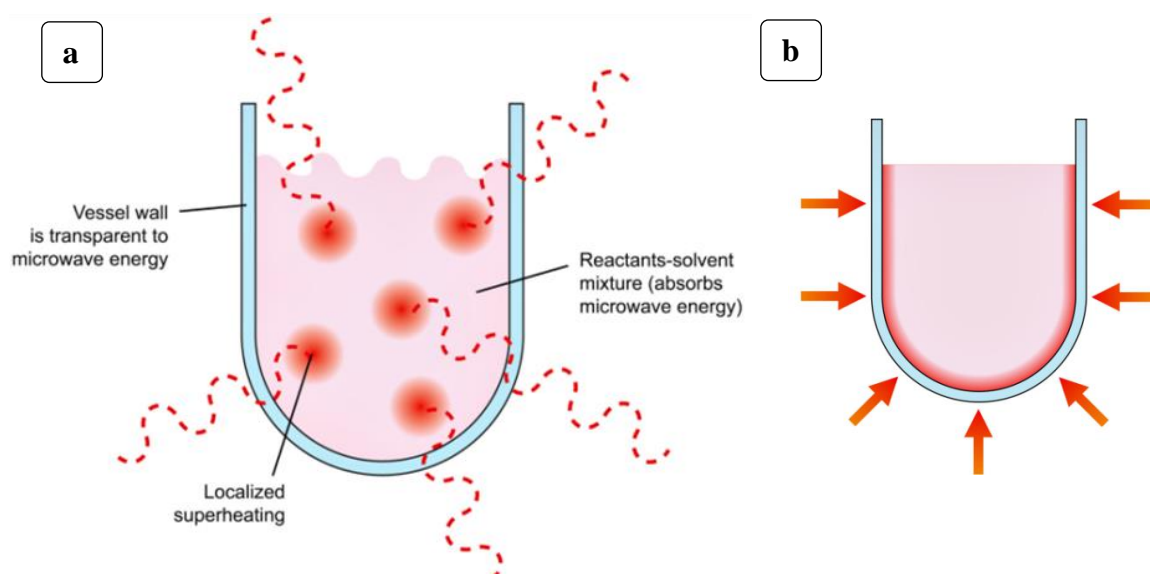
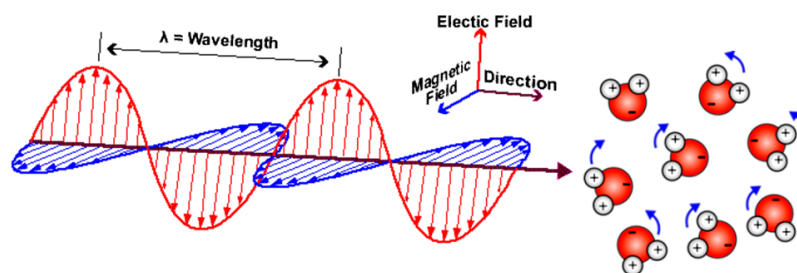


**Figure 1. 4.** (a) Microwave heating and (b) conventional heating [110]



Water Molecules Rotations

**Figure 1. 5.** *Water molecule rotations in an alternating electrical field under microwave irradiation.*

Microwave irradiation was primarily used to carry out analytical chemistry such as pyrolysis, digestion, extraction, fat analysis and protein hydrolysis, moisture/solids analysis and spectroscopic analysis [111, 115-117]. Later, microwave technology was exploited for material processing including processing of alloys, ceramics, metals, powders metallurgy, materials joining, coatings, and claddings. The major interest has been done in the area of sintering of various ceramics.

Further to explore the advantages of microwave heating, microwave assisted chemical reactions has emerged as a novel route for materials synthesis, mainly applied to liquid-phase syntheses, including solvent-free and water-mediated reactions [114, 118, 119]. Then, new horizons for novel materials syntheses opened thanks to the combination of microwave chemistry and the full spectrum of available liquid-phase synthesis routes. The broad variety of possible combinations is presented in **Figure 1.6**. The development of MW-assisted syntheses by controlling MW parameters (temperature, pressure, power, and ramping of temperature) and choice of solvents may mark an important step towards next generation of high performances and tailor-made materials.

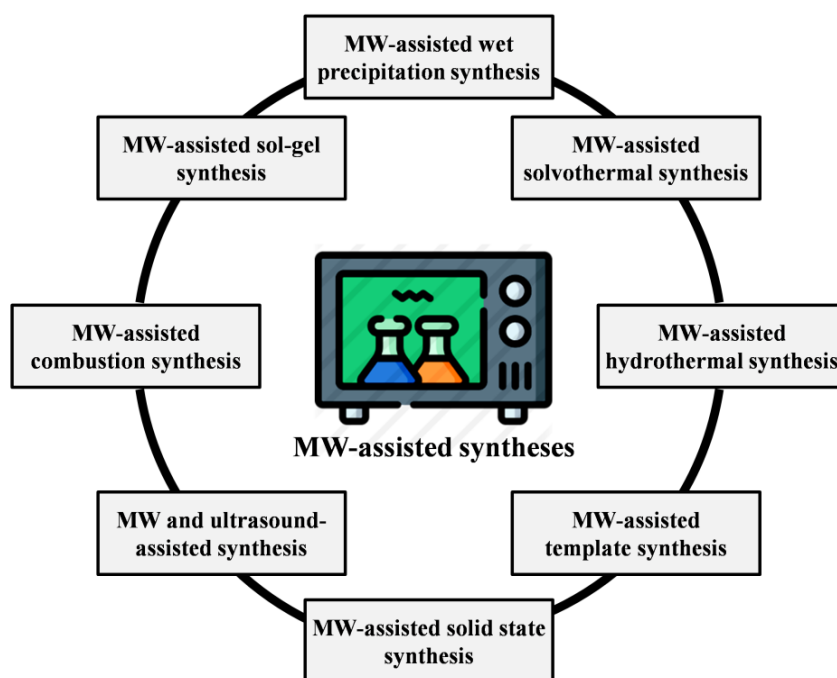


**Figure 1. 6.** *Possible combinations of microwave chemistry with common synthesis routes.*

Microwave-assisted routes have been applied for the one-pot synthesis of a variety of high quality of organic materials, inorganic materials, and hybrid materials. Recently, the application of microwave chemistry has been extended to include the synthesis of nanomaterials, metal/ metal oxide nanoparticles, and nanostructures.

Substitution of classical energy input by microwave energy has shown great advantages in chemical homogeneity, high sinterability and purity, controlled size and shape, narrow size distributions and enhanced mechanical and electrical properties of the final product.

It is obvious that both reaction temperature and heating mode influence the nucleation and crystal growth, and consequently the crystal size and shape of the final product. It has been proven that the ability of microwaves to heat a reaction mixture very rapidly by direct dipolar coupling of MW energy affects the nucleation and crystallization rates [120]. Homogeneous and volumetric heating provokes homogeneities in the growth process, thus producing improved nucleation processes and consequently narrow size distributions [112, 114]. In this respect, it is observed that prolonged irradiation time increases the particle size, so the simplest way to control the crystal size is to minimize the irradiation time.

Catalytic materials, whose overall properties are strongly dependent on their synthesis routes, could benefit a great deal from MW heating. In particular, the ability of MW heating to drive the catalyst structure at the nanoscale will further enable the rational design of catalytic materials.

### 1.2.2 Microwave assisted solution combustion synthesis

Combustion Synthesis (CS) or Self-propagating High-temperature Synthesis (SHS) is an alternative route to prepare a wide range of advanced materials, including metal oxide catalysts. This method originated from the discovery of solid state self-propagating reactions, by Merzhanov et al. from Institute of Chemical Physics (Chernogolovka, Russia) [121].

By definition, CS is a synthesis route for producing materials by using exothermic self-sustained redox chemical reactions between an oxidizer and a fuel; once the initial exothermic reactive system is ignited by an external heat source, a rapid high-temperature wave propagates (fire) through the reactive system in a self-sustained manner producing heat, light, and ash [122]. All these elements make up a fire triangle **Figure 1.7**.



**Figure 1. 7.** *Fire triangle.*

Combustion synthesis process can be classified into three main categories based on physical state of the initial reaction medium: gas-phase combustion, condensed phase synthesis, and Solution Combustion Synthesis (SCS) or Solution Combustion (SC) (initial medium is an aqueous reactive solution) [122,123].

SCS was accidentally discovered in the mid-1980s by Kingsley and Patil [124] from the Indian Institute of Science (Bangalore, India), when aluminum nitrate hydrate ( $\text{Al}(\text{NO}_3)_3 \cdot 9\text{H}_2\text{O}$ ), used as an oxidizer, and urea ( $\text{CO}(\text{NH}_2)_2$ ) as a fuel, were dissolved in distilled water and placed in a muffle furnace maintained at 500 °C. It was found that when the solution boiled, a spontaneous ignition occurred and underwent smoldering combustion with formation of  $\alpha\text{-Al}_2\text{O}_3$  powder. Based on this unlooked-for experiment, the SC method was explored and a large number of binary and extremely complex oxides were prepared.

Since its appearance, research interest in SC technique has been on a steady increase. Indeed, the number of published articles has increased by a factor of approximately 7 over the period 2002-2015, and more than 5000 SC research papers on SC chemistry have been published

over the last 20 years (**Figure 1.8**). This remarkable growth can be attributed to the simplicity of the technique, the diversity of the SC-based methods and its ability to be applied for the preparation of a wide variety of technologically useful materials with improved properties.

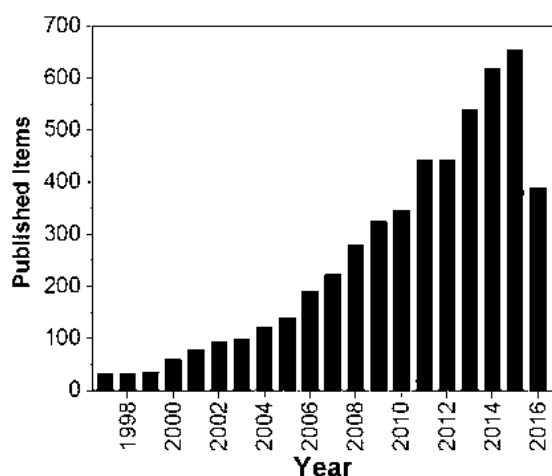


**Figure 1. 8.** Number of published articles on SC chemistry between 1998 and 2016 [125].

Typically, we can define SCS as an exothermic self-sustained redox reaction, taking place in homogeneous solution containing at least an oxidizing agent and a suitable fuel used as reducing agent. Reaction initiation is achieved through external heating, which maintains high temperatures to decompose all solution precursors. The temperature reached when the reaction initiates in the reactive mixture is called the ignition temperature. The crystallized material is the main product, while  $\text{H}_2\text{O}$ ,  $\text{CO}_2$ , and  $\text{N}_2$  are usually the gaseous by-products formed in the combustion reaction [122]. **Figure 1.9** shows metal oxide product obtained from combustion of an aqueous solution of fuel and oxidizers, in a preheated furnace.

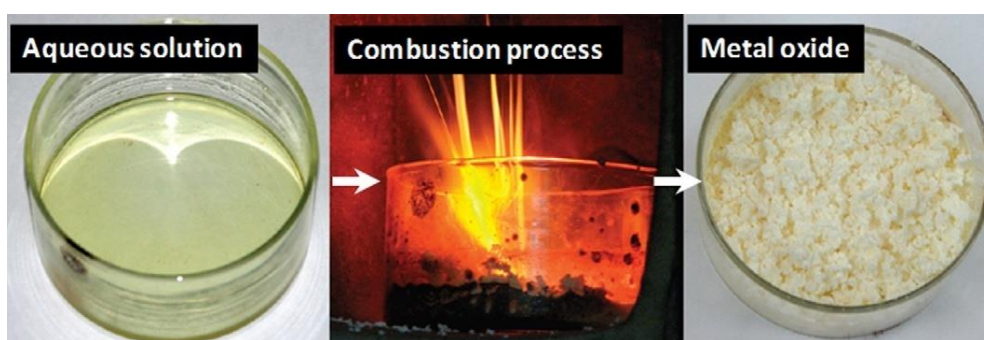


**Figure 1. 9.** SCS of metal oxide from aqueous solution [126].

### 1.2.2.1 Theory of combustion reaction

The solution combustion method involves applying the thermochemical concepts of propellant chemistry developed by Jain et al. [127]. These concepts contribute to the estimation of the mixture ratio (RV/OV) of fuel-oxidizer compositions.

RV/OV ratio can be determined by the following equation **Eq. 1.1**.

$$\frac{RV}{OV} = \frac{\sum \text{Mole number of reducing agent} * \text{reducing valence}}{(-1) \sum \text{Mole number of oxidizing agent} * \text{oxidizing valence}} \quad \text{Eq. 1.1}$$

The oxidizing elements have negative valences and the reducing elements have positive valences. Metals, carbon and hydrogen are considered as reducing elements with the corresponding metal valence, (+4) for carbon and (+1) for hydrogen. On the other hand, oxygen is considered as an oxidizing element with the valence (-2). The elemental valence of nitrogen is zero. Hydration water does not affect the overall system valence, so it is not involved in the overall valence calculation.

The total reducing valence is calculated by summing the elemental reducing and oxidizing valences in fuel, while the total oxidizing valence is determined by summing the elemental oxidizing and reducing valences in the oxidizer.

When  $RV/OV = 1$ , the redox system (fuel-oxidizer mixture) is in the stoichiometric condition and the maximum of energy is achieved, ensuring the complete burning of the fuel. When  $RV/OV < 1$ , the redox system is in the fuel-lean condition and molecular oxygen is released. Whereas when  $RV/OV > 1$ , the redox system is in the fuel-rich condition, requiring atmospheric oxygen for the complete burning of the fuel. The thermochemistry of the redox mixture seems to be mostly controlled by the total composition of oxidizing and reducing elements of the mixture [123].

### 1.2.2.2 Solution combustion parameters

The combustion reaction is greatly influenced by several parameters such as the chemical composition of precursors, stoichiometry of the reactants (RV/OV ratio), the heating method, the atmosphere, and the pH value [120]. The main parameters that have been extensively investigated in the literature are the chemical composition of precursor, stoichiometry of the reactants and the heating method. The influence of these parameters on the SC process is explored in terms of combustion sustainability, reaction exothermicity (enthalpy and flame temperature), and burning rate. The properties of the solution combustion synthesized materials, such as crystalline phase, particle size, morphology, surface area and agglomeration degree depend heavily on these parameters. The possibility of tuning the combustion parameters offers remarkable opportunities for the synthesis of a wide variety of materials.

### 1.2.2.2.1 Chemical composition of precursors

#### ▪ Fuels

The choice of the fuel is critical in SCS. A suitable fuel should have a high solubility in the solvent used (in most cases water), evolve large amounts of harmless gases, be compatible to the oxidizer leading to a controlled combustion, be readily available and non-toxic, and should have a low ignition temperature (below 500 °C) [121]. In general, fuels serve the following purposes:

- Burn C–H bonds (electrons acceptor) releasing heat and simple gaseous molecules of CO<sub>2</sub> and H<sub>2</sub>O.
- Form complexes with metal ions assuring homogeneous mixing of the metal cations in solution
- Decompose into combustible gases like HNCO, NH<sub>3</sub> that ignite with NO<sub>x</sub>.

A wide variety of fuels are available for the SC method such as urea, glycine (C<sub>2</sub>H<sub>5</sub>NO<sub>2</sub>), hydrazine (N<sub>2</sub>H<sub>4</sub>), carbonylhydrazide (CH<sub>6</sub>N<sub>4</sub>O), acetylacetone (C<sub>5</sub>H<sub>8</sub>O<sub>2</sub>) and citric acid (C<sub>6</sub>H<sub>8</sub>O<sub>7</sub>) [121].

The combustion behavior of various fuels differs in relation to the chemical activity of the ligand groups of the fuel molecule. The fuel properties can considerably affect the exothermicity of the combustion process, the burning rate, and the volume of gases generated during combustion. Depending upon the fuel used, the combustion reaction will be flaming type (volume combustion) or non-flaming type (smoldering or layer-by-layer combustion). For instance, flaming type combustion is characterized by high burning rate and a high combustion temperature (>1000 °C), which is usually higher than the ignition temperature. In this case, a violent exothermic reaction occurs in the entire volume of the reactive mixture with the release of large amount of gases. Flaming type combustion can be associated to the generation of gaseous intermediate such as nitrogen oxides (NO<sub>x</sub>), isocyanic acid (HNCO), ammonia (NH<sub>3</sub>), and carbon dioxide (CO<sub>2</sub>). Because of the high combustion temperature, the particles undergo slight sintering resulting in larger agglomerated particles. Even though the particles are agglomerated, the crystallite sizes will be in the submicron/nanosized range due to the short period of heating. On the other hand, in smoldering type combustion, the combustion reaction is much controlled, and propagates slowly from one layer to another in the reaction mixture. In this approach, combustion reaction is characterized by a reduced flame temperature (<1000 °C) and low burning rate [125, 128, 129]. **Figure 1.10** illustrates

the dynamic of the combustion front in flaming type and smoldering type combustion reactions, respectively.

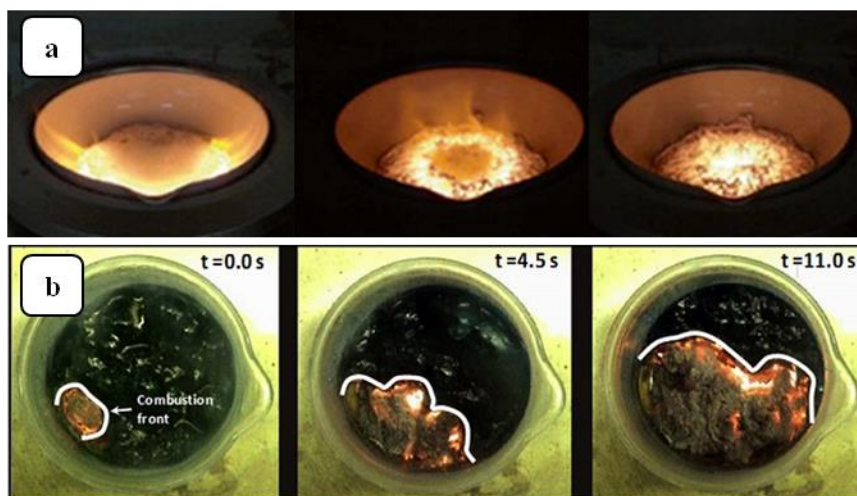


**Figure 1. 10.** (a) *Flaming type* and (b) *smoldering type combustion reactions* [130, 131].

As general behavior, the low combustion temperature favors small particle sizes and prevents the particles from agglomeration, but leaves behind higher levels of impurities in the final products (carbon particles, hydroxides, carbonates etc.). The type of fuel appears to be specific for the metal precursors employed and/or the type of mixed metal oxide formed. It is worth noting that urea is still among the most attractive fuels studied for preparing a variety of mixed metal oxides, resulting in the formation of highly thermally stable, pure and homogeneous product, contrary to others fuels that need further thermal treatments after the combustion process at high temperatures to burn away residual impurities.

#### ▪ Oxidizers

Oxidizers provide oxygen (electrons donor) and assist in burning C–H bonds. Salts, like nitrates, metal sulphates and carbonates are chosen as oxidizing agents. Nitrate salts are the preferred metal precursors, because they are low temperature oxidizer sources and have great water solubility [121]. Metal nitrates are used at a large scale and considered as essential metal precursors for the synthesis of simple and mixed metal oxides.

**Table 1. 9.** *Most common precursors and solvents used for SCS [121, 129].*

Fuel	Oxidizer	Solvent
Urea ( $\text{CH}_4\text{N}_2\text{O}$ )	Metal nitrates and nitrate hydrates	Water
Glycine ( $\text{C}_2\text{H}_5\text{NO}_2$ )	Metal chlorides	Alcohols
Citric acid ( $\text{C}_6\text{H}_8\text{O}_7$ )	Metal carbonates	Hydrocarbons
Carbohydrazide ( $\text{CH}_6\text{N}_4\text{O}$ )	Ammonium nitrates ( $\text{N}_2\text{H}_4\text{O}_3$ )	Formaldehyde
Hydrazine ( $\text{N}_2\text{H}_4$ )	Nitric acid ( $\text{HNO}_3$ )	
Acetyl acetone ( $\text{C}_5\text{H}_8\text{O}_2$ )		
Sorbitol ( $\text{C}_6\text{H}_{14}\text{O}_6$ )		
Plant leaf extracts		
Sucrose		
Glucose		
Cellulose		

#### 1.2.2.2.2 Stoichiometry of the reactants (RV/OV ratio)

Stoichiometry is one of the most important parameters in SCS. The properties of solution combustion-derived products are influenced not only by the nature or type of fuel but also by the RV/OV ratio. Generally, the deviation from the stoichiometry affects the maximum combustion temperature and the volume of gases generated during the combustion reaction, which in turn tune the crystalline phase, particle size, morphology, pore size, porosity, surface area and agglomeration degree [129]. Fuel-lean conditions in SCS usually result in a decrease of the maximum combustion temperature with a consequent reduction of the volume of gases evolved. Whereas, Fuel-rich conditions result in an increase of the maximum combustion temperature and the volume of gases generated. An RV/OV value very far from the stoichiometry can lead to an organic-rich and amorphous product, which needs a further calcination step [120, 121].

#### 1.2.2.2.3 Heating method

Ignition technique is also an important parameter of the SCS. Different electrical heating devices, such as muffle oven, hot plate, aluminum open cylindrical reactor, and pressure reactor have been used for supplying the required energy for heating the initial reactive solution. Each of these ignition techniques characterizes a specific combustion route. However, for the most part, the prepared material exhibits local inhomogeneity, caused by the thermal gradient between the interior and exterior of the heated solution. Recently, an alternative method of combustion initiation based on microwave heating has been developed to enhance the results of traditional CS processing. Microwave irradiation has several

advantages over conventional heating methods, including short reaction times, improved reaction rate, lower operating temperatures and volumetric heating [132, 133]. It was also found that continuous microwave heating favors a continuous emission of the evolving gases all along the process, leading to a well-controlled dissipation of the heat. The matching between the two emerging technologies (SCS and microwave heating) gives origin to the so called “microwave-assisted solution combustion synthesis” route. The coupling of these two technologies enable to produce improved materials with unique properties such as, structural uniformity, high purity, fine and more uniform particles size, small agglomerates, high surface area, and enhanced porosity.

### 1.2.2.3 Mechanism of oxide forming

In the literature, only few studies reported on the mechanism of SCS reactions. Typically, they are based on the results of the different thermal analyses of the precursors (thermogravimetric analysis (TGA), differential thermal analysis (DTA), differential scanning calorimetry analysis (DSC), etc) and on the combustion behavior of the precursors and their reactive mixtures.

Kingsley and Patil [124] have proposed the combustion synthesis mechanism for  $\alpha$ -Al<sub>2</sub>O<sub>3</sub> powder using stoichiometric amounts of aluminum nitrate hydrate and urea dissolved in water and heated in a muffle furnace at 500 °C.

In the first stage, dehydration of aluminum nitrate hydrate, as well as decomposition of urea, take place with formation of Al(OH)(NO<sub>3</sub>)<sub>2</sub> gel, urea nitrate (CH<sub>5</sub>N<sub>3</sub>O<sub>4</sub>), biuret (C<sub>2</sub>H<sub>5</sub>N<sub>3</sub>O<sub>2</sub>), cyanuric acid ((HNCO)<sub>3</sub>), and ammonia (NH<sub>3</sub>). In the second stage, gel mixture foams are obtained due to the generation of gaseous decomposition products. It was suggested that the foam, resulted from the matching between cyanuric acid and gel nitrate, is also combustible. The gaseous decomposition products are a mixture of nitrogen oxides (N<sub>2</sub>O<sub>4</sub>, NO<sub>2</sub>, N<sub>2</sub>O<sub>5</sub>), NH<sub>3</sub>, and HNCO, which are hypergolic when in contact with each other. In the last stage, the foam burns upon contact with the hypergolic mixture of gases with the appearance of a flame [121]. At high in situ temperature the foam decomposes to yield 100%  $\alpha$ -Al<sub>2</sub>O<sub>3</sub>. This proposed mechanism is illustrated in **Figure 1.11**.

The authors noted that, the foam alone could not initiate ignition and the presence of hypergolic gases is needed for a successful ignition. Also, if the mixture is heated at a slow rate, the time required to reach the ignition temperature is longer, allowing the release of the gases from the foam and in this way, ignition initiation is not possible.

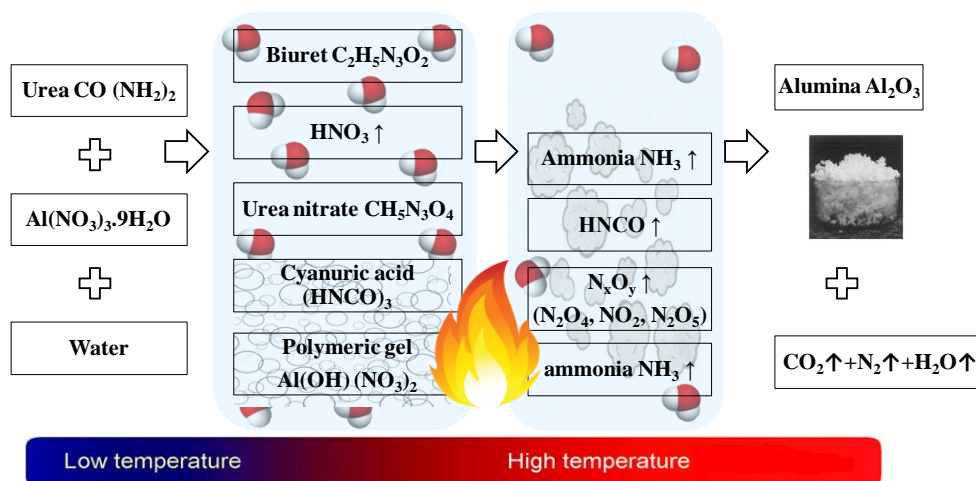


**Figure 1. 11.** Mechanism of aluminum nitrate–urea combustion reaction.

#### 1.2.2.4 Metal oxides prepared by SCS

Wide variety of binary, ternary or even more complicated oxides have been obtained by SCS. In the following paragraphs, several examples of metal oxides-based SCS are provided, with particular emphasis on alumina derived materials. Details of the preparation conditions (composition of the combustion mixture, ignition method), properties and applications of the final materials are included.

##### 1.2.2.4.1 $\text{Al}_2\text{O}_3$

SC has been used to prepare  $\text{Al}_2\text{O}_3$  nano-powders using aluminum nitrate as oxidizing agent. The structural, morphological and textural properties of SC-derived products vary depending on the fuel nature and the method of reaction initiation. In the presence of urea, well-crystallized  $\alpha$ - $\text{Al}_2\text{O}_3$  powders with a surface area ranging from 5 to  $114 \text{ m}^2\text{g}^{-1}$  were obtained.  $\alpha$ - $\text{Al}_2\text{O}_3$  powders were characterized by nearly hexagonal and irregular platelet particles with sizes ranging from 200 to 800 nm [124,134,135]. Other fuel-types produce amorphous powders with different nanoparticle morphologies; the aluminum nitrate–glycine combustion product presents spherical-shaped particles with a diameter size in the range of 50–250 nm [136], and the nitrate–citric acid combustion product displays particles with irregular shapes [137].

##### 1.2.2.4.2 NiO

Wen et al. prepared NiO/Ni composites using nickel nitrate and nickel acetate combined with different fuels, such as hydrazine hydrate, glycine and citric acid [138, 139]. It was found that addition of NaF to nickel nitrate–citric acid solutions increases gas evolution rate during SCS,

resulting in a macroporous product with small particle sizes ( $\sim 20\text{--}30$  nm), and exhibits excellent dye absorption ability, as well as lithium storage capacity [138]. For nickel nitrate + hydrazine hydrate + glycine solutions, it was found that addition of nickel acetate is a key factor to achieve high porosity, while the amount of fuel influences the morphology of the porous structure [139].

#### 1.2.2.4.3 $\text{Co}_3\text{O}_4$

Cobalt oxide nanofoam was obtained from the combustion of aqueous solutions containing stoichiometric amounts of cobalt nitrate and glycine solutions in a glass beaker [140] or stainless-steel vessel [141] on a hot plate preheated at  $300\text{--}400$  °C. Porous  $\text{Co}_3\text{O}_4$  nanostructures was also produced from combustion of cobalt nitrate–glycine solutions in preheated furnace maintained at  $400$  °C, followed by calcination in air at  $355$  °C for 1 h [142].

Sahoo et al. [143] heated stoichiometric cobalt nitrate–urea solutions in a furnace preheated to different temperatures, from  $300$  to  $800$  °C. It was noticed that the size of  $\text{Co}_3\text{O}_4$  nanoparticles increases by increasing the furnace temperature, with a corresponding decrease of the surface area. Ai and Jiang [144] produced highly porous  $\text{Co}_3\text{O}_4$  foams, with small particle size, using microwave-assisted combustion of cobalt nitrate–urea solutions. Rashad et al. [145] prepared  $\text{Co}_3\text{O}_4$  nanocrystals by the microwave-assisted synthesis without any post-annealing treatment from a solution containing  $\text{Co}(\text{NO}_3)_2 \cdot 6\text{H}_2\text{O}$  and urea under microwave irradiation for 20 min.

#### 1.2.2.4.4 $\text{CuO}$

Flower-like nanoCuO was synthesized by SC method using cupric nitrate and glycine mixtures ignited in a furnace at  $300$  °C. The CuO nanoflowers were composed of wide nanopetals and they exhibited a very good photocatalytic activity [146]. CuO nanorodswere obtained starting from copper nitrate mixed with citric acid, as fuel. The prepared nanoCuO showed effective antimicrobial and photocatalytic activities [147]. Recently, green SCS of various oxide nanopowders has been reported using leaf extracts, such as *Tinospolacordifolia* [148] and *Calotropis gigantean* [149] as biofuels, in the preparation of spherical CuO nanoparticles. In both cases, the plant leaf extract was mixed with copper nitrates and treated in a furnace at  $400$  °C. The SCS of nickel, cobalt and copper oxides are summarized in **Table 1.10**.

#### 1.2.2.4.5 Ni/Al<sub>2</sub>O<sub>3</sub>

Roy et al. [152, 153] have studied the effect of preparation methods and surface treatment of a SC alumina support on the performance of Ni/Al<sub>2</sub>O<sub>3</sub> catalysts for ethanol reforming. First series of Ni/Al<sub>2</sub>O<sub>3</sub> catalysts with different Ni loadings (2, 5, and 10 wt%) were prepared by sol-gel method. For the second series, the Al<sub>2</sub>O<sub>3</sub> support was prepared by the solution combustion synthesis method. Then, Ni (2, 5, and 10 wt%) was dispersed on the support by a standard wet impregnation method. Prior to the catalytic run, the free NiO particles on the support surface were reduced under hydrogen flow. The Ni/Al<sub>2</sub>O<sub>3</sub> catalysts, synthesized by the combustion method, presented a higher metal dispersion and ethanol conversion, compared to those prepared by sol-gel method [152]. In order to study the effect of surface modification, 10 wt% of Ni was dispersed on both modified and unmodified SC powders using the standard wet impregnation method, and then the samples were thermally treated at 350 °C. The surface modification of Al<sub>2</sub>O<sub>3</sub>, carried out by plasma pre-treatment, led to a Ni catalyst with enhanced catalytic activity and selectivity [153]. Similarly, Cross et al. [154] have prepared dispersed Ni nanoparticles on  $\gamma$ -Al<sub>2</sub>O<sub>3</sub> support for ethanol decomposition reactions. In a typical experiment, ring-shaped  $\gamma$ -Al<sub>2</sub>O<sub>3</sub> pellets were immersed into a reactive solution of nickel nitrate hydrate (Ni(NO<sub>3</sub>)<sub>2</sub>·6H<sub>2</sub>O) and glycine for 1 s to 30 min, and then placed on a hot plate maintained at 500 °C to initiate the combustion. To keep the metal dispersion, the catalyst pellets were reduced with hydrogen at 300 °C. The authors have reported that short impregnation times lead to a non-uniform distribution of Ni into the pellets, thus negatively affecting the catalyst selectivity to hydrogen, during ethanol decomposition. Zhao et al. [155] have prepared Ni/Al<sub>2</sub>O<sub>3</sub> catalysts with various Ni contents (from 10 to 50 wt%) by the solution combustion method, and 30 wt % Ni/Al<sub>2</sub>O<sub>3</sub> catalyst by the impregnation method, for CO methanation. Prior to the reaction, the catalysts were heated under H<sub>2</sub> flow to reduce NiO to metallic Ni. SCS-derived catalysts exhibited a higher catalytic activity than that of 20 wt% Ni/Al<sub>2</sub>O<sub>3</sub> catalysts obtained by the classical impregnation. The SC-catalysts displayed good temperature stability and total CO conversion already at 320 °C. Zeng et al. [156] succeeded in further improving the catalytic activity of Ni/Al<sub>2</sub>O<sub>3</sub> catalysts up to 100 % conversion of CO, in the 300–320 °C range, by adding titanium (Ti) species with loadings varying from 1 to 5 wt%.

In the same context, Gao et al. [157] have prepared Ni/Al<sub>2</sub>O<sub>3</sub> catalysts (with 20 wt% Ni loading) by microwave assisted solution combustion using urea, glycine, ethylene glycol, or citric acid as fuels. The catalysts were then tested in CO methanation. The microstructure and

performance of the reduced Ni/Al<sub>2</sub>O<sub>3</sub> catalysts seem to strongly depend on the type of fuel used during the synthesis. Further studies were carried out by Gao et al. aiming to evaluate the influence of the urea quantity [158] and fuel additives (ammonium acetate, starch and polyethylene glycol (PEG)) [159] on the combustion process, the microstructure, and the intrinsic catalytic activity of Ni/Al<sub>2</sub>O<sub>3</sub> catalysts. They found that the combustion enthalpy increased with the urea/metal nitrates ratio. The presence of high urea amounts leads to a high combustion temperature, facilitating NiO migration into the Al<sub>2</sub>O<sub>3</sub> matrix to form the NiAl<sub>2</sub>O<sub>4</sub> spinel and that displays a low activity. If ammonium acetate is used as a fuel additive the nanostructure and activity of the Ni/Al<sub>2</sub>O<sub>3</sub> catalysts are higher than those obtained for the catalysts prepared with starch and PEG.

#### **1.2.2.4.6 Co/Al<sub>2</sub>O<sub>3</sub>**

Highly active supported Co oxide catalysts for methane oxidation were prepared by Zavyalova et al. [160], using a combination of wetness impregnation and combustion method.  $\gamma$ -Al<sub>2</sub>O<sub>3</sub> supports impregnated with aqueous solutions of various reactive mixtures (cobalt acetate (Co(CH<sub>3</sub>COO)<sub>2</sub>), cobalt nitrate (Co(NO<sub>3</sub>)<sub>2</sub>)/cobalt acetate, and mixtures of cobalt nitrate with urea, citric acid, glycine, and glycerin (C<sub>3</sub>H<sub>5</sub>(OH)<sub>3</sub>) were dried at 110 °C and ignited on a hot plate preheated in the 230–250 °C range. For comparison purposes, a 10 wt% Co<sub>3</sub>O<sub>4</sub>/ $\gamma$ -Al<sub>2</sub>O<sub>3</sub> catalyst was prepared by the conventional impregnation method. The catalysts obtained with the combination of impregnation and combustion method from equimolar redox mixtures of cobalt nitrate/glycine or cobalt nitrate/cobalt acetate were found to have the highest activity in methane oxidation (complete conversion of methane at 400–425 °C). Another example of Co<sub>3</sub>O<sub>4</sub>/Al<sub>2</sub>O<sub>3</sub> catalyst was obtained by SC using  $\alpha$ -Al<sub>2</sub>O<sub>3</sub> supports instead of  $\gamma$ -Al<sub>2</sub>O<sub>3</sub> supports, and tested for phenol decomposition. Activated  $\alpha$ -Al<sub>2</sub>O<sub>3</sub> supports were mixed with nitrate–urea mixtures, stirred for 30 min and heated in furnace at 500 °C for 30 min [161]. The physicochemical characterizations showed that crystallites of Co<sub>3</sub>O<sub>4</sub> and  $\alpha$ -Al<sub>2</sub>O<sub>3</sub> were present as two distinct chemical phases, with bigger particle size than those obtained with  $\gamma$ -Al<sub>2</sub>O<sub>3</sub> supports, as reported in previous works [160].

#### **1.2.2.4.7 Cu/Al<sub>2</sub>O<sub>3</sub>**

A Cu/Al<sub>2</sub>O<sub>3</sub> nanocomposite was obtained by SCS method using an aqueous solution mixture of copper nitrates (Cu(NO<sub>3</sub>)<sub>2</sub>), aluminum nitrates, urea and graphite [150]. Graphite was initially added in order to prevent oxidation of copper into copper oxide after the completion

of the combustion reaction. It was noted that the combustion leads to a good dispersion of the nanosized alumina on the copper matrix. Park et al. [151] have prepared bulk  $\text{Al}_2\text{O}_3$  with well dispersed Cu-phase, using combustion of metal nitrates and urea solutions, followed by a reduction treatment, in order to reduce CuO to Cu. Also in this case, the combustion route showed good results in the efficient dispersion of fine  $\text{Al}_2\text{O}_3$  particles.

**Table 1. 10.** *Survey of different metal oxides prepared by SCS.*

Metal oxides	Composition of the combustion mixture	Method of reaction initiation	Phase/Particle shape/Size/ Surface area <sup>3</sup>	Application	Reference
Al <sub>2</sub> O <sub>3</sub>	- Aluminum nitrate - Urea - SP <sup>1</sup>	- Muffle furnace - 500 ± 10 °C - < 5 min	- α-phase; - Hexagonal platelet; - 0.2–0.8 μm; - 8.3 m <sup>2</sup> g <sup>-1</sup>	NM <sup>2</sup>	[124]
Al <sub>2</sub> O <sub>3</sub>	- Aluminum nitrate - Urea	- Hot plate - 480 °C	- α-phase; - Irregular plates; - 13–15 nm; - 100–114 m <sup>2</sup> g <sup>-1</sup>	NM	[134]
Al <sub>2</sub> O <sub>3</sub>	- Aluminum nitrate - Urea - SP	- MW oven (2.45 GHz, 900 W) - 3–5 min	- α-phase; - Spherical; - 18–20 nm	NM	[135]
Al <sub>2</sub> O <sub>3</sub>	- Aluminum nitrate - Glycine	- Muffle furnace - 350–450 °C	- Amorphous; - 50–250 nm; - 100–114 m <sup>2</sup> g <sup>-1</sup>	NM	[136]
Al <sub>2</sub> O <sub>3</sub>	- Aluminum nitrate - Citric acid	- Muffle furnace	- Amorphous; - Irregular shapes; - 322–887 nm; - 4.5–9.5 m <sup>2</sup> g <sup>-1</sup>	NM	[137]
NiO/Ni	- Nickel nitrate - Citric acid - NaF	- Muffle furnace - 400 °C	- 20–30 nm; - 20.6 m <sup>2</sup> g <sup>-1</sup> ; - Porous structure	- Dye-Absorption - Lithium Storage	[138]
NiO/Ni	- Nickel nitrate - Citric acid - Nickel nitrate - Nickel acetate - Hydrazine hydrate - Glycine	- Muffle furnace - 400 °C	- 2.6 m <sup>2</sup> g <sup>-1</sup> ; - flake structure - 2D and 3D macroporous structure	- Lithium Storage	[139]
Co <sub>3</sub> O <sub>4</sub>	- Cobalt nitrate - Glycine - SP	- Hot plate - 300–400 °C	Glass beaker : - 26–32 m <sup>2</sup> g <sup>-1</sup> ; 4–20 nm Steel vessel: - 24 m <sup>2</sup> g <sup>-1</sup> ; 15.5 nm	- Hydrolysis of sodium borohydride	[140, 141]

$\text{Co}_3\text{O}_4$	- Cobalt nitrate - Glycine - SP	- Muffle furnace - 400 °C, 16 min	- 12 nm; - 59 m <sup>2</sup> g <sup>-1</sup> ; - Porous structure	- Lithium Storage	[142]
$\text{Co}_3\text{O}_4$	- Cobalt nitrate - Urea - SP	- Muffle furnace - 300 °C, 1h - 400 °C, 30 min - 600 °C, 30 min - 800 °C, 30 min	- 5–18nm/38.58 m <sup>2</sup> g <sup>-1</sup> ; - 12–20nm/14.37 m <sup>2</sup> g <sup>-1</sup> ; - 75–150nm/2.65 m <sup>2</sup> g <sup>-1</sup> ; - 200–400nm/1.59 m <sup>2</sup> g <sup>-1</sup>	- NM	[143]
$\text{Co}_3\text{O}_4$	- Cobalt nitrate - Urea - SP	- MW oven (2.45 GHz, 800 W) - 15 min	- 67 nm	- NM	[144]
$\text{Co}_3\text{O}_4$	- Cobalt nitrate - Urea	- MW oven (2.45 GHz, 800 W) - 20 min	- 13–14nm	- NM	[145]
$\text{CuO}$	- Copper nitrate - Glycine - SP	- Muffle furnace - 300 °C	- 3.5 µm; - Flower-like structure	- Photocatalysis	[146]
$\text{CuO}$	- Copper nitrate - Citric acid - SP	- Muffle furnace - 300 °C, 20min	- 11 nm; - Nanorodstructure	- Photocatalysis - Antimicrobial agent	[147]
$\text{CuO}$	- Copper nitrate - Tinospolacordifolia	- Muffle furnace - 400 °C, 5min	- ~100 nm; - Sponge like structure	- Photocatalysis - Antioxidant and antibacterial agent	[148]
$\text{CuO}$	- Copper nitrate - Calotropis gigantean	- Hot plate - 60–80 °C	- ~20 nm; - Spherical	- Dye-Sensitized Solar Cells Applications	[149]

<sup>1</sup> Stoichiometric proportions.

<sup>2</sup> Not mentioned.

<sup>3</sup> Phase, particle shape, size and surface area of combustion products were mentioned as indicated by the original author.

### 1.2.3 Advantages and disadvantages

The advantages of microwave-assisted solution combustion synthesis can be summarized as follows:

- Homogenous mixing and heating of reactant at the molecular level
- High combustion temperatures resulting in high crystallinity and high purity of the produced materials
- Short reaction time and high amount of gaseous products evolved, favoring the formation of small crystallite, with high porosity and high surface area
- Minimum external energy requirement for the synthesis
- Simple and time efficient
- Possibility to tune the composition of the obtained materials
- Adapted to fabricate various materials for various applications

Microwave-assisted SCS may present some disadvantages, which have to be taken into consideration before any implementation at large-scale. One of the main issues to solve in microwave-assisted SCS applications is the relatively low degree of controllability of the phases and morphologies of the synthesized materials. This fact arises from the ultrafast and complex nature of the combustion process, which makes the preparation of regular and uniform nanostructures a challenging task. This leads to another issue related to the lack of understanding of the SC reaction mechanisms and kinetics. The mechanisms of structure formation for SCS products remain generally unknown.

In some cases, a calcination step after synthesis is required, which makes it a two-step technology. Here, the selection of the fuel and the stoichiometry of the reactants are of particular importance. Indeed, inadequate processing parameters could result in amorphous and organic-rich materials and then a calcination step is often required to enhance the crystallinity of the materials. Another key issue is related to environmental impacts of hazardous ( $\text{NO}_2$ ,  $\text{NO}$ ,  $\text{N}_2\text{O}$ ,  $\text{N}_2\text{O}_5$ ) gases that might be released during large-scale applications of SC processes. Strategies to capture these harmful gases need to be developed.

## Conclusions

This chapter aimed to describe the characteristics of Ni, Co and Cu oxide-based catalytic materials and explain their potential in heterogeneous catalysis, especially in the oxidation of carbon monoxide. These metal oxides showed high activity in the catalytic oxidation of CO due to their interesting electronic surface properties, such as presence of cationic and anionic vacancies, the ability of transition metal cations to undergo oxidation and reduction, as well as the presence of highly mobile oxygen inside their structure. Additionally, these metal oxides are considered to be good alternative to the expensive noble-metal catalysts. However, one of the most fundamental issues about single or unsupported Ni, Co or Cu oxides is the low stability and high sensitivity to deactivation or poisoning. Those issues have been the driving force for many research efforts for establishing strategies for improving the stability and activity of single metal-oxide catalysts, by dispersing the oxides on various catalyst supports, using metal dopants, or mixing them with different metal oxides. In this respect, mixed oxide catalysts have shown a clear improvement over single oxides, such as better thermal stability and higher catalytic performances.

There are several methods for the preparation of mixed oxides. The choice of the preparation method is crucial in controlling the physicochemical properties, as well as the catalytic properties. The solution combustion method has emerged as one of the most promising routes for the synthesis of metal oxide. This method is greatly influenced by several parameters, mainly the chemical composition of precursors, the stoichiometry of the reactants (RV/OV ratio), and the heating method. The combination of the MW heating and the solution combustion method leads to the so called “microwave-assisted solution combustion synthesis” route. The combustion-based reactions that used to take hours to complete with the conventional heating can now be done in minutes, giving researchers time to be more creative and test new ideas. Moreover, this novel route provides a promising approach to defined structures, morphologies and compositions.

The synthesis of alumina-based Ni, Co or Cu oxides by solution combustion technique has been studied in several prior works. However, only few studies report on the synthesis of alumina-based Ni, Co or Cu oxides by microwave assisted solution combustion method and the characteristics of these metal oxides remain unclear.

Despite the numerous studies on Ni, Co or Cu-based catalysts using conventional methods of catalyst preparation, the use of microwave assisted solution combustion technology for the

preparation of these materials has been less investigated thus far. In addition, and more importantly, investigation of CO oxidation over these catalytic materials has never been conducted before.

## Résumé en Français du chapitre 1

Ce chapitre a pour objectif de décrire les caractéristiques des catalyseurs d'oxydes métalliques à base des métaux de transition Ni, Co et Cu et d'expliquer leur potentiel en catalyse hétérogène, notamment dans l'oxydation du monoxyde de carbone (CO). Ces oxydes métalliques ont montré une activité élevée dans les réactions d'oxydation catalytique en raison de leurs propriétés de surface électroniques intéressantes, telles que la présence de lacunes cationiques et anioniques, la capacité des cations de métaux de transition à subir l'oxydation et la réduction, ainsi que la présence d'oxygène hautement mobile dans leur structure. De plus, ces oxydes métalliques sont considérés comme une bonne alternative aux catalyseurs coûteux en métaux nobles.

Il existe plusieurs méthodes pour la préparation des oxydes mixtes. Le choix de la méthode de préparation est crucial pour contrôler les propriétés physico-chimiques, ainsi que les propriétés catalytiques. Ces oxydes métalliques peuvent être synthétisés par différentes méthodes telles que la méthode céramique, co-précipitation, la méthode sol-gel et imprégnation. La méthode de préparation par combustion en solution s'est récemment montrée être une alternative viable aux préparations classiques par les méthodes conventionnelles cités ci-dessus. Cette méthode pouvait être décrite à l'aide du triangle de feu dont les éléments de base sont: l'énergie, le combustible (Réducteur) et le comburant (oxydant). Le combustible a pour rôle d'accepter les électrons, oxyder les groupements CH, et former des complexes avec les ions métalliques. Le comburant a pour fonction de donner les électrons et de fournir de l'oxygène. Les nitrates, les sulfates et les carbonates métalliques sont choisis comme des précurseurs métalliques, et sont les réactifs les plus utilisés comme des comburants. La glycine, l'éthylène glycol et l'urée sont parmi les combustibles les plus employés. La synthèse par combustion est une méthode basée sur le principe qu'une fois le combustible et le comburant sont mixés ensemble sous chauffage, une réaction de combustion se produit à la température d'inflammation et devient auto-propageante dans un certain intervalle de temps. Les nitrates métalliques sont les plus appréciés en raison de leur grande solubilité dans l'eau, permettant une plus grande homogénéisation. L'urée est l'un des combustibles les plus appropriés en raison de sa grande solubilité dans l'eau, de sa compatibilité avec les nitrates métalliques et de sa possibilité de conduire la réaction de combustion de manière plus contrôlable.

Cette méthode est fortement influencée par plusieurs paramètres, principalement la composition chimique des précurseurs, la stœchiométrie des réactifs (le ratio molaire d'équivalence (RV/OV) et la méthode de chauffage. Les méthodes de chauffage traditionnelles conduisent fréquemment à un gradient de température entre l'intérieur et l'extérieur de la solution, ce qui entraîne l'hétérogénéité du matériau préparé. Une méthode alternative, récemment proposée pour l'initiation de la combustion, est le chauffage par micro-ondes, qui présente plusieurs avantages par rapport aux méthodes conventionnelles: des temps de réaction courts, l'obtention de particules de petites tailles et de distribution homogène et une grande pureté des phases. Sous irradiation par micro-ondes, le mélange en solution est chauffé uniformément, ce qui produit des catalyseurs de composition uniforme et qui généralement présentent une activité catalytique accrue. La combinaison du chauffage par micro-ondes et de la méthode de combustion en solution conduit à la voie de synthèse dite: «synthèse par combustion en solution assistée par micro-ondes». Cette nouvelle voie offre une approche prometteuse pour la synthèse des oxydes métalliques ayant des structures, des morphologies et des compositions améliorées.

La synthèse des oxydes à base de Ni, Co ou Cu par la méthode de combustion en solution a été étudiée dans plusieurs travaux antérieurs. La synthèse de ces oxydes par la méthode de combustion en solution assistée par micro-ondes reste cependant peu étudiée et seules quelques descriptions de leurs propriétés ont été données.

## CHAPTER 2. MATERIALS AND METHODS

## Table of contents

Introduction .....	55
2.1 Catalysts preparation .....	55
2.1.1 Catalyst samples .....	55
2.1.2 Chemical reagents .....	56
2.1.3 Synthesis procedures .....	56
2.1.4 Theoretical calculations .....	57
2.2 Catalysts characterization .....	61
2.2.1 X-ray fluorescence spectroscopy (XRF) .....	62
2.2.2 X-ray diffraction (XRD) .....	62
2.2.3 N <sub>2</sub> adsorption-desorption analysis .....	62
2.2.4 Scanning electron microscopy (SEM) coupled with energy dispersive X-ray spectrometry (SEM-EDX) .....	63
2.2.5 Transmission electron microscopy (TEM) .....	63
2.2.6 X-ray photoelectron spectroscopy (XPS) .....	63
2.3 Catalytic testing .....	64
2.3.1 Experimental setup .....	64
2.3.2 Operating conditions .....	65
Conclusions .....	67
Résumé en Français du chapitre 2 .....	68

## Introduction

This chapter exposes the materials and methods used to accomplish the thesis objectives. The first part is devoted to the description of the chemical reagents, theoretical calculations and synthesis procedures. The second part deals with the different techniques used for the physicochemical characterization of the synthesized materials. The last part presents experimental details related to the measurement of the catalytic activity.

## 2.1 Catalysts preparation

### 2.1.1 Catalyst samples

In order to gain insights into the influence of the reactants stoichiometry (RV/OV ratio) on the surface and structure properties of the catalysts and its intrinsic catalytic activity, alumina-based binary metal oxide catalysts, with 2 and 10 wt% transition metal loading, were prepared by changing the RV/OV ratio to 0.9, 1.0 and 1.1 and the catalysts were labeled as XMAI-x (where X= 2 and 10, and represented the metal loading (wt%) in the catalyst; x = 0.9, 1.0, and 1.1, and represented the RV/OV ratio; M = Ni, Cu or Co). In all cases, the RV/OV ratio was calculated according to Jain et al.'s propellant theory [127].

To investigate the effect of the metal (M) content on the physicochemical and catalytic properties of the catalysts, alumina-based binary metal oxide catalysts were prepared with varied transition metal contents from 5 to 20 wt% and a constant RV/OV ratio of 1.1. These samples were labeled as XMAI (where X= 5, 10, 15 and 20, and represented the metal loading (wt%) in the catalyst; M = Ni, Cu or Co).

Alumina-based ternary metal oxide catalysts, with a constant transition metal loading of 5 wt% and a constant RV/OV ratio of 1.0, were also investigated. The samples were labeled as 5M5MAI (where 5 = transition metal loading (wt%); M = Ni, Cu or Co).

Given the diversity of the samples used in this study, it is thought that obtaining different data from the studied materials would allow reliable comparisons between different samples, and consequently achieve the determination of optimal synthesis conditions.

### 2.1.2 Chemical reagents

In the present investigation, metal nitrates (oxidizing agent) were chosen as metal precursors due to their high water solubility, allowing a greater homogenization. Urea (reducing agent) was selected because of its high solubility in water, its compatibility with metal nitrates, and its capacity to carry-on the combustion reaction in a more controllable way. A summary of the main chemical reagents used in this study is provided in **Table 2.1**.

**Table 2.1.** *Specifications of chemical reagents.*

Designation	Formula	Supplier	Purity (%)	Molar mass (gmol <sup>-1</sup> )
Aluminium (III) nitrate nanohydrate	Al(NO <sub>3</sub> ) <sub>3</sub> ·9H <sub>2</sub> O	Sigma aldrich	≥99.99	375.13
Nickel (II) nitrate hexahydrate	Ni(NO <sub>3</sub> ) <sub>2</sub> ·6H <sub>2</sub> O	Honeywell Fluka	≥99	290.81
Cobalt (II) nitrate hexahydrate	Co (NO <sub>3</sub> ) <sub>2</sub> ·6H <sub>2</sub> O	Honeywell Fluka	≥ 99	291.04
Copper (II) nitrate trihydrate	Cu (NO <sub>3</sub> ) <sub>2</sub> ·3H <sub>2</sub> O	Honeywell Fluka	≥ 99	241.6
Urea	CO(NH <sub>2</sub> ) <sub>2</sub>	Honeywell Fluka	>99	60.06

### 2.1.3 Synthesis procedures

In this work, all catalysts were synthesized by the microwave assisted solution combustion method. At first, appropriate amounts of aluminium nitrate nanohydrate (Al(NO<sub>3</sub>)<sub>3</sub>·9H<sub>2</sub>O) and metal nitrate hydrate M(NO<sub>3</sub>)<sub>2</sub>·xH<sub>2</sub>O (where M = Ni, Cu or Co; x = 6, 3, 6, and represent the number of water molecules) were dissolved in the minimum volume of doubled distilled water and magnetically stirred until complete dissolution. Then, the appropriate amount of urea was added into the solution under continuous stirring (450 rpm), during 1h at 60 °C, to evaporate the excess of water. The solution was then transferred into a Pyrex beaker and heated in a microwave oven working at 700 W, 2.45 GHz. During a typical microwave heating process, the aqueous solution boils and eventually decomposes. Then, a spontaneous ignition starts up with the release of a large amount of gases. Foamy and porous powders are then produced. The whole combustion process, for all samples, ends-up in less than 10 min whereas actual time of ignition was less than 5s. The main steps of the synthesis process are illustrated in **Figure 2.1**. Here, it should be noted that high temperature combustion could be achieved in Pyrex containers due to the thermal insulation properties of alumina. After synthesis, the obtained powders were calcined (air atmosphere) in a muffle oven at 500 °C for

12h with a heating rate of  $5\text{ }^{\circ}\text{Cmin}^{-1}$ , to decompose the unburnt urea and nitrates and further stabilize the material structure.

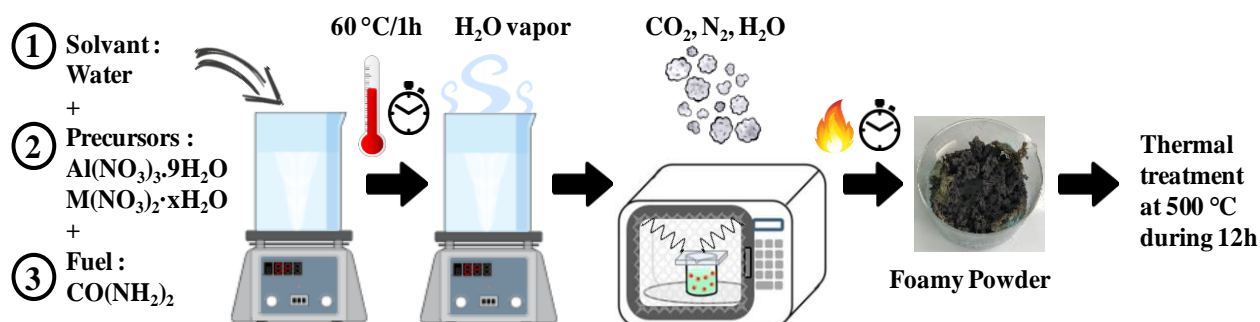


**Figure 2.1.** Steps involved in microwave assisted solution combustion synthesis.

#### 2.1.4 Theoretical calculations

The mass of aluminium nitrate was adjusted to synthesize laboratory quantities (1.5–2.5 g) of catalyst sufficient for the characterizations and the catalytic test measurements.

The mass of the divalent metal nitrate was calculated according to the required metal content (wt %) in the final catalyst. It is worth noting that the transition metal content X is determined with respect to the total mass of catalyst, as presented in **Eq 2.1**:

$$X(M) = \frac{m_M}{m_M + m_{\text{Al}_2\text{O}_3}} * 100 \quad \text{Eq. 2.1}$$

Where:

$m_M$  : Mass of transition metal

$m_{\text{Al}_2\text{O}_3}$  : Mass of alumina

The mass of urea was deduced from equation **Eq. 1.1** (**Chapter 1, page 35**), after fixing the value of RV/OV ratio.

In order to better understand the approach for estimating the required amount of urea, the next sections will provide the set up to calculate the required urea content.

As mentioned earlier in **Chapter 1**, the RV/OV ratio can be written by the following equation:

$$\frac{RV}{OV} = \frac{\sum \text{Mole number of reducing agent} * \text{reducing valence}}{(-1) \sum \text{Mole number of oxidizing agent} * \text{oxidizing valence}} \quad \text{Eq. 1.1}$$

Applying the thermochemical concepts of propellant chemistry, the oxidizing and reducing valences of different reactants can be calculated as described in **Table 2.2**.

**Table 2.2.** *Oxidizing and reducing valences of different chemical reagents.*

Reactant	Elemental valences	Total oxidizing valence	Total reducing valence
Al(NO <sub>3</sub> ) <sub>3</sub> ·9H <sub>2</sub> O	1Al = +3; 3N = 0; 9O = -18; 9H <sub>2</sub> O=0	-15	-
Ni(NO <sub>3</sub> ) <sub>2</sub> ·6H <sub>2</sub> O	1Ni = +2; 2N = 0; 6O = -12; 6H <sub>2</sub> O= 0	-10	-
Co (NO <sub>3</sub> ) <sub>2</sub> ·6H <sub>2</sub> O	1Co = +2; 2N = 0; 6O = -12; 6H <sub>2</sub> O= 0	-10	-
Cu (NO <sub>3</sub> ) <sub>2</sub> ·3H <sub>2</sub> O	1Cu = +2; 2N = 0; 6O = -12; 3H <sub>2</sub> O= 0	-10	-
CO(NH <sub>2</sub> ) <sub>2</sub>	1C = +4; 4H = +4; 2N = 0; 1O = -2	-	+6

Taking into account the valence values of different reactants, given in **Table 2.2**, **Eq. 1.1** can be simplified as follows:

For single oxide:

$$\frac{RV}{OV} = \frac{6 * n}{(-1)(\text{Total oxidizing valence} * n_M)} = x \quad \text{Eq. 2.2}$$

For alumina-based binary oxide:

$$\frac{RV}{OV} = \frac{6 * n}{(-1)((-10) * n_{M1} + (-15) * n_{Al})} = x \quad \text{Eq. 2.3}$$

Thus, required number of moles of urea can be defined as:

$$n = \frac{x * (10 * n_{M1} + 15 * n_{Al})}{6} \quad \text{Eq. 2.4}$$

For alumina based ternary oxide:

$$\frac{RV}{OV} = \frac{6 * n}{(-1)((-10) * n_{M1} + (-10) * n_{M2} + (-15) * n_{Al})} = x \quad \text{Eq. 2.5}$$

Thus, required number of moles of urea can be determined by the following equation:

$$n = \frac{x * (10 * n_{M1} + 10 * n_{M2} + 15 * n_{Al})}{6} \quad \text{Eq. 2.6}$$

With:

n : Quantity of urea (mol)

n<sub>M</sub>: Mole quantity of metal nitrate hydrate (mol)

n<sub>M1</sub>, n<sub>M2</sub>: Quantity of divalent metalnitrate hydrate (mol)

n<sub>Al</sub>: Quantity of aluminium (III) nitrate hydrate (mol)

For balancing chemical equation reactions, the values of the total reducing and oxidizing valences can serve as numerical coefficients for the oxidizers and the fuel.

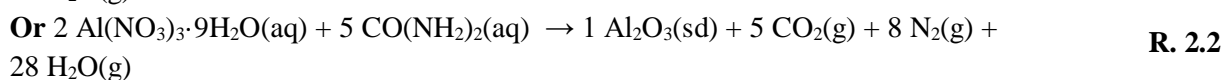
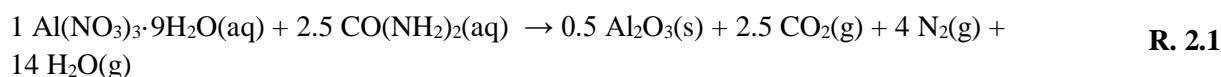
In the case of alumina single oxide synthesis, (RV/OV) ratio can be presented as:

$$\frac{RV}{OV} = \frac{6 * n}{(-1)((-15) * n_{Al})} = x \quad \text{Eq. 2.7}$$

Considering one mole of  $Al(NO_3)_3 \cdot 9H_2O$  ( $n_{Al} = 1$ ), the (RV/OV) ratio can be simplified as:

$$\frac{RV}{OV} = \frac{6 * n}{15 * (n_{Al} = 1)} = x \leftrightarrow n = 2.5x \quad \text{Eq. 2.8}$$

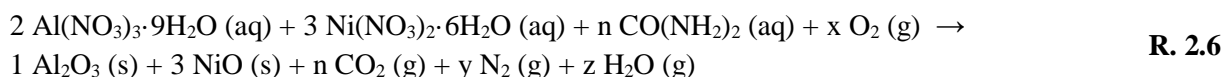
Therefore, for every (1mole) of  $Al(NO_3)_3 \cdot 9H_2O$ , (2.5x moles) of urea are required. Assuming stoichiometric composition of the redox mixture (RV/OV=x=1), the combustion reaction for the synthesis of alumina can be written as follows:



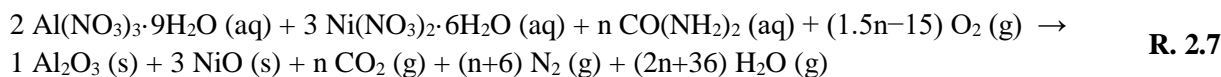
This method can be applied for the different combustion reaction systems that can be represented as follows:



For alumina based binary oxide, the reaction combustion can be written as follows:



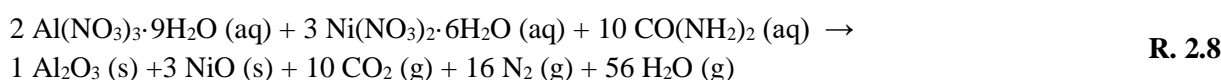
x,y et z coefficients can be written as function of n (x,y et z =f(n)) and the previous reaction equation can be expressed by :



Based on reaction **R. 2.7**, RV/ OV ratio is presented as:

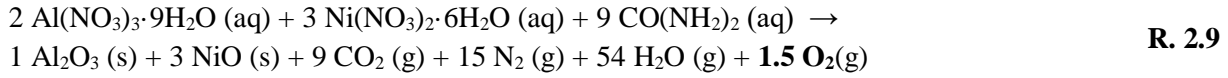
$$\frac{RV}{OV} = \frac{6 * n}{(-1)((-15) * (n_{Al} = 2) + (-10) * (n_{Ni} = 3))} = \frac{n}{10} \quad \text{Eq. 2.9}$$

$$\underline{\text{If } RV/OV=1 \rightarrow n=10}$$



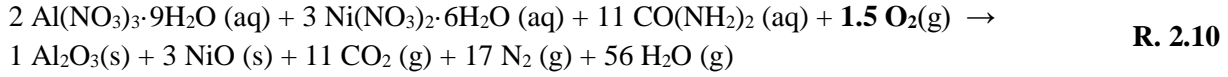
→ The redox system is stoichiometrically balanced; it does not require external oxygen for complete oxidation of the fuel.

If RV/OV=0.9→ n=9



→ The redox mixture is in the fuel-lean condition, molecular oxygen is produced (excess of oxygen).

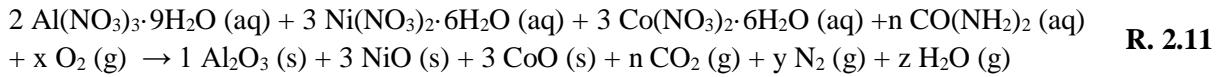
If RV/OV=1.1→ n=11



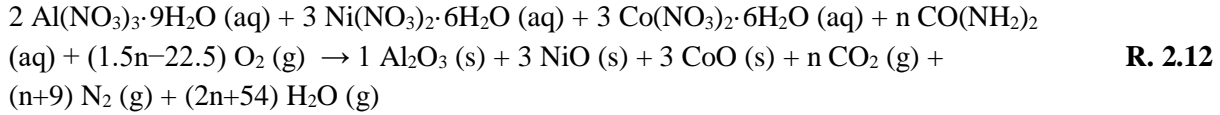
→The redox system is in “fuel-rich condition” (excess of fuel) and requires atmospheric oxygen to completely oxidize urea.

The balance of the reaction combustion of alumina-based Co or Cu oxide is performed in the same manner.

For alumina based ternary oxide, the reaction combustion can be expressed as follows:



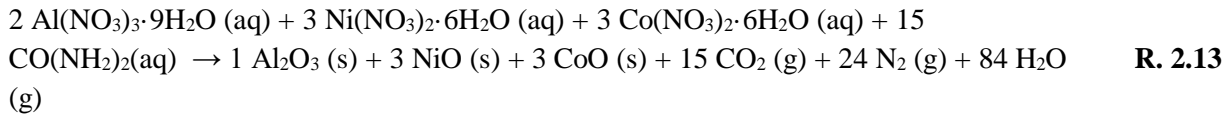
Expressing x,y et z =f(n), the reaction combustion can be presented as:



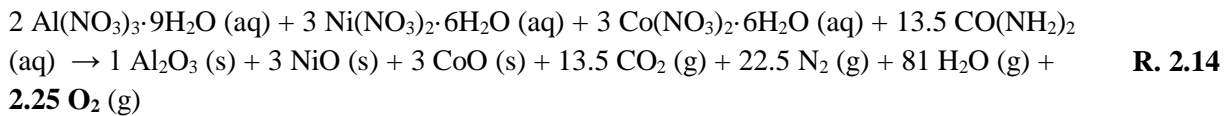
Based on reaction **R. 2.12**, the RV/ OV ratio can be calculated as:

$$\frac{\text{RV}}{\text{OV}} = \frac{6 * n}{(-1)((-10) * (n_{\text{Ni}} = 3) + (-10) * (n_{\text{Co}} = 3) + (-15) * (n_{\text{Al}} = 2))} = \frac{6n}{90} \quad \text{Eq. 2.10}$$

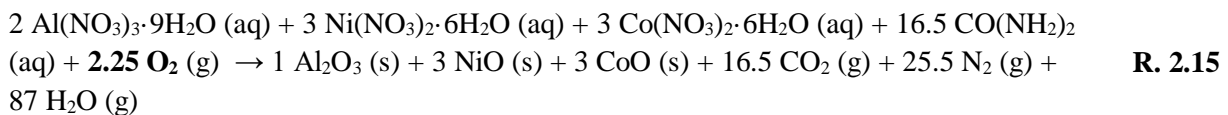
If RV/OV=1→ n=15



If RV/OV=0.9→ n=13.5



If RV/OV=1.1→ n=16.5



The above results of theoretical calculations can be summarized in **Figure 2.2**, which illustrates the influence of the value of RV/OV ratio on the moles of urea involved in the reaction.

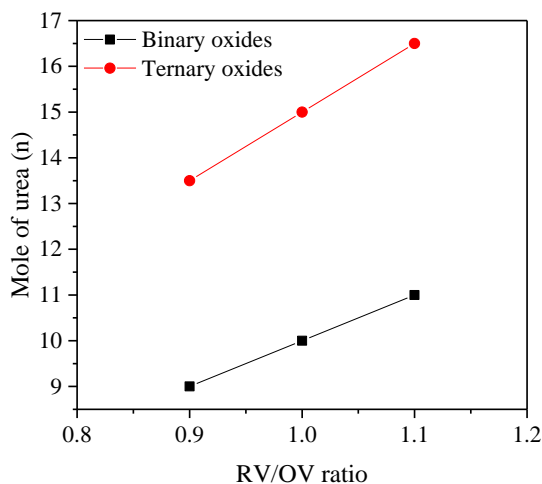


**Figure 2.2.** Variations of the mole of urea involved in the system as a function of RV/OV ratio.

## 2.2 Catalysts characterization

Different characterization techniques were employed for this study including: X-Ray Fluorescence spectrometry (XRF), powder X-Ray Diffraction (XRD), N<sub>2</sub> adsorption-desorption analysis, Scanning Electron Microscopy (SEM), Transmission Electron Microscopy (TEM) and X-ray Photoelectron Spectroscopy (XPS). Information supplied by the different techniques is outlined in **Table 2.3**. All of the techniques described in this chapter are performed on the calcined catalyst samples.

**Table 2. 3.** Main techniques used for catalysts characterization.

Technique	Provides information about :
X-ray fluorescence spectrometry (XRF)	Metal loadings (wt % or atomic ratio)
X-ray diffraction (XRD)	Structural properties, crystallographic parameters and crystallite size of crystalline solids
N <sub>2</sub> adsorption-desorption analysis	Textural properties (surface area, total pore volume, pore distribution).
Scanning electron microscopy coupled with energy dispersive X-ray spectrometry (SEM-EDX)	Surface morphology, microstructure, elemental analyse and distribution of elements (5 µm of depth)
Transmission electron microscopy coupled with energy dispersive X-ray spectrometry (EDX), dot maps and selected area electron diffraction (SAED)	Morphology of nanoparticles (shape and size), elemental composition (both qualitative and quantitative), elemental distribution and structural information on crystals.
X-ray photoelectron spectrometry (XPS)	Chemical analysis of the extreme surface (9 nm) and chemical environment

### 2.2.1 X-ray fluorescence spectroscopy (XRF)

Elemental analyses were carried out by Wavelength Dispersive X-ray Fluorescence (WDXRF) using a PANalyticalZetium (4 kW) spectrometer, equipped with rhodium tube, a scintillation detector for optimum determination of all elements from sodium to uranium. Previous to analysis, pellets of the samples (13 mm of diameter and 1 mm of thickness) were obtained by pressing the powders under 7-ton pressure during 5 min. Measurements were conducted in a He gas atmosphere.

### 2.2.2 X-ray diffraction (XRD)

Powder X-ray diffraction (XRD) analyses were done using a PANalytical MPD X'Pert Pro diffractometer operating with Cu K  $\alpha$  radiation,  $\lambda = 0.15406$  nm at 40 mA and 45 kV. Data were recorded at room temperature, applying 2 theta ( $2\theta^\circ$ ) scanning range of  $10-90^\circ$ , and a step size of  $0.017^\circ$  with a scan step time of 220 s. Data processing was then carried out using HighScore software. Phase identification of the materials was made according to the Joint Committee on Powder Diffraction Standards (JCPDS) database cards provided by the International Centre for Diffraction Data ICDD. During data processing and interpretation, the average crystallite size of the solid sample is approximated using Scherrer formula that can be written as [162]:

$$D = \frac{0.9 \lambda}{\beta \cos \theta} \quad \text{Eq. 2.13}$$

Where:

D: Average crystallite size ( $\text{\AA}$ )

$\lambda$ : X-ray wavelength  $\text{CuK}\alpha = 1.54056 \text{ \AA}$

$\beta$ : Full width at half maximum (FWHM)

$\theta$ : Diffraction angle ( $^\circ$ )

### 2.2.3 N<sub>2</sub> adsorption-desorption analysis

Nitrogen adsorption-desorption isotherms were acquired at  $-196^\circ\text{C}$  by means of Micromeritics ASAP2040 apparatus. Prior to analysis, the powders were outgassed under vacuum at  $200^\circ\text{C}$  for 10 h to remove the physisorbed gases. Determination of physisorption isotherms and associated hysteresis loops was done according to the International Union of Pure and Applied Chemistry (IUPAC) classifications [163, 164]. The specific surface areas were calculated by the Brunauer-Emmett-Teller (BET) method [165]. Total pore volume and

average pore diameter were determined using the standard Barrett-Joyner-Halenda (BJH) method [166] applied to the desorption branch of the isotherm.

#### **2.2.4 Scanning electron microscopy (SEM) coupled with energy dispersive X-ray spectrometry (SEM-EDX)**

Scanning electron microscopy (SEM) was carried out on a PHILIPS XL30 microscope equipped with an energy dispersive X-ray analysis spectrometer. SEM micrographs were acquired at 7 kV accelerating voltage, while SEM-EDX microanalysis were conducted at 15 kV accelerating voltage, with a probe size of about 2 nm. Prior to the observations, the powders were spread onto the surface of a carbon tape and sputter-coated with carbon.

#### **2.2.5 Transmission electron microscopy (TEM)**

Morphology characterization was an important aspect of this research, given that different synthesis parameters would lead to different particle shapes and sizes. Other information obtained from this technique was found important in fully understanding the correlation between the different analyses obtained from the other techniques that will be discussed elsewhere in this report. Transmission electron microscopy (TEM) was performed with a Jeol ARM-200F microscope, operating at 200 kV, with a probe size of about 0.08 nm. Prior to the TEM measurement, the samples were crushed and deposited on carbon coated Au grid after sonication of the powder into chloroform. Energy dispersive X-ray (EDX), dot maps, and selected area electron diffraction (SAED) have been also performed.

#### **2.2.6 X-ray photoelectron spectroscopy (XPS)**

X-ray photoelectron spectroscopy (XPS) measurements were done on a VG Scienta SES 2002 spectrometer equipped with a monochromatic Al K  $\alpha$  X-ray source (Al K  $\alpha$  = 1486.6 eV) and a hemispherical analyzer. The spectra were recorded using a pass energy of 100 eV, along with pressure of  $10^{-9}$  Pa in the analysis chamber. The analyzed zone has a surface of 24 mm<sup>2</sup> and an analysis depth between 3 and 10 nm depending on the studied material. Binding energies (BEs) were calibrated by taking C 1s peak (284.7 eV) of contaminating carbon as reference. The peaks were fitted by Gaussian-Lorentzian functions using the XPS-CASA software (casa XPS software 2.3.18 Ltd).

## 2.3 Catalytic testing

### 2.3.1 Experimental setup

Measurements of the catalytic activity were performed in isothermal mode and at atmospheric pressure on the fresh catalysts in a fixed bed reactor (vertical), with an internal diameter of 16 mm. 40–60 mesh particle size fractions of the sieved catalysts were disposed on a fritted quartz filter disc; inside the reactor tube. Then, the reactor was placed in an electric tubular oven and heated from ambient temperature to the desired reaction temperature, at a heating rate of 5 °Cmin<sup>-1</sup>. The reaction temperature was continuously monitored by means of a thermocouple placed in the middle of the catalytic bed.

CO oxidation was used as model reaction ( $\text{CO} + \frac{1}{2}\text{O}_2 \rightarrow \text{CO}_2$ ). Then, a gas mixture containing 0.05 vol% CO and 1.0 vol% O<sub>2</sub> in N<sub>2</sub> was injected in the reactor with a total gas flow rate of 50 NLh<sup>-1</sup>. The flow rate of CO, N<sub>2</sub> and air in the reactor was regulated by numerical gas flow meters. The outlet gas products were quantitatively analyzed each minute by an online gas analyzer using MLT Analyzer software (Version 3.6.X) combined with NGA 2000 platform. Scheme of installation for CO oxidation is given in **Figure 2.3**.

The conversion of CO was calculated using **Eq 2.14**:

$$\text{CO conversion \%} = (([\text{CO}]_{\text{in}} - [\text{CO}]_{\text{out}}) / [\text{CO}]_{\text{in}}) * 100 \quad \text{Eq 2.14}$$

Where [CO]<sub>in</sub> and [CO]<sub>out</sub> represent the CO concentrations in the inlet gas and outlet gas, respectively.

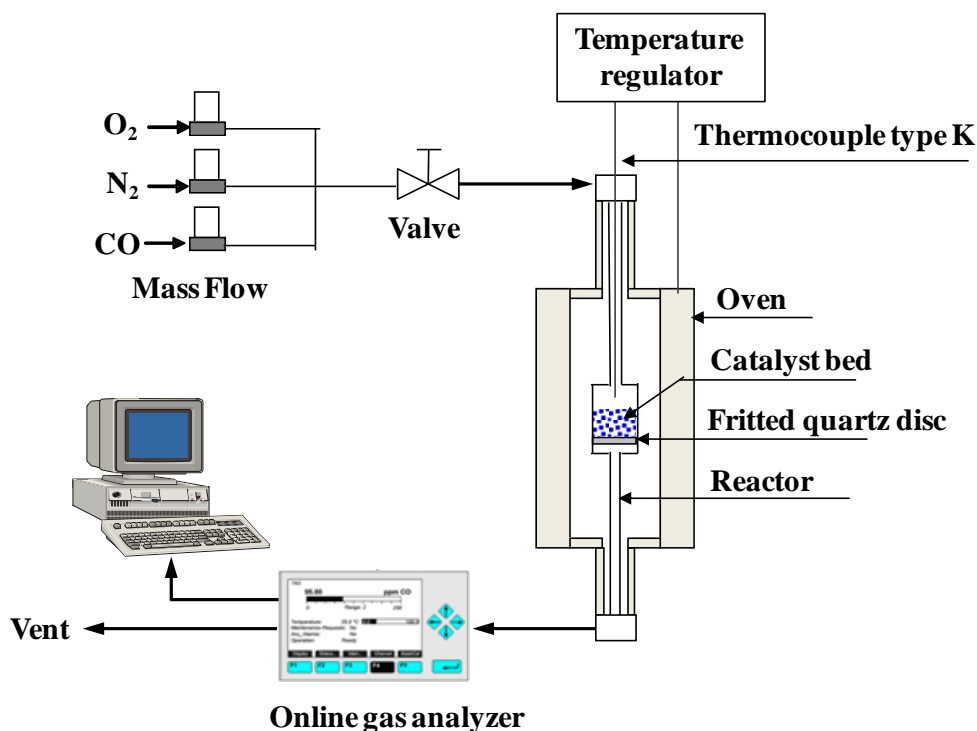


**Figure 2.3.** Scheme of installation used for the catalytic tests.

### 2.3.2 Operating conditions

#### Reaction temperature

The catalytic activity of the catalyst samples was conducted with the same range of temperature using two different procedures.

With the aim of determining the light-off of the catalysts, the samples were gradually heated from ambient temperature to the temperature, at which 100 % conversion of CO was reached ( $T_{100}$ ), with a heating rate of  $5\text{ }^{\circ}\text{Cmin}^{-1}$ .

To further check the influence of the reaction temperature on the conversion of CO, a test was conducted using another heating program. The reaction was started in the manner described in the previous section, but once the temperature reached a specific value (100  $^{\circ}\text{C}$ , 150  $^{\circ}\text{C}$  and 200  $^{\circ}\text{C}$  for Cu containing catalysts/300  $^{\circ}\text{C}$ , 400  $^{\circ}\text{C}$  and 500  $^{\circ}\text{C}$  for Ni or Co containing catalysts), the reactor was kept isothermal for 30 minutes on-stream. The heating rate was the same for both temperature programs. **Figure 2.4** shows the two different procedures previously described.

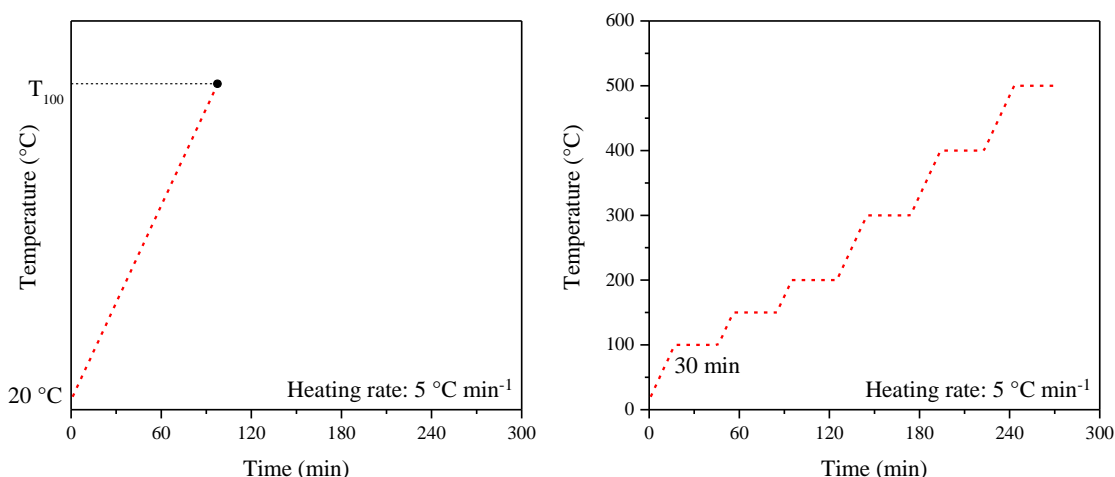


**Figure 2.4.** Catalytic procedures used to determine the light-off temperature,  $T_{100}$  and the isothermal CO conversion at specific temperatures.

#### Determination of the catalyst content necessary to perform the catalytic tests

The mass of catalyst used for the experimentations was calculated considering the total volume of catalyst, the space velocity (VVH) (average value 60000 h<sup>-1</sup>) and the total gas flow rate ( $D_V$ ) (average value 50 NLh<sup>-1</sup>). The catalyst mass was calculated with respect to the following equation:

$$VVH = \frac{D_V}{V_{cata}} = \frac{D_V * \rho}{m_{cata}} \leftrightarrow m_{cata} = \frac{D_V * \rho}{VVH} \quad \text{Eq. 2.15}$$

Where:

$m_{cata}$ : Mass of catalyst (g)

$D_V$ : Total gas flow rate (Lh<sup>-1</sup>)

$V_{cata}$ : Volume of the catalyst (L)

$\rho$ : Density (gL<sup>-1</sup>)

Operating conditions employed for the catalytic tests are summarized in **Table 2.4**.

**Table 2.4.** Operating conditions for catalytic testing.

Catalysts properties					
Form		Diameter	Catalysts density		Catalysts mass
Granular		40–60 mesh	0.7–1 gcm <sup>−3</sup>		0.6–1.2 g
Reaction conditions					
Pressure	Gas mixture	Temperature	Space velocity	Gas flow rate	Catalyst bed length
Atmospheric	0.05 vol% CO + 1.0 vol% O <sub>2</sub> in N <sub>2</sub>	20–500 °C	60000 h <sup>−1</sup>	50 NLh <sup>−1</sup>	≈ 4 mm

## Conclusions

This chapter presented the samples used in this study as well as their method of preparation. Two types of metal oxide were studied: alumina-based binary metal oxides and alumina-based ternary metal oxides. Alumina-based binary metal oxides were prepared with different RV/OV ratios and varied transition metal contents. These metal oxides are intended to be used as catalysts for the conversion of CO into CO<sub>2</sub>. Then, the analytical techniques used to characterize the physicochemical properties of the catalysts at different scales have been described. Finally, the pilot used for the catalytic tests was presented. The operating conditions employed for CO oxidation have also been described.

The characterization of the catalyst samples has been an important aspect of this research project, which deals with the quantitative measure of the physical and chemical properties, assumed to be responsible for their performance in CO oxidation. Physical properties such as the surface area, porosity, morphology, particle size and dispersion, must be well explored and defined. Similarly, determining the chemical composition, crystalline structure, and nature of the catalytic components and their interactions is a critical goal in characterization. These measurements are valuable in elucidating the impacts of the initial chemical precursor's composition on the final properties and, even more importantly, in producing an optimized catalytic system.

## Résumé en Français du chapitre 2

Ce chapitre présente les matériaux catalytiques synthétisés dans cette étude avec une attention particulière portée sur les méthodes de calcul et le raisonnement sur lequel se fondent la préparation de ces matériaux. Les principales techniques utilisées pour caractériser les propriétés physico-chimiques des catalyseurs synthétisés à différentes échelles ont été exposées. La mise en œuvre des tests catalytiques et le pilote utilisé pour les tests catalytiques ont été présentés. Les conditions opératoires utilisées pour l'oxydation du CO ont été également décrites.

Les échantillons préparés dans le cadre de cette étude sont des oxydes binaires et ternaires à base des métaux de transition (le nickel, le cobalt et le cuivre). Des oxydes métalliques binaires à base de Ni, Co ou Cu, avec différents ratio RV/OV et avec une teneur en métal de transition de 10 %, ont été préparés pour examiner l'influence de la stœchiométrie sur les propriétés physicochimiques et catalytiques. Des oxydes métalliques binaires à base de Ni, Co ou Cu, avec un ratio RV/OV fixe ( $RV/OV=1.1$ ) et avec différentes teneurs en métal de transition (5 à 20 % massique) ont été également préparés pour étudier l'influence de la teneur en métal de transition sur leurs propriétés physicochimiques et catalytiques. Des oxydes métalliques ternaires à base d'un mélange bimétallique des métaux de transition (Ni et Co, Ni et Cu ou Co et Cu), avec une teneur en métal de transition de 5 % en masse et un ratio RV/OV constant ( $RV/OV=1.0$ ), ont été préparés à fin d'évaluer l'effet de synergie des oxydes métalliques.

Ces oxydes métalliques ont été préparés par la méthode de combustion en solution assistée par micro-ondes, qui consiste à faire dissoudre les précurseurs d'oxydes métalliques de type nitrates et l'urée dans l'eau, puis maintenir la solution sous agitation à 60°C pendant 1 h, avant de soumettre la solution à une irradiation sous micro-ondes. Les oxydes métalliques obtenus ont été calcinés à 500 °C pendant 12h, afin de les stabiliser structuralement et thermiquement.

A partir de ces oxydes métalliques, des caractérisations ont été menés par différentes techniques afin de comprendre leurs propriétés chimiques et physiques et les corrélés avec leurs performances catalytiques. Parmi les propriétés chimiques identifiées, on peut souligner la détermination de la composition chimique globale des catalyseurs obtenue par spectroscopie de fluorescence X, la composition chimique en surface et la structure cristalline des oxydes formés. Ces données ont été obtenues à l'aide de la spectrométrie de fluorescence

des rayons X (XRF), la spectroscopie photo-électronique par rayons X (XPS), et la spectroscopie à rayons X à dispersion d'énergie (EDX), respectivement.

Les propriétés physiques ont été déterminées à l'aide de la diffraction des rayons X (XRD), la microscopie électronique à transmission (TEM), la microscopie électronique à balayage (SEM), et l'adsorption d'azote à -196 °C. Ces techniques donnent des informations par rapport à la structure globale, la structure en surface, la microstructure et les propriétés texturales, respectivement.

La caractérisation des échantillons a constitué un aspect important de ce projet de recherche, qui traite l'analyse qualitative et quantitative des propriétés physiques et chimiques, supposées être responsables de leurs performances en oxydation du CO. En effet, les conditions expérimentales de mise en œuvre des catalyseurs étudiés influent de façon conséquente sur la nature des phases formées et des espèces présentes à la surface des matériaux élaborés.

Ces analyses sont également précieuses pour élucider les impacts de la composition initiale du milieu réactionnel (la stœchiométrie), la teneur en métal de transition et la composition du mélange bimétallique (effet de synergie) sur les propriétés finales, et plus important encore, pour produire un matériau catalytique dont les performances sont optimales.

Ces oxydes métalliques ont été destinés à être utilisés comme catalyseurs pour la conversion du CO en CO<sub>2</sub>. La mise en œuvre des tests catalytiques a été réalisée dans un réacteur à lit fixe traversé et à flux gazeux continue. Le dispositif expérimental utilisé a été mis en place spécifiquement pour cette étude. Il est constitué d'un tube en quartz au milieu duquel un fritté poreux permet de déposer des grains de catalyseurs au travers desquels le mélange gazeux s'écoule à débit constant. L'unité pilote utilisée permet de travailler soit en mode isotherme soit lors d'une rampe en température permettant de déterminer des paramètres caractéristiques des catalyseurs étudiés (température de light-off, T<sub>50</sub>, T<sub>100</sub>). Les conditions expérimentales permettant d'évaluer les performances des différents catalyseurs étudiés ont été définies à partir de l'étude bibliographique menée dans le cadre de ces travaux de thèse, de sorte à disposer de données de référence pour cette étude.

## CHAPTER 3. CATALYST CHARACTERIZATION

---

## Table of contents

Introduction .....	73
3.1 Binary oxide catalysts .....	73
3.1.1 Effect of stoichiometry (RV/OV ratio) .....	73
3.1.1.1 Effect of stoichiometry (RV/OV ratio) - metal loading = 10 wt% .....	73
3.1.1.1.1 XRF .....	73
3.1.1.1.2 XRD .....	74
3.1.1.1.2.1 Nickel based catalysts .....	74
3.1.1.1.2.2 Cobalt based catalysts .....	75
3.1.1.1.2.3 Copper based catalysts .....	76
3.1.1.1.3 N <sub>2</sub> adsorption-desorption isotherms .....	78
3.1.1.1.3.1 Nickel based catalysts .....	79
3.1.1.1.3.2 Cobalt based catalysts .....	80
3.1.1.1.3.3 Copper based catalysts .....	81
3.1.1.1.4 SEM .....	83
3.1.1.1.4.1 Nickel based catalysts .....	83
3.1.1.1.4.2 Cobalt based catalysts .....	84
3.1.1.1.4.3 Copper based catalysts .....	85
3.1.1.1.5 XPS .....	87
3.1.1.1.5.1 Nickel based catalysts .....	87
3.1.1.1.5.2 Cobalt based catalysts .....	88
3.1.1.1.5.3 Copper based catalysts .....	89
3.1.1.1.6 TEM .....	91
3.1.1.1.6.1 Nickel based catalysts .....	91
3.1.1.1.6.2 Cobalt based catalysts .....	92
3.1.1.1.6.3 Copper based catalysts .....	94
3.1.1.2 Effect of stoichiometry (RV/OV ratio) - metal loading = 2 wt% .....	96
3.1.1.2.1 XRD .....	96
3.1.1.2.2 N <sub>2</sub> adsorption-desorption isotherms .....	99
3.1.1.2.3 SEM .....	101
3.1.2 Effect of metal loading .....	104
3.1.2.1 XRF .....	104

3.1.2.2	XRD .....	104
3.1.2.2.1	Nickel based catalysts .....	104
3.1.2.2.2	Cobalt based catalysts .....	107
3.1.2.2.3	Copper based catalysts .....	109
3.1.2.3	N <sub>2</sub> adsorption-desorption isotherms .....	110
3.1.2.3.1	Nickel based catalysts .....	110
3.1.2.3.2	Cobalt based catalysts .....	110
3.1.2.3.3	Copper based catalysts .....	111
3.1.2.4	SEM.....	112
3.1.2.4.1	Nickel based catalysts .....	112
3.1.2.4.2	Cobalt based catalysts .....	114
3.1.2.4.3	Copper based catalysts .....	115
3.1.2.5	SEM-EDX.....	116
3.1.2.5.1	Nickel based catalysts .....	116
3.1.2.5.2	Cobalt based catalysts .....	117
3.1.2.5.3	Copper based catalysts .....	117
3.2	Ternary oxide catalysts.....	118
3.2.1	XRD .....	118
3.2.2	N <sub>2</sub> adsorption-desorption isotherms .....	120
3.2.3	SEM.....	121
3.2.4	XPS.....	122
3.2.5	TEM .....	124
	Conclusions .....	130
	Résumé en Français du chapitre 3 .....	132

## Introduction

This chapter provides a thorough study and discussion regarding the physicochemical properties of the various metal oxide catalysts stated in the previous chapter. The first part is related to the effects of stoichiometry (RV/OV ratio) and metal content on the properties of alumina-based binary metal oxide catalysts. The second part is devoted to the differences in the physicochemical properties of alumina-based ternary metal oxide catalysts, with the aim of understanding the effect of the presence of a supplementary component in alumina-based mixed oxide catalysts. The objective of this chapter is to elucidate the major differences between the catalyst samples, to give a possible explanation of their different behaviors and to connect the analysis data obtained from the different characterization techniques.

### 3.1 Binary oxide catalysts

#### 3.1.1 Effect of stoichiometry (RV/OV ratio)

This section reports on a systematic study conducted on the characterization of alumina-based binary metal oxide catalysts. The focus is on the understanding of how the variations on stoichiometry influence the phase composition, structure, crystallite size and morphology of the binary oxide catalysts. Two series of catalysts were studied; in the first, the metal loading was maintained at 10 wt%, while in the second, the metal loading was fixed at 2 wt%.

##### 3.1.1.1 Effect of stoichiometry (RV/OV ratio) - metal loading = 10 wt%

###### 3.1.1.1.1 XRF

The metal loadings (Ni, Co and Cu) (wt%) in the bulk materials determined by XRF are given in **Table 3.1**. Experimental data are in good agreement with theoretical results, as most samples present a metal content close to 10 wt%. Indeed, the nickel content in 10NiAl-x sample is between 9.64 and 10.30 wt%. For the 10CoAl-x sample, the cobalt content is between 9.97 and 10.70 wt%, whereas for 10CuAl-x sample an amount between 9.80 and 10.70 wt% Cu is detected. It should be noticed that deviation from the stoichiometry results in more slightly shifted values.

**Table 3. 1.** *Elemental analysis of the 10MAl–x calcined catalysts.*

Sample identity	Metal loading (wt%)		
	Ni	Co	Cu
10NiAl–0.9	9.64	–	–
10NiAl–1.0	10	–	–
10NiAl–1.1	10.30	–	–
10CoAl–0.9	–	10.14	–
10CoAl–1.0	–	9.97	–
10CoAl–1.1	–	10.70	–
10CuAl–0.9	–	–	9.80
10CuAl–1.0	–	–	9.90
10CuAl–1.1	–	–	10.70

### 3.1.1.1.2 XRD

#### 3.1.1.1.2.1 Nickel based catalysts

The XRD patterns of nickel-based catalysts, with different RV/OV ratios and a constant nickel loading of 10 wt%, are shown in **Figure 3.1**. All 10NiAl–x catalyst samples exhibited broad diffraction peaks of  $\text{NiAl}_2\text{O}_4$  phase (JCPDS 01–078–6951) without any obvious diffraction peaks of NiO phase. The comparison of the slightly higher  $2\theta$  values of the formed spinel with those of a stoichiometric  $\text{NiAl}_2\text{O}_4$  spinel provided by JCPDS file 01–078–6951 indicates that a non-stoichiometric  $\text{NiAl}_2\text{O}_4$  phase was formed [167]. These peaks, corresponding to  $\text{NiAl}_2\text{O}_4$ , can be also assigned to a defect spinel of  $\gamma\text{-Al}_{2.67}\text{O}_4$  phase (JCPDS 04–005–4662), since its diffraction lines overlap with those of nickel aluminates. Based on **Figure 3.1**, no clear changes were observed in the peak positions, while a very slight variation in the peak intensities can be revealed when changing the RV/OV ratio. Looking to previous studies carried-out on 10 wt % Ni– $\text{Al}_2\text{O}_3$  catalyst, observations in conflict among each other can be found about the state of Ni. Formation of a defect  $\text{NiAl}_2\text{O}_4$  phase has been reported by Li et al. [167] and Kiš et al. [168]. Other investigators have shown that NiO and  $\text{NiAl}_2\text{O}_4$  phases were the main phases present [155]. Differently, in other studies, only  $\gamma\text{-Al}_2\text{O}_3$  and  $\text{NiAl}_2\text{O}_4$  phases were formed, and NiO species displayed to be highly dispersed on  $\gamma\text{-Al}_2\text{O}_3$  support by formation of  $\text{NiAl}_2\text{O}_4$  phase [68, 169].

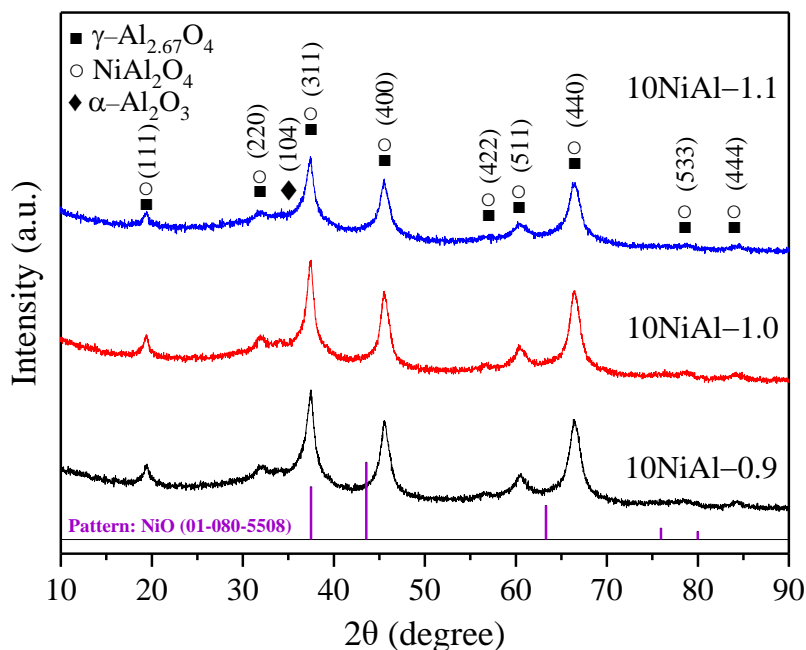


**Figure 3. 1.** XRD patterns of 10NiAl-*x* calcined catalysts.

#### 3.1.1.1.2.2 Cobalt based catalysts

The XRD pattern of 10CoAl-*x* catalyst samples is shown in **Figure 3.2**. All 10CoAl-*x* catalyst samples exhibited diffraction peaks of a defect spinel  $\gamma$ -alumina ( $\gamma$ -Al<sub>2.67</sub>O<sub>4</sub>) (JCPDS 04-005-4662), which overlapped with the peaks of stoichiometric CoAl<sub>2</sub>O<sub>4</sub> spinel (JCPDS 00-003-0896). Moreover, the XRD patterns of these samples showed diffraction peaks corresponding to the presence of  $\alpha$ -Al<sub>2</sub>O<sub>3</sub> (JCPDS 00-042-1468). Unfortunately, it was difficult to distinguish the diffraction peaks of Co<sub>3</sub>O<sub>4</sub>, because this phase presents overlapped diffraction lines with the  $\gamma$ -Al<sub>2.67</sub>O<sub>4</sub> and CoAl<sub>2</sub>O<sub>4</sub> phases. As in the case of nickel-based catalysts, the transition metal oxide was not easy to identify, suggesting that these species may be highly dispersed over the  $\gamma$ -Al<sub>2.67</sub>O<sub>4</sub> surface, incorporated into the  $\gamma$ -Al<sub>2.67</sub>O<sub>4</sub> lattice to form spinel phases, or that the size of their crystallites was smaller than the detection limit of XRD measurements. A glancing view over the intensity of the signals reveals that the intensity of the diffraction peaks gradually increases by increasing the RV/OV value from 0.9 to 1.1. These peaks become sharper and more consistent with the 10CoAl-1.1 catalyst sample. The increase in intensity and sharpness of the peaks may be due the higher amount of CoAl<sub>2</sub>O<sub>4</sub> spinel in the catalyst. On the other hand, low amount of fuel (fuel lean conditions: R=0.9) led to a significant decrease in crystallinity, indicating that  $\gamma$ -Al<sub>2.67</sub>O<sub>4</sub> is the major phase in 10CoAl-0.9 catalyst.

Formation of cobalt aluminates spinel structure is believed to be more evident for 10CoAl-1.1 catalyst sample, which indicates a stronger interaction between cobalt species

and alumina, when the RV/OV ratio increases. Crystallinity enhancement could be attributed to the spinel formation, which might be promoted by the increase of flame temperature with the growing value of RV/OV [158]. XRD results of 10CoAl- $x$  catalyst samples are in agreement with previous studies. Indeed, formation of cobalt aluminates is a quite common phenomenon in cobalt oxide–alumina systems, regardless of their method of synthesis or the cobalt metal loadings [86, 94, 71].

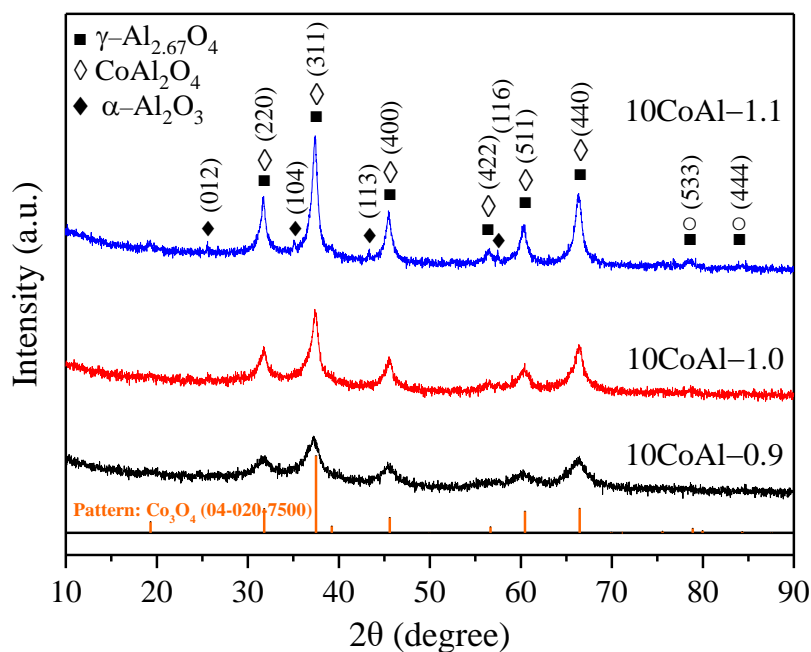


**Figure 3. 2.** XRD patterns of 10CoAl- $x$  calcined catalysts.

### 3.1.1.1.2.3 Copper based catalysts

**Figure 3.3** shows well-defined XRD patterns of 10CuAl- $x$  catalyst samples. All 10CuAl- $x$  catalysts exhibited diffraction peaks of  $\alpha$ -Al<sub>2</sub>O<sub>3</sub> (JCPDS 00-042-1468), as well as diffraction peaks of CuO (JCPDS 00-005-0661). Contrary to the other samples, 10CuAl- $x$  catalyst samples did not exhibit crystalline phases attributed to  $\gamma$ -Al<sub>2</sub>O<sub>3</sub> or to spinel phases (CuAl<sub>2</sub>O<sub>4</sub>). Moreover, the 10CuAl-1.0 catalyst sample displayed high intensity diffraction peaks of  $\alpha$ -Al<sub>2</sub>O<sub>3</sub>, as compared to those obtained from non-stoichiometric conditions, indicating that the 10CuAl-1.0 catalyst presents a higher crystallinity. The XRD patterns of 10CuAl- $x$  were different than those obtained for CuO–Al<sub>2</sub>O<sub>3</sub> catalysts prepared by impregnation method [95]. The authors reported on the formation of CuO species and CuAl<sub>2</sub>O<sub>4</sub>. In general, CuAl<sub>2</sub>O<sub>4</sub> spinel is the result of a solid-solid interaction between CuO and Al<sub>2</sub>O<sub>3</sub> once the calcination temperature reaches 700 °C [99-101].

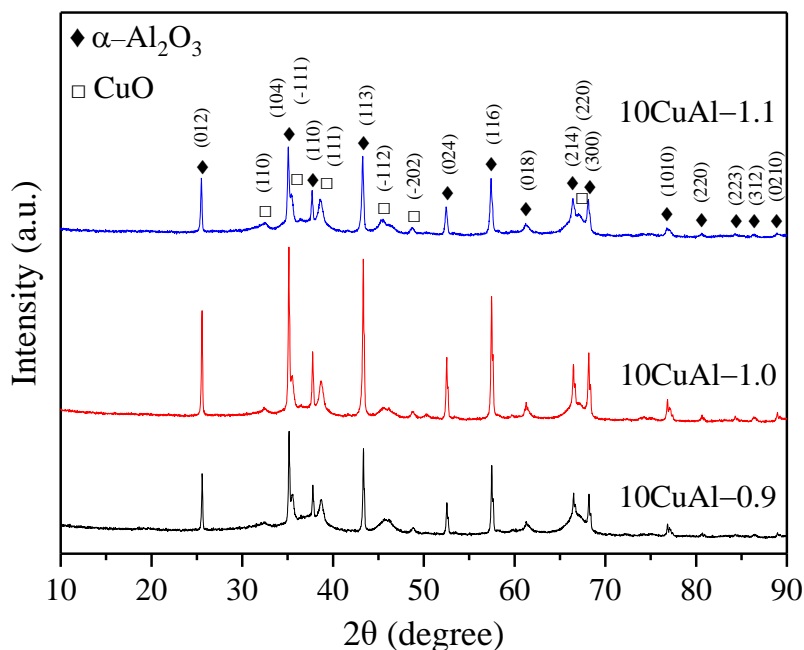


**Figure 3. 3.** XRD patterns of 10CuAl-*x* calcined catalysts.

The average crystallite size of  $\text{NiAl}_2\text{O}_4$ ,  $\text{CoAl}_2\text{O}_4$  and  $\text{CuO}$ , with different RV/OV ratios, as estimated by applying the Scherrer's equation, is summarized in **Table 3.2**. 10NiAl-*x* and 10CoAl-*x* catalyst samples have almost the same crystal size, while 10CuAl-*x* catalyst samples have the largest crystal size (between 35 and 44 nm). It can also be seen that crystal size increases, in all cases, with increasing the RV/OV ratio from 0.9 to 1.1. The observed increase in crystallite size could be attributed to an increase in the combustion temperature, which promotes the crystal growth.

**Table 3. 2.** Structural properties of 10MAl-*x* calcined catalysts.

Sample identity	Crystallite size (nm)		
	$\text{NiAl}_2\text{O}_4/\gamma\text{-Al}_{2.67}\text{O}_4^{\text{a}}$	$\text{CoAl}_2\text{O}_4/\gamma\text{-Al}_{2.67}\text{O}_4^{\text{b}}$	$\text{CuO}^{\text{c}}$
10NiAl-0.9	16	—	—
10NiAl-1.0	26	—	—
10NiAl-1.1	48	—	—
10CoAl-0.9	—	11	—
10CoAl-1.0	—	26	—
10CoAl-1.1	—	33	—
10CuAl-0.9	—	—	35
10CuAl-1.0	—	—	38
10CuAl-1.1	—	—	44

<sup>a</sup> Crystallite size estimated by Scherrer's equation at  $2\theta = 37.58^\circ, 37.47^\circ, 37.5^\circ$

<sup>b</sup> Crystallite size estimated by Scherrer's equation at  $2\theta = 37.28^\circ, 37.53^\circ, 37.39^\circ$

<sup>c</sup> Crystallite size estimated by Scherrer's equation at  $2\theta = 38.63^\circ, 38.7^\circ, 38.56^\circ$

### Discussion

A mixture of  $\gamma$ -alumina and metal aluminates ( $\text{MAl}_2\text{O}_4$ ) were present in the structure of  $10\text{NiAl-x}$  and  $10\text{CoAl-x}$  catalyst samples, while  $\text{CuO}$  and  $\alpha\text{-Al}_2\text{O}_3$  separated phases were identified in the  $10\text{CuAl-x}$  catalyst samples. This result suggests that the urea-nickel/cobalt nitrates interactions in the solution lead to the formation of  $\gamma$ -alumina and the metal oxides ( $\text{NiO}$  or  $\text{CoO}$ ) that interact further to yield  $\text{MAl}_2\text{O}_4$ .

The presence of  $\text{CuO}$  and  $\alpha\text{-Al}_2\text{O}_3$  separated phases in  $10\text{CuAl-x}$  samples and the existence of  $\gamma$ -alumina in  $10\text{NiAl-x}$  and  $10\text{CoAl-x}$  samples treated at high temperatures raises questions about the nucleation and crystallization process of the different phases. Indeed, according to the literature, the formation of well-crystallized  $\alpha\text{-Al}_2\text{O}_3$  occurs at high temperatures above  $\approx 1100^\circ\text{C}$ , while  $\gamma\text{-Al}_2\text{O}_3$  is obtained at lower temperatures ( $<800^\circ\text{C}$ ). On the other hand, it is generally acknowledged that the existence of aluminates spinel phases is detected at elevated temperatures  $\approx 700^\circ\text{C}$ . These conflicting results suggest that the metal oxide hinders the nucleation and phase transformations of  $\text{Al}_2\text{O}_3$  in these catalysts.

There were no changes in the catalyst phase composition, and no detectable peaks of  $\text{NiO}$  or  $\text{Co}_x\text{O}_y$  species were observed by varying the RV/OV ratio, which suggests that the RV/OV ratio has no effect on inhibiting the spinel formation (in the studied RV/OV range). By increasing the RV/OV ratio, it is accepted that the flame temperature would continuously increase, facilitating the metal oxides migration into the  $\text{Al}_2\text{O}_3$  matrix to form metal aluminates.

The RV/OV ratio seems to affect the crystallinity degree of the obtained phases. Indeed, in most cases, fuel-lean and fuel-rich conditions result in a decrease of the XRD signal intensities, whereas catalyst samples obtained from stoichiometric compositions (RV/OV = 1.0) exhibited the optimal crystallinity. This can be interpreted by the incomplete reaction between urea and metal nitrates, which led to amorphous materials. Thus, the proper combination of chemical reagents is essential for optimum combustion reactions. To further confirm this effect, additional  $10\text{MAl-x}$  samples with RV/OV values of 0.8 and 1.2 were synthesized and characterized. Their XRD patterns are given in **Figure A.1** (See **Annex A**).

#### **3.1.1.1.3 $\text{N}_2$ adsorption-desorption isotherms**

The textural properties of the calcined catalysts were examined by nitrogen adsorption-desorption measurements. For comparison purposes, well crystallized  $\alpha\text{-Al}_2\text{O}_3$  samples were

prepared by microwave-assisted solution combustion, using different compositions of aluminum nitrate-urea mixtures. The samples were then calcined in a muffle oven at 500 °C for 2 h. The N<sub>2</sub> adsorption-desorption isotherms and textural properties of the obtained powders are included in **Figure A.2** and **Table A.1**, respectively (See **Annex A**).

#### 3.1.1.1.3.1 Nickel based catalysts

**Figure 3.4** shows the N<sub>2</sub> adsorption-desorption isotherm of the calcined 10NiAl-*x* catalyst samples. The isotherms of 10NiAl-*x* samples are of type I, characteristic of microporous solids with relatively low external surface areas, with H4-type hysteresis loops that can be associated with the presence of narrow slit-like pores. **Table 3.3** lists the textural properties of 10NiAl-*x* catalysts. The BET surface area of the calcined catalysts with different RV/OV varied from 69.4 to 135.1 m<sup>2</sup>g<sup>-1</sup>; the 10NiAl-1.1 catalyst exhibited the highest surface area. The pore volume ranged between 0.04 and 0.08 cm<sup>3</sup>g<sup>-1</sup>, while the average pore diameter was between 2.7 and 3.5 nm. It is worth to notice that the surface area values varied proportionally to the pore volume, while the average pore diameter increased with the diminution of the pore volume.

The BET surface area clearly increased when the RV/OV ratio increased from 0.9 to 1.1. Moreover, the mesostructures of 10NiAl-*x* catalyst samples were found to be sensitive to the RV/OV ratio. The pore volume increased and the pore diameter slightly decreased when the RV/OV value rises from 0.9 to 1.1.

The literature has revealed that high RV/OV ratio (fuel-rich condition) results in an increase of the combustion temperature with a consequent rise in the volume of gases evolved [158]. Thus, it is proposed that in the case of 10NiAl-1.1 catalyst a sustained combustion led to a higher number of micropores produced by the important volume of combustion gases, resulting in an increase of the BET surface area.

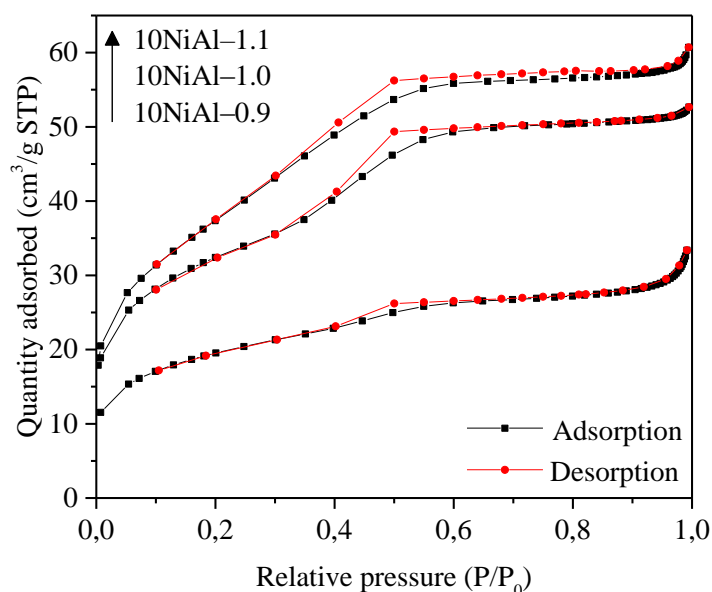


**Figure 3. 4.** *N<sub>2</sub> adsorption-desorption isotherm of 10NiAl-*x* calcined catalysts.*

#### 3.1.1.1.3.2 Cobalt based catalysts

**Figure 3.5** shows the N<sub>2</sub> adsorption-desorption isotherm of the calcined 10CoAl-*x* catalyst samples. The isotherms of CoAl-0.9 and CoAl-1.0 samples are of type (I+IV), with H4-type hysteresis loops. On the other hand, 10CoAl-1.1 catalyst sample showed type IV isotherm, characteristic of mesoporous solids, with H3-type hysteresis loop related to aggregates of plate-like particles, giving rise to slit-shaped pores. The textural properties of the different calcined solids are summarized in **Table 3.3**. The BET surface area for the catalyst samples varied from 16.1 to 45.9 m<sup>2</sup>g<sup>-1</sup> and the pore volume ranged between 0.02 and 0.03 cm<sup>3</sup>g<sup>-1</sup>, while the average pore size increased from 3.8 to 7.9 nm. The 10CoAl-0.9 catalyst exhibited the highest surface area as well as the largest average pore size. In comparison with 10NiAl-*x* catalyst samples, the RV/OV ratio seems to have an opposite effect on the textural properties of the 10CoAl-*x* catalyst samples. In fact, the surface area decreased significantly by increasing the fuel/nitrates ratio. Meanwhile, the pore diameter increased when the RV/OV value rises from 0.9 to 1.1. This is probably due, on the one hand, to the higher RV/OV ratio that can lead to a higher flame temperature, resulting in a more sintering extent and agglomeration of the particles and consequently to low surface areas, and, on the other hand, to excessive bulk cobalt aluminates formation, the increased RV/OV ratio may affect the textural properties of the solids and consequently decreases the surface area.

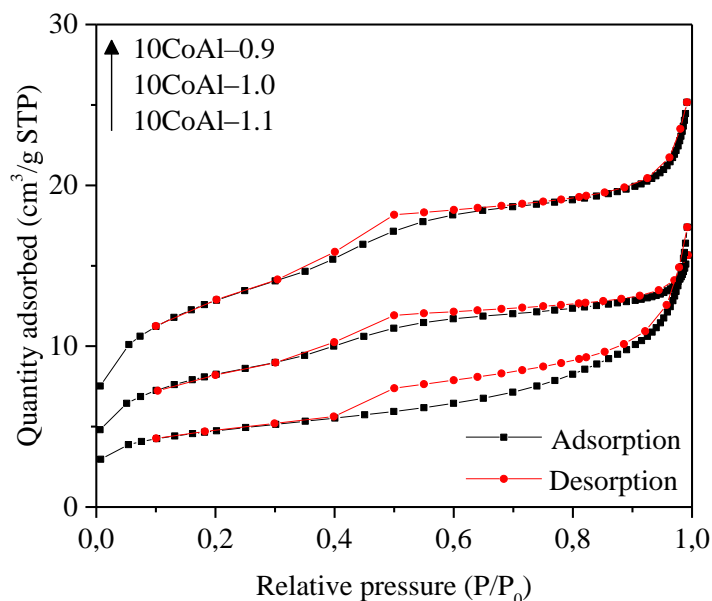


**Figure 3. 5.**  $N_2$  adsorption-desorption isotherm of  $10CoAl-x$  calcined catalysts.

### 3.1.1.1.3.3 Copper based catalysts

As revealed in **Figure 3.6**, all  $10CuAl-x$  samples exhibited II-type isotherms with H3-type hysteresis loops. The textural properties of these catalysts are given in **Table 3.3**. Noteworthy is the surface areas of  $10CuAl-x$  catalyst samples that were rather lower than that of nickel or cobalt based catalysts. The  $10CuAl-1.0$  catalyst presented the maximum surface area of  $25.7 \text{ m}^2\text{g}^{-1}$  and the smallest pore diameter, while the  $10CuAl-0.9$  catalyst exhibited the minimum surface area of  $13.5 \text{ m}^2\text{g}^{-1}$  and the largest pore size. The pore volume remained constant when varying the RV/OV ratio. It is worth to notice that the variation trend of the textural properties for  $10CuAl-x$  catalysts is similar to that of the  $Al-x$  samples (See **Annex A, Figure A.2**). Meanwhile, the BET surface areas of  $10CuAl-x$  samples are notably smaller than those of the  $Al-x$  samples.

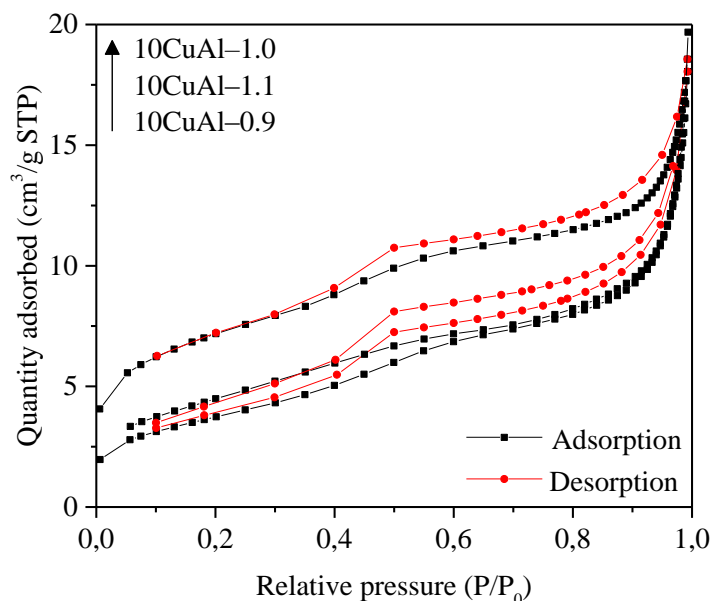


**Figure 3. 6.**  $N_2$  adsorption-desorption isotherm of  $10CuAl-x$  calcined catalysts.

**Table 3. 3.** Textural properties of  $10MAI-x$  calcined catalysts.

Sample identity	BET surface area ( $m^2g^{-1}$ )	Pore volume <sup>a</sup> ( $cm^3g^{-1}$ )	Pore diameter <sup>b</sup> (nm)
10NiAl-0.9	69.4	0.04	3.5
10NiAl-1.0	115.3	0.07	2.9
10NiAl-1.1	135.1	0.08	2.7
10CoAl-0.9	45.9	0.03	3.9
10CoAl-1.0	31.5	0.02	3.8
10CoAl-1.1	16.1	0.02	7.9
10CuAl-0.9	13.5	0.03	7.0
10CuAl-1.0	25.7	0.03	5.0
10CuAl-1.1	16.4	0.03	6.5

<sup>a</sup> BJH desorption pore volume.

<sup>b</sup> BJH desorption average pore diameter.

### Discussion

The relatively low surface area, obtained for almost all samples, can be associated to the high flame temperature reached during the combustion process. Indeed, a high flame temperature leads to a slight sintering of the particles, resulting in a more extent agglomeration of the particles and consequently to low surface areas.

Among the different samples synthesized using various RV/OV ratios, 10NiAl-1.1 was found to have the highest surface area, whereas the 10CoAl-1.1 catalyst had the smallest surface area. The textural properties of the different samples seem to be linked to their phase composition, and most probably to the phase transformation in alumina, as a major

component for the enhancement of the surface area and the mesoporosity. Indeed, the highest surface area obtained for the 10NiAl-x samples could be associated with the presence of  $\gamma$ -alumina phase, while the low surface area measured for the 10CoAl-x sample is potentially due to the formation of aluminates, whose surface area are generally low.

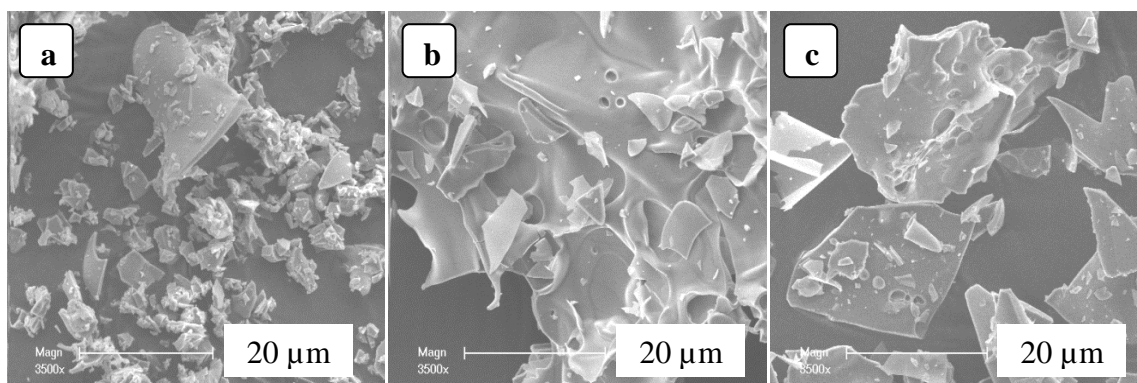
Furthermore, the textural properties of the various samples are found to be sensitive to the RV/OV ratio. This could be explained by the fact that the combustion behavior of different urea/nitrates mixtures affects the exothermicity of the combustion reaction and the volume of the gases generated during the combustion process, which both contribute to the tuning of the final textural properties of the combustion-synthesized samples.

#### 3.1.1.1.4 SEM

The morphology and the surface feature of the calcined catalysts were examined by SEM. For comparison purposes,  $\alpha$ -Al<sub>2</sub>O<sub>3</sub> calcined sample has been also examined. The SEM micrographs of Al-1.0 sample, obtained from a stoichiometric mixture of urea-nitrates, are shown in **Figure A.3** (See **Annex A**). The  $\alpha$ -Al<sub>2</sub>O<sub>3</sub> calcined sample had nearly hexagonal platelet particles with sizes ranging from 0.1 to 13  $\mu$ m.

##### 3.1.1.1.4.1 Nickel based catalysts

The SEM micrographs of the 10NiAl-x samples, with various RV/OV ratios, are collected in **Figure 3.7**. No significant differences were observed among the morphologies of the different 10NiAl-x samples. The agglomerates of the 10NiAl-x samples exhibited “flaky-like” morphology with an average size of the agglomerates higher than 50  $\mu$ m. These agglomerates were constituted by nearly hexagonal platelet particles (similar to that of  $\alpha$ -Al<sub>2</sub>O<sub>3</sub> calcined sample). The surface of the agglomerated particles showed the presence of cracks and voids, which reflects the inherent nature of the combustion reaction.



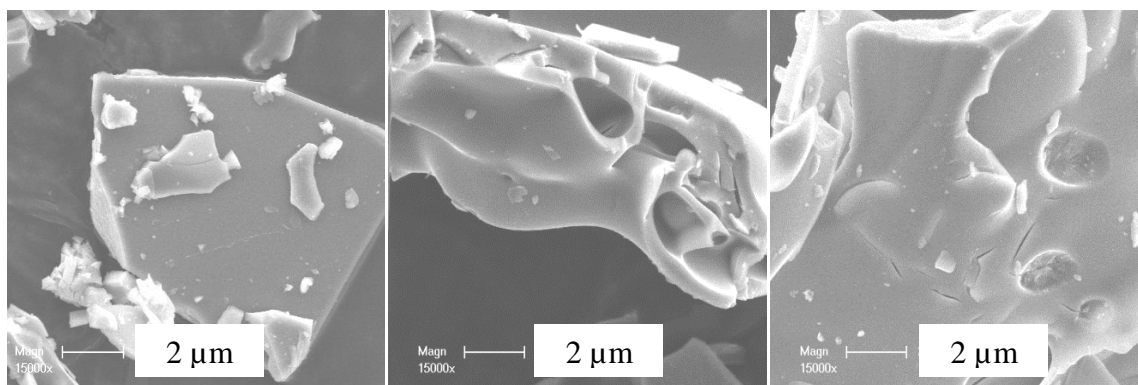
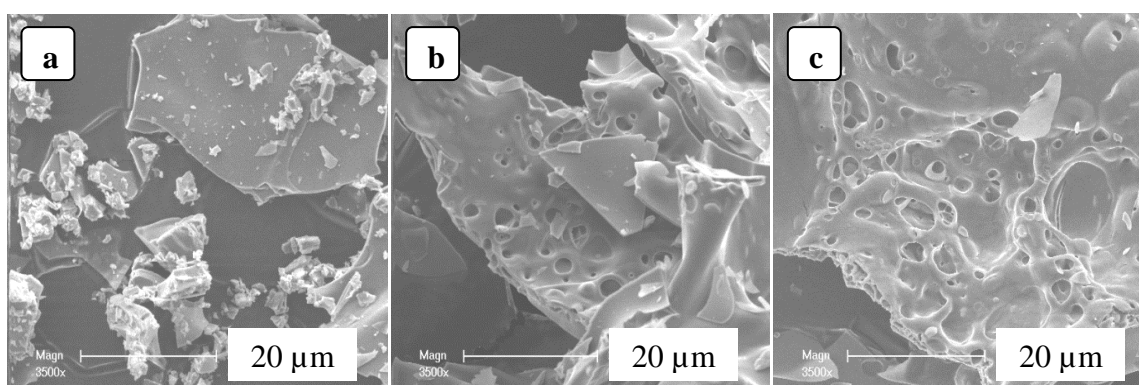


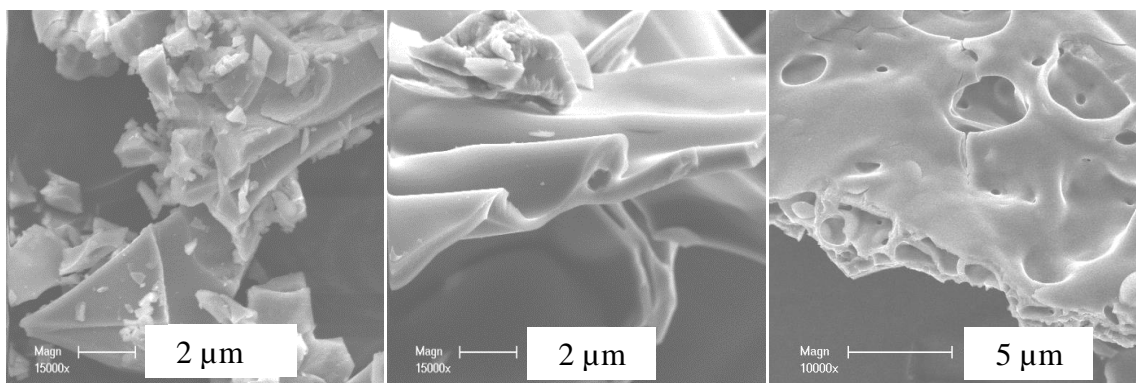
**Figure 3. 7.** SEM images of (a) 10NiAl-0.9, (b) 10NiAl-1.0 and (c) 10NiAl-1.1 calcined samples.

#### 3.1.1.1.4.2 Cobalt based catalysts

**Figure 3.8** shows the SEM images of the calcined 10CoAl-x catalysts. Some distinctions could be observed among the morphologies of the different 10CoAl-x samples.

For sample 10CoAl-0.9, the SEM images exhibited “flaky-like” morphology, similar to that obtained for 10NiAl-x samples. For 10CoAl-1.0 and 10CoAl-1.1 samples, the micrographs exhibited foamy and platelet agglomerated particles with an average size higher than that of 10CoAl-0.9, and a wide distribution of large voids in their structure, which are formed from the escaping gases during the combustion. It is assumed that the combustion temperature and gases volume increase by increasing the RV/OV ratio, during the combustion process, resulting in the agglomerates growth and large holes.

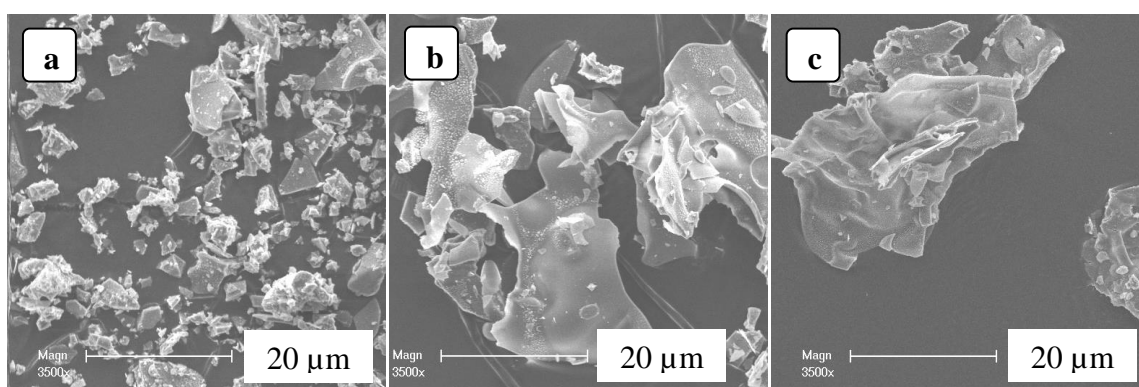




**Figure 3. 8.** SEM images of (a) 10CoAl-0.9, (b) 10CoAl-1.0 and (c) 10CoAl-1.1 calcined samples.

#### 3.1.1.1.4.3 Copper based catalysts

**Figure 3.9** displays the SEM images of the 10CoAl-x catalysts. The micrographs of different samples showed foamy and “flaky-like” agglomerated particles. When observing SEM images by increasing the magnification to  $\times 15000$ , quasi-spherical nanoparticles can be seen, which could be attributed to the CuO. By further increasing magnification to  $\times 100000$ , it can be seen that the size and distribution of these nanoparticles on the surface are quite different. For 10CuAl-0.9 catalyst, small particle size and regional agglomeration are observed. For 10CuAl-1.0 catalyst, the nanoparticles are uniformly dispersed, without any agglomeration. A significantly larger particle size and apparent agglomeration are observed in the 10CuAl-1.1 catalyst. Further study by TEM coupled with dot maps and SAED should be carried-out to determine the structure and chemical compositions of the observed nanoparticles.



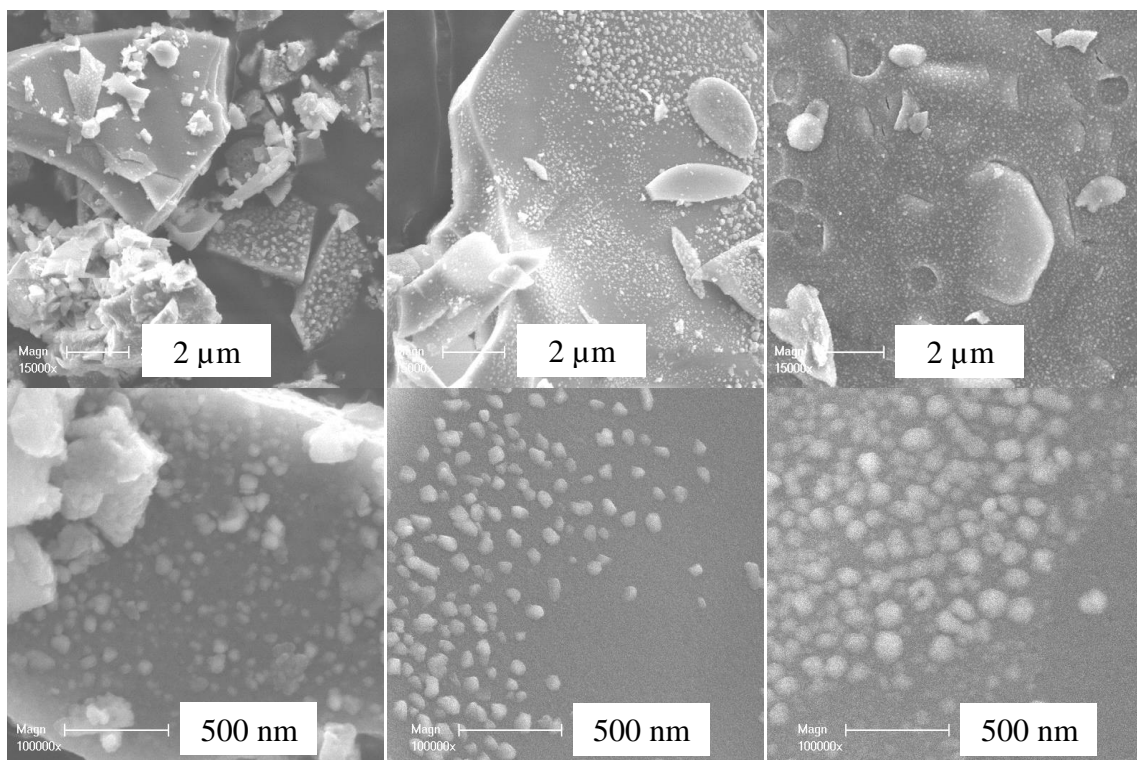


**Figure 3. 9.** SEM images of (a) 10CuAl-0.9, (b) 10CuAl-1.0 and (c) 10CuAl-1.1 calcined samples.

### Discussion

The agglomerates of the combustion-synthesized 10MAI-x catalysts presented a foamy and “flaky-like” morphology. These morphologies are commonly observed for combustion-synthesized alumina powders; therefore, the addition of transition metal oxides to alumina induces textural modification without any substantial changes at the microscopic scale. The observed foamy morphology might facilitate the access to the internal surface of the catalyst and potentially improve the catalytic activity.

The surface features of the calcined samples prepared with various RV/OV are somewhat different. 10NiAl-x and 10CoAl-x samples presented soft surfaces, while quasi-spherical nanoparticles were dispersed on the surface of 10CuAl-x. The agglomeration behavior and particle size of the observed nanoparticles were greatly affected by the RV/OV ratio. It appears that the lower RV/OV ratio, the smaller the particles could form. These results are consistent with those obtained from XRD characterization, where the particle size of CuO decreases with decreasing RV/OV molar ratio.

The increase of RV/OV ratio results in a greater agglomeration and highly foamed materials. These results suggested that a higher RV/OV ratio produces a higher combustion temperature and larger volume of gaseous products.

To further check the effect of the RV/OV ratio, 10MAI-x samples (Where  $x = 0.8$  and  $1.2$ ) were examined by SEM and their micrographs are provided in **Figures A.4–9** (See **Annex A**). There were no clear changes in the morphology of nickel and cobalt based catalysts, while a sever agglomeration with irregular distribution of agglomerated particles were detected for copper-based catalysts. It is believed that an uncontrollable combustion reaction takes place, when further increasing or decreasing the RV/OV ratio. Thus, it can be roughly concluded that the controllability over the phases and morphologies of the products is strictly linked to the stoichiometry of the reactants.

### 3.1.1.1.5 XPS

The previously reported techniques have successfully assisted in providing valuable insights into the bulk properties of catalysts (extending below the catalytic surface). Meanwhile, the composition of the catalyst surface, as opposed to its bulk, is also of critical importance since the active sites exist on the catalyst surface, wherein chemisorptions, chemical reaction, and desorption would take place.

#### 3.1.1.1.5.1 Nickel based catalysts

The Ni  $2p_{3/2}$ , Al  $2p$  and O  $1s$  XP spectra of 10NiAl-x catalysts are displayed in **Figure 3.10**. For straight comparison, the electron binding energies (BE) for 10NiAl-x catalyst samples are listed in **Table 3.4**. The surface of 10NiAl-x catalysts was characterized by a Ni  $2p_{3/2}$  main peak centered at about 855.9 eV, accompanied by two satellites at higher binding energies of  $861.9 \pm 0.2$  eV and  $866.8 \pm 0.4$  eV, corresponding to the  $Ni^{2+}$  in the  $NiAl_2O_4$  spinel. These results are in agreement with literature values reporting that the Ni  $2p_{2/3}$  binding energy varies from 855.6 to 857.9 eV for  $NiAl_2O_4$ . The band at 855.8 eV could also be assigned to  $Ni^{2+}$  in  $Ni(OH)_2$ , but the absence of asymmetry for the peak at 861 eV excluded the presence of  $Ni(OH)_2$  [96, 170-173]. From Al  $2p$  and O  $1s$  XP spectra, it can be noted that the BE of the Al  $2p$  and O  $1s$  peaks of all samples are quite similar. It is therefore impossible to draw any conclusion, based on the position of the Al  $2p$  or O  $1s$  peak, about the chemical transformations of nickel species with increasing the RV/OV value.

In order to quantitatively compare the Ni concentration on the surface of the different catalysts, the surface Ni/Al atomic ratios were calculated by XPS. As shown in **Figure 3.10 (a)**, the measured Ni/Al atomic ratios vary from 0.074 to 0.086. A higher surface Ni/Al atomic ratio was observed for the 10NiAl-1.0 sample, indicating a higher Ni concentration on the surface of 10NiAl-1.0 catalyst.

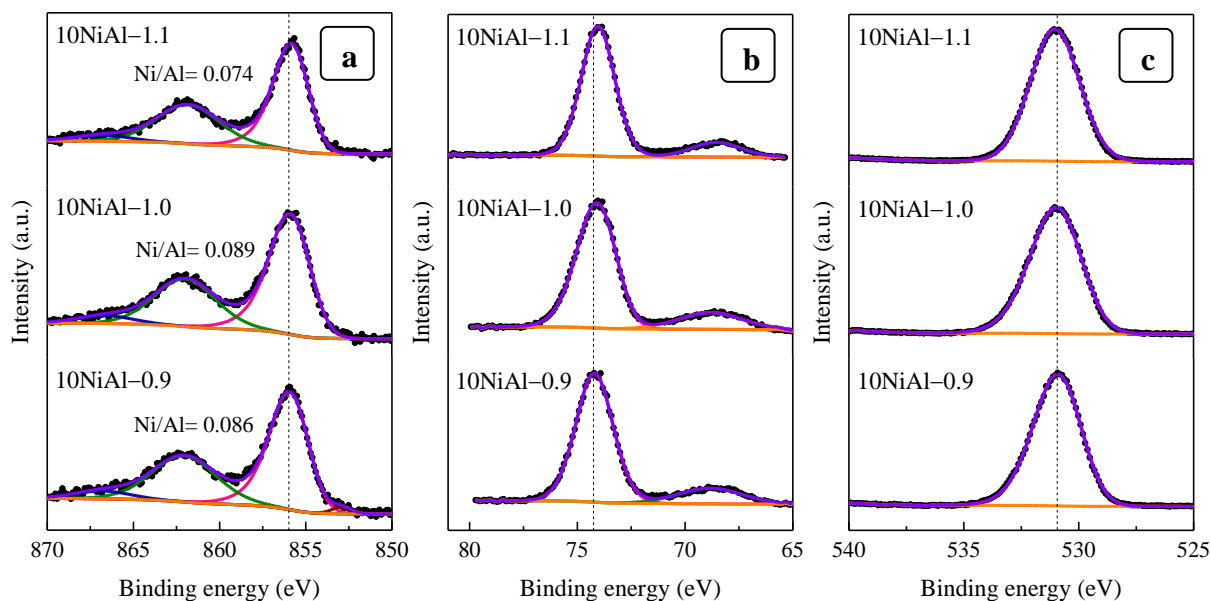


**Figure 3. 10.** (a) Ni 2p<sub>3/2</sub>, (b) Al 2p and (c) O 1s XP spectra for 10NiAl-*x* calcined samples.

**Table 3. 4.** BEs of the Ni 2p<sub>3/2</sub>, Al 2p and O 1s XP spectra for 10NiAl-*x* calcined samples.

Sample identity	Ni 2p <sub>3/2</sub> (eV)	Al 2p (eV)	O 1s (eV)
10NiAl-0.9	856.02	74.22	530.92
10NiAl-1.0	855.94	74.14	530.94
10NiAl-1.1	855.86	74.06	531.06

### 3.1.1.1.5.2 Cobalt based catalysts

The Co 2p<sub>3/2</sub>, Al 2p and O 1s XP spectra of 10CoAl-*x* catalysts are shown in **Figure 3.11**. The BE for 10CoAl-*x* catalyst samples are listed in **Table 3.5**.

The Co 2p<sub>3/2</sub> spectrums, acquired for the 10CoAl-*x* catalysts, showed peaks at approximately 781.31–781.42 eV with their broad satellite peaks at around 786.21, 786.32 and 786.22 eV. These peaks can be assigned to Co<sup>2+</sup> in CoAl<sub>2</sub>O<sub>4</sub>, based on values reported in the literature [174, 175] and suggest that CoAl<sub>2</sub>O<sub>4</sub> is the predominant phase present on the sample surfaces. The absence of peaks around 780 eV indicates that Co<sub>2</sub>O<sub>3</sub>, CoO and Co<sub>3</sub>O<sub>4</sub> species are absent [170]. Moreover, no peaks were detected around 780.4 eV, indicating the absence of the Co(OH)<sub>2</sub> phase [170]. Concerning the Al 2p and O 1s XP spectra, no additional information can be retrieved.

The values of the relative ratio of Co species determined by XPS are included in **Figure 3.11 (a)**. The values of Co/Al ratios vary from 0.068 to 0.08. The maximum value was detected for the 10CoAl-1.0 sample, indicating a higher Co concentration on the surface of 10CoAl-1.0 catalyst.

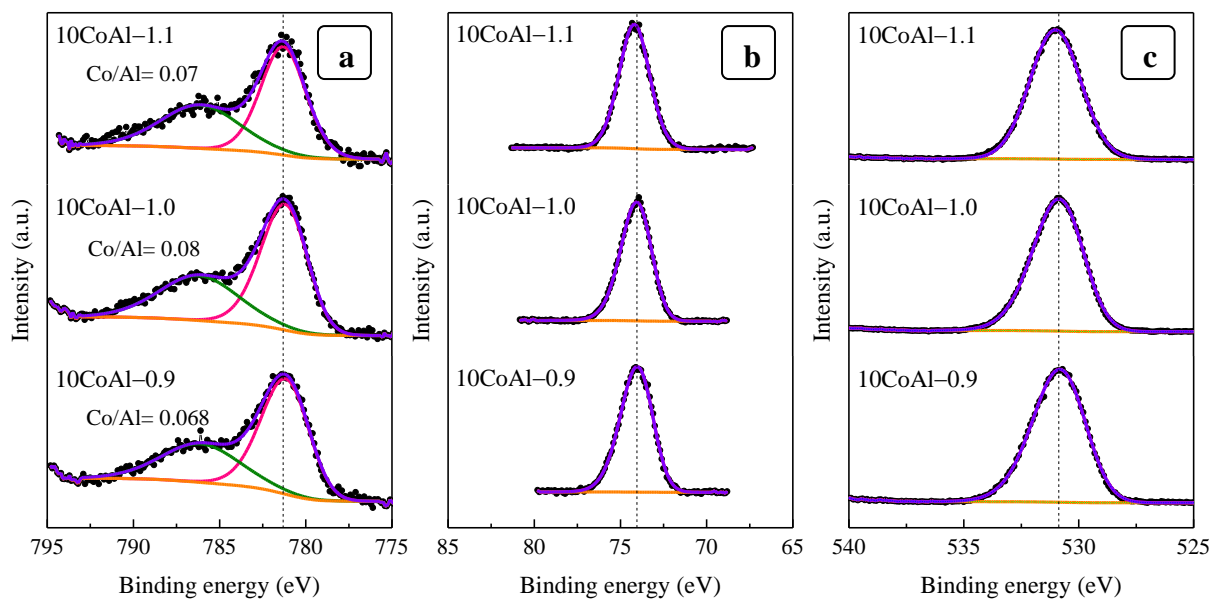


**Figure 3. 11.** (a) Co 2p<sub>3/2</sub>, (b) Al 2p and (c) O 1s XP spectra for 10CoAl-*x* calcined samples.

**Table 3. 5.** BEs of the Co 2p<sub>3/2</sub>, Al 2p and O 1s XP spectra for 10CoAl-*x* calcined samples.

Sample identity	Co 2p <sub>3/2</sub> (eV)	Al 2p (eV)	O 1s (eV)
10CoAl-0.9	781.31	74.00	530.81
10CoAl-1.0	781.33	74.03	530.83
10CoAl-1.1	781.42	74.22	531.02

### 3.1.1.1.5.3 Copper based catalysts

The Cu 2p<sub>3/2</sub>, Al 2p and O 1s XP spectra of 10CuAl-*x* catalysts are displayed in **Figure 3.12**. The BE for 10CuAl-*x* catalyst samples are listed in **Table 3.6**.

The Cu 2p<sub>2/3</sub> signals obtained for 10CuAl-*x* catalysts could be fitted to a principal peak at approximately 933.36–933.68 eV and two satellite peaks at BE of  $940.88 \pm 0.1$  and  $943.1 \pm 0.2$  eV, corresponding to Cu<sup>2+</sup> in CuO, by referring to literature values [176, 177]. The use of the modified Auger parameter (Cu 2p<sub>3/2</sub>, Cu LMM) accurately confirmed the existence of CuO, in agreement with the data previously reported in the literature [179]. In addition, no CuAlO<sub>2</sub> and Cu<sub>2</sub>O phases were present in the sample due to the absence of peaks at around 932 eV and 932.4 eV, respectively [178-181]. In the same way, the absence of peaks around 935 eV confirmed the absence of Cu(OH)<sub>2</sub> and CuAl<sub>2</sub>O<sub>4</sub> phases [176, 177, 179].

The values of the Cu/Al surface ratios calculated from the XPS are included in **Figure 3.12** (a). The maximum Cu/Al atomic ratio of 0.26 was achieved in the 10CuAl-1.0 catalyst obtained from stoichiometric conditions, suggesting a higher distribution of Cu species over the alumina surface.

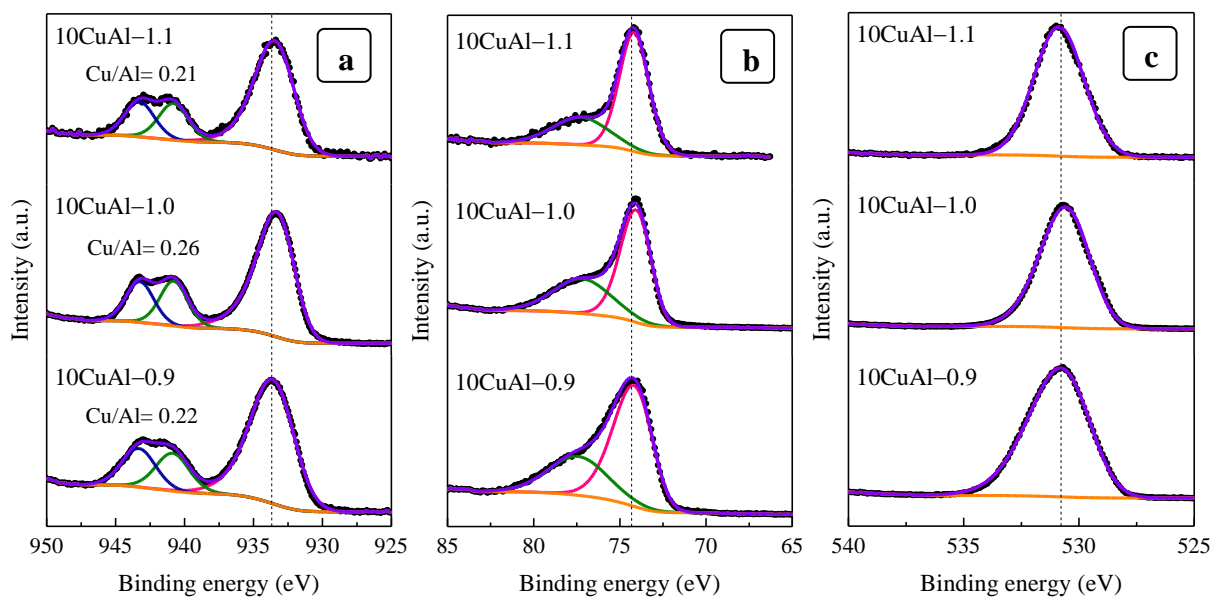


**Figure 3. 12.** (a) Cu 2p<sub>3/2</sub>, (b) Al 2p and (c) O 1s XP spectra for 10CuAl-*x* calcined samples.

**Table 3. 6.** BEs of the Cu 2p<sub>3/2</sub>, Al 2p and O 1s XP spectra for 10CuAl-*x* calcined samples.

Sample identity	Cu 2p <sub>3/2</sub> (eV)	Al 2p (eV)	O 1s (eV)
10CuAl-0.9	933.68	74.28	530.78
10CuAl-1.0	933.36	74.16	530.56
10CuAl-1.1	933.58	74.28	530.88

### Discussion

Nickel, cobalt and copper oxides are generally considered to exist in two forms on the alumina surface, free and fixed. Free metal oxides exist on the catalyst without interacting with the alumina surface, while fixed metal oxides, originate from the chemical interaction between alumina and the metal oxides, form stoichiometric and non-stoichiometric metal aluminates ( $\text{MAl}_2\text{O}_4$ ). According to the XPS survey, nickel and cobalt oxides were present on the surface of 10NiAl-*x* and 10CoAl-*x* catalysts as metal aluminates surface spinels ( $\text{MAl}_2\text{O}_4$ ), while free copper oxides were the main species on the surface of 10CoAl-*x* catalyst. These results indicate that  $\gamma$ -alumina might give stronger interactions with the metal oxides than  $\alpha$ -alumina.

XPS also offered valuable information regarding the surface composition of these bimetallic catalysts. Surprisingly, the surface M/Al atomic ratios were maximized for the samples obtained from stoichiometric conditions (RV/OV=1).

For 10NiAl-*x* and 10CoAl-*x* catalysts, a lower surface M/Al atomic ratio was obtained for the 10MAI-1.1 sample, suggesting an enhanced diffusion of metal oxide into the bulk

alumina with the increasing temperature combustion resulting from the increasing value of the RV/OV ratio. The surface M/Al ratio is expected to affect, subsequently, the catalytic activity of the combustion synthesized catalysts.

#### **3.1.1.1.6 TEM**

TEM characterization was carried out only for the 10MAI–1.1 calcined samples to elucidate the variation of the metal oxide nanoparticles size and their dispersion on the surface of the alumina matrix. Cu, Co, and Ni metal oxide nanoparticles can be assimilated to dense areas in the sample that inhibit electron transmission. When subjected to electron beam, these nanoparticles yield dark spots on TEM images, so they could be clearly distinguished from the light grey alumina phase, and hence, their size can be determined. It should be noted that the TEM technique involves the use of a small fraction of the catalyst, so data obtained from this technique does not always represent the entire sample. Nevertheless, it provides a direct measure of the catalytic components.

##### **3.1.1.1.6.1 Nickel based catalysts**

The TEM micrographs of 10NiAl–1.1 calcined sample are displayed in **Figure 3.13**. Nickel-based oxide nanoparticles, about 8–29 nm in size, appeared to be uniformly dispersed on the entire surface of the bulk  $\text{Al}_2\text{O}_3$  phase. No agglomeration phenomenon was observed. Using image analysis, the nanoparticles size distribution can be determined. The histograms of nanoparticle size distribution are shown in the inset of **Figure 3.13 (a)**. According to **Figure 3.13 (d)**, a d-spacing of the lattice was 0.463 nm, which could be assigned to the cubic  $\text{NiAl}_2\text{O}_4$  (111) plane.

TEM-EDX analysis results of 10NiAl–1.1 sample are represented in **Figure 3.14**. The table inserted in **Figure 3.14 (a)** reports the element content of the catalysts. Obviously, the Ni content in the 10NiAl–1.1 sample was higher than the target value (10 wt%). It can also be seen that Ni is highly dispersed on the surface of 10NiAl–1.1 catalyst. The above analyses are in good agreement with the results obtained from XPS, in which the 10NiAl–1.1 sample shows the presence of aluminate spinel structures.

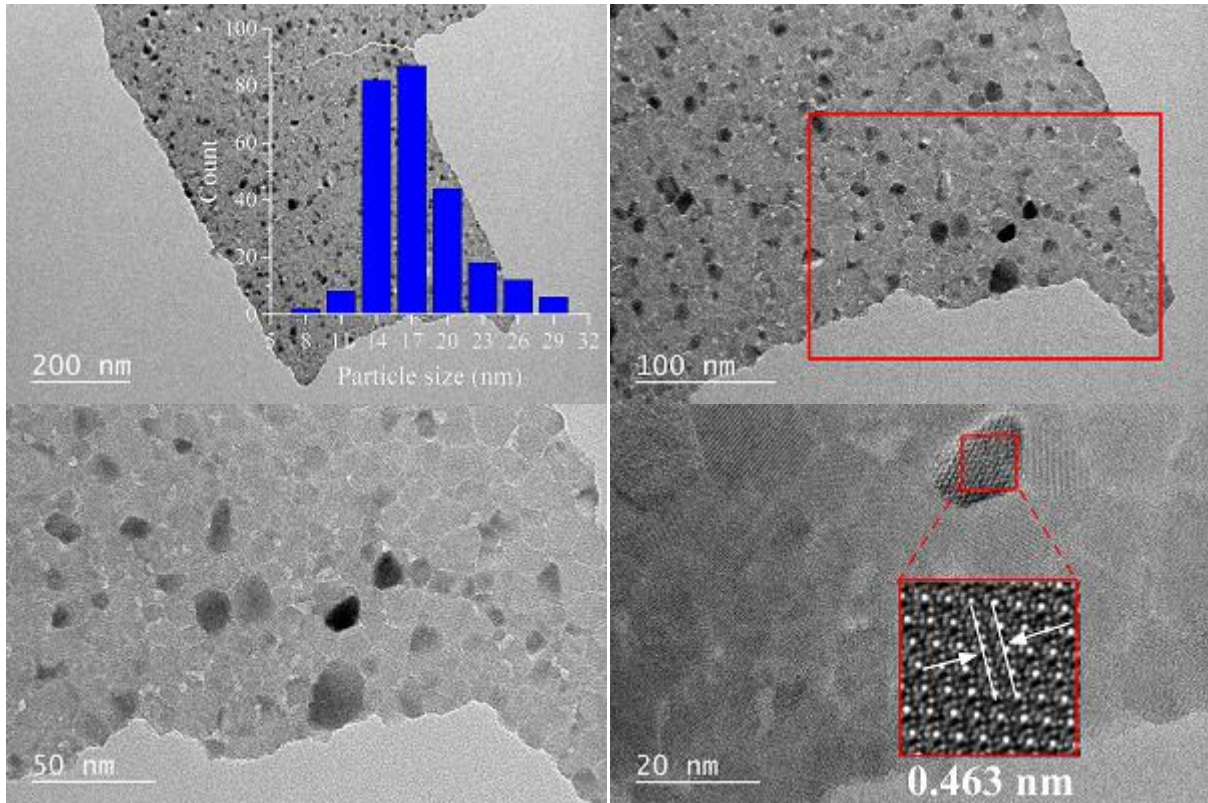


**Figure 3. 13.** TEM images (inset, nanoparticle size distribution) of 10NiAl–1.1 calcined sample.

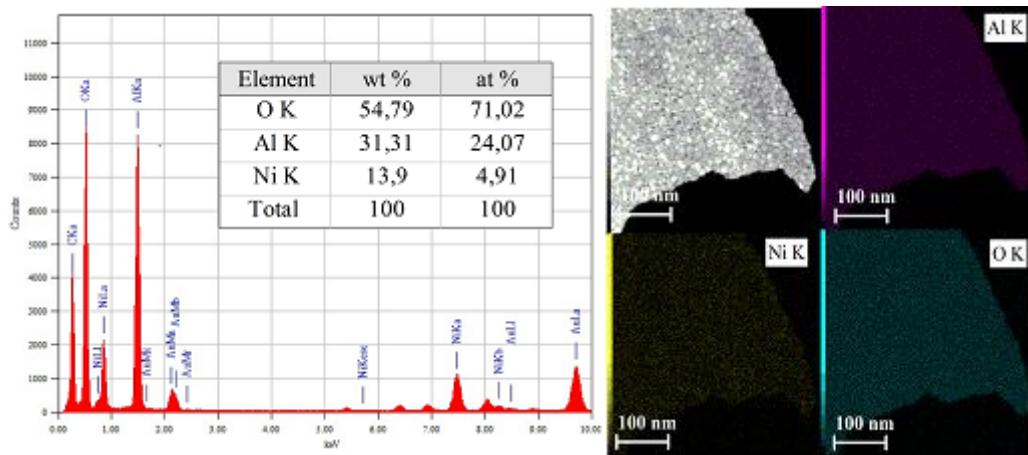


**Figure 3. 14.** TEM-EDX and dot mapping analyses of 10NiAl–1.1 calcined sample.

#### 3.1.1.1.6.2 Cobalt based catalysts

The TEM micrographs of 10CoAl–1.1 calcined sample are displayed in **Figure 3.15**. As visualized in **Figure 3.15**, cobalt-based oxide nanoparticles, about 6–22 nm in size, seemed to be uniformly dispersed on the surface of the bulk  $\text{Al}_2\text{O}_3$  phase without any agglomeration. **Figure 3.15 (d)** shows a fringe spacing of 0.286 nm, corresponding to the cubic  $\text{CoAl}_2\text{O}_4$  (220) plane.

TEM-EDX analysis results of 10CoAl-1.1 sample are represented in **Figure 3.16**. Similar to the 10NiAl-1.1 sample, the measured Co content in the 10CoAl-1.1 sample was above 10 wt% (**Figure 3.16 (a)**). It can be also observed from **Figure 3.16 (b)** that Co is uniformly dispersed on the surface of 10CoAl-1.1 catalyst with almost no distinction. The SAED patterns of the region highlighted in the red square in **Figure 3.16** are reported in **Figure 3.17**. The SAED patterns of the 10CoAl-1.1 sample consisted of continuous concentric rings that could be assigned to CoO (220), (111), (200), and to  $\text{CoAl}_2\text{O}_4$  (422), (220). The above observations are consistent with the results obtained from both DRX and XPS analyses that showed that cobalt phase is dispersed on the alumina matrix as “surface spinels”.

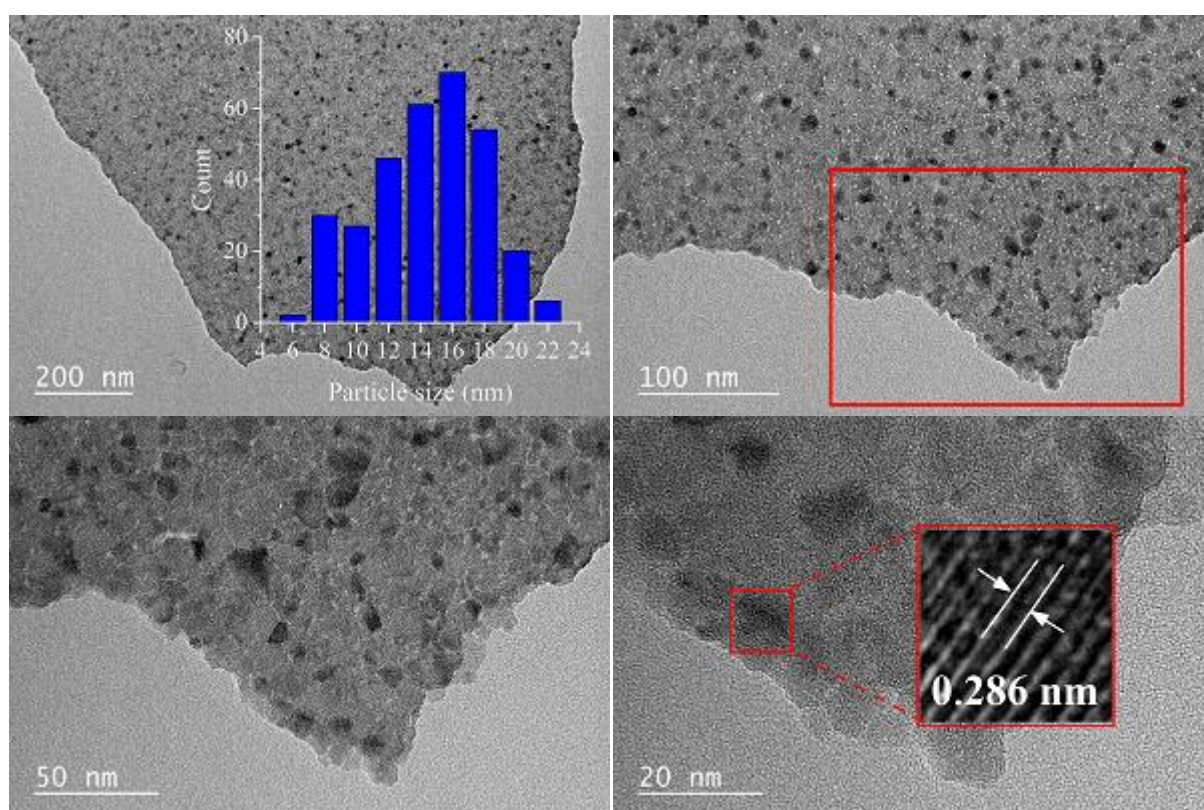


**Figure 3. 15.** TEM images (inset, nanoparticle size distribution) of 10CoAl-1.1 calcined sample.

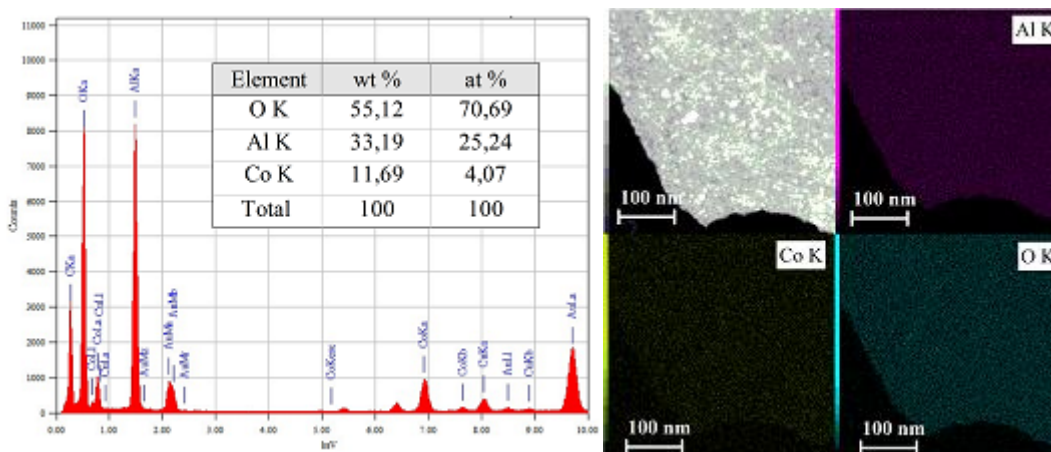


**Figure 3. 16.** TEM-EDX and dot mapping analyses of 10CoAl-1.1 calcined sample.

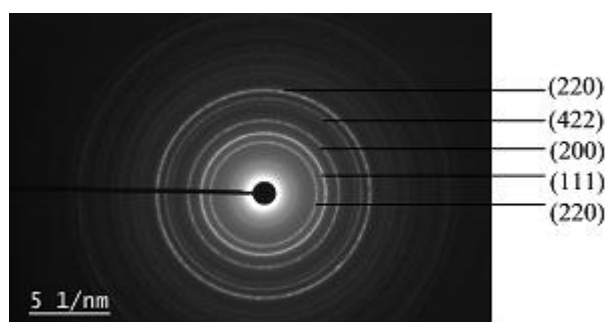


**Figure 3. 17.** SAED patterns of 10CoAl-1.1 calcined sample.

#### 3.1.1.1.6.3 Copper based catalysts

TEM images of 10CuAl-1.1 catalyst sample are given in **Figure 3.18**. Differently, the 10CuAl-1.1 sample presented a much larger distribution (5–95 nm) of copper oxide crystallites with an irregular distribution and agglomeration on the surface of the bulk  $\text{Al}_2\text{O}_3$  phase. According to **Figure 3.18 (d)**, the d-spacing of the lattice fringe was 0.123 nm, corresponding to the  $\text{Cu}_2\text{O}$  (222) lattice spacing.

TEM-EDX analysis results of 10CuAl-1.1 sample are given in **Figure 3.19**. The Cu content in the 10CuAl-1.1 sample was 14.05 wt%. Moreover, unlike the other samples, a nonhomogeneous distribution of Cu-containing species on the surface of 10Cu-Al sample was observed (**Figure 3.19 (b)**). These results are consistent with the observation obtained by the observation of TEM micrographs that showed “bulk-like” CuO phase aggregates on the surface of the catalyst leading to a high local Cu concentration.

In the corresponding SAED patterns, the discrete diffraction spots formed discontinuous concentric rings corresponding to monoclinic CuO (110), (002), (020), (131), (420), and cubic  $\text{Cu}_2\text{O}$  (200), (220), (222), (422), as shown in **Figure 3.20**.

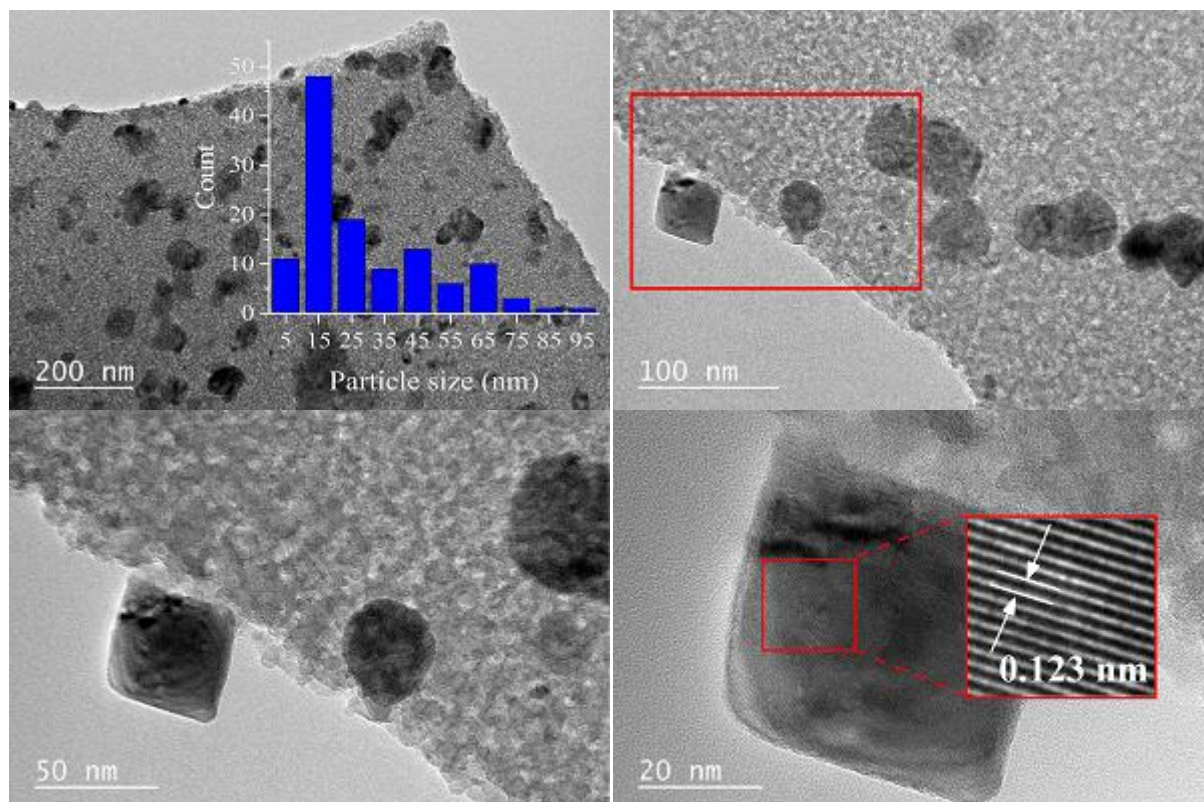


**Figure 3. 18.** TEM images (inset, nanoparticle size distribution) of 10CuAl-1.1 calcined sample.

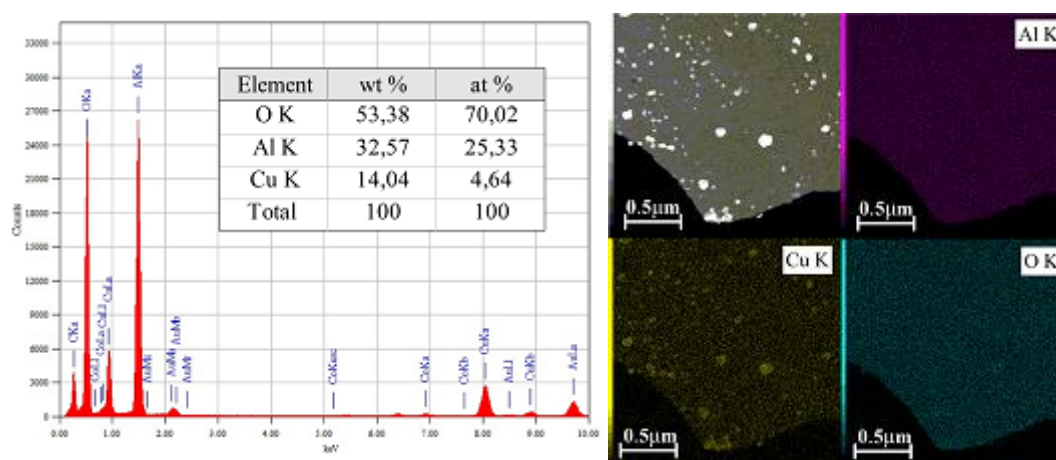


**Figure 3. 19.** TEM-EDX and dot mapping analyses of 10CuAl-1.1 calcined sample.

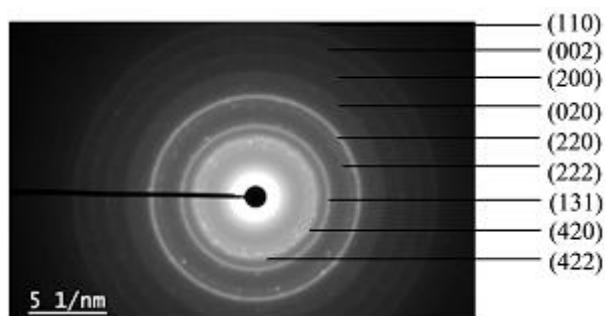


**Figure 3. 20.** SAED patterns of 10CuAl-1.1 calcined sample.

### **Discussion**

The 10NiAl-1.1 and 10CoAl-1.1 samples present smaller particle size and narrower distribution of nanoparticles than the 10CuAl-1.1 sample. This observation can be explained by the fact that Ni and Co-containing phases were dispersed on the alumina surface as  $\text{CoAl}_2\text{O}_4$  and  $\text{NiAl}_2\text{O}_4$  “surface spinels”.

For 10CuAl-1.1 sample, copper was mainly present as CuO. Because of the low surface area of 10CuAl-1.1, the dispersion of the metal oxide particles was less efficient, and CuO nanoparticles partially aggregate on the alumina surface, thus resulting in the increasing of the particle sizes.

The EDX analyses confirmed that all the samples do not contain unexpected impurities. The nickel, cobalt and copper contents are higher than those theoretically expected from the amount of precursors added during the preparation of the samples (10 wt%), and from those measured by X-ray fluorescence. The main difference between XRF and EDX results can be explained by the different probing depth provided by these two techniques. Indeed, TEM-EDX probe the material up to 100 nm depth, thus giving information only on the composition of the surface layer of the samples.

The TEM-SAED technique was successfully exploited to provide detailed information on the phase compositions and structure of the crystallites. Indeed, SAED results accurately confirmed the presence of  $\text{NiAl}_2\text{O}_4$  and  $\text{CoAl}_2\text{O}_4$  “surface spinels” in the 10NiAl-1.1 and 10CoAl-1.1 samples, respectively. The existence of non-incorporated CuO particles in 10CuAl-1.1 sample was also confirmed.

#### **3.1.1.2 Effect of stoichiometry (RV/OV ratio) - metal loading = 2 wt%**

In order to gain a deeper understanding of the influence of the RV/OV ratio on the microstructures of alumina-based binary metal oxide catalysts, three series of 2MAI-x samples were studied using XRF, XRD,  $\text{N}_2$  adsorption-desorption and SEM techniques. XRF, XRD, BET and SEM analysis of these catalysts are discussed in detail below.

##### **3.1.1.2.1 XRD**

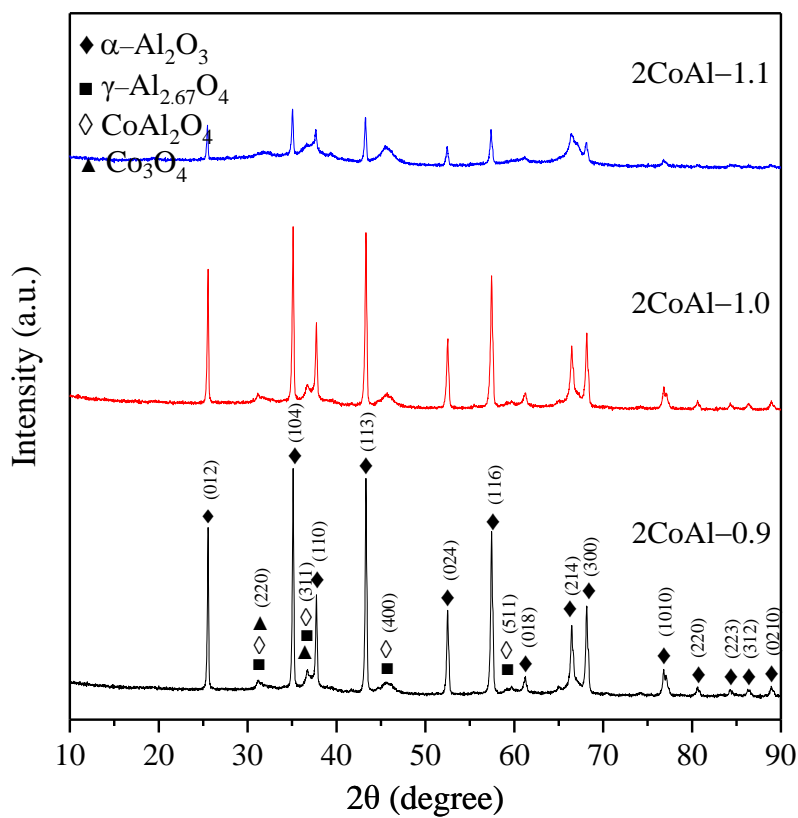
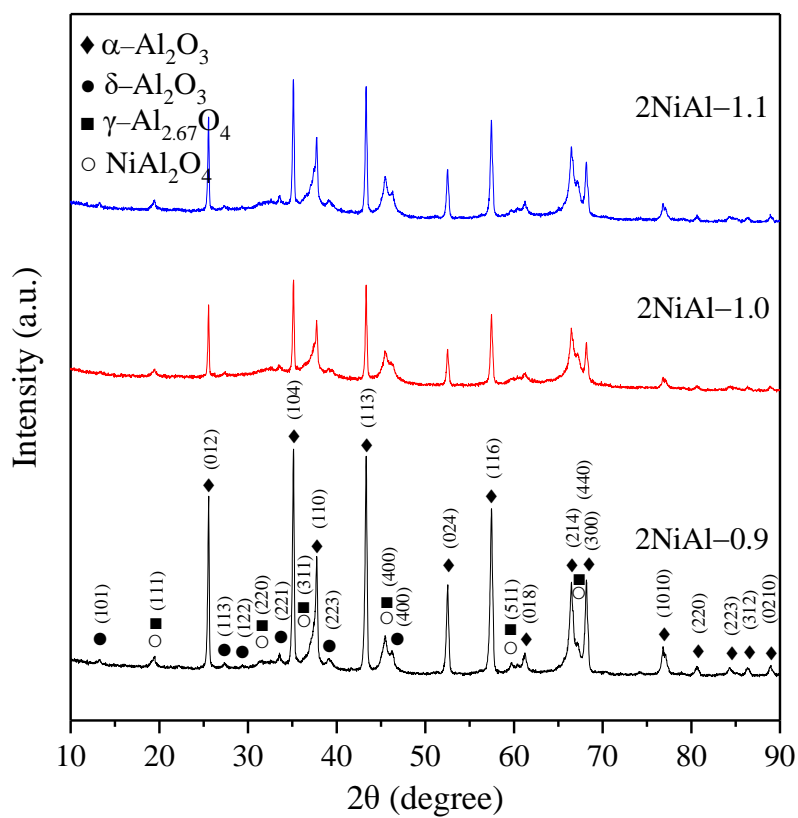
The XRD patterns of 2MAI-x catalyst samples, with different RV/OV ratios and a constant metal loading of 2 wt%, are displayed in **Figure 3.21**. It may be pointed out that the three series of 2MAI-x samples showed the presence of  $\alpha\text{-Al}_2\text{O}_3$  as a major phase.

The XRD patterns of 2NiAl-x samples show the presence of NiAl<sub>2</sub>O<sub>4</sub> (JCPDS 01-078-6951),  $\gamma$ -Al<sub>2.67</sub>O<sub>4</sub> (JCPDS 04-005-4662),  $\delta$ -Al<sub>2</sub>O<sub>3</sub> (JCPDS 00-046-1215) and  $\alpha$ -Al<sub>2</sub>O<sub>3</sub> (JCPDS 00-042-1468) phases. The characteristic diffraction peaks corresponding to the  $\alpha$ -Al<sub>2</sub>O<sub>3</sub> phase lose their intensity by increasing the RV/OV value from 0.9 to 1.1. A slight increment in the intensity of the peaks corresponding to  $\gamma$ -Al<sub>2.67</sub>O<sub>4</sub> and NiAl<sub>2</sub>O<sub>4</sub> can be noticed when increasing the RV/OV ratio, suggesting changes in the phase composition when increasing RV/OV ratio.

The XRD patterns of 2CoAl-x samples exhibit diffraction peaks of  $\gamma$ -Al<sub>2.67</sub>O<sub>4</sub> (JCPDS 04-005-4662),  $\alpha$ -Al<sub>2</sub>O<sub>3</sub> (JCPDS 00-042-1468), CoAl<sub>2</sub>O<sub>4</sub> (JCPDS 00-003-0896) and Co<sub>3</sub>O<sub>4</sub> (JCPDS 04-020-7500) phases. It is important to highlight that both Co<sub>3</sub>O<sub>4</sub> and CoAl<sub>2</sub>O<sub>4</sub> have almost identical diffraction peaks. Therefore, it was not possible to distinguish which species was formed using the only diffraction measurements. As in the case of 2NiAl-x samples, a decrease in the intensity of the peaks corresponding to  $\alpha$ -Al<sub>2</sub>O<sub>3</sub> can be observed with the increasing of the RV/OV ratio.

The XRD patterns of 2CuAl-x samples reveal the presence of  $\alpha$ -Al<sub>2</sub>O<sub>3</sub> (JCPDS 00-042-1468) and CuO (JCPDS 00-005-0661) phases. Similarly, fluctuations in the intensity of  $\alpha$ -Al<sub>2</sub>O<sub>3</sub> peaks can be noticed for the other samples. The 2CuAl-1.0 sample presents the highest intensity diffraction peaks of  $\alpha$ -Al<sub>2</sub>O<sub>3</sub>, suggesting that 2CuAl-1.0 sample has the optimized crystallinity.

The XRD results reveal that increasing the RV/OV ratio from 0.9 to 1.1 leads to a crystallinity decrease, together with the appearance of aluminates phases, particularly in nickel and cobalt based samples. The decrease in intensity and sharpness of the peaks can be correlated to the existence of aluminates phases in these samples. Thus, aluminates formation can be activated with increasing the RV/OV ratio and their amounts gradually increase when the RV/OV ratio further increases. The effect of the RV/OV ratio on the phase evolution of 2MAI-x samples is similar to those of 10MAI-x samples.



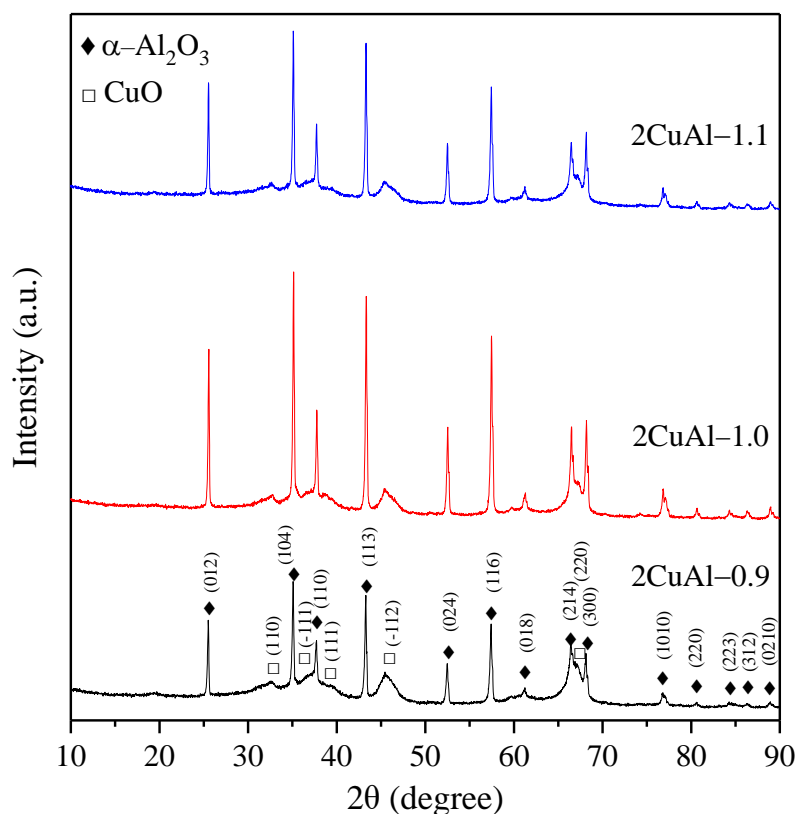


**Figure 3. 21.** XRD patterns of 2MAI-*x* calcined catalysts.

#### 3.1.1.2.2 N<sub>2</sub> adsorption-desorption isotherms

The N<sub>2</sub> adsorption-desorption isotherms of 2MAI-*x* catalyst samples with different RV/OV ratios are shown in **Figure 3.22**. All the 2MAI-*x* samples give type (I+IV) isotherms, with H4-type hysteresis loops. The BET surface area, total pore volume and average pore size of 2NiAl-*x* catalyst are listed in **Table 3.7**.

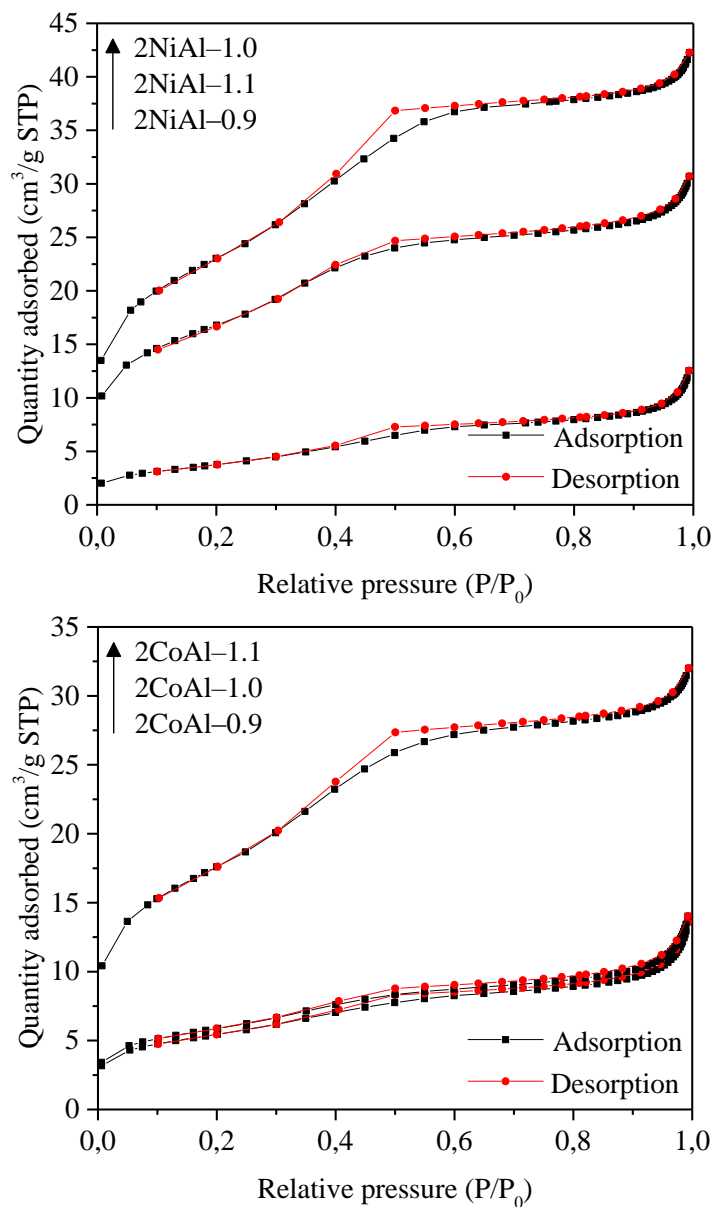
The BET surface areas of 2NiAl-*x* samples are in the range 14.04 to 80.94 m<sup>2</sup>g<sup>-1</sup>. The pore volume increases with increased surface area, while the pore size decreases. The 2NiAl-1.0 sample presents the highest surface area as well as the largest average pore size.

The BET surface area of the 2CoAl-*x* samples varies from 19.02 to 62.02 m<sup>2</sup>g<sup>-1</sup>. The pore volume ranges between 0.02 and 0.04 cm<sup>3</sup>g<sup>-1</sup>, while the average pore diameter varies from 3.20 to 4.68 nm. The BET surface area and pore volume increase when the RV/OV ratio increases. The pore size, on the other hand, decreases with increasing RV/OV ratio.

For the 2CuAl-*x* series, the BET surface areas vary from 20.44 to 67.02 m<sup>2</sup>g<sup>-1</sup> and the 2CuAl-1.0 sample exhibited the highest surface area.

Among the investigated samples, 2NiAl-1.1 was found to have the highest surface area, which is obviously the same observation for 10NiAl-*x* series.

For all the samples here studied, the textural properties within a given series are found to be affected by the RV/OV ratio, and a linear relationship is observed between BET surface and pore volume. However, there is no clear correlation between the textural and structural properties.



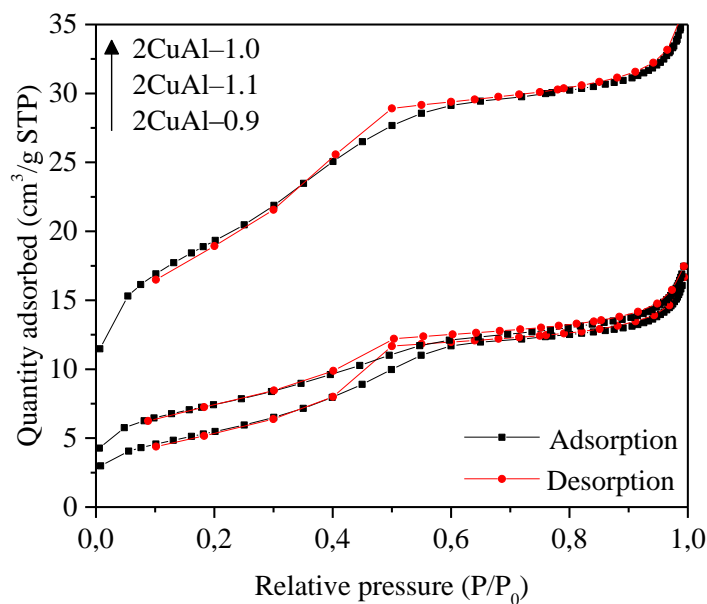


**Figure 3. 22.**  $N_2$  adsorption-desorption isotherm of  $MAI-x$  calcined catalysts.

**Table 3. 7.** Physico-chemical properties of  $2MAI-x$  calcined catalysts.

Sample identity	Metal loading <sup>a</sup> (wt %)	BET surface area (m <sup>2</sup> /g)	Pore volume <sup>b</sup> (cm <sup>3</sup> g <sup>-1</sup> )	Pore diameter <sup>c</sup> (nm)
2NiAl-0.9	1.78 (Ni)	14.04	0.02	4.80
2NiAl-1.0	1.87 (Ni)	80.94	0.06	3.21
2NiAl-1.1	1.80 (Ni)	59.06	0.04	3.31
2CoAl-0.9	1.91 (Co)	19.02	0.02	4.68
2CoAl-1.0	1.81 (Co)	20.41	0.02	4.49
2CoAl-1.1	1.88 (Co)	62.02	0.04	3.20
2CuAl-0.9	1.69 (Cu)	20.44	0.03	4.28
2CuAl-1.0	1.56 (Cu)	67.02	0.05	3.43
2CuAl-1.1	1.60 (Cu)	25.67	0.03	4.46

<sup>a</sup>XRF elemental analysis.

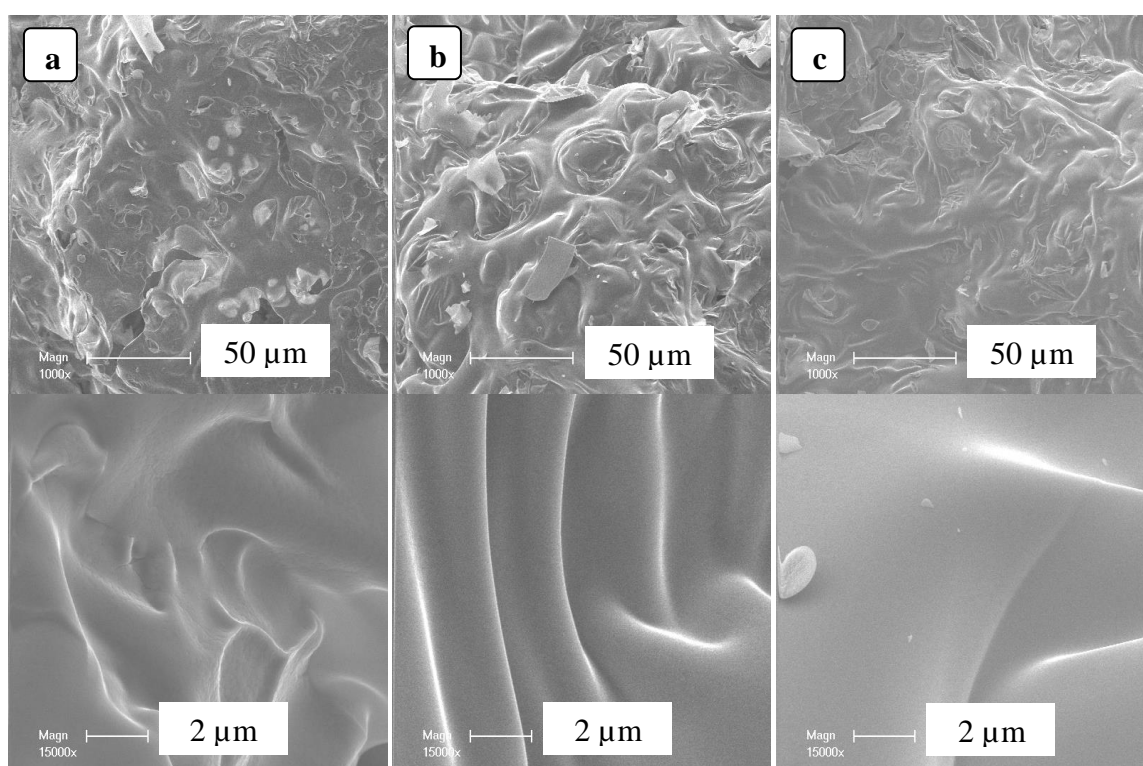
<sup>b</sup>BJHdesorption average pore diameter.

<sup>c</sup>BJHdesorption pore volume.

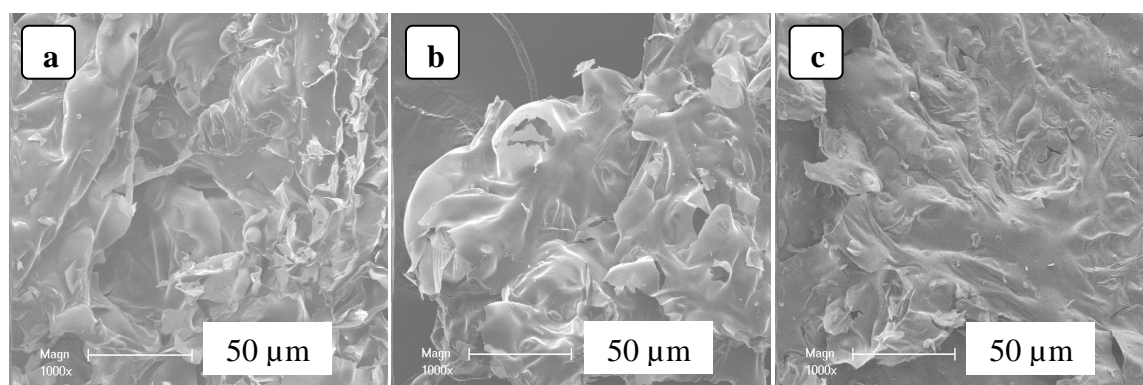
### 3.1.1.2.3 SEM

The SEM micrographs of the 2NiAl- $x$ , 2CoAl- $x$  and 2CuAl- $x$  samples are presented in **Figure 3.23**, **3.24** and **3.25**, respectively. The micrographs of all samples show foamy and agglomerated particles with a wide distribution and presence of some voids in their structure. The formation of these features is attributed to the fact that the particles tend to aggregate and swell at the temperatures of the combustion synthesis process. It is important to note that no significant difference appears by observing the morphologies of 2NiAl- $x$  and 2CoAl- $x$  samples, with various RV/OV ratios. It can also be noticed that the surface of 2CuAl- $x$

samples shows the presence of quasi-spherical nanoparticles attributed to the CuO particles. Clearly, the size and distribution of these nanoparticles are affected by changing RV/OV ratio. Among the  $2\text{CuAl}-x$  samples, the  $2\text{CuAl}-1.0$  presented the highest dispersion of CuO particles and smallest particle size. On the other hand, the particle growth and agglomeration, observed for  $2\text{CuAl}-0.9$  and  $2\text{CuAl}-1.1$  samples, is associated with the characteristics of the combustion process. In such cases, the heating effect due to the combustion and the heat dissipation by gas evolution are not controlled, leading to uncontrolled morphologies and a non-uniform dispersion of particles. These observations are similar to those obtained for  $10\text{MAl}-1.1$  samples.



**Figure 3. 23.** SEM images of (a)  $2\text{NiAl}-0.9$ , (b)  $2\text{NiAl}-1.0$  and (c)  $2\text{NiAl}-1.1$  calcined samples.



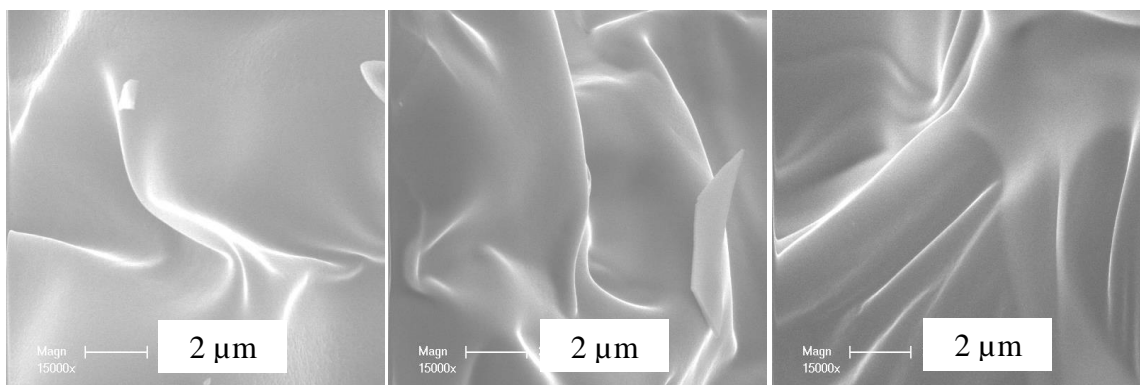


**Figure 3. 24.** SEM images of (a) 2CoAl-0.9, (b) 2CoAl-1.0 and (c) 2CoAl-1.1 calcined samples.

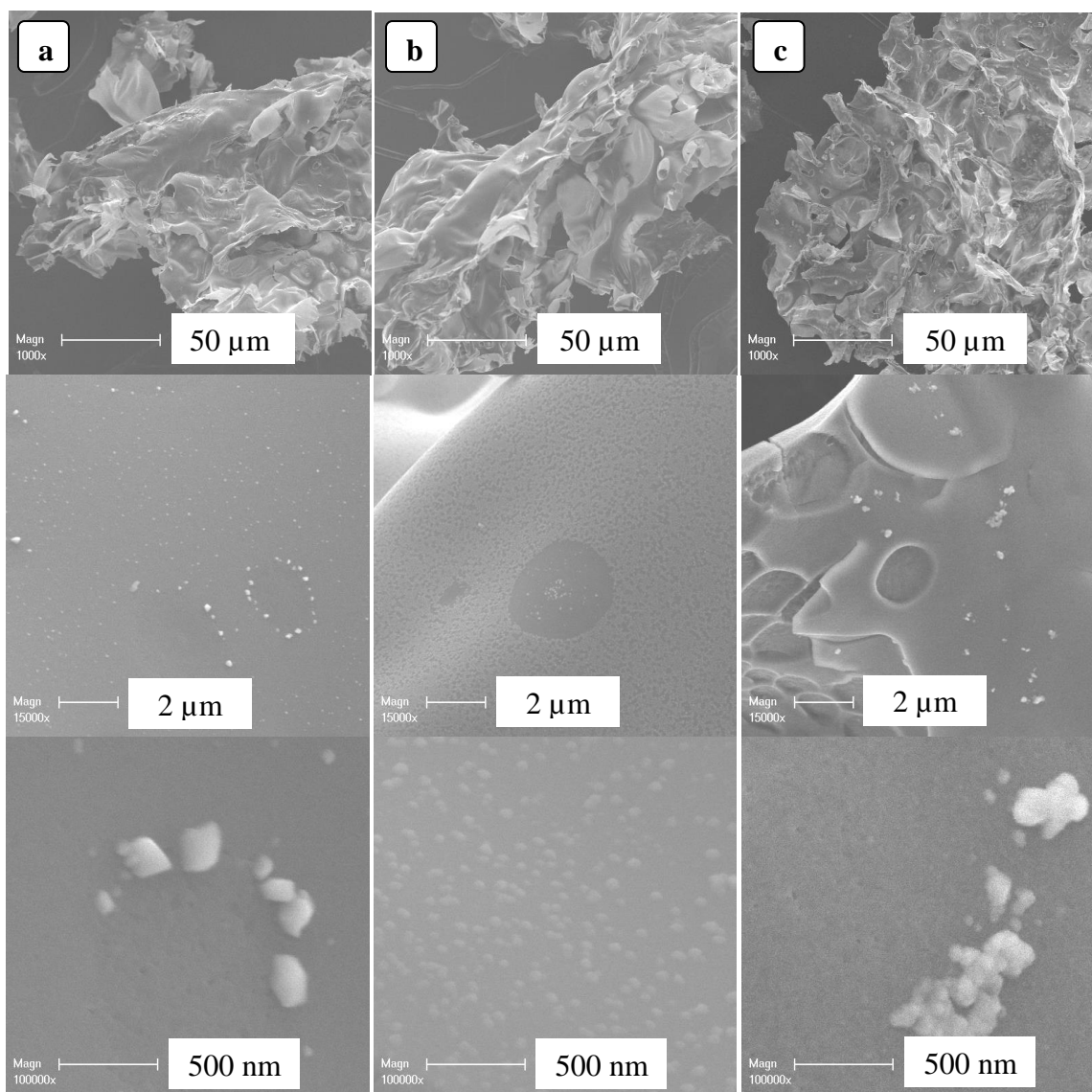


**Figure 3. 25.** SEM images of (a) 2CuAl-0.9, (b) 2CuAl-1.0 and (c) 2CuAl-1.1 calcined samples.

### 3.1.2 Effect of metal loading

RV/OV ratio was maintained at 1.1 throughout this study in order to investigate the effect of metal loading on the phase composition, structure, size and shape of binary oxide catalysts. The metal loading was tuned from 5 to 20 wt%.

#### 3.1.2.1 XRF

The metal loadings (Ni, Co and Cu) (wt%) of the catalysts with different metal contents determined by XRF are given in **Table 3.8**. The bulk metal content of the different samples is between 6.04–19.56, 4.85–19.75 and 6.31–19.26 wt% for nickel, cobalt and copper-based catalysts, respectively. The actual metal contents, measured by XRF, are in agreement with theoretical values.

**Table 3. 8.** *Elemental analysis of the XMAI calcined catalysts.*

Sample identity	Metal loading (wt%)		
	Ni	Co	Cu
5NiAl	6.04	—	—
10NiAl	10.30	—	—
15NiAl	14.14	—	—
20NiAl	19.56	—	—
5CoAl	—	4.85	—
10CoAl	—	10.70	—
15CoAl	—	15.86	—
20CoAl	—	19.75	—
5CuAl	—	—	6.31
10CuAl	—	—	10.70
15CuAl	—	—	14.99
20CuAl	—	—	19.26

#### 3.1.2.2 XRD

##### 3.1.2.2.1 Nickel based catalysts

**Figure 3.26** compares the XRD patterns of the XNiAl calcined samples with various nickel loadings. The diffraction peaks of 5NiAl sample were indexed as cubic  $\gamma$ - $\text{Al}_{2.67}\text{O}_4$  (JCPDS 04-005-4662), cubic  $\text{NiAl}_2\text{O}_4$  (JCPDS 01-078-6951), rhombohedral  $\alpha$ - $\text{Al}_2\text{O}_3$  (JCPDS 00-042-1468) and cubic  $\delta$ - $\text{Al}_2\text{O}_3$  (JCPDS 00-046-1215). By increasing the nickel content in the catalyst, from 5 to 15 wt%, the XRD patterns reveal that the 10NiAl and 15NiAl samples were less crystalline, as manifested by the broad peaks assigned to the  $\gamma$ - $\text{Al}_{2.67}\text{O}_4$  and  $\text{NiAl}_2\text{O}_4$

phases. By further increasing the Ni content to 20 wt%, the diffraction peaks of 20NiAl sample fit well those of  $\text{NiAl}_2\text{O}_4$  and did not show any extra diffraction peaks in comparison to 10NiAl and 15NiAl samples. No diffraction peaks, attributed to the nickel oxide, are observed even at 20 wt% nickel loading.

Due to the peak broadening and overlapping, it is difficult to clearly distinguish between  $\gamma\text{-Al}_{2.67}\text{O}_4$  and  $\text{NiAl}_2\text{O}_4$  phases. So, the main diffraction peak in the  $2\theta$  range of  $35\text{--}40^\circ$  was enlarged to reveal the differences, as illustrated in the rectangle presented in **Figure 3.26**. It is found that (311) diffraction peak is slightly shifted to lower diffraction angle with increasing Ni contents (this observation is also highlighted by the dotted lines). It is also observed that XRD peak shifting and intensity differences are consistent with 20NiAl sample. Moreover, the intensity of the  $\gamma\text{-Al}_{2.67}\text{O}_4$  phase peaks increases with increasing the Ni loadings. This indicates that the crystallization of the solids increases by increasing the Ni content, as manifested by the sharp peaks.

According to the Bragg's Law:  $\lambda = 2d_{hkl} \sin \theta_{hkl} \leftrightarrow \sin \theta_{hkl} = \lambda / 2d_{hkl}$  (where  $d$  is the spacing between the planes in the atomic lattice,  $\theta_{hkl}$  is the diffraction angle, and  $\lambda$  is the wavelength of incident X-ray wavelength), the diffraction angle  $\theta$  will decrease with the increasing  $d$ -spacing. This indicates that the crystal planes of the  $\text{NiAl}_2\text{O}_4$  have larger  $d$ -spacing and larger lattice constant while those of  $\gamma\text{-Al}_{2.67}\text{O}_4$  have shorter  $d$ -spacing and smaller lattice constant. **Table 3.9** illustrates the lattice parameters and  $d$ -spacing values retrieved from JCPDS files of  $\gamma\text{-Al}_{2.67}\text{O}_4$  (JCPDS 04-005-4662) and  $\text{NiAl}_2\text{O}_4$  (JCPDS 01-078-6951), which are consistent with the latest observations.

**Table 3. 9.** *Structural properties of  $\gamma\text{-Al}_{2.67}\text{O}_4$  and  $\text{NiAl}_2\text{O}_4$ .*

	Lattice parameter (Å)	$d$ -spacing (Å)	Unit cell volume ( $10^6 \text{ pm}^3$ )
$\gamma\text{-Al}_{2.67}\text{O}_4$ (311)	$a = b = c = 7.948$	2.396	502.08
$\text{NiAl}_2\text{O}_4$ (311)	$a = b = c = 8.031$	2.421	517.94

The diffraction lines of the  $\alpha\text{-Al}_2\text{O}_3$  phase are only detected in the sample containing the lowest Ni loading. The reason for the  $\alpha\text{-Al}_2\text{O}_3$  formation at lower Ni loading might be due to the tendency of aluminum nitrate-urea mixture to form  $\alpha\text{-Al}_2\text{O}_3$  phase by solution combustion synthesis method. By increasing the Ni content up to 20 wt%, only diffraction peaks of the  $\text{NiAl}_2\text{O}_4$  and the  $\gamma\text{-Al}_{2.67}\text{O}_4$  are observed, suggesting that the addition of NiO phase exerts an effect on the crystallization process of the alumina phase. To acquire further insight on the effect of nickel loadings on the solid phase evolution, additional samples with 1 and 2 wt% nickel contents as well as nickel oxide were synthesized via solution combustion

method and characterized by XRD. Their XRD patterns are provided in **Figure A.10** (See **Annex A**).

The  $\alpha/\gamma$  phase ratios of the different samples, plotted as a function of the Ni content from 1 up to 20 wt% (**Figure 3.27**), form an exponential decay curve with a maximum of the  $\alpha/\gamma$  phase ratio of about 18, obtained at 1 wt% of Ni. The  $\alpha/\gamma$  ratio values decrease dramatically by increasing the nickel amount, until the complete disappearing of the  $\alpha\text{-Al}_2\text{O}_3$  phase at 10 wt%.

When increasing Ni content, the main diffraction peaks of  $\gamma\text{-Al}_{2.67}\text{O}_4$  shift to lower angles and the intensity of the peaks increases; this could be explained by the diffusion of NiO particles into the alumina structure to form the  $\text{NiAl}_2\text{O}_4$  phase. It is reasonably possible that low nickel loadings lead to the formation of amorphous surface nickel aluminates bearing some resemblance to bulk cobalt aluminates. The maximum of interaction between NiO and alumina to produce  $\text{NiAl}_2\text{O}_4$  is reached at 20 wt% Ni content.

It is well documented in the literature that high temperatures promote the solid-solid interaction between NiO and alumina to form  $\text{NiAl}_2\text{O}_4$ , thus the increased Ni contents might result in higher temperatures facilitating the incorporation of NiO into alumina. Meanwhile, it is curious that no crystallites of NiO were detected even at high Ni loading. Since Ni loadings do not exceed the limit of  $\text{NiAl}_2\text{O}_4$  phase formation (the saturation of all available lattice sites is not reached), it is believed that NiO locally interact with alumina to form  $\text{NiAl}_2\text{O}_4$ , leading to structural inhomogeneities in the obtained oxides.

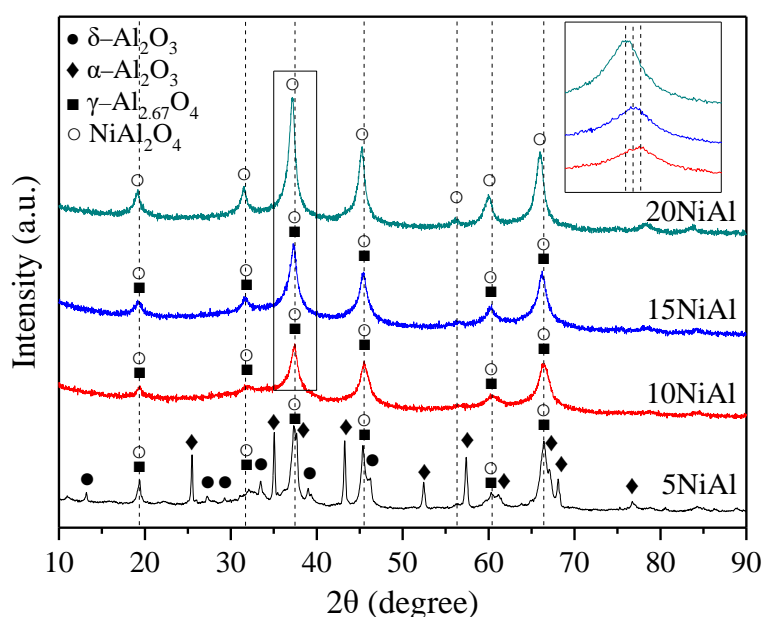


**Figure 3. 26.** XRD patterns of  $X\text{NiAl}$  calcined catalysts.

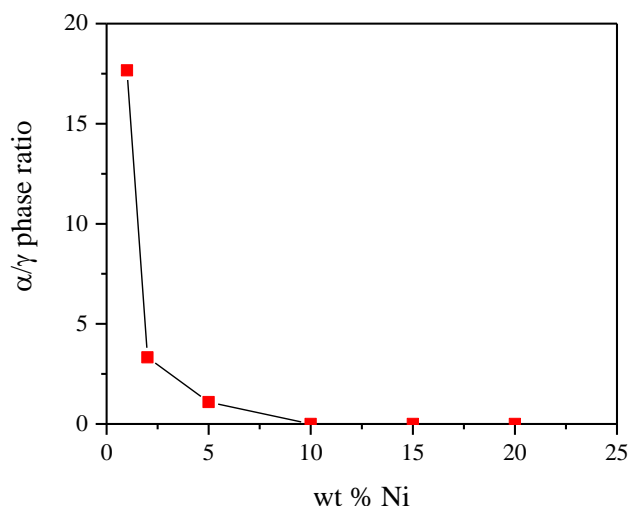


**Figure 3. 27.** Effect of nickel content on the  $\alpha/\gamma$  phase ratio.

### 3.1.2.2.2 Cobalt based catalysts

The XRD patterns of the different XCoAl calcined samples with Co content from 5 to 20 wt% are shown in **Figure 3.28**. For 5CoAl sample, diffraction peaks of cubic  $\gamma\text{-Al}_{2.67}\text{O}_4$  (JCPDS 04-005-4662), cubic  $\text{CoAl}_2\text{O}_4$  (JCPDS 00-003-0896), rhombohedral  $\alpha\text{-Al}_2\text{O}_3$  (JCPDS 00-042-1468) and cubic  $\text{Co}_3\text{O}_4$  (JCPDS 04-020-7500) are observed. By increasing the cobalt content in the catalyst, from 5 to 10 wt%, the peaks related to  $\alpha\text{-Al}_2\text{O}_3$  and  $\text{Co}_3\text{O}_4$  phases disappear, and only overlapped peaks of  $\gamma\text{-Al}_{2.67}\text{O}_4$  and  $\text{CoAl}_2\text{O}_4$  are observed. As the cobalt loading increased up to 15 wt%, all the peaks are slightly shifted to lower diffraction angle and  $\text{Co}_3\text{O}_4$  phase appears again. For high Co loading, the peak shifting becomes more relevant and the diffraction peaks of 20CoAl sample fit that of  $\text{Co}_3\text{O}_4$ . In addition, the intensity of the peaks decreases as the cobalt loading is increased. This result clearly indicates that the nature of the cobalt species varies with the cobalt loading and the formation of cobalt oxide, as a separate phase, takes place at high cobalt concentrations (>15 wt%). In order to justify this shift, the lattice parameters and d-spacing values extracted from JCPDS files of  $\gamma\text{-Al}_{2.67}\text{O}_4$  (JCPDS 04-005-4662),  $\text{CoAl}_2\text{O}_4$  (JCPDS 00-003-0896) and  $\text{Co}_3\text{O}_4$  (JCPDS 04-020-7500) are compared and summarized in **Table 3.10**.

**Table 3. 10.** Structural properties of  $\gamma\text{-Al}_{2.67}\text{O}_4$ ,  $\text{Co}_3\text{O}_4$  and  $\text{CoAl}_2\text{O}_4$ .

	Lattice parameter (Å)	d-spacing (Å)	Unit cell volume ( $10^6 \text{ pm}^3$ )
$\gamma\text{-Al}_{2.67}\text{O}_4$ (311)	$a = b = c = 7.948$	2.396	502.08
$\text{Co}_3\text{O}_4$ (311)	$a = b = c = 7.951$	2.397	502.65
$\text{CoAl}_2\text{O}_4$ (311)	$a = b = c = 8.080$	2.440	527.51

To further study the effect of cobalt loading on phase evolution in cobalt based catalysts, additional samples with 1 and 2 wt% cobalt contents as well as cobalt oxide ( $\text{Co}_3\text{O}_4$ ) were synthesized via solution combustion method and characterized by XRD. Their XRD patterns are depicted in **Figure A.11** (See **Annex A**). Similar to nickel-based catalysts, the  $\alpha/\gamma$  phase ratios of the different cobalt-based catalysts as a function of the Co content form an exponential decay curve with a maximum of the  $\alpha/\gamma$  phase ratio of about 20, obtained at 1 wt% of Co (**Figure 3.29**). It can be concluded that peak shifting is dependent on the amount of Co and it is due not only to the incorporation of CoO phase into the alumina phase, but also to the formation of cobalt oxide.

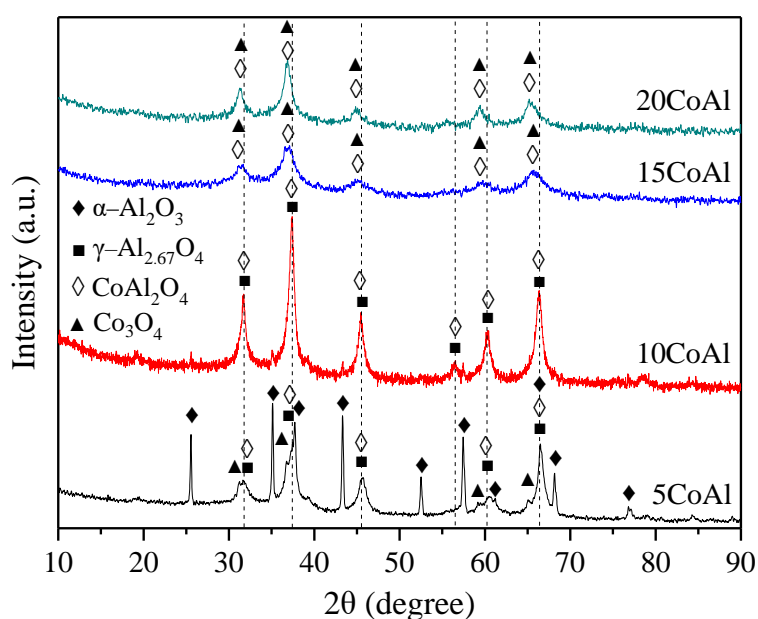


**Figure 3. 28.** XRD patterns of XCoAl calcined catalysts.

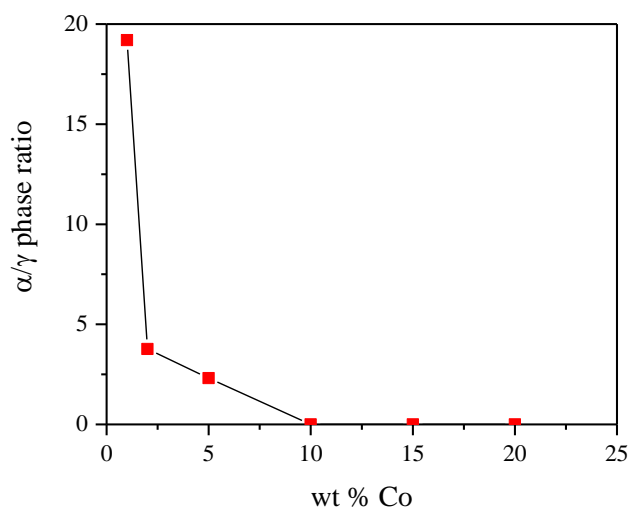


**Figure 3. 29.** Effect of cobalt content on the  $\alpha/\gamma$  phase ratio.

### 3.1.2.2.3 Copper based catalysts

The XRD spectra of XCuAl calcined samples with various copper loadings are presented in **Figure 3.30**. As shown in **Figure 3.30**, all diffraction peaks of different samples are assigned to the rhombohedral  $\alpha$ -Al<sub>2</sub>O<sub>3</sub> (JCPDS 00-042-1468) and monoclinic CuO (JCPDS 00-005-0661).

Raising the copper loading from 5 to 20 wt% resulted in an increase in the intensity of the diffraction peaks of both  $\alpha$ -Al<sub>2</sub>O<sub>3</sub> and CuO with any subsequent appearance of new peaks. This indicates that metal loading does not affect phase evolution in copper-based catalysts. In other words, the interaction between CuO and Al<sub>2</sub>O<sub>3</sub> to produce copper aluminates does not occur even at high copper loadings. The crystallite size of copper oxide was calculated using the Scherrer equation, as presented in **Table 3.11**. According to **Table 3.11**, by increasing the metal content, the CuO crystallite size increases from 15 nm to 51 nm. The differences in particle size can be correlated to the synthesis temperature, which is affected by the metal loading.

**Table 3. 11.** CuO crystallite size of XCuAl calcined catalysts.

Sample identity	CuO <sup>a</sup> crystallite size (nm)
5CuAl	15
10CuAl	44
15CuAl	46
20CuAl	51

<sup>a</sup>Crystallite size estimated by Scherrer's equation at  $2\theta \approx 38.5^\circ$

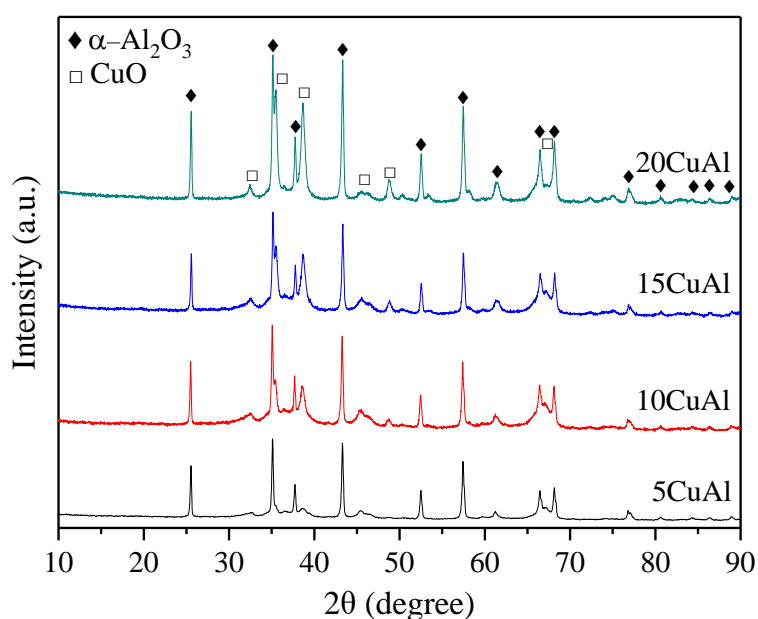


**Figure 3. 30.** XRD patterns of XCuAl calcined catalysts.

### 3.1.2.3 N<sub>2</sub> adsorption-desorption isotherms

#### 3.1.2.3.1 Nickel based catalysts

The N<sub>2</sub> adsorption-desorption isotherms of the XNiAl calcined samples are shown in **Figure 3.31**. All isotherms are of type I with H4-type hysteresis loops. **Table 3.12** shows the effect of nickel loading on the textural properties of nickel-based catalysts. The BET surface area of the catalysts increases with increasing nickel loadings from 5 to 15 wt %, then decreases slightly with rising nickel loading to 20 wt %. The 5NiAl and 15NiAl catalyst samples show the lowest (18.97 m<sup>2</sup>g<sup>-1</sup>) and the highest (170.38 m<sup>2</sup>g<sup>-1</sup>) BET surface area, respectively. These trends can be correlated to the phase composition of the nickel-based catalysts; the increase in BET surface area for 5NiAl, 10NiAl and 15NiAl samples is probably due to the excessive formation of  $\gamma$ -alumina phase and amorphous surface nickel aluminates. Since bulk aluminates have lower surface areas than  $\gamma$ -alumina, the higher amount of nickel solid formed in 20NiAl sample might lead to a decrease in BET surface area.

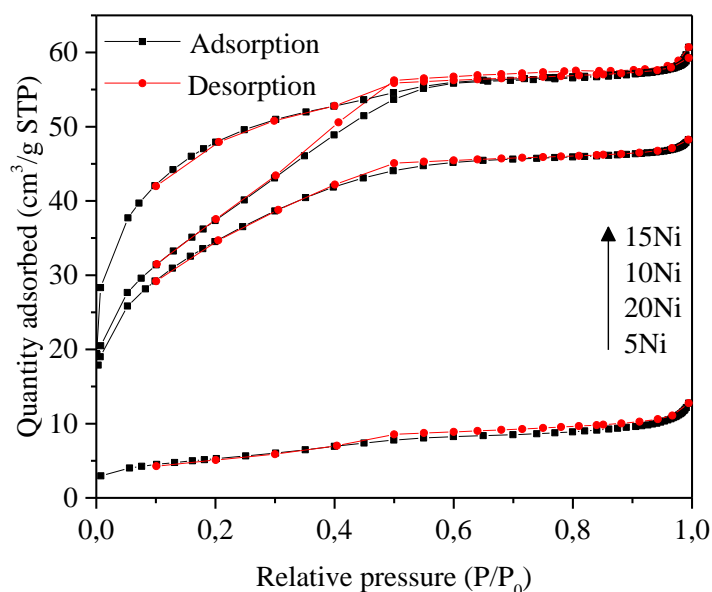


**Figure 3. 31.** *N<sub>2</sub> adsorption-desorption isotherms of XNiAl calcined samples.*

#### 3.1.2.3.2 Cobalt based catalysts

The N<sub>2</sub> adsorption-desorption isotherms of the XCoAl calcined samples are shown in **Figure 3.32**. All isotherms are of type IV, with H4-type hysteresis loops. The textural properties of the XCoAl calcined samples, with different Co composition, are reported in **Table 3.12**. The BET surface area and the pore volume of the XCoAl samples gradually increases as the cobalt content increases from 10.53 m<sup>2</sup>g<sup>-1</sup> to 90.88 m<sup>2</sup>g<sup>-1</sup> and from 0.02 to 0.07 cm<sup>3</sup>g<sup>-1</sup>, respectively. These results clearly indicate the role of the phase composition in controlling the BET surface

area, which is supported by the XRD analysis; the alumina phase evolution and cobalt oxide formation, resulting from the increased amount of cobalt, might be a key factor in enhancing the surface area of cobalt based catalysts.

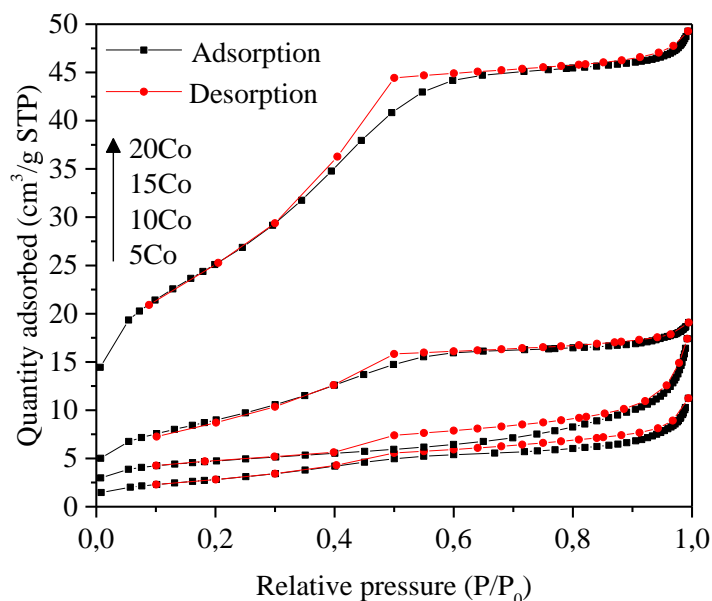


**Figure 3. 32.**  $N_2$ adsorption-desorption isotherms of XCoAl calcined samples.

### 3.1.2.3.3 Copper based catalysts

The  $N_2$  adsorption-desorption isotherms of the XCuAl calcined samples are shown in **Figure 3.33**. All isotherms are of type II with H3-type hysteresis loops. The textural properties of the XCuAl calcined samples are reported in **Table 3.12**. As it can be seen from **Table 3.12**, copper-based catalysts have the lowest BET surface areas as compared to nickel and cobalt based catalysts. The relatively low surface area, obtained for XCuAl calcined samples, can be related to the presence of  $\alpha$ -alumina phase. The surface area of XCuAl samples does not seem to be sensitive to copper loading. The values slowly increase by varying the Cu content from 5 to 15 wt%, then decrease with the excess of Cu content. It is possible that copper nanoparticles are agglomerated in the 20CuAl sample, resulting in a decrease of the surface area.

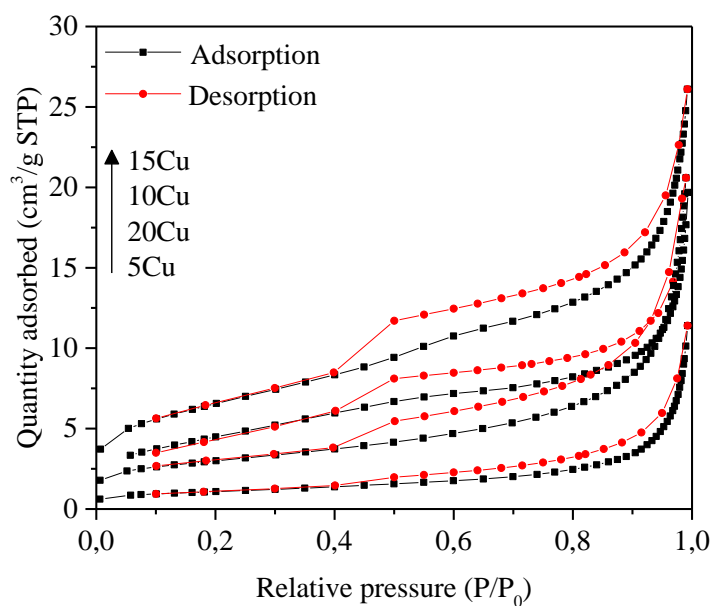


**Figure 3. 33.**  $N_2$  adsorption-desorption isotherms of  $XCuAl$  calcined samples

**Table 3. 12.** Textural properties of  $XMAI$  calcined catalysts.

Sample identity	BET surface Area ( $m^2/g$ )	Pore volume <sup>a</sup> ( $cm^3g^{-1}$ )	Pore diameter <sup>b</sup> (nm)
5NiAl	18.97	0.02	4.09
10NiAl	135.10	0.08	2.71
15NiAl	170.38	0.03	3.32
20NiAl	124.04	0.04	3.08
5CoAl	10.53	0.02	5.43
10CoAl	16.67	0.02	7.96
15CoAl	32.91	0.03	3.44
20CoAl	90.88	0.07	3.43
5CuAl	5.84	0.02	8.03
10CuAl	16.38	0.03	6.51
15CuAl	23.46	0.04	6.61
20CuAl	10.33	0.03	11.45

<sup>a</sup> BJH desorption pore volume.

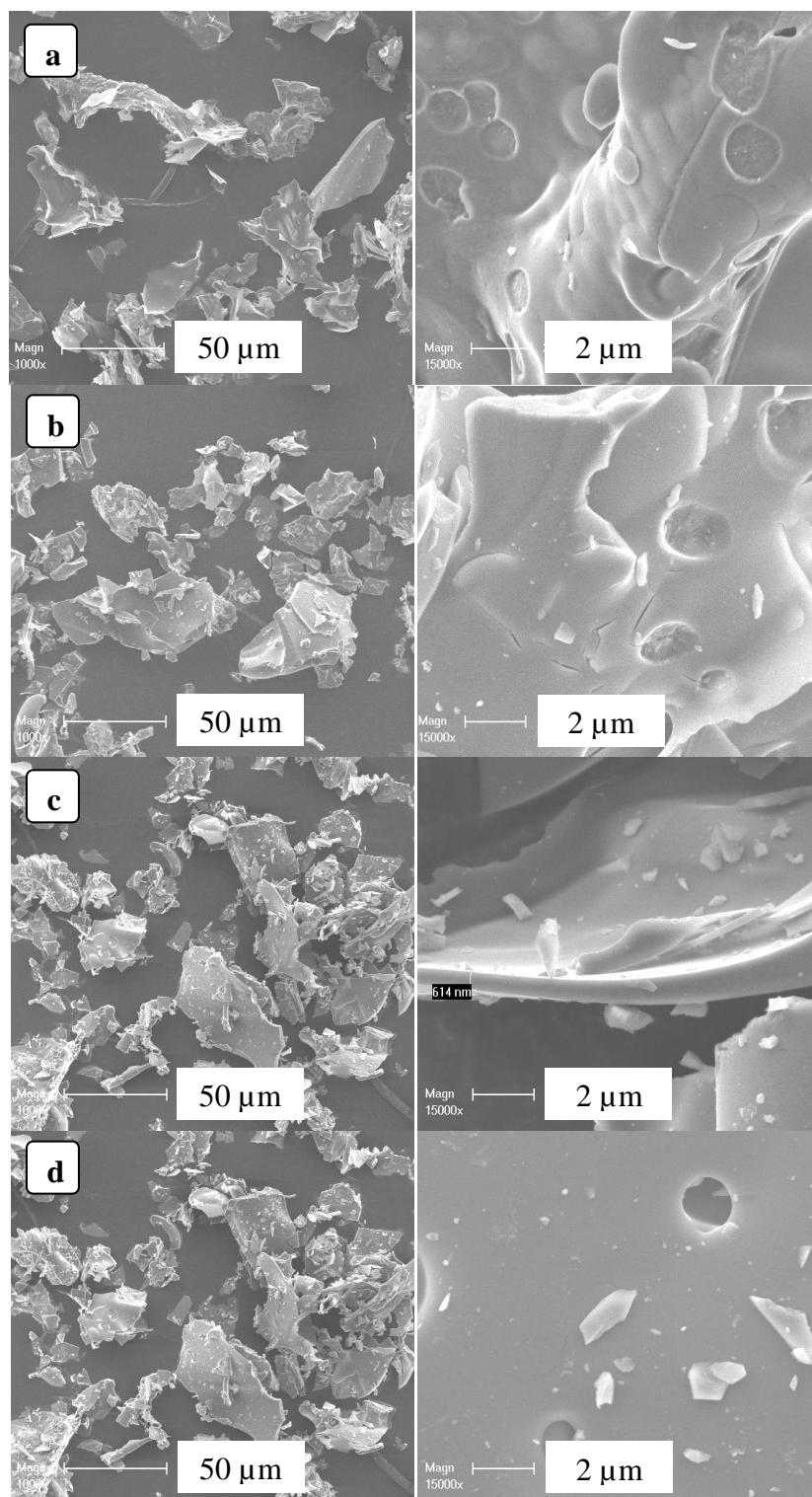
<sup>b</sup> BJH desorption average pore diameter.

### 3.1.2.4 SEM

#### 3.1.2.4.1 Nickel based catalysts

The SEM images of the  $XNiAl$  samples with 5 to 20 wt% nickel loadings are presented in **Figure 3.34**. The agglomerates of the different  $XNiAl$  samples have platelet and flake particles with an average size greater than  $50 \mu m$ . The surface of the agglomerates showed the presence of cracks and voids, which reflects the inherent nature of the combustion reaction. Micrograph of the 20NiAl sample showed small holes, corresponding to the gas release

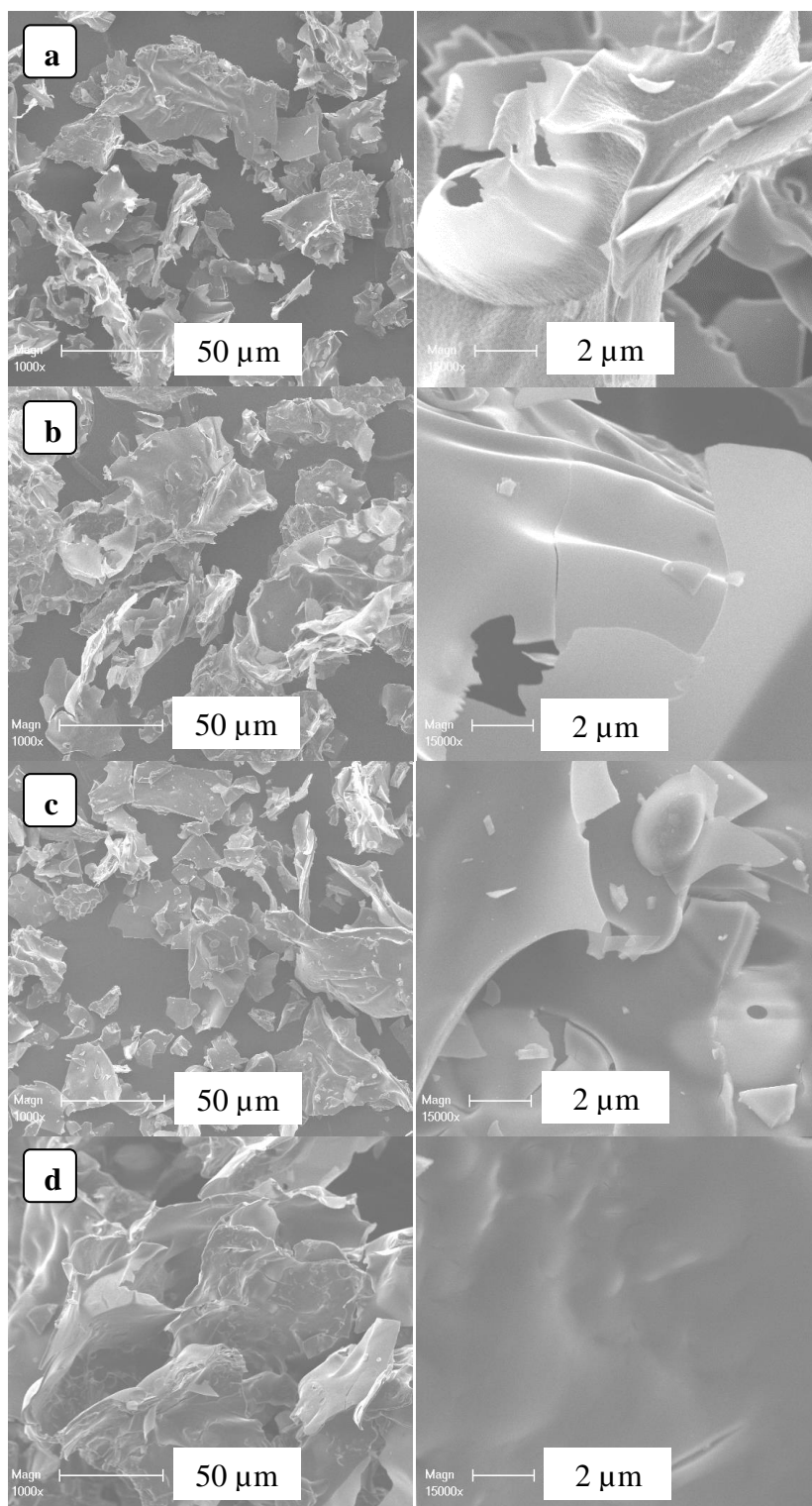
during the combustion process. The surface morphology in overall samples does not seem to be affected by increasing the nickel loading, suggesting that their combustion characteristics are approximately the same.



**Figure 3. 34.** SEM images of (a) 5NiAl, (b) 10NiAl, (c) 15NiAl and (d) 20NiAl calcined samples.

### 3.1.2.4.2 Cobalt based catalysts

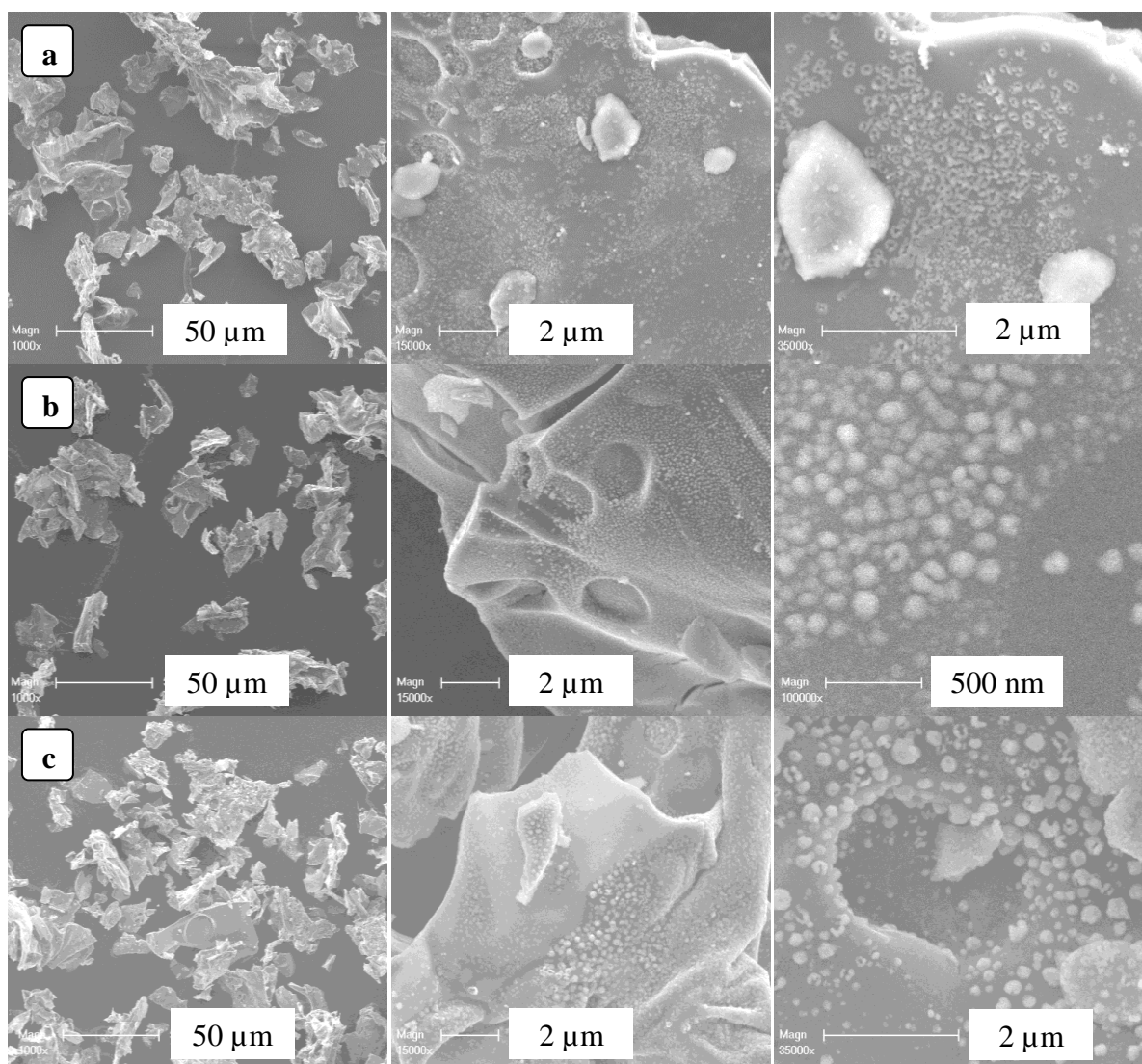
The SEM micrographs of the XCoAl samples with 5 to 20 wt% cobalt loading are given in **Figure 3.35**. the XCoAl samples exhibit “flaky-like” morphology, similarly to XNiAl samples. No differences are noticed on the SEM micrographs among the XCoAl samples.



**Figure 3. 35.** SEM images of (a) 5CoAl, (b) 10CoAl, (c) 15CoAl and (d) 20CoAl calcined samples.

### 3.1.2.4.3 Copper based catalysts

The SEM images of the XCuAl samples are presented in **Figure 3.36**. The agglomerates of the different XCuAl samples have platelet particles with an average size smaller than 50  $\mu\text{m}$ . SEM micrographs show that the entire surface of the XCuAl samples presented a granular aspect, asserted by the dispersion of spherical particles on their surfaces. Noticeably, with the increasing copper loading, the particle size is getting larger, and larger agglomeration particles gradually appear on the surface. Therefore, the metal loading has significant effect on the size, dispersion and aggregation of particles.



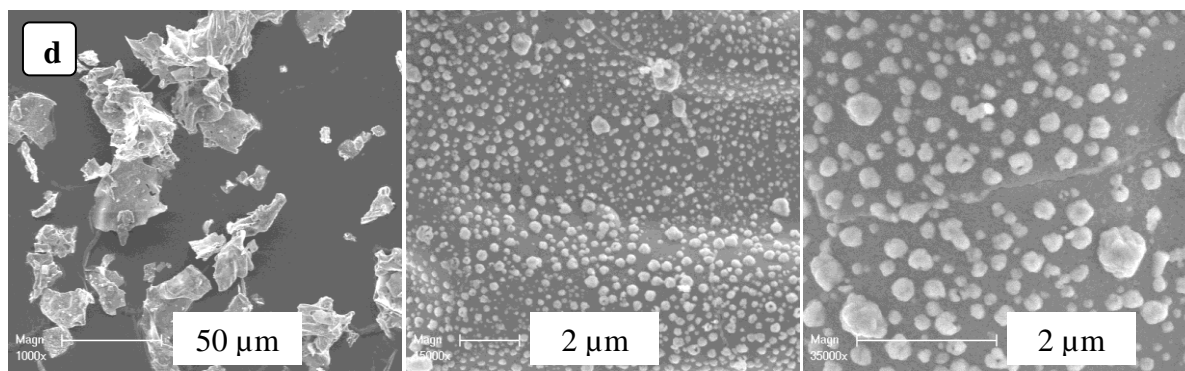


**Figure 3.36.** SEM images of (a) 5CuAl, (b) 10CuAl, (c) 15CuAl and (d) 20CuAl calcined samples.

### 3.1.2.5 SEM-EDX

#### 3.1.2.5.1 Nickel based catalysts

The elemental distribution maps, provided from SEM-EDX microanalysis, of the XNiAl catalysts are given in **Figure 3.37**. As revealed in **Figure 3.37**, mapping images of Ni show uniform distribution of Ni on the 10NiAl, 15NiAl and 20NiAl sample. In all cases, aluminum and oxygen almost cover the entire surface. The high weight percentage of alumina in comparison to nickel may lead to a high distribution of Al and O elements on the surface. Since the depth resolution in the SEM-EDX microanalysis is on the order of few microns (5 μm), Ni dispersion could not be determined exactly by SEM-EDX.

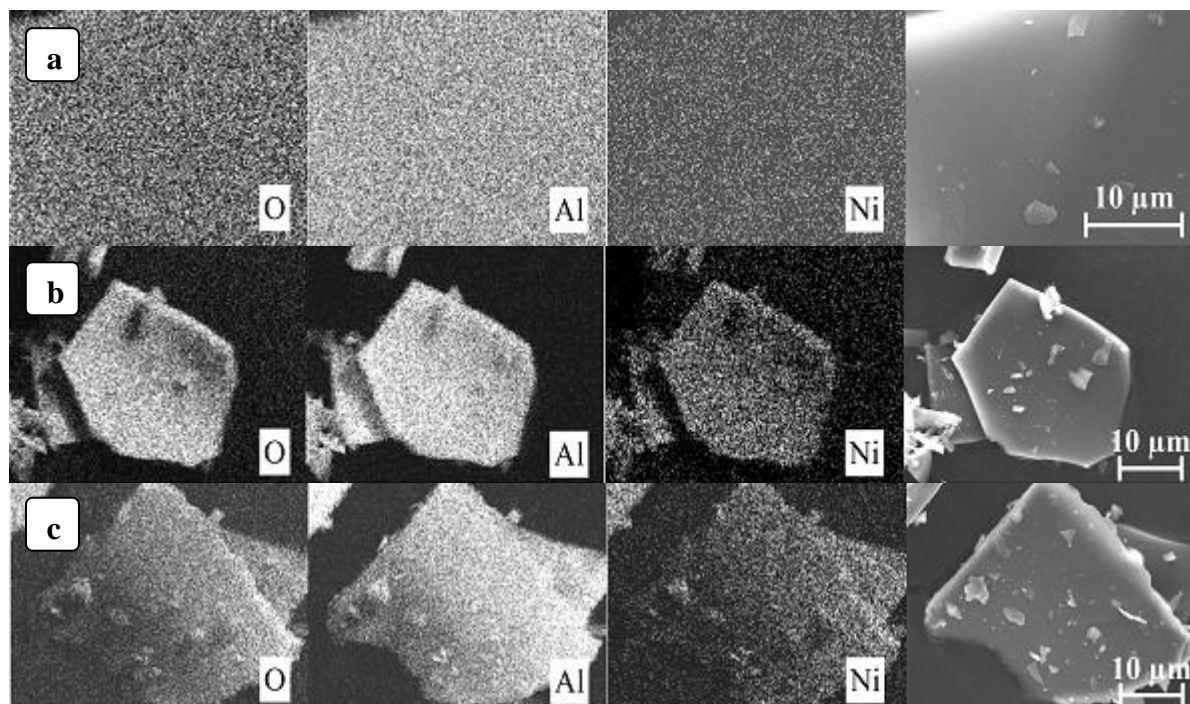


**Figure 3.37.** SEM-EDX elemental distribution maps of (a) 10NiAl, (b) 15NiAl and (c) 20NiAl calcined samples.

### 3.1.2.5.2 Cobalt based catalysts

SEM-EDX elemental mapping analyses of the XCoAl catalysts are reported **Figure 3.38**. As visualized in **Figure 3.38**, O, Al and Co elements are highly dispersed on the surface of the 10CoAl, 15CoAl and 20CoAl samples.

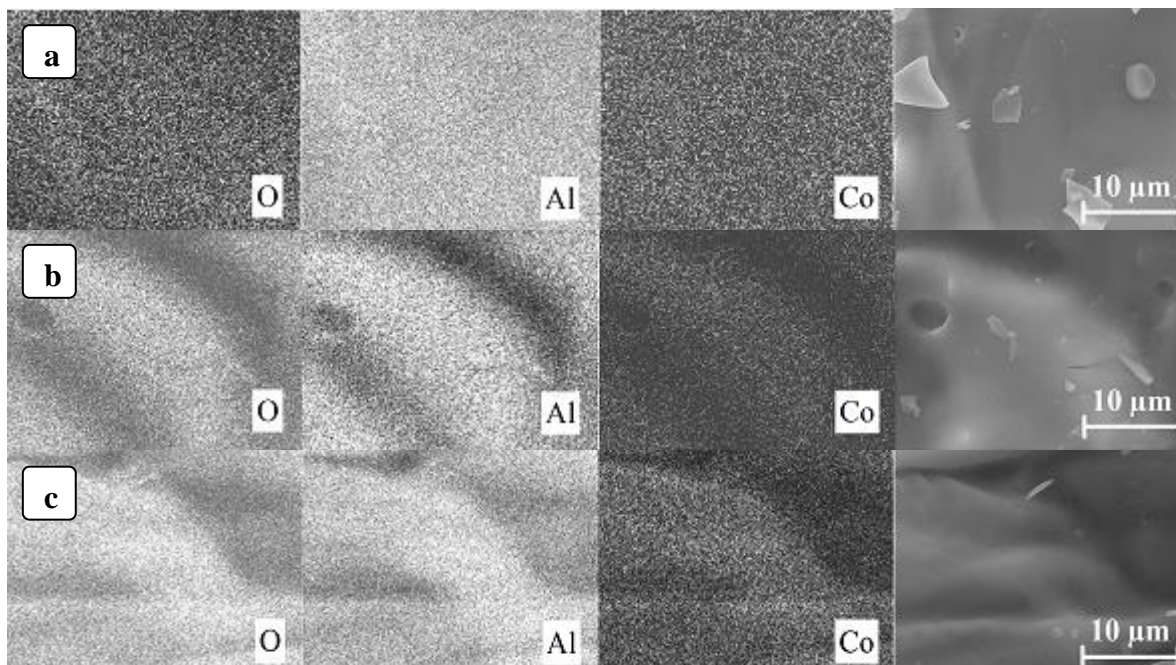


**Figure 3. 38.** SEM-EDX elemental distribution maps of (a) 10CoAl, (b) 15CoAl and (c) 20CoAl calcined samples.

It is clear from **Figure 3.37** and **Figure 3.38**, that nickel and cobalt show similar elemental mapping patterns in all metal contents. The high dispersion homogeneity of the Ni and Co elements on the alumina surface could be assigned to the incorporation of Ni and Co species into the alumina structure to form metal aluminate ( $\text{MAl}_2\text{O}_4$ ). In this case, rather than being completely incorporated into the alumina structure, a surface spinel may be formed.

### 3.1.2.5.3 Copper based catalysts

The elemental distribution maps of the XCuAl catalysts are given in **Figure 3.39**. As can be seen from **Figure 3.39**, aluminum and oxygen dispersion, for all copper contents, is equally uniform. Comparing the EDX mapping patterns of Cu, it is clear that copper dispersion decreases by increasing the copper loading. A better coverage of copper can be found in 10CuAl sample. In contrast, for high contents of copper, a non-homogeneous distribution of Cu-containing species on the surface is observed. Therefore, it can be concluded that enhancement of copper loading has a significant influence on the decrease of the copper dispersion.

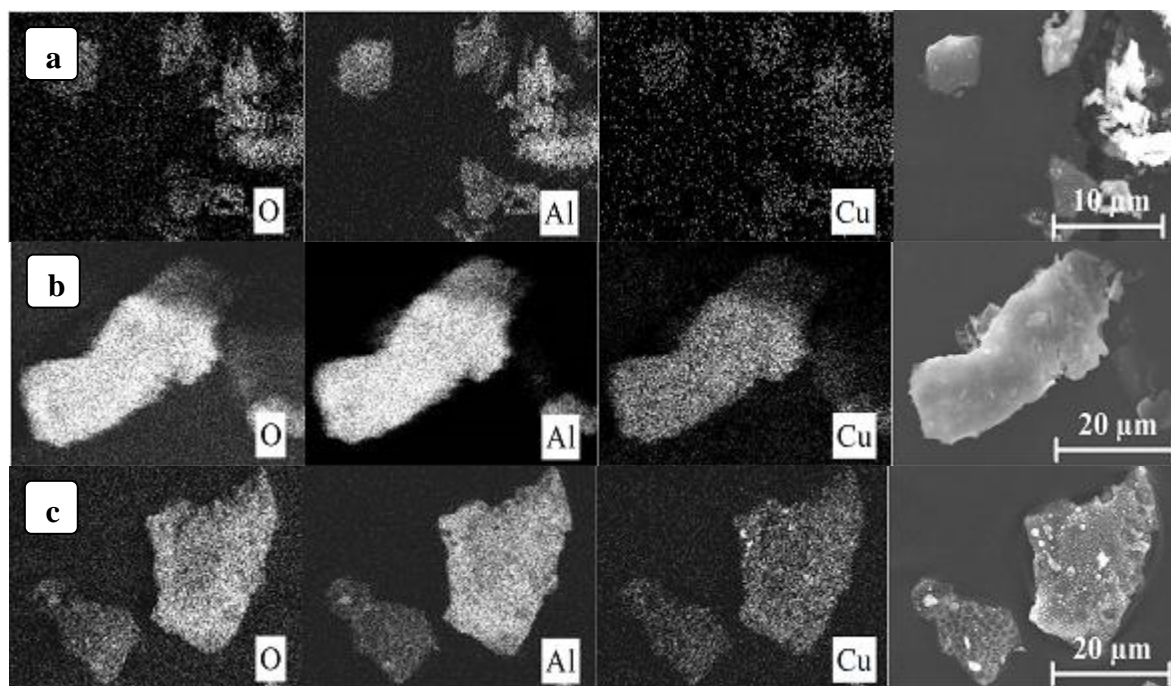


**Figure 3. 39.** SEM-EDX elemental distribution maps of (a) 10CuAl, (b) 15CuAl and (c) 20CuAl calcined samples.

## 3.2 Ternary oxide catalysts

This section includes the results of an extensive investigation of the bulk and surface properties of ternary mixed oxides. The present investigation was undertaken based on the idea that the combination of two active oxides would lead to the creation of new systems with new physicochemical properties. Attempts have been made to explore the chemical state of the different components and to study the interaction between the active oxides and alumina. Alumina-based ternary metal oxide catalysts were characterized using XRD,  $N_2$  adsorption-desorption, SEM, XPS and TEM techniques.

### 3.2.1 XRD

The XRD patterns of the 5Ni5CoAl, 5Ni5CuAl and 5Co5CuAl calcined catalysts are represented in **Figure 3.40**. The XRD profile of the 5Ni5CoAl catalyst showed broad and overlapped diffraction peaks at  $2\theta = 31.7^\circ$ ,  $37.5^\circ$ ,  $45.7^\circ$ ,  $60.3^\circ$  and  $66.4^\circ$ , which are assigned to  $\gamma$ - $Al_{2.67}O_4$  (JCPDS 04-005-4662),  $CoAl_2O_4$  (JCPDS 00-003-0896), and  $NiAl_2O_4$  (JCPDS 01-078-6951). Besides, small reflections related to  $\alpha$ - $Al_2O_3$  (JCPDS 00-042-1468) at  $2\theta = 35.1^\circ$  and  $43.4^\circ$  are detected. The diffraction peaks of  $\gamma$ - $Al_{2.67}O_4$  are very close to those of  $CoAl_2O_4$  and  $NiAl_2O_4$  phases. So, their attribution remains open to discussion and further characterization is needed. Nevertheless, the absence of any diffraction peaks of NiO or  $Co_3O_4$  phases can support the possible diffusion of these species into the alumina lattice

forming  $\text{NiAl}_2\text{O}_4$  and  $\text{CoAl}_2\text{O}_4$  phases. The intimate contact between the active components and alumina upon the solution combustion method could facilitate the diffusion of  $\text{NiO}$  or  $\text{Co}_3\text{O}_4$  phases into alumina lattice leading to aluminates formation. In addition, as previously explained, the high temperature synthesis promotes the formation of these phases, which were reported to occur at elevated temperatures. The combination of these two factors could accurately justify the existence of nickel and cobalt aluminates in the 5Ni5CoAl catalyst.

XRD patterns of the 5Ni5CuAl catalyst show, similarly to the 5Ni5CoAl catalyst, major diffraction peaks of  $\gamma\text{-Al}_{2.67}\text{O}_4$  (JCPDS 04-005-4662) and  $\text{NiAl}_2\text{O}_4$  (JCPDS 01-078-6951). The depicted peaks at  $2\theta = 25.5^\circ$ ,  $35.5^\circ$ ,  $43.4^\circ$  and  $57.2^\circ$  were assigned to  $\alpha\text{-Al}_2\text{O}_3$  (JCPDS 00-042-1468). Moreover, small peaks of  $\text{CuO}$  (JCPDS 04-015-5864) were detected. There is, however, no detectable peak to justify the existence of  $\text{NiO}$ .

For the 5Co5CuAl catalyst, the observed peaks at  $2\theta = 31.52^\circ$ ,  $37.1^\circ$ ,  $45.6^\circ$ ,  $60.3^\circ$  and  $66.5^\circ$  are assigned to  $\gamma\text{-Al}_{2.67}\text{O}_4$  (JCPDS 04-005-4662) and  $\text{CoAl}_2\text{O}_4$  (JCPDS 00-003-0896) phases. It is difficult to distinguish between  $\gamma\text{-Al}_{2.67}\text{O}_4$  and  $\text{CoAl}_2\text{O}_4$  phases from XRD measurements because their diffraction patterns are similar. Additionally, weak diffraction peaks of  $\text{CuO}$  (JCPDS 04-015-5864) are observed. It is expected that  $\text{CuO}$  species in 5Co5CuAl catalyst are well dispersed. However, no bulk crystalline phases corresponding to  $\text{Co}_3\text{O}_4$  could be observed. The low intensity of the  $\gamma\text{-Al}_{2.67}\text{O}_4$  and/or  $\text{CoAl}_2\text{O}_4$  peaks suggests that these phases are mostly in an amorphous state.

### **Discussion**

The absence of any diffraction peaks of  $\text{NiO}$  or  $\text{Co}_3\text{O}_4$  phases indicates their diffusion in gamma alumina lattice producing  $\text{NiAl}_2\text{O}_4$  and  $\text{CoAl}_2\text{O}_4$  phases. This fact is consistent with the binary oxides XRD results. According to the literature, interaction between transition alumina and Ni, Co or Cu oxides to form aluminates is quite common. However, in the present study, there is no evidence for the formation of copper aluminates. Moreover, the addition of a second phase to nickel and cobalt containing samples does not seem to affect the interaction between alumina and  $\text{NiO}$  or  $\text{Co}_3\text{O}_4$  phases. These findings indicate that the combustion method has a leading role in controlling the chemical interaction between the different phase components.

The relative intensities of diffraction lines in 5Ni5CoAl catalyst are higher than those in the case of 5Ni5CuAl and 5Co5CuAl catalysts due to the excessive presence of bulk  $\text{NiAl}_2\text{O}_4$  and

$\text{CoAl}_2\text{O}_4$  phases. Furthermore, it can be expected that the dispersion of CuO is slightly higher in the 5Co5CuAl as compared to the 5Ni5CuAl sample.

The existence of  $\text{NiAl}_2\text{O}_4$  and  $\text{CoAl}_2\text{O}_4$  compounds in the 5Ni5CuAl and 5Co5CuAl samples indicates that the addition of copper to cobalt or nickel containing catalysts does not inhibit the spinel formation.

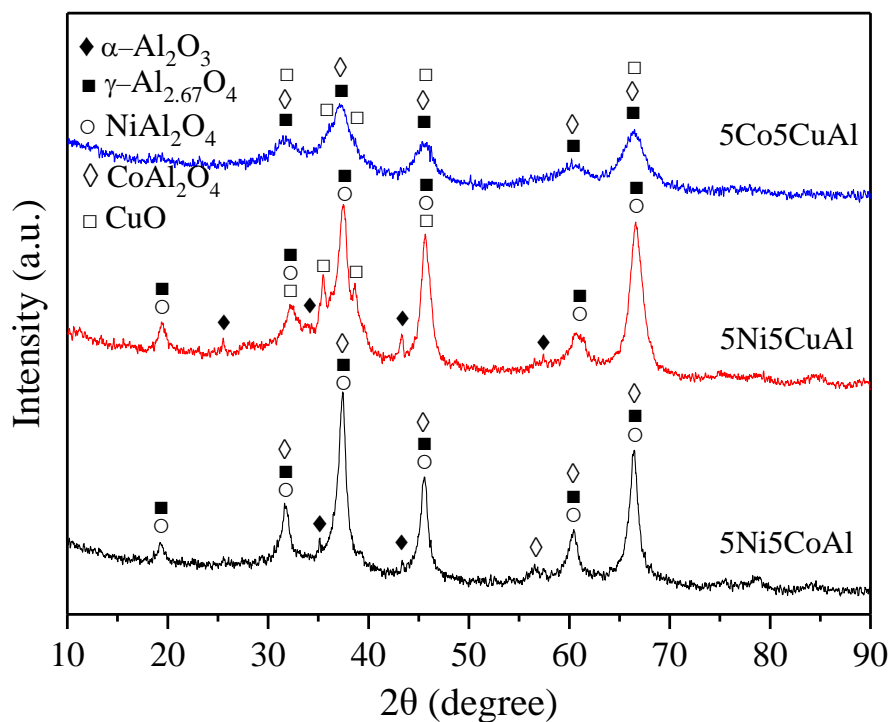


**Figure 3. 40.** XRD patterns of 5M5MAI calcined catalysts.

### 3.2.2 $\text{N}_2$ adsorption-desorption isotherms

The  $\text{N}_2$  adsorption-desorption isotherms of the 5M5MAI calcined samples are shown in **Figure 3.41**. The isotherms of 5M5MAI calcined samples are of type IV, with H4-type hysteresis loops. **Table 3.12** summarizes the textural properties and the elemental analysis of the 5M5MAI calcined samples.

As can be noted from **Table 3.12**, all the samples exhibited low surface areas ranging from 22.8 to 31.2  $\text{m}^2\text{g}^{-1}$ . These results were expected since the combustion method leads to low surface areas. In addition, the prepared catalysts show similarities in pore volumes and pore diameters. Most of the binary systems with a constant metal loading of 10 wt % present surface area values higher than those of the ternary systems. The 5Co5CuAl sample exhibits slightly higher surface area than the other two samples. It seems that the homogeneous distribution of CuO increases the catalyst surface area.

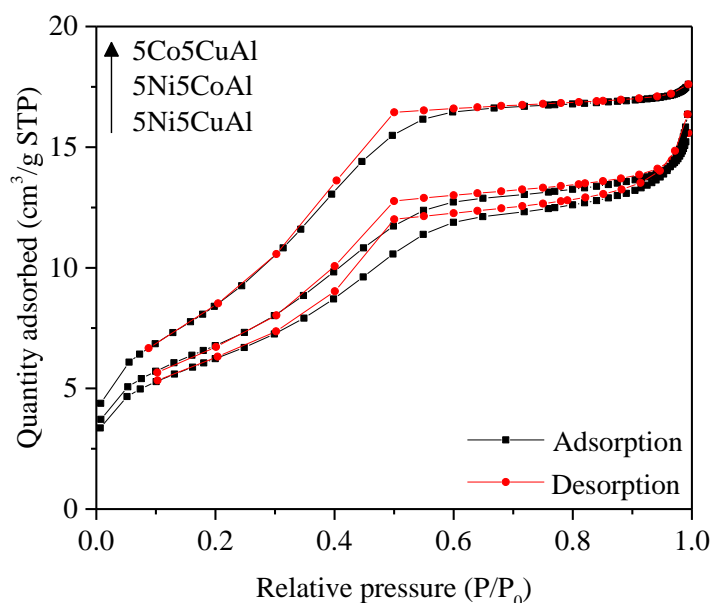


**Figure 3. 41.**  $N_2$  adsorption-desorption isotherm of 5M5MAI calcined catalysts.

**Table 3. 13.** XRF elemental analysis and textural properties of 5M5MAI calcined catalysts.

Sample identity	Metal loading (wt %)			BET surface area ( $m^2g^{-1}$ )	Pore volume <sup>a</sup> ( $cm^3g^{-1}$ )	Pore diameter <sup>b</sup> (nm)
	Ni	Co	Cu			
5Ni5CoAl	5.60	5.66	—	25.0	0.03	3.60
5Ni5CuAl	5.22	—	5.88	22.8	0.03	4.00
5Co5CuAl	—	6.65	6.06	31.2	0.03	3.10

<sup>a</sup>BJHdesorption average pore diameter.

<sup>b</sup>BJHdesorption pore volume.

### 3.2.3 SEM

The SEM micrographs of the 5M5MAI calcined catalysts are illustrated in **Figure 3.42**. The images are magnified at two scales: 50  $\mu m$  and 2  $\mu m$ . According to the SEM images, no significant morphological differences are observed between the binary and ternary oxides. It can be seen that the synthesized catalysts have “flaky-like” morphology with an average size of the agglomerates higher than 50  $\mu m$ .

From the SEM micrographs of 5Ni5CuAl and 5Co5CuAl samples, one can notice the formation of spherical nanoparticles on the surface of these catalysts. The average particle size of these particles is found to be in the range of 20–100 nm. The area enclosed by the rectangle reveals that 5Co5CuAl sample exhibited more uniform particle distribution with regular shapes and without clear agglomerated particles. It is assumed that the addition of cobalt or nickel to copper containing catalysts leads to increased particle size.

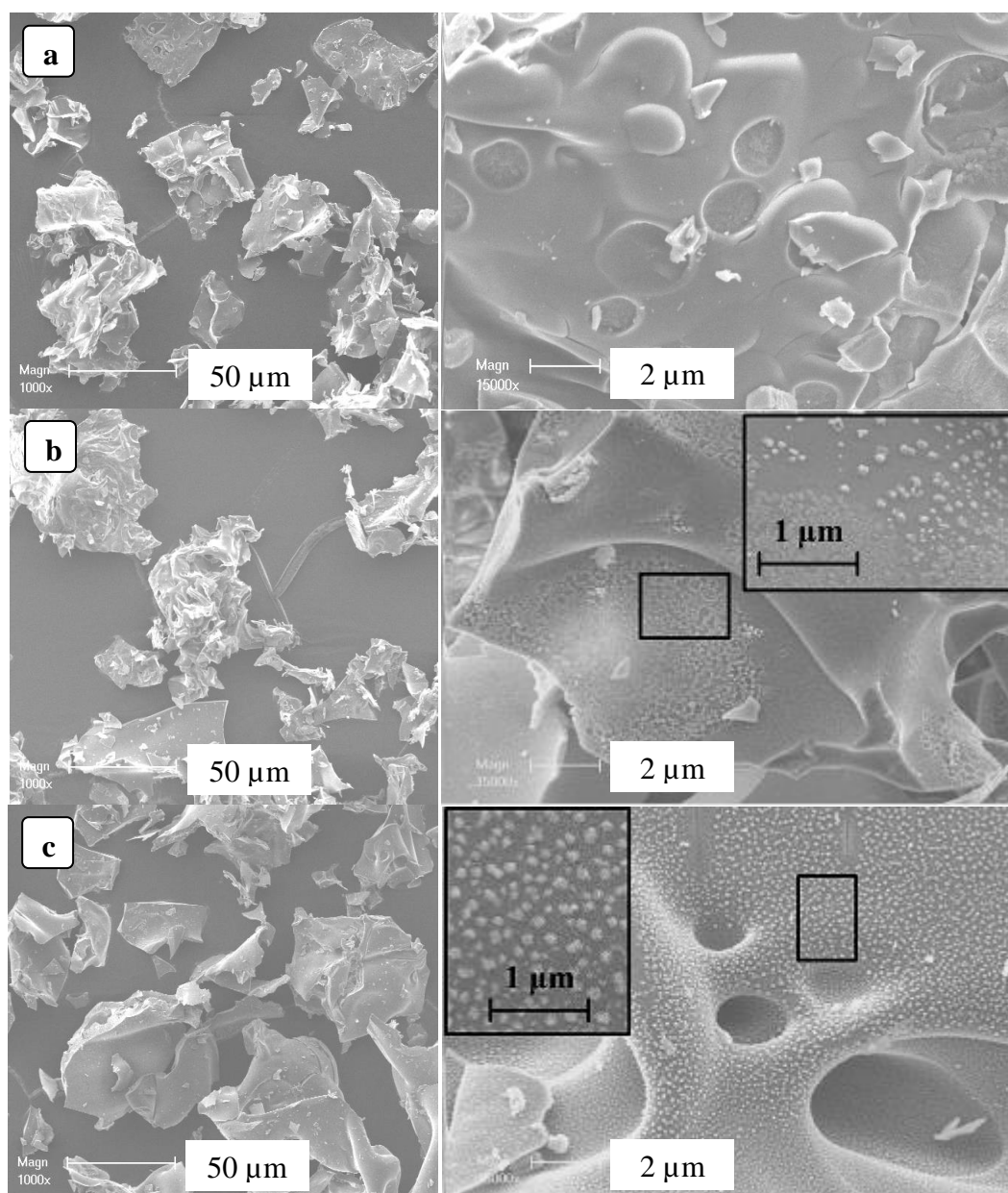


**Figure 3.42.** SEM images of (a) 5Ni5CoAl, (b) 5Ni5CuAl and (c) 5Co5CuAl calcined samples.

### 3.2.4 XPS

XPS analyses of the calcined catalysts were performed to obtain insights into the surface properties of the bimetallic catalysts. The Ni 2p<sub>3/2</sub>, Co 2p<sub>3/2</sub> and Cu 2p<sub>3/2</sub> XP spectra of 5M5MAI catalysts are depicted in **Figure 3.43**. Surface M/Al (M= Ni, Co, Cu) atomic ratios determined by XPS of various catalysts are summarized in **Table 3.13**.

As shown in **Figure 3.43 (a)**, the Ni 2p<sub>3/2</sub> signal is composed of a main peak centered at 855.34 eV, accompanied by two satellites at BEs of 861.77 and 866.8 eV, which is assigned to the Ni<sup>2+</sup> in NiAl<sub>2</sub>O<sub>4</sub>. The presence of Co<sup>2+</sup> in CoAl<sub>2</sub>O<sub>4</sub> is also confirmed by the Co 2p<sub>3/2</sub>

peak at 781.14 eV, accompanied by the satellite peak at around 786.09 eV. Compared with our previous XPS studies, the combination of Ni and Co in the bimetallic 5Ni5CoAl sample does not seem to affect the positions of both Ni 2p<sub>3/2</sub> and Co 2p<sub>3/2</sub> peaks. This further confirms the existence of NiAl<sub>2</sub>O<sub>4</sub> and CoAl<sub>2</sub>O<sub>4</sub> compounds on the 5Ni5CoAl catalyst surface.

For the 5Ni5CuAl catalyst sample, the Ni 2p<sub>3/2</sub> signal shows a peak at 855.35 eV with two satellite peaks at BEs of 861.78 and 866.8 eV. Ni peak positions are exactly the same for 5Ni5CoAl and 5Ni5CuAl which means that the Ni species are in the same oxidation state in both samples. The Cu 2p<sub>2/3</sub> signal showed a peak at 933.17 eV and two satellite peaks at BEs of 940.93 and 943.39 eV, corresponding to Cu<sup>2+</sup> in CuO.

The Co 2p<sub>3/2</sub> spectra of 5Co5CuAl catalyst shows a peak at BE of 780.57 eV, accompanied by a satellite peak at 786.21 eV, corresponding to the Co<sup>2+</sup> in CoAl<sub>2</sub>O<sub>4</sub>. The Cu 2p<sub>2/3</sub> spectrum shows a peak at 933.43 eV with two satellite peaks at BEs of 940.9 and 943.44 eV, which is ascribed to Cu<sup>2+</sup> in CuO.

According to **Table 3.14**, the surface Ni/Al and Co/Al atomic ratios for the 5Ni5CoAl catalyst are found to be 0.035 and 0.033, respectively. The Cu/Al ratios of 5Ni5CuAl and 5Co5CuAl samples are consistently higher than the values obtained for Ni/Al and Co/Al ratios, which indicates the existence of higher amounts of Cu<sup>2+</sup> on the surface than those of Ni<sup>2+</sup> and Co<sup>2+</sup>. In other words, aggregated copper oxides may disperse on the surface of the catalysts, while nickel oxides or cobalt oxide diffuse into the alumina lattice, resulting in a decrease of Ni/Al and Co/Al ratios.

Surface Cu/Al ratios are 0.136 and 0.076 for 5Ni5CuAl and 5Co5CuAl catalysts, respectively. The highest Cu/Al ratio obtained for 5Ni5CuAl catalyst could be assigned to the high dispersion of Cu species. While the lowest Cu/Al ratio obtained for 5Co5CuAl suggests that some amounts of Cu species diffuse from the surface to the bulk phase. The higher concentration of Cu on the surface may favor better catalyst performance.

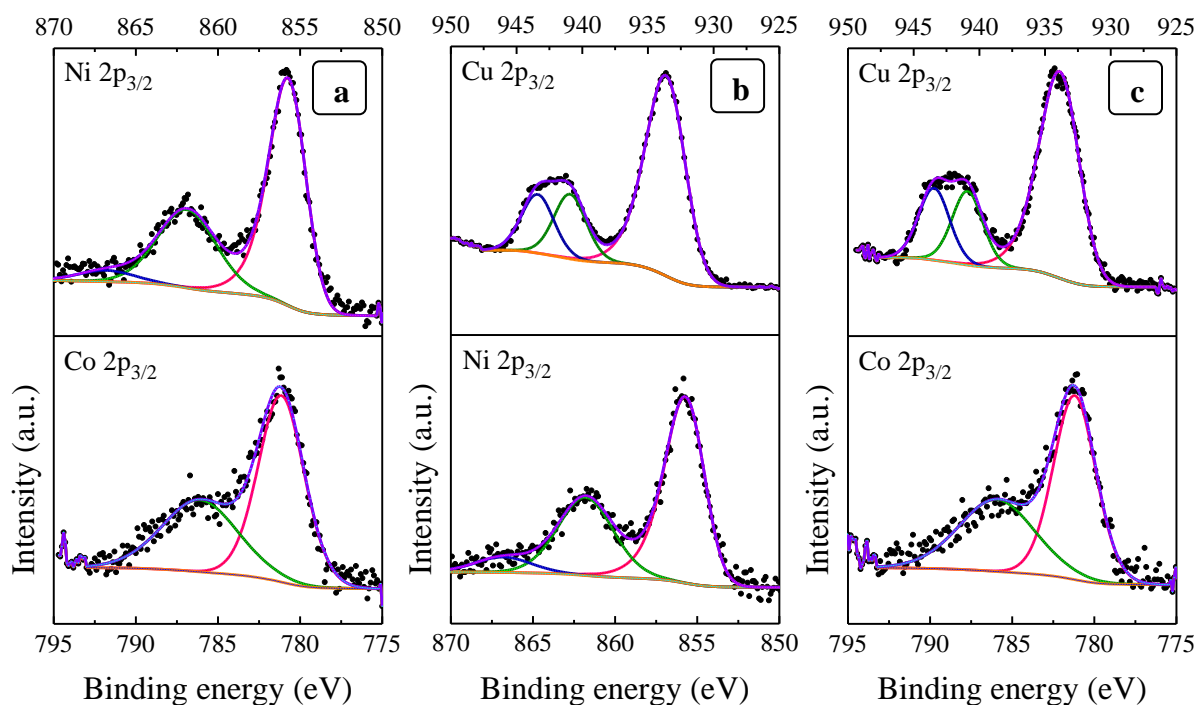


**Figure 3. 43.** XPS spectra of (a) 5Ni5CoAl, (b) 5Ni5CuAl and (c) 5Co5CuAl calcined samples.

**Table 3. 14.** Surface M/Al atomic ratios determined by XPS for 5M5MAI calcined samples.

Sample identity	Surface atomic ratio		
	Ni/Al	Co/Al	Cu/Al
5Ni5CoAl	0.035	0.033	—
5Ni5CuAl	0.032	—	0.136
5Co5CuAl	—	0.038	0.076

### 3.2.5 TEM

The TEM micrographs of 5M5MAI samples are illustrated in **Figure 3.44-46**. Ni, Co and Cu metal oxide nanoparticles have been easily observed on the surface of the catalysts, due to the color contrast between the metal oxide and alumina.

As it can be seen from **Figure 3.44**, Ni and Co metal oxide nanoparticles were uniformly dispersed on the surface of the 5Ni5CoAl bulk catalyst, with an average particle size ranged between 5 and 20 nm. There are no significant differences between TEM micrographs of the monometallic catalysts, studied previously, and those of the bimetallic catalysts.

**Figure 3.44 (d)** showed many crystal lattice planes of the 5Ni5CoAl catalyst with d-spacing of 0.284 and 0.286 nm, corresponding to the cubic  $\text{NiAl}_2\text{O}_4$  (220) plane and to the cubic  $\text{CoAl}_2\text{O}_4$  (220) plane, respectively. Therefore, the homogeneous dispersion of the Ni and Co metal oxide nanoparticles in 5Ni5CoAl catalyst is attributed to the formation of the well-dispersed (monolayer structures)  $\text{CoAl}_2\text{O}_4$  and  $\text{NiAl}_2\text{O}_4$  “surface spinels”.

According to **Figure 3.45** and **3.46**, three dimensional CuO nanoparticles, ranging from 20 to 100 nm in size, were identified in both 5Ni5CuAl and 5Co5CuAl catalysts. A slightly larger CuO particle size and an apparent agglomeration are observed in the 5Ni5CuAl catalyst. It is seen that elongation of CuO nanoparticles is due to their sintering and agglomeration. In comparison with the investigated monometallic catalyst, it seems that the nickel/cobalt addition to copper containing catalyst has a clear effect in increasing the particle size.

For 5Ni5CuAl catalyst, d-spacing of 0.233 and 0.253 nm, corresponding to the CuO (111) and (002) planes, are obtained, whereas 5Co5CuAl catalyst gives lattice planes with d-spacing of 0.138 and 0.201 nm for the CuO (220) plane and the CoAl<sub>2</sub>O<sub>4</sub> (400) plane, respectively.

EDX spectra and elemental compositions of the 5M5MAI calcined samples are reported in **Figure 3.47**. The metal loadings (in weight percent) obtained from EDX analyses match with the nominal percentages (5 wt%), within the permissible limits, which confirms the validity of the preparation procedure. Obviously, the quantitative amounts of the copper are slightly higher than the actual metal loadings, suggesting that copper species is mostly present on the catalyst surface.

**Figure 3.48** shows EDX dot-mapping analyses of 5Ni5CoAl and 5Ni5CuAl calcined samples. As it can be observed from **Figures 3.48 (a)** and **3.48 (b)**, Ni and Co elements are homogeneously dispersed on the surface of 5Ni5CuAl and 5Co5CuAl samples, respectively. The dispersion of Cu over these two samples is not similar; indeed, a high local Cu concentration is observed on the surface of 5Co5CuAl sample. These results are consistent with the observation of TEM micrographs that shows large particles of CuO and an apparent agglomeration in 5Co5CuAl sample.

TEM images (inset) and their corresponding SAED patterns are shown in **Figure 3.49**. The SAED patterns of the 5Ni5CoAl sample consist of continuous concentric rings that could be assigned to  $\alpha$ -Al<sub>2</sub>O<sub>3</sub> (300) plane, CoAl<sub>2</sub>O<sub>4</sub> (440) plane, and to NiAl<sub>2</sub>O<sub>4</sub> (400), (311) and (220) planes.

For the 5Ni5CuAl sample, the diffraction spot forms concentric rings corresponding to  $\alpha$ -Al<sub>2</sub>O<sub>3</sub> (300) plane, NiAl<sub>2</sub>O<sub>4</sub> (440) and (400) planes, and to CuO (111) and (002) planes.

For the 5Co5CuAl sample, five diffraction rings are observed, which could be indexed as the CuO (220), (111) and (110) planes, as well as the CoAl<sub>2</sub>O<sub>4</sub> (440) and (331) planes. The results of SAED further confirm the presence of NiAl<sub>2</sub>O<sub>4</sub> and CoAl<sub>2</sub>O<sub>4</sub> “surface spinels” in the different samples. Moreover, the formation of free CuO particles in both 5Ni5CuAl and

5Co5CuAl samples is asserted. Notably, nickel and cobalt oxides are not identified in all samples, which confirms their incorporation into the alumina structure, in accordance with the results of both XRD and XPS.

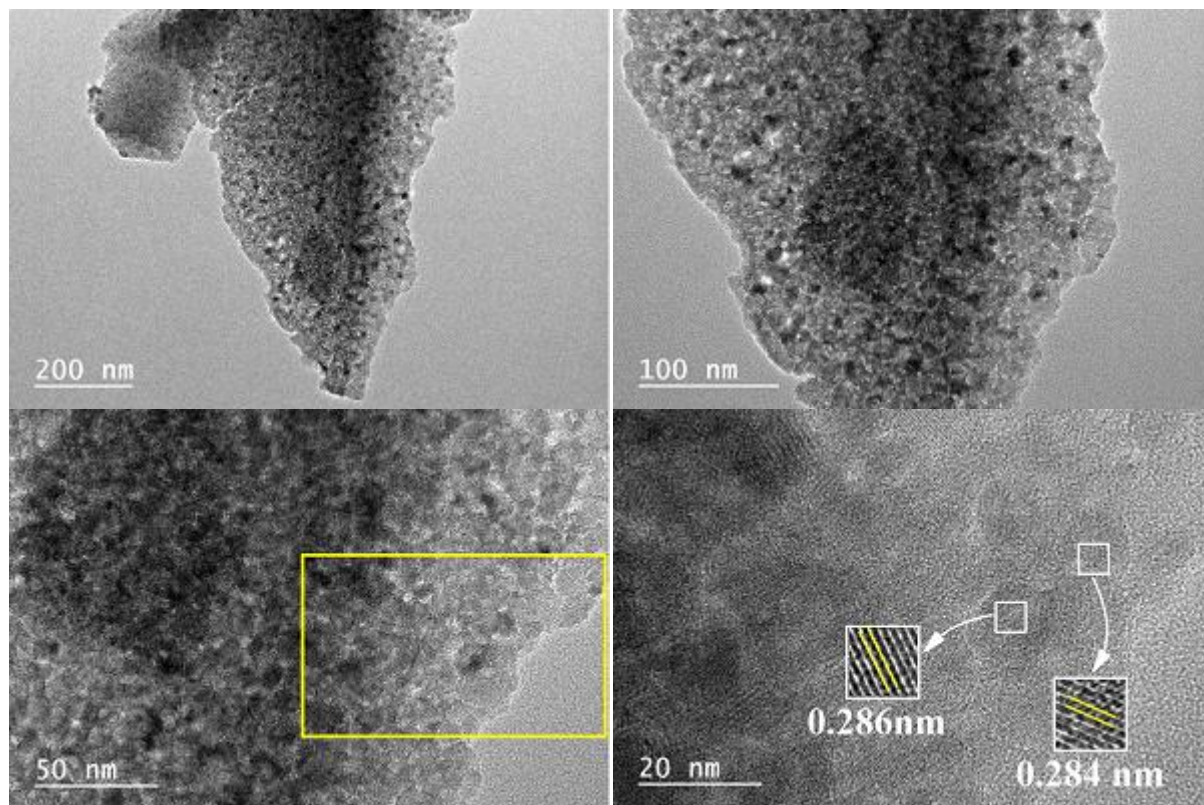


**Figure 3. 44.** *TEM images of 5Ni5CoAl calcined sample.*

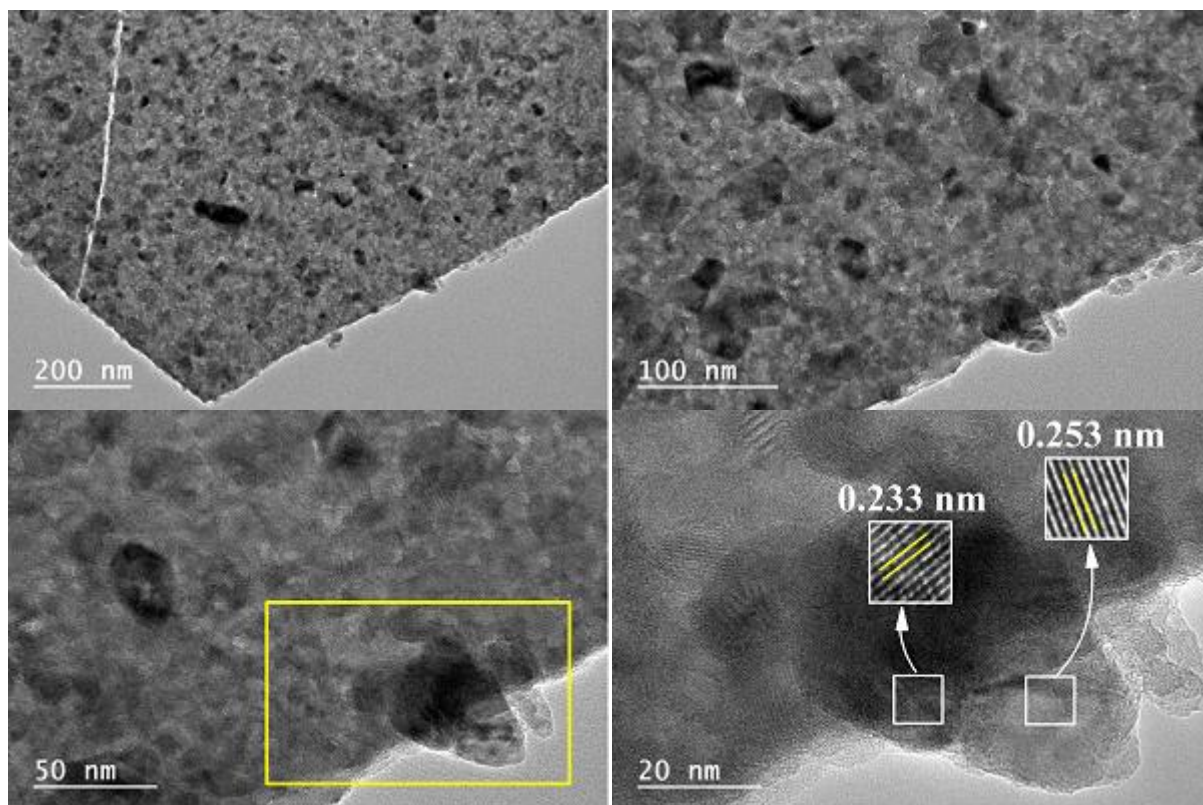


**Figure 3. 45.** *TEM images of 5Ni5CuAl calcined sample.*

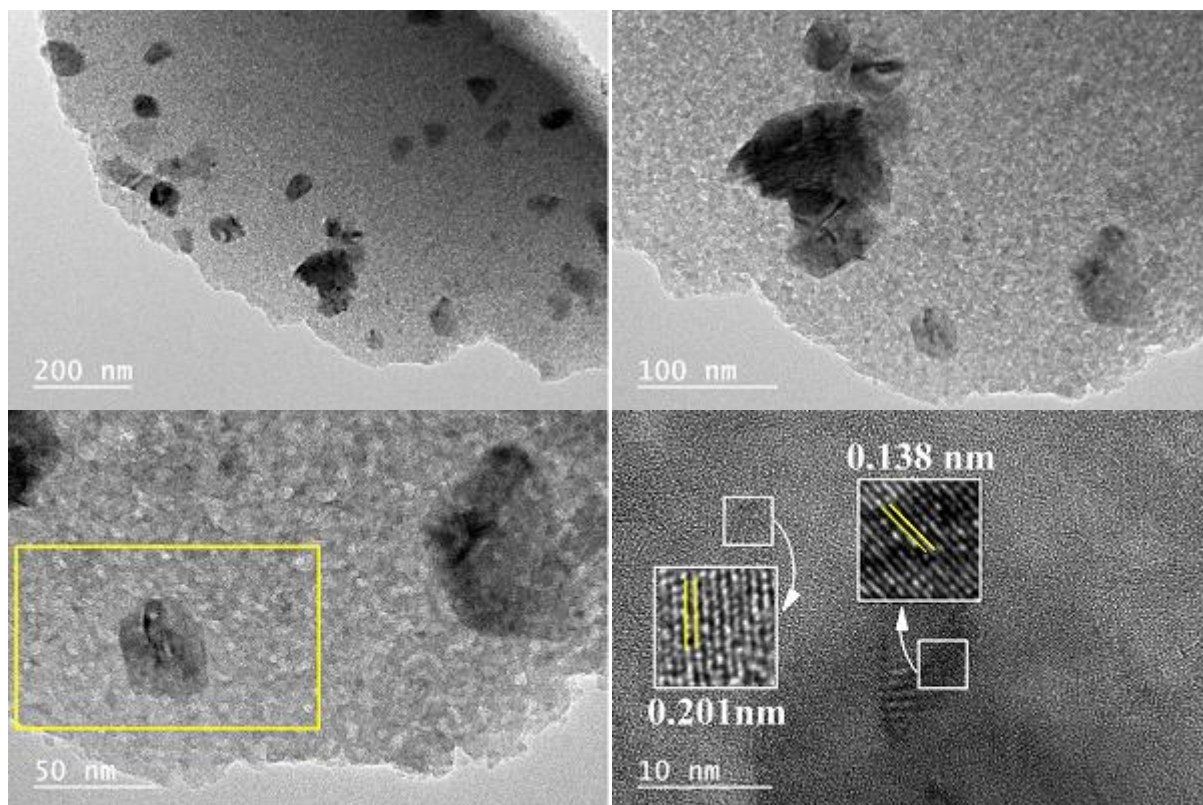


**Figure 3. 46.** *TEM images of 5Co5CuAl calcined sample.*

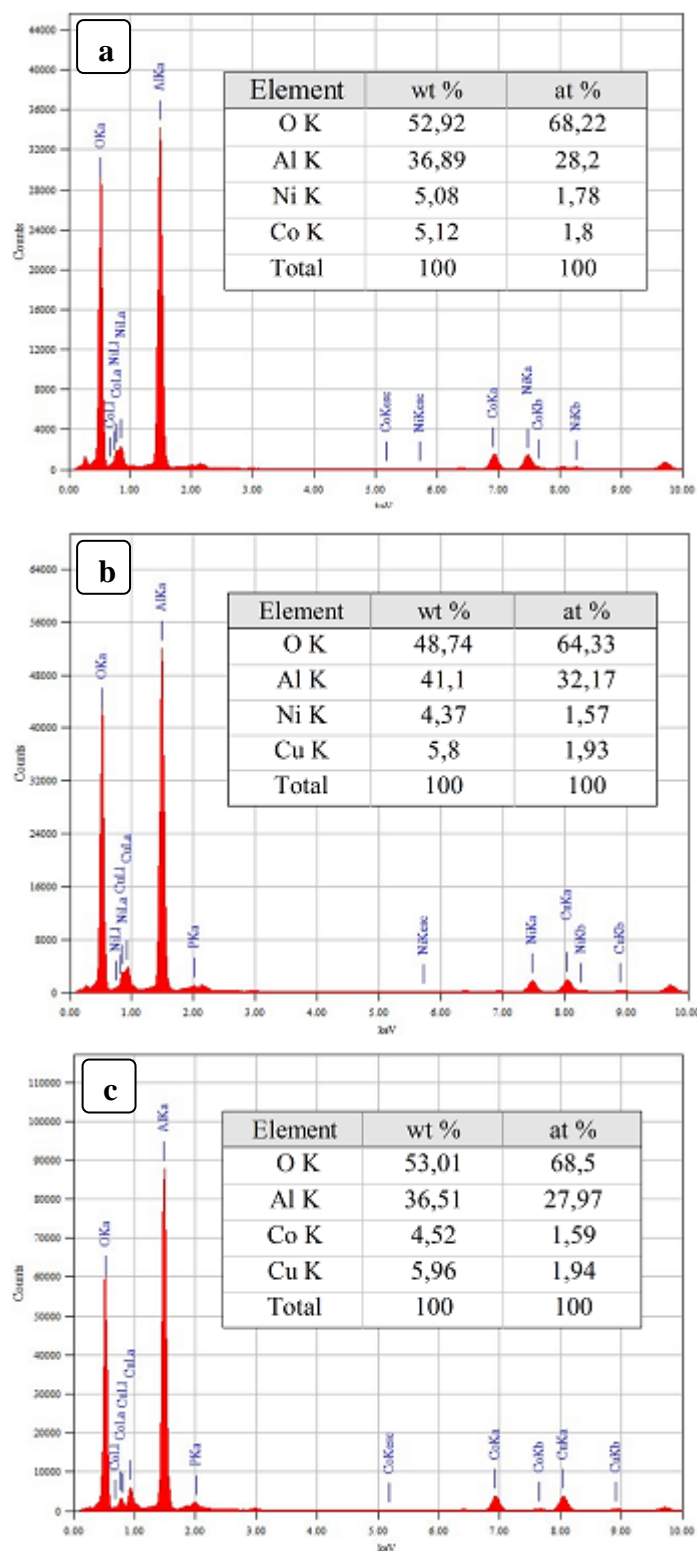


**Figure 3. 47.** TEM-EDX elemental analyses of (a) 5Ni5CoAl (b) 5Ni5CuAl and (c) 5Co5CuAl calcined samples.

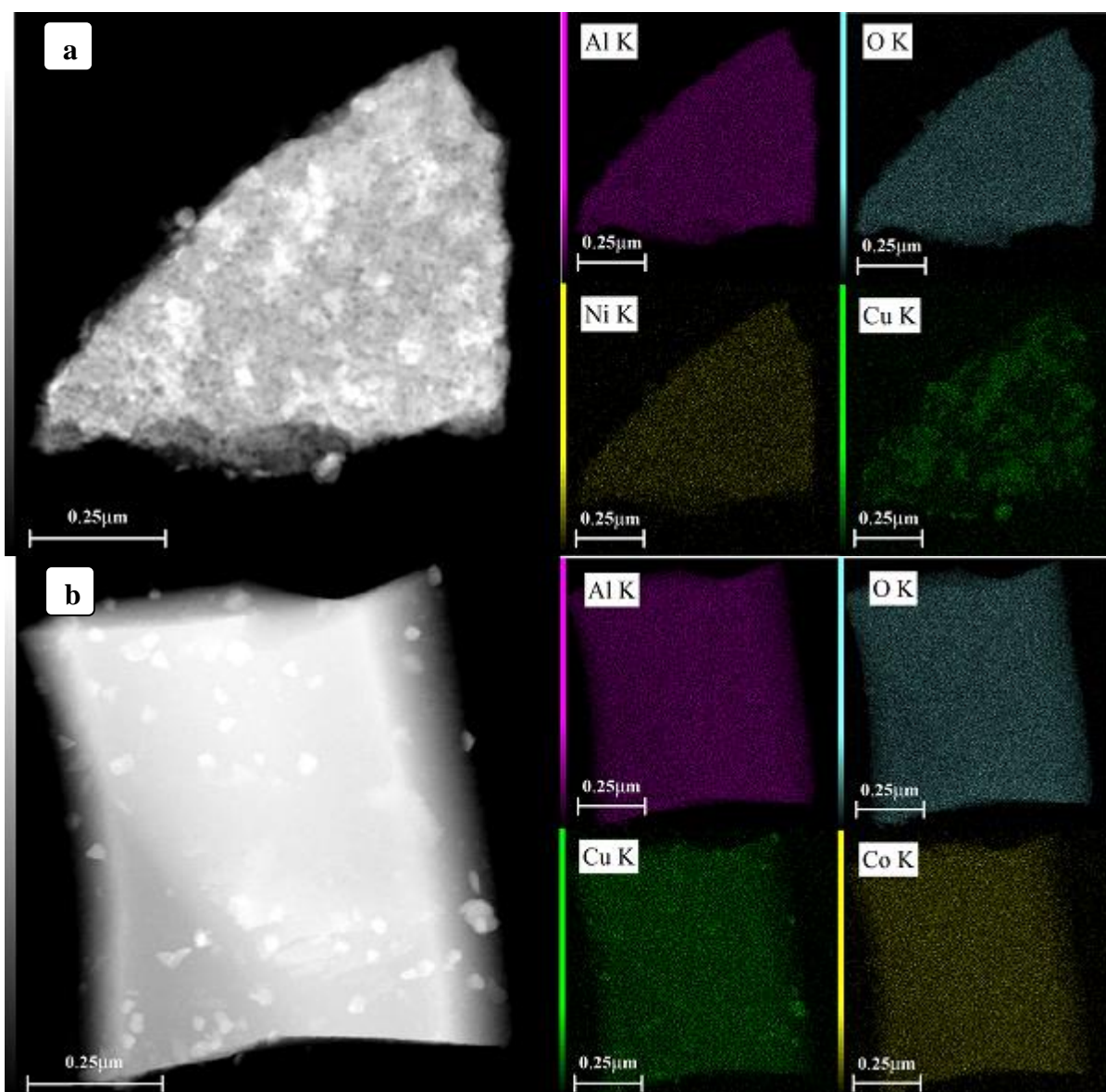


**Figure 3. 48.** TEM-EDX dot-mapping analyses of (a) 5Ni5CuAl and (b) 5Co5CuAl calcined samples.

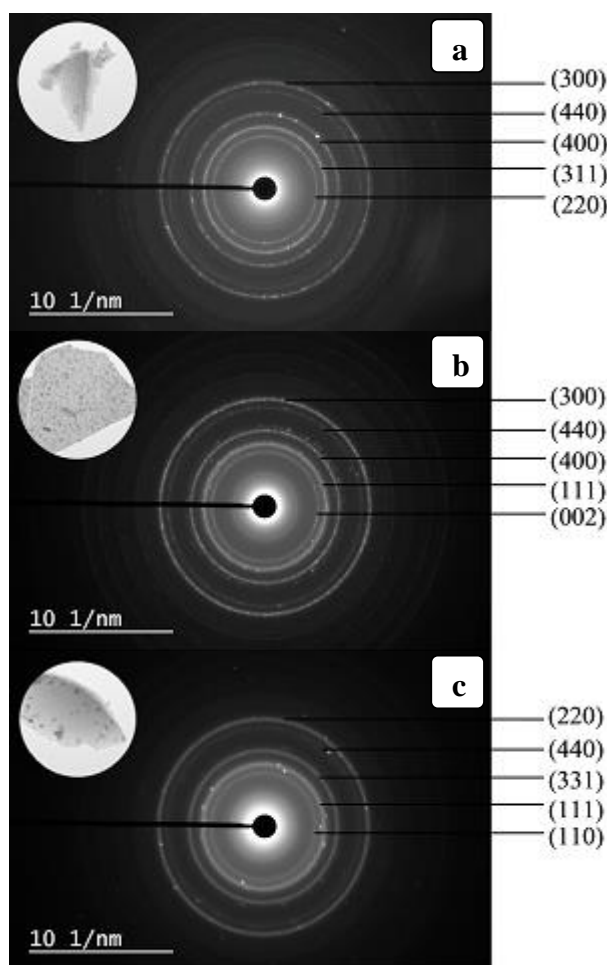


**Figure 3. 49.** SAED patterns of (a) 5Ni5CoAl (b) 5Ni5CuAl and (c) 5Co5CuAl calcined samples.

## Conclusions

In this chapter, it has been shown that the combustion synthesis is a facile one-step approach to prepare binary and ternary metal oxide catalysts with homogeneous composition. This method can be easily extended to other complex mixed oxides.

Both binary and ternary alumina-based oxides present relatively low surface area. The obtained low surface can be associated to the sintering deriving by the high flame temperature reached during the combustion process.

The bulk and surface characterizations of the combustion synthesized 10MAI-x catalysts have shown that a mixture of  $\gamma$ -alumina and metal aluminates  $\text{MAI}_2\text{O}_4$  “surface spinel”/bulk phases are present in the 10NiAl-x and 10CoAl-x samples. On the other hand, a mixture of  $\alpha$ - $\text{Al}_2\text{O}_3$  and “bulk-like” CuO separated phases, as well as small amount of  $\text{Cu}_2\text{O}$  species are present on the 10CuAl-x samples. The chemical and physical surface and bulk properties of alumina-based binary metal oxide catalysts seem to be related to the combustion behavior of

the starting reactant mixtures. The formation of metal aluminates occurs at high temperature (above 700 °C), and combustion mixtures containing nickel or cobalt precursors might lead to higher combustion temperature, promoting the diffusion of the metal oxide into the alumina matrix.

Stoichiometry plays a critical role in controlling not only the phase composition, but also on the shape, morphology and crystallite size of the as-synthesized 10MAI-x catalysts. All the described characterization suggests that the best properties are reached for the 10MAI-1.0 catalysts.

The characterizations performed on the 2MAI-x catalysts, synthesized by combustion, have shown that a mixture of  $\text{NiAl}_2\text{O}_4$ ,  $\gamma\text{-Al}_{2.67}\text{O}_4$ ,  $\delta\text{-Al}_2\text{O}_3$ , and  $\alpha\text{-Al}_2\text{O}_3$  phases are present in the 2NiAl-x samples. On the other hand, a mixture of  $\gamma\text{-Al}_{2.67}\text{O}_4$ ,  $\alpha\text{-Al}_2\text{O}_3$ ,  $\text{CoAl}_2\text{O}_4$ , and  $\text{Co}_3\text{O}_4$  phases are present on the 2CoAl-x samples. Similar to the 10CuAl-x samples, 2CuAl-x samples have shown the presence of  $\alpha\text{-Al}_2\text{O}_3$  and CuO phases. The effect of the RV/OV ratio on the phase distribution evolution of the 2MAI-x samples is similar to that on the 10MAI-x samples; the increasing of the RV/OV ratio from 0.9 to 1.1, particularly in nickel and cobalt based samples, promotes the formation of aluminates phases.

The XRD results of the XMAI catalysts showed that increasing the nickel and cobalt metal loading in leads to the enhancement of the alumina-Ni/Co interactions, resulting in the incorporation of metal ions into the alumina lattice. At higher metal contents the saturation of all available lattice sites is reached and the excess of metal ions rearranges in a “bulk-like” metal oxide. For the Cu-containing catalysts, a higher copper loading results in a higher crystallinity and larger particle sizes. The BET analysis showed that by increasing the metal loadings up to 15 wt% an increase of the catalyst surface area is obtained. Furthermore, the higher is the amount of metal added, the lower the surface area. The SEM results show that the metal loading has no significant effect on the surface morphology of nickel and cobalt containing catalysts, while growth and sintering of the copper oxide particles are observed at higher metal loadings in the copper containing catalyst.

Lastly, it has found that both binary and ternary alumina-based oxides present very similar surface and bulk proprieties. In all cases, nickel and cobalt species tends to form surface/bulk spinels, while copper species preferentially form “bulk-like” CuO segregated phases. Moreover, copper oxides were not effective in preventing the formation of  $\text{NiAl}_2\text{O}_4$  and  $\text{CoAl}_2\text{O}_4$  spinels.

## Résumé en Français du chapitre 3

L'objectif de ce chapitre est de fournir une étude approfondie concernant les principaux résultats obtenus suite aux caractérisations physico-chimiques des divers oxydes métalliques rapportés dans le chapitre 2. Il présente, en premier lieu, l'étude de l'influence de la stœchiométrie et de la teneur en métal de transition sur les propriétés physico-chimiques des oxydes métalliques binaires, et en deuxième lieu, l'étude de l'effet de synergie du mélange bimétallique sur les propriétés physico-chimiques des oxydes métalliques ternaires.

En ce qui concerne les résultants de l'étude de l'influence de la stœchiométrie :

Les caractérisations structurales par diffraction X sur les oxydes binaires ont montrées l'obtention d'un mélange d'alumine  $\gamma$  et d'aluminates métalliques ( $MA_2O_4$ ) pour les oxydes à base de Ni ou Co, tandis que les phases CuO et  $\alpha$ - $Al_2O_3$  ont été identifiées dans les oxydes à base de Cu. Ce résultat suggère que les oxydes métalliques NiO ou CoO interagissent avec la phase  $\gamma$ -alumine pour former les phases aluminates. Il n'y a eu aucun changement dans la composition des phases et aucun pic d'oxydes de Co ou Ni n'a été observé en faisant varier le rapport RV/OV, ce qui suggère que le ratio RV/OV n'a aucun effet sur l'inhibition de la formation de spinelle. En revanche, le rapport RV/OV semble affecter le degré de cristallinité des phases obtenues. En effet, dans la plupart des cas, les conditions pauvres en carburant et riches en carburant entraînent une diminution des intensités du signal XRD, tandis que les échantillons de catalyseur obtenus à partir des compositions stœchiométriques (RV/OV= 1.0) ont présentés la cristallinité optimale. Cela peut être interprété par la réaction incomplète entre l'urée et les nitrates métalliques, qui a conduit à des matériaux amorphes ou mal cristallisés. Ainsi, un ratio RV/OV=1 est souhaitable pour avoir une meilleure cristallinité des produits finaux.

Les caractérisations texturales ont révélé que la surface spécifique obtenue est pratiquement faible pour la plupart des oxydes binaires synthétisés. Cela peut être associé à la température de flamme élevée atteinte pendant le processus de combustion, qui conduit à un frittage des particules et par conséquent à des faibles surfaces. De plus, les propriétés texturales des différents échantillons se sont révélées sensibles à la stœchiométrie. Cela pourrait être lié au processus de combustion différenciée des différents mélanges urée-nitrates (mélanges pauvres ou riches en carburant), qui affecte la température de flamme et le volume des gaz générés.

Les caractérisations par MEB des oxydes à base de Ni ou Co ont montrés des agglomérats à morphologie mousseuse (cas des oxydes à base de Co) et plaquettaire, présentant des surfaces lisses. La morphologie mousseuse observée pourrait être due à l'évolution des fortes quantités de gaz pendant le processus de combustion. Les propriétés microstructurales des oxydes à base de Ni ou Co ont été insensibles à la stœchiométrie. Les oxydes à base de Cu ont présenté des microstructures similaires à celle obtenus avec Ni et Co mais, avec présence des nanoparticules quasi-sphériques en surface. La taille et la distribution de ces nanoparticules ont été affectées par le rapport RV/OV.

Selon l'analyse par XPS, et quelque soit le ratio RV/OV, les oxydes de Ni ou Co étaient présents à la surface des oxydes à base de Ni ou Co sous forme des «spinelles de surface» d'aluminates métalliques ( $MAl_2O_4$ ), tandis que l'oxyde CuO était la principale espèce présente à la surface des oxydes à base de Cu. Ces résultats indiquent que l'alumine  $\gamma$  pourrait donner à des interactions plus fortes avec les oxydes de métaux de transition que l'alumine  $\alpha$ . L'analyse par XPS a fourni également des informations précieuses concernant la composition de la surface de ces oxydes binaires. Des rapports atomiques M/Al faibles ont été obtenus pour les oxydes à base de Ni ou Co, suggérant une diffusion de l'oxyde du métal de transition dans la structure d'alumine, aboutissant ainsi à une baisse du ratio M/Al. Le rapport M/Al de surface devrait affecter considérablement, par la suite, l'activité catalytique de ces oxydes binaires. D'après l'étude par XPS, il a été constaté que la stœchiométrie n'affecte pas la nature des espèces présentes à la surface mais affecte la composition chimique superficielle.

Les caractérisations TEM, effectuée uniquement pour les échantillons obtenus avec un ratio RV/OV=1, ont confirmé la présence des cristallites d'aluminates dans les oxydes à base de Ni et Co. L'existence des nanoparticules de CuO, non incorporées, dans l'oxyde à base de Cu a été également confirmée. À la lumière des données obtenues par l'étude de l'influence de la stœchiométrie, il a été conclu que la stœchiométrie jouait un rôle essentiel dans le contrôle des propriétés physico-chimiques des oxydes binaires, ainsi que les meilleures propriétés étaient atteintes pour les oxydes synthétisés avec un ratio RV/OV= 1.

En ce qui concerne les résultants de l'étude de l'influence de la teneur en métal de transition:

Les caractérisations XRD des oxydes à base de Ni ou Co ont montré que l'augmentation de la teneur en Ni ou Co conduit à la formation d'aluminates. La formation des oxydes de cobalt a été obtenue sous le seuil de 15 % en masse, en revanche aucune cristallite de NiO n'ait été détectée même à une teneur de 20 % en masse en Ni. Cela signifie que les interactions solide-

solide entre les oxydes de cobalt ou nickel et l'alumine se produisent différemment, dans ces oxydes binaires, et en fonction de la teneur en métal de transition. A l'apposé des oxydes à base de Ni ou Co, la teneur en Cu n'a pas affecté l'évolution des phases cristallines dans ces oxydes, et quelque soit la teneur en Cu, seuls les phases CuO et  $\alpha$ -Al<sub>2</sub>O<sub>3</sub> ont été identifiées.

L'analyse BET a montré une augmentation de la surface spécifique en faisant varier la teneur en métal de 5 à 15 % en masse. Puis elle a diminué sous le seuil de 15 % en masse pour les oxydes à base de nickel et cuivre. En revanche, aucune constatation significative n'a été établie quant à l'effet du teneur en métal sur l'évolution du volume poreux et du diamètre moyen des pores pour ces oxydes binaires.

Les résultats MEB ont montré que la charge métallique n'a pas d'effet significatif sur les caractéristiques morphologiques des oxydes à base de Ni ou Co. Cependant, l'augmentation de la teneur en Cu, pour les oxydes à base de Cu, a conduit à la croissance et l'agglomération des particules d'oxyde de cuivre.

Finalement, en ce qui concerne les résultants de l'étude de l'effet de synergie:

L'étude des propriétés des oxydes ternaires a montré que ces matériaux ont présentés globalement des caractéristiques structurales, texturales et morphologiques similaires à celles des oxydes binaires. Ces oxydes ternaires combinent les différentes propriétés de chacun des oxydes binaires. Outre, l'introduction du Cu dans les systèmes de combustion Ni-Al ou Co-Al n'inhibe pas la formation des phases spinelles.

## CHAPTER 4. CATALYST ACTIVITY EVALUATION

---

## Table of contents

Introduction .....	137
4.1 Catalysts efficiency: Catalytic oxidation of CO over binary oxide catalysts .....	137
4.1.1 Effect of RV/OV ratio on the catalytic performance .....	137
4.1.1.1 Effect of RV/OV ratio on CO oxidation activity over 10MAI-x calcined catalysts	137
4.1.1.1.1 Nickel-based catalysts .....	137
4.1.1.1.2 Cobalt-based catalysts .....	139
4.1.1.1.3 Copper-based catalysts .....	140
4.1.1.1.4 Comparison study of the different 10MAI-x calcined catalysts .....	141
4.1.1.2 Effect of RV/OV ratio on CO oxidation activity over 2MAI-x calcined catalysts	145
4.1.1.2.1 Nickel-based catalysts .....	145
4.1.1.2.2 Cobalt-based catalysts .....	146
4.1.1.2.3 Copper-based catalysts .....	147
4.1.2 Effect of metal loading on the catalytic performance .....	148
4.1.2.1 Nickel-based catalysts .....	148
4.1.2.2 Cobalt-based catalysts .....	149
4.1.2.3 Copper-based catalysts .....	151
4.2 Catalysts efficiency: Catalytic oxidation of CO over ternary oxides catalysts .....	155
4.3 Comparison with the literature .....	159
Conclusions .....	160
Résumé en Français du chapitre 4 .....	162

## Introduction

The present chapter focuses on the study of the catalytic properties of alumina-based mixed oxide materials. The influence of the RV/OV ratio and metal content on catalytic performance is discussed and explained, and optimal values of these parameters are determined. The influence of other factors on the CO oxidation activity such as the nature of active phase and solid-solid interaction between the metal oxide and alumina is also considered. Ultimately, this chapter provides insight on the impact of the bulk and surface properties of alumina-based mixed oxide catalysts on the catalytic activity in CO oxidation.

### 4.1 Catalysts efficiency: Catalytic oxidation of CO over binary oxide catalysts

This section examines the influence of RV/OV ratio and metal content on the intrinsic catalytic activity of binary oxide catalysts with the aim of achieving a deep understanding of the correlation between the structural, morphological and surface properties of the catalysts and their catalytic activity for CO oxidation. In this reaction, carbon dioxide is the sole product and the conversion of CO is defined as the percentage of CO to be converted into CO<sub>2</sub>. This investigation was conducted, under completely similar conditions, on two series of the binary oxide catalysts, in which the metal loading was maintained at two values; 10 and 2 wt%.

#### 4.1.1 Effect of RV/OV ratio on the catalytic performance

##### 4.1.1.1 Effect of RV/OV ratio on CO oxidation activity over 10NiAl–x calcined catalysts

###### 4.1.1.1.1 Nickel-based catalysts

The conversion of CO on nickel-based catalysts, with different RV/OV ratios and a constant nickel loading of 10 wt%, as a function of the reaction temperature (up to 500 °C), is presented in **Figure 4.1 (a)**. A comparison of the light-off temperatures for 10NiAl catalysts is reported in **Table 4.1**. T<sub>1</sub>, T<sub>50</sub> and T<sub>100</sub> respectively represent the characteristic temperatures for the start-up of the oxidation, the half, and the full conversion of CO into CO<sub>2</sub>.

The oxidation of CO over the 10NiAl–0.9, 10NiAl–1.0 and 10NiAl–1.1 catalysts began at 270, 254, and 301 °C respectively. The CO conversion overall 10NiAl–x catalysts gradually

increased with the increasing temperature, without reaching total conversion of CO at 500 °C. The maximum CO conversion achieved at 500 °C over the 10NiAl-0.9, 10NiAl-1.0 and 10NiAl-1.1 catalysts was of 29 %, 44 % and 19 %, respectively. Comparing the CO oxidation activity of 10NiAl- $x$  catalysts, the best activity was obtained for 10NiAl-1.0 catalyst, and the worst for 10NiAl-1.1. Thus, enhancement of RV/OV ratio has no beneficial effect on the catalytic performance of the nickel-based catalysts.

To further check the influence of the reaction temperature on the CO conversion, the activity of the catalysts was measured at steady state for three different reaction temperatures, during 30 min on-stream, in the 300–500 °C range, as shown in **Figure 4.1 (b)**. The 10NiAl- $x$  catalyst exhibited a very low CO conversion (less than 5 %) at 300 °C. Then, the reaction ran-out to reach a CO conversion of 7 %, 9 % and 5 % at 400 °C, for the 10NiAl-0.9, 10NiAl-1.0 and 10NiAl-1.1 catalyst, respectively. It can be deduced that the 10NiAl- $x$  catalysts had relatively low activity over the range of 300 to 500 °C, and increasing the temperature led to enhancement of the CO conversion for all samples.

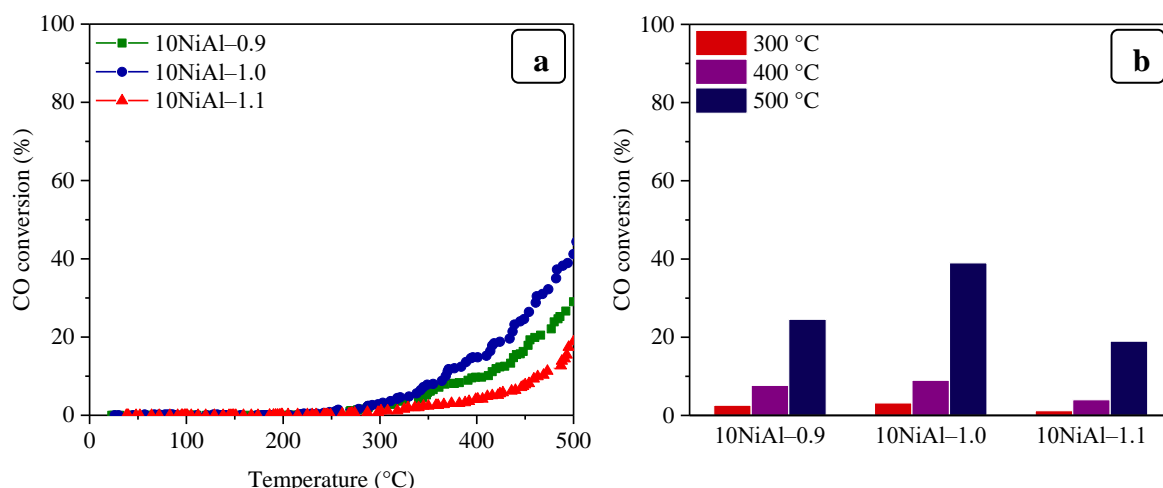


**Figure 4. 1.** (a) CO conversion under transient and (b) steady state conditions over the 10NiAl- $x$  calcined catalysts.

**Table 4. 1.** Effect of RV/OV ratio on the light-off temperatures of 10NiAl- $x$  catalyst samples.

Sample identity	T <sub>1</sub>	T <sub>50</sub>	T <sub>100</sub>
10NiAl-0.9	270	—	—
10NiAl-1.0	254	—	—
10NiAl-1.1	301	—	—

#### 4.1.1.1.2 Cobalt-based catalysts

The catalytic performances of 10CoAl- $x$  calcined catalysts were investigated in the same manner as the nickel-based catalysts. The results are depicted in **Figure 4.2**. The light-off and  $T_{50}$  temperatures of 10CoAl- $x$  calcined catalysts are presented in **Table 4.2**.

The catalytic activity of the 10CoAl-0.9 and 10CoAl-1.0 catalysts for CO oxidation seemed to be superior as compared to 10CoAl-1.1 catalyst; the oxidation of CO over the 10CoAl-0.9 and 10CoAl-1.0 catalysts started at 209 °C and 235 °C respectively, while with the 10CoAl-1.1 catalyst, the CO conversion started at 246 °C. The CO conversion over the 10CoAl-0.9 and 10CoAl-1.0 catalysts gradually increased with temperature and reached 50 % at around 400 °C, while with the 10CoAl-1.1 catalyst this conversion was not achieved at 400 °C. The maximum CO conversion obtained at 500 °C over the 10CoAl-0.9 and 10CoAl-1.0 catalysts was of 90 %. However, the 10CoAl-1.1 catalyst showed the lowest final conversion (approximately 50 %). It is worth pointing out that, similarly to nickel based catalysts, at RV/OV ratio higher than 1 the catalytic activity of cobalt based catalysts for the oxidation of CO is disadvantaged.

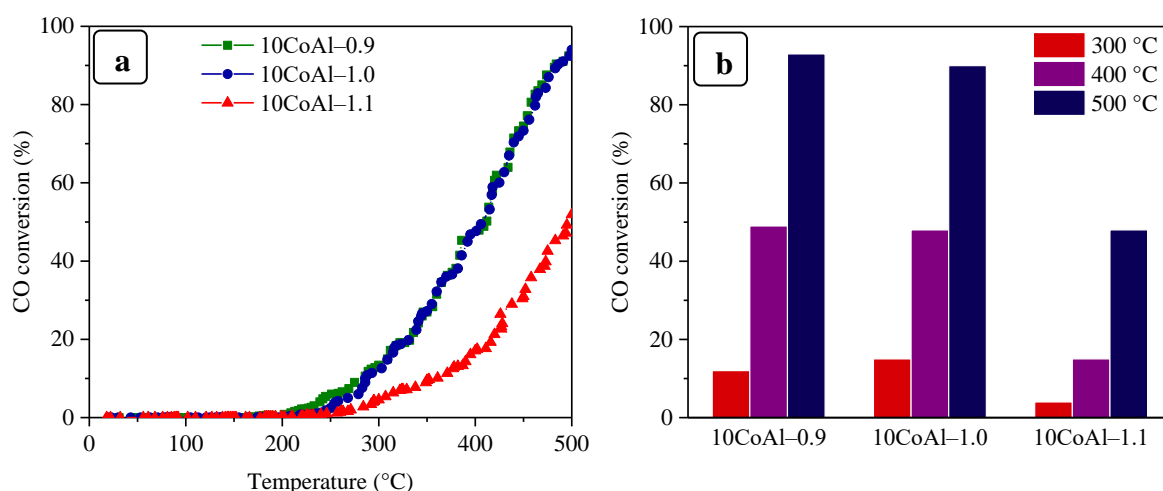


**Figure 4. 2.** (a) CO conversion under transient and (b) steady state conditions over the 10CoAl- $x$  calcined catalysts.

**Table 4. 2.** Effect of RV/OV ratio on the light-off and  $T_{50}$  temperatures of 10CoAl- $x$  catalyst samples.

Sample identity	$T_1$	$T_{50}$	$T_{100}$
10CoAl-0.9	209	412	—
10CoAl-1.0	235	406	—
10CoAl-1.1	246	497	—

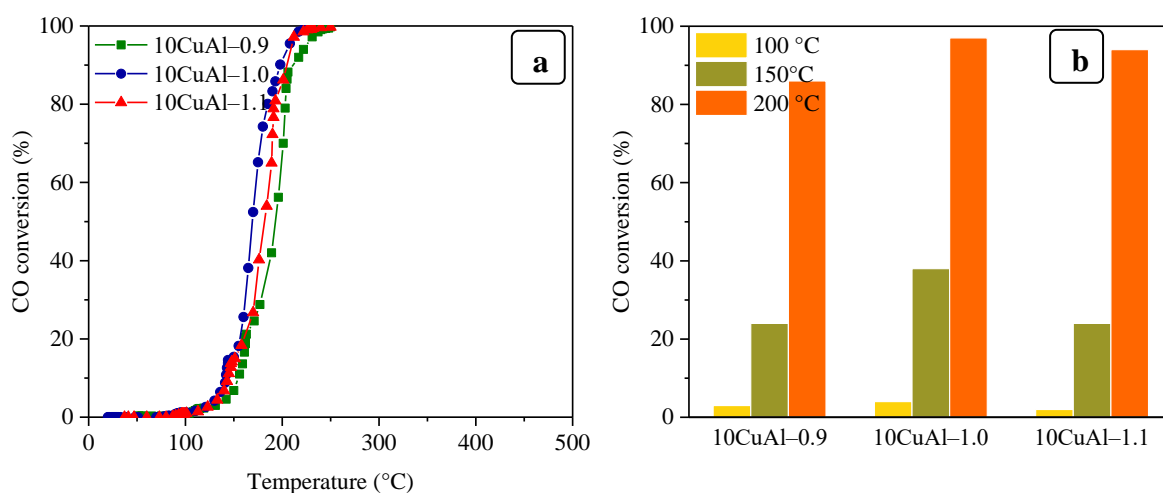
#### 4.1.1.1.3 Copper-based catalysts

The catalytic performances, the light-off,  $T_{50}$  and  $T_{100}$  temperatures for CO oxidation of the 10CuAl- $x$  calcined catalysts are shown in **Figure 4.3** and **Table 4.3**, respectively.

As it can be seen from **Figure 4.3 (a)**, the activity profiles of the 10CuAl- $x$  catalysts were characterized by a reduced conversion at low temperatures (typically less than 100 °C), followed by a sharp increase in a narrow range of temperature to end up with a gradual increase in conversion over the range of 190 to 250 °C. It was obvious that copper-based catalysts were fairly more active than cobalt and nickel-based catalysts for the oxidation of CO. As suggested in chapter 3, it is expected that both the highly dispersed CuO and bulk CuO species were responsible for the high CO oxidation activity.

A quick glance on **Figure 4.3 (b)** reveals that the 10CuAl-1.0 catalyst exhibited the highest CO conversion values (around 5 %, 40 % and 98 % at 100 °C, 150 °C and 200 °C, respectively). The 10CuAl-0.9 catalyst presented the lowest performances with a CO conversion of 25 % and 85 % at 150 °C and 200 °C, respectively.

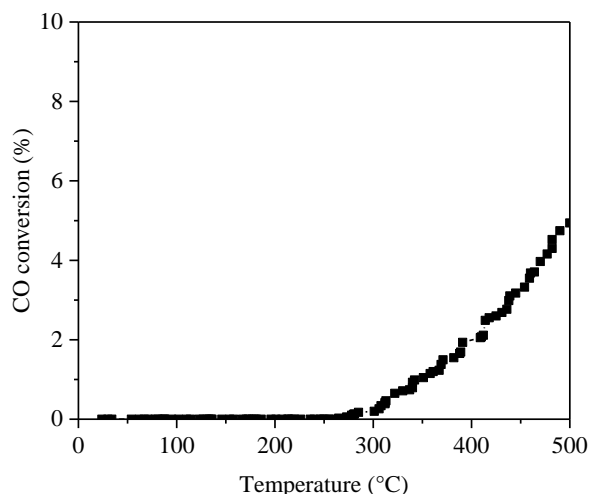
The activity of  $\text{Al}_2\text{O}_3$ , prepared by microwave-assisted solution combustion, was also examined in **Figure 4.4**. The CO conversion in the presence of alumina started at around 270 °C and reached only 5 % conversion at 500 °C. Hence, the addition of Ni, Co or Cu to alumina results in a considerable increase in catalytic activity.



**Figure 4. 3.** (a) CO conversion under transient and (b) steady state conditions over the 10CuAl- $x$  calcined catalysts.

**Table 4. 3.** *Effect of RV/OV ratio on the light-off,  $T_{50}$  and  $T_{100}$  temperatures of 10CuAl- $x$  catalyst samples.*

Sample identity	$T_1$	$T_{50}$	$T_{100}$
10CuAl-0.9	96	190	250
10CuAl-1.0	90	170	225
10CuAl-1.1	97	180	250

**Figure 4. 4.** *CO conversion over  $Al_2O_3$ .*

#### 4.1.1.1.4 Comparison study of the different 10MAI- $x$ calcined catalysts

The catalytic performances of the different 10MAI- $x$  calcined catalysts for CO oxidation were shown in **Figure 4.5**. The 10MAI- $x$  catalysts showed a clear difference in their oxidation activity for CO. Copper-based catalysts showed the highest CO oxidation activity at low temperature when compared to nickel and cobalt based catalysts. The order of activity of the different catalysts was the following: 10CuAl- $x$  > 10CoAl- $x$  > 10NiAl- $x$ . For the 10CuAl- $x$  catalysts, the CO conversion began at low temperature (around 90 °C) and rapidly increased with the temperature in the 100 to 250 °C range, reaching 100 % conversion. For the other two series, the conversion of CO started at higher temperatures (between 200 °C and 300 °C) and gradually increased with temperature, but never reaching the total conversion of CO. At a higher reaction temperature (500 °C), the series of 10CoAl- $x$  catalysts significantly outperformed the series of 10NiAl- $x$  catalysts.

The difference in catalytic activity is probably related to their different surface properties. The highest CO oxidation activity observed for 10CuAl- $x$  is due to the absence of “surface spinel” phase, which is known to be inactive for CO oxidation [98, 99]. In addition, the highest activity obtained with the catalysts containing copper is related to the important redox

properties of this metal which tends to completely oxidize during the reaction to form  $\text{Cu}^+$  and  $\text{Cu}^{2+}$  species at the surface, and consequently improves the performance of the catalyst.

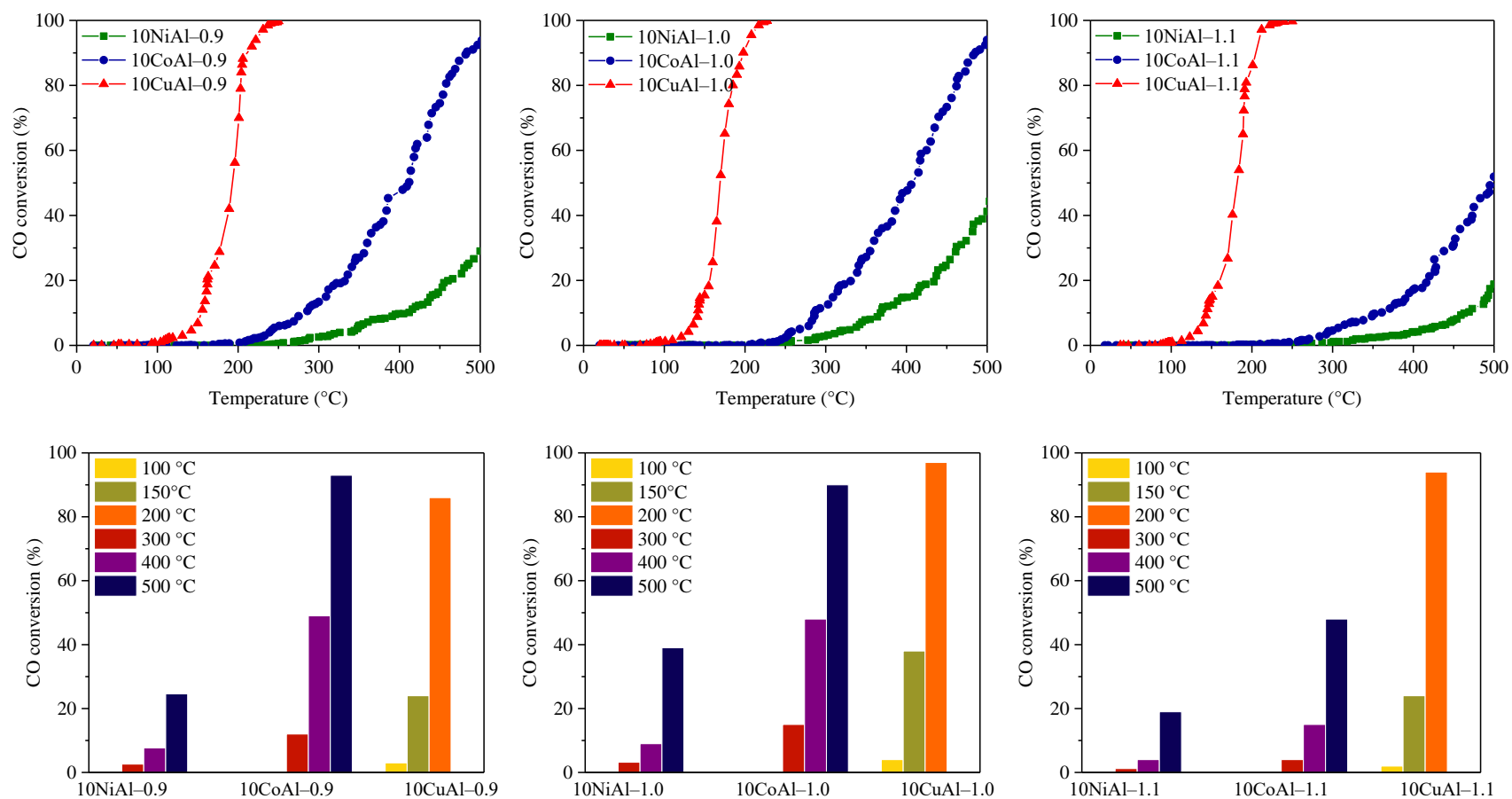


**Figure 4. 5.** Comparison of the catalytic performances of the different 10MAI- $x$  calcined catalysts for CO oxidation under transient and steady state conditions.

### Discussion

The following discussion on the effect of the reaction temperature and the RV/OV ratio on the CO oxidation activity of the 10MAl-x calcined catalysts is based on the previous mentioned results.

The results indicated that the catalytic activity was strongly affected by the temperature of reaction. As a general behavior, the activity profiles of the catalysts were characterized by a reduced conversion at low temperatures, followed by an increase in conversion at higher temperatures, hence an increase of the temperature greatly enhances the catalysts' activity. This is probably due to the influence of the surface redox reactions. At low temperature, CO can adsorb on the surface of the metal oxide and saturate all active sites, thus inhibiting the adsorption of molecular O<sub>2</sub>. By increasing the temperature (up to around 300 °C), CO starts to desorb from the surface of the catalysts, leaving free sites on which O<sub>2</sub> can adsorb. The conversion of CO can then take place. A further increase of the temperature induces a further CO desorption, thus resulting in an improved conversion of CO.

It is seen that, by increasing the RV/OV ratio from 0.9 to 1.1 for 10NiAl-x and 10CoAl-x catalyst samples, more aluminate spinel structures (**Chapter 3, pages 8–10**) and lower CO conversion are observed.

Among the different synthesized catalysts, the 10NiAl-x catalyst samples exhibited the largest surface areas and the worst performances for converting CO, whereas the 10CuAl-x catalyst samples had the smallest surface areas and the highest activities. In addition, it was found that stoichiometric compositions (RV/OV = 1.0) lead to an optimal crystallinity and that the catalytic activity is maximized for the catalysts prepared with the RV/OV ratio of 1.0. The present results suggest that CO oxidation reaction on these materials is structure sensitive and the alumina-metal interaction plays a crucial role in the CO oxidation activity. On the other hand, the maximum in M/Al atomic ratio, obtained with RV/OV ratio equal to 1, corresponds to the maximum in CO oxidation activity, as evidenced by the results of the catalytic tests. Although the origin of this linear correlation is not clear, it may be expected that the most abundant active sites, which might be formed on the surface of samples obtained with stoichiometric conditions, lead to more active catalysts.

The performances of the different catalysts were in accordance with their characterizations; indeed, the catalysts prepared with stoichiometric compositions were found to have the

optimal structural properties and the best catalytic activities. In contrast, use of a non-stoichiometric RV/OV ratio resulted in a non-controlled combustion reaction (for the synthesis process of the catalysts), thus leading to poor structural properties and weak CO oxidation activities.

#### 4.1.1.2 Effect of RV/OV ratio on CO oxidation activity over 2MAI- $x$ calcined catalysts

##### 4.1.1.2.1 Nickel-based catalysts

**Figure 4.6** depicts the catalytic performances of 2NiAl- $x$  calcined catalysts. This evaluation was carried out from ambient-temperature up to 500 °C, under the same reaction conditions as 10MAI- $x$  calcined catalysts. The light-off temperatures for 2NiAl- $x$  calcined catalysts are reported in **Table 4.4**.

It is shown from the light-off curves that 2NiAl- $x$  catalysts have almost similar catalytic performances independently of RV/OV ratio; the oxidation of CO over the various catalysts started at around 300 °C then slightly increased with the temperature and achieved a maximum CO conversion of approximately 10 % at 500 °C. Moreover, it was found that 2NiAl- $x$  catalysts have comparable activities at different reaction temperatures, with a CO conversion of approximately 2 %, 5 % and 10 % at 300 °C, 400 °C and 500 °C, respectively.

It is clear that 2NiAl- $x$  catalysts presented a lower activity than the 10NiAl- $x$  catalysts. It is expected that changing the nickel content resulted in a variation in the catalysts' activity. The effect of metal loading on the catalytic performance will be further studied in the next section.

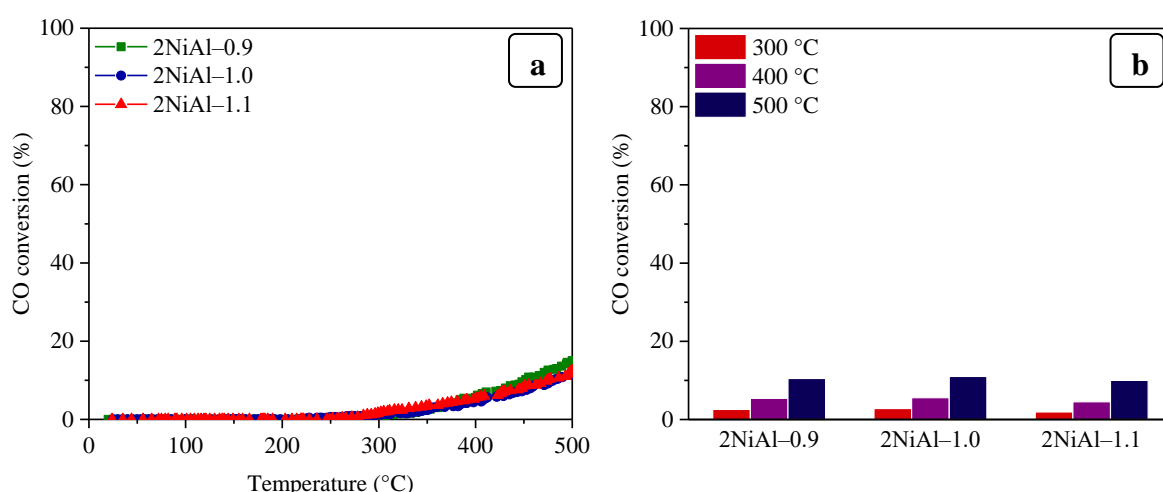


**Figure 4. 6.** (a) CO conversion under transient and (b) steady state conditions over the 2NiAl- $x$  calcined catalysts.

**Table 4. 4.** *Effect of RV/OV ratio on the light-off temperatures of 2NiAl-x catalyst samples.*

Sample identity	T <sub>1</sub>	T <sub>50</sub>	T <sub>100</sub>
2NiAl-0.9	306	—	—
2NiAl-1.0	291	—	—
2NiAl-1.1	284	—	—

#### 4.1.1.2.2 Cobalt-based catalysts

**Figure 4.7** shows the catalytic performance of 2CoAl-x calcined catalysts prepared with different RV/OV ratios for CO oxidation. The light-off and T<sub>50</sub> temperatures of 2CoAl-x calcined catalysts are listed in **Table 4.5**.

As seen from **Figure 4.7 (a)**, the CO conversion activity over the 2CoAl-x calcined catalysts depends on the reaction temperature. For the 2CoAl-0.9 and 2CoAl-1.0 catalysts, the increase of temperature, in the region 100–400 °C, is accompanied by a continuous increase of the CO oxidation. As the reaction temperature increases, from 400 to 500 °C, the conversion of CO over the 2CoAl-0.9 and 2CoAl-1.0 catalysts remained practically constant at 80 % and 70 %, respectively. Contrary to these two samples, the increase of the CO conversion with the reaction temperature over the 2CoAl-1.1 catalyst was not so pronounced in the temperature range 200–500 °C and the maximum CO conversion achieved was approximately 40 % at 500 °C.

According to **Figure 4.7 (b)**, the CO oxidation activity of the 2CoAl-0.9 catalyst appear to be superior as compared to 2CoAl-1.0 and 2CoAl-1.1 catalysts and achieved the highest CO conversion in the 300–500 °C temperature range. The increase of the RV/OV ratio to 1.1 resulted in a catalyst, which exhibited lower activity despite its higher surface area. This result can be attributed to the solid-solid interaction effect between alumina and cobalt species, which is enhanced with increasing the RV/OV ratio.

It is worth noting that the CO oxidation activity over the 2CoAl-x catalysts was lower than most of the 10CoAl-x catalysts displayed in previous section. Indeed, 10CoAl-x catalysts were almost two times more active than the catalyst prepared with 2 wt% cobalt content.

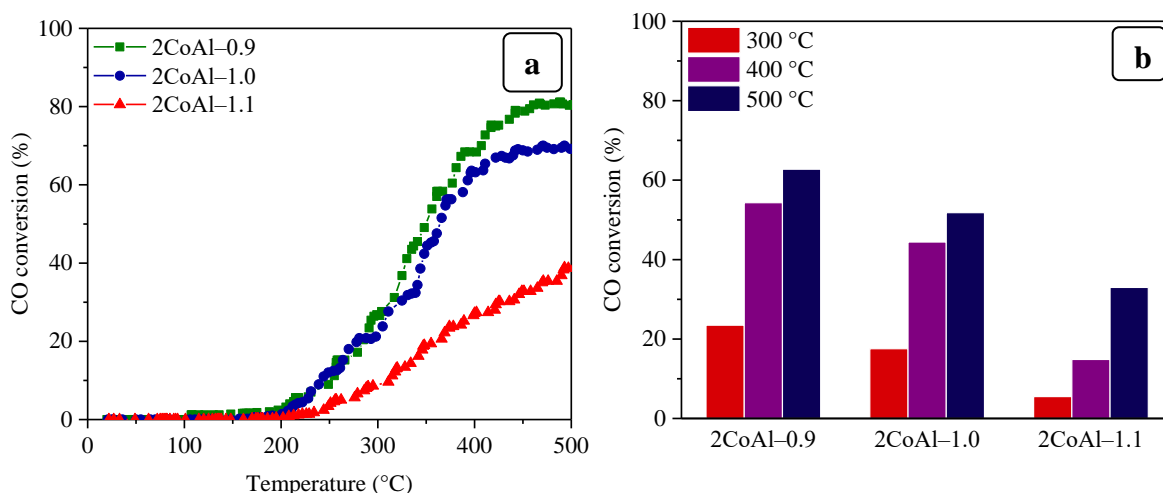


**Figure 4. 7.** (a) CO conversion under transient and (b) steady state conditions over the 2CoAl- $x$  calcined catalysts.

**Table 4. 5.** Effect of RV/OV ratio on the light-off and  $T_{50}$  temperatures of 2CoAl- $x$  catalyst samples.

Sample identity	$T_1$	$T_{50}$	$T_{100}$
2CoAl-0.9	190	356	—
2CoAl-1.0	191	366	—
2CoAl-1.1	213	—	—

#### 4.1.1.2.3 Copper-based catalysts

The CO conversion as a function of temperature over 2CuAl- $x$  calcined catalysts is depicted in **Figure 4.8 (a)**. To further check the influence of the reaction temperature on the CO conversion, the catalytic oxidation of CO on 2CuAl- $x$  catalysts was measured at six reaction temperatures, varied between 150 and 400 °C, during 30 min on-stream, as shown in **Figure 4.8 (b)**. The light-off,  $T_{50}$  and  $T_{100}$  temperatures of 2CuAl- $x$  calcined catalysts are presented in **Table 4.6**.

Among the three tested catalysts, the 2CuAl-1.0 was the most active while the 2CuAl-1.1 was the less active. The conversion of CO over the 2CuAl-0.9, 2CuAl-1.0 and 2CuAl-1.1 catalysts started at 170, 122, and 165 °C respectively, then increased rapidly and the temperature at which 50 % conversion of CO is obtained, was found equal to 240, 206, and 280 °C for the 2CuAl-0.9, 2CuAl-1.0 and 2CuAl-1.1 catalysts, respectively. The maximum CO conversion achieved over the 2CuAl-1.0 sample was 99 % at 300 °C. The temperature at which a similar CO conversion was obtained with the 2CuAl-0.9 and 2CuAl-1.1 catalysts was 400 °C. The best CO oxidation activity obtained with the 2CuAl-1.0 sample is probably because of the highest dispersion of CuO particles and smallest particle size, as well as the optimized crystallinity, as described in the XRD and MEB analyses.

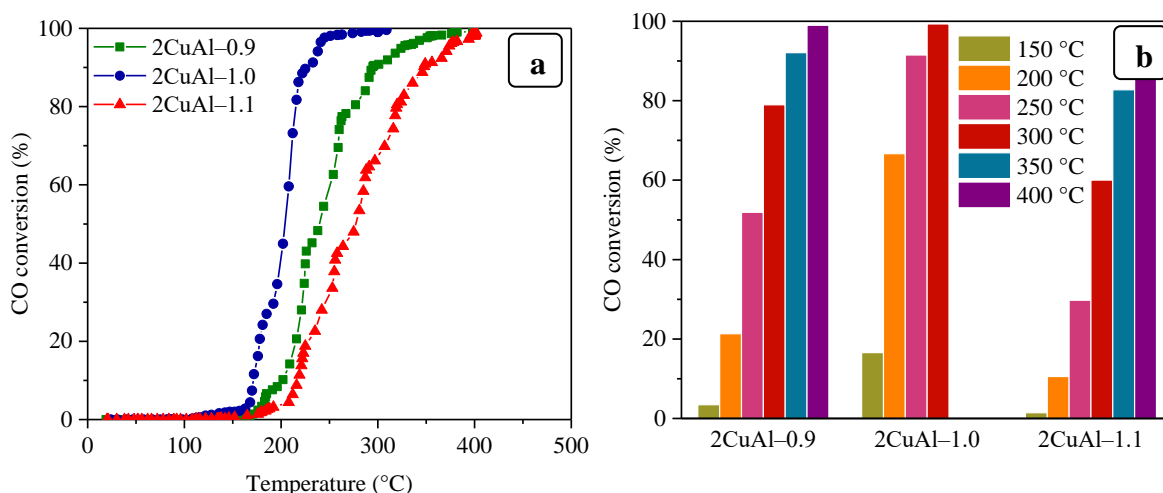


**Figure 4. 8.** (a) CO conversion under transient and (b) steady state conditions over the 2CuAl- $x$  calcined catalysts.

**Table 4. 6.** Effect of RV/OV ratio on the light-off,  $T_{50}$  and  $T_{100}$  temperatures of 2CuAl- $x$  catalyst samples.

Sample identity	$T_1$	$T_{50}$	$T_{100}$
2CuAl-0.9	170	240	381
2CuAl-1.0	122	206	251
2CuAl-1.1	165	280	396

#### 4.1.2 Effect of metal loading on the catalytic performance

##### 4.1.2.1 Nickel-based catalysts

The catalytic performances of XNiAl calcined catalysts with Ni content varying from 5 to 20 wt % for the total oxidation of CO are shown in **Figure 4.9**. **Table 4.7** lists the light-off temperatures of nickel-based catalysts.

**Figure 4.9 (a)** reveals that the light-off curve of XNiAl catalysts shifted to lower temperatures with increasing the nickel content in the catalyst from 5 to 20 wt %. Moreover, the 20NiAl catalyst appeared to be the most active at low temperature.

When Ni content was less than 10 wt %, the CO conversion started in the temperature range of 300–340 °C then gradually increased with the increasing temperature. The maximum CO conversion achieved at 500 °C over the 5NiAl and 10NiAl catalysts was of 15 % and 19 %, respectively.

Contrarily to what occurred with the 5NiAl and 10NiAl catalysts, the CO oxidation activity of the 15NiAl and 20NiAl catalysts was much higher for the entire range of temperature; the CO conversion begun at 249 and 227 °C over the 15NiAl and 20NiAl catalysts then increased to

50 % at 377 and 361 °C, respectively, and attained full CO conversion at 500 °C. These results indicated that nickel enrichment of the catalyst contributed to the activity increase.

**Figure 4.9 (b)** shows the effect of reaction temperature on CO conversion over the XNiAl calcined catalysts. It can be observed that increasing the temperature led to enhancement of the CO conversion for all samples. The 5NiAl and 10NiAl catalysts had comparable activities, with a CO conversion of approximately 2 %, 5 % and 18 % at 300, 400 and 500 °C, respectively. Whereas, the 15NiAl and 20NiAl catalysts had significantly higher activity than the 5NiAl and 10NiAl catalysts and the CO conversion at 500 °C was 5 times higher than that of 5NiAl and 10NiAl catalysts.

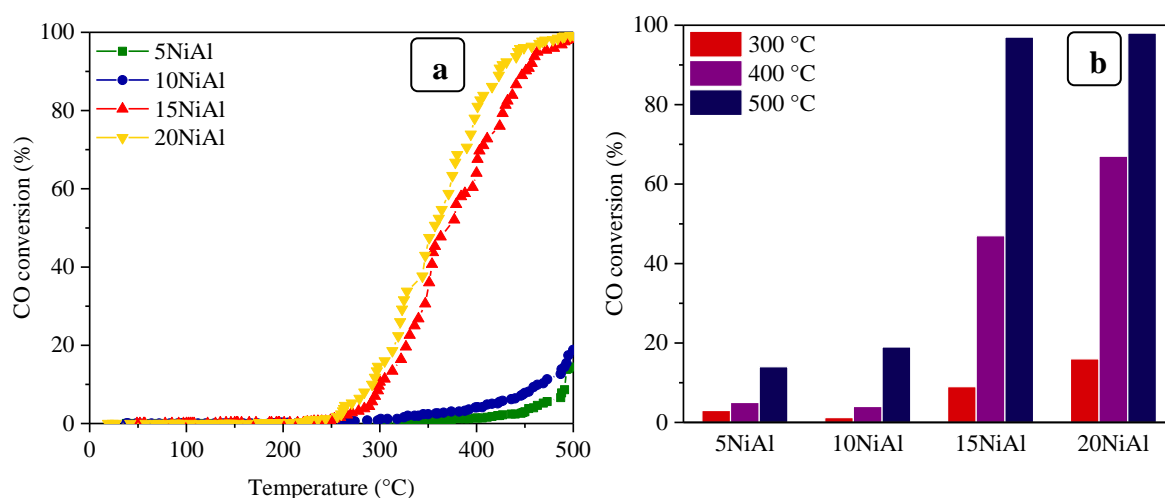


**Figure 4. 9.** (a) CO conversion under transient and (b) steady state conditions over the XNiAl calcined catalysts.

**Table 4. 7.** Effect of metal loading on the light-off,  $T_{50}$  and  $T_{100}$  temperatures of XNiAl calcined catalysts.

Sample identity	$T_1$	$T_{50}$	$T_{100}$
5NiAl	340	—	—
10NiAl	301	—	—
15NiAl	249	377	500
20NiAl	227	361	500

#### 4.1.2.2 Cobalt-based catalysts

The CO conversions according to temperature as well as the light-off temperatures of CO oxidation for the XCoAl calcined catalysts are presented in **Figure 4.10** and **Table 4.8**. It is clear that XCoAl catalysts had a catalytic activity much greater than those of the XNiAl catalysts and a high activity at 500 °C.

The experimental data showed that the CO oxidation activity reduced with increasing the cobalt content up to 10 wt %, and the activity of 10CoAl catalyst is the lowest. Moreover, the light-off reaction temperature (T<sub>1</sub>) increased from 192 °C to 246 °C with increasing the cobalt content from 5 to 10 wt %. In contrast, a converse effect of the metal loading on the catalytic activity was found when the metal content exceeded 10 wt %. Indeed, with further increasing the cobalt content from 10 to 20 wt % the catalytic activity increased and the light-off temperature of the 20NiAl catalyst was lower than that of the 15CoAl sample. Full conversion of CO was observed only over the 20NiAl catalyst, which occurred at around 400 °C. In summary, the order of activity of the different catalysts was the follow: 20CoAl > 15CoAl > 5CoAl > 10CoAl.

In order to clearly understand the effect of cobalt loading, on CO oxidation activity, over cobalt based catalysts, additional test was conducted on Co-containing sample with a metal loading of 1 wt %, as shown in **Figure 4.10**. The results revealed that the 1CoAl catalyst significantly outperformed the 5CoAl and 10CoAl catalysts in the 300–450 °C temperature range. But, at a higher reaction temperature (between 450 and 500 °C), the light-off curves of 1CoAl catalyst converged towards the same CO conversions values as that of 5CoAl catalyst.

The experimental results presented thus far clearly indicate that the cobalt loadings had a negative effect on the catalytic activity when its enrichment level is bellow 10 wt %. Nevertheless, the catalytic activity of cobalt based catalysts enhances with increasing the cobalt loading when the Co loading exceeds 10 wt %.

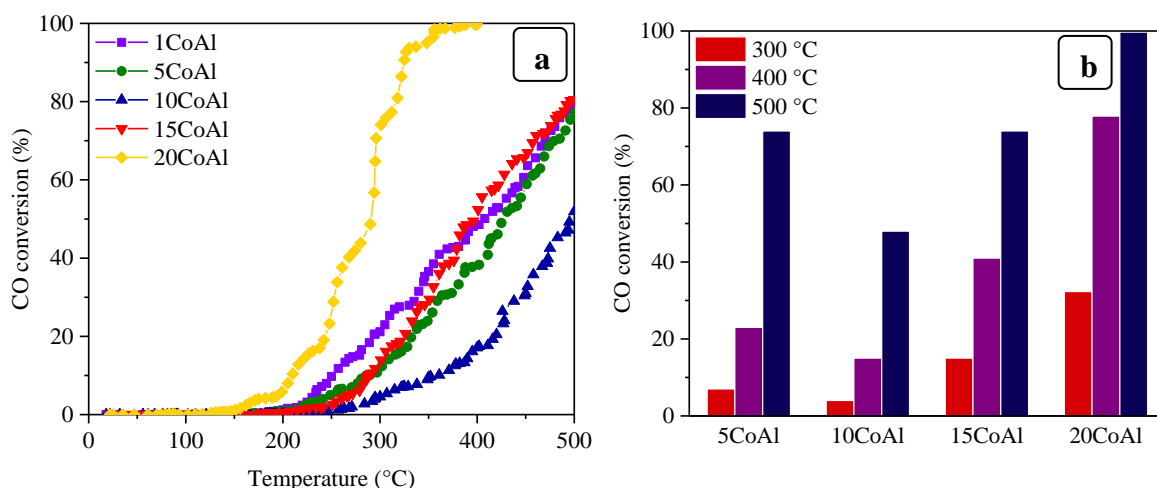


**Figure 4. 10.** (a) CO conversion under transient and (b) steady state over the XCoAl calcined catalysts.

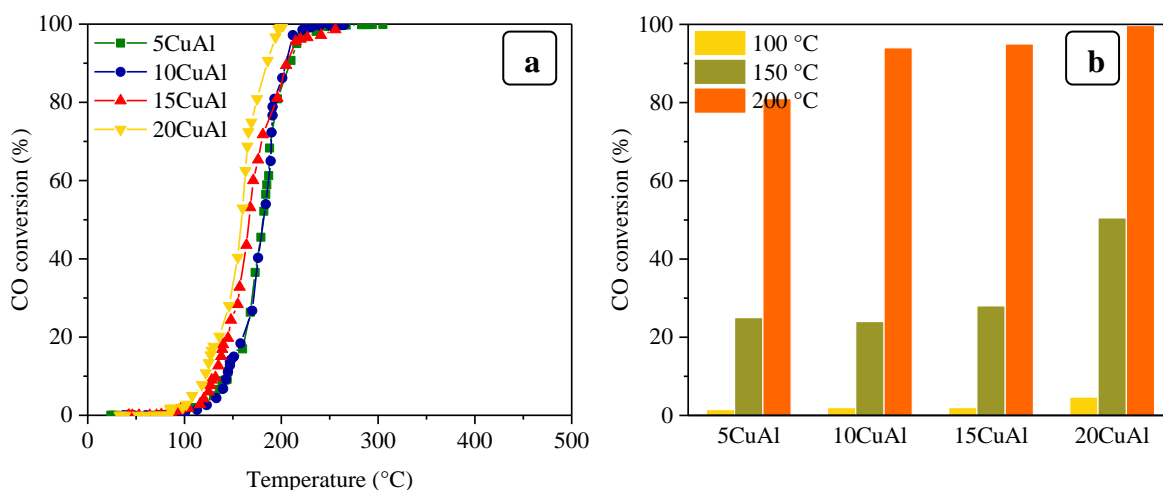
**Table 4. 8.** *Effect of metal loading on the light-off,  $T_{50}$  and  $T_{100}$  temperatures of XCoAl calcined catalysts.*

Catalyst identity	$T_1$	$T_{50}$	$T_{100}$
1CoAl	190	408	—
5CoAl	192	431	—
10CoAl	246	497	—
15CoAl	208	396	—
20CoAl	151	294	356

#### 4.1.2.3 Copper-based catalysts

The effect of metal loading on the CO oxidation activity and light-off temperatures of copper-based catalysts is shown in **Figure 4.11** and **Table 4.9**.

As shown in **Figure 4.11**, the light-off curves of the 5CuAl and 10CuAl catalysts virtually overlapped. As the copper loading exceeds 10 wt %, the light-off curves were slightly shifted to lower temperatures by about 10 °C. The light-off temperatures ( $T_1$ ) on all the catalysts were typically around 90 °C. The temperature at which 50 % conversion of CO is obtained was 180, 180, 168 and 160 °C for the 5CuAl, 10CuAl, 15CuAl and 20CuAl catalyst, respectively. Complete conversion of CO was achieved at 267 °C with 5CuAl catalyst, around 250 °C with 10CuAl and 15CuAl catalysts and 202 °C for 20CuAl catalyst. It seems that the copper content had negligible effect on the CO oxidation activity and only a small amount of copper (5 wt %) is needed to obtain a high CO oxidation activity.

**Figure 4. 11.** (a) *CO conversion under transient and (b) steady state conditions over the XCoAl calcined catalysts.*

**Table 4. 9.** *Effect of metal loading on the light-off,  $T_{50}$  and  $T_{100}$  temperatures of XCuAl calcined catalysts.*

Sample identity	$T_1$	$T_{50}$	$T_{100}$
5CuAl	98	180	267
10CuAl	97	180	250
15CuAl	86	168	256
20CuAl	85	160	202

### **Discussion**

An assessment of the characterization and the CO oxidation activity results of the synthesized XMAI catalysts is provided in **Table 4.10**. It is clear that the higher amount of metal content, the more active is the catalyst. Further, one can observe that a catalyst is more active if its crystallization degree is higher. This factor together with the existence of crystalline metal oxide phases, qualitatively explains the trends observed in **Table 4.10**.

Moreover, higher surface area and superior metal dispersion are not sufficient to achieve an active CO oxidation catalyst; the enhanced activity of the nickel and cobalt based catalyst resulted mainly from the interaction of nickel/cobalt oxides and alumina.

It is generally known that the catalytic activity enhances with the increasing metal loading in the catalyst, since the interaction of gaseous molecules with the oxide surfaces enhanced with a greater amount of the metal oxide active phase. On the basis of the considered results, it was confirmed that CO oxidation activity increases with increasing metal loading.

The variation trend of the catalytic activity with increasing metal loading can be understood by considering the evolution trend of the catalysts' properties; for nickel and cobalt-based catalysts, the extent of the interaction between the nickel/cobalt species and the alumina seemed to have a pronounced effect on catalyst activity. Based on characterization results, the low metal concentrations led to the formation of amorphous surface aluminates bearing some resemblance to bulk aluminates. However, the unstable Ni/Co active species, which have medium interaction with alumina, did not seem to exhibit good performances in CO oxidation. By increasing metal concentrations, the interaction between the metal oxides and alumina is enhanced and more well-crystallized bulk aluminates as well as well-dispersed "surface spinels" are formed. Metal oxides strongly interacting with alumina resulted in a higher CO oxidation activity. The higher metal loadings, specifically in cobalt-based catalysts, resulted in the formation of "bulk-like" metal oxide phases, which enhance the

catalysts' activity. Thus, the structure and phase evolution, with the increasing metal loading, seemed to be favorable for the catalytic process, leading to a higher CO oxidation activity.

In the case of copper-based catalyst, the catalytic activity was not strongly affected by the copper content and it was slightly enhanced with increasing the Cu loading from 10 to 20 wt %. Based on the characterization results, at low copper content, copper is presented as a well dispersed CuO on the alumina surface. Whereas, at high copper loading ( $> 10$  wt %), larger crystallite CuO particles were formed and a severe agglomeration of particles was observed. It is therefore proposed that the highly crystallized CuO has stronger effect on the catalytic activities than the dispersed CuO.

The observed trends in CO oxidation activity with variation of the metal content did not correlate with the surface area of the catalysts.

**Table 4. 10.** *Main data of the characterization and catalytic activity tests over XMAI calcined catalysts.*

Sample identity	Phase detected <sup>a</sup>	Degree of crystallinity <sup>a</sup>	Crystallite size <sup>a</sup> (nm)	BET surface area <sup>b</sup> (m <sup>2</sup> g <sup>-1</sup> )	Metal dispersion <sup>c</sup>	CO oxidation activity	
						T <sub>50</sub> <sup>d</sup> (°C)	T <sub>100</sub> <sup>e</sup> (°C)
5NiAl	$\gamma$ -Al <sub>2.67</sub> O <sub>4</sub> , $\alpha$ -Al <sub>2</sub> O <sub>3</sub> , $\delta$ -Al <sub>2</sub> O <sub>3</sub> , NiAl <sub>2</sub> O <sub>4</sub>	++ <sup>g</sup>	—	18.97	High	—	—
10NiAl	$\gamma$ -Al <sub>2.67</sub> O <sub>4</sub> , NiAl <sub>2</sub> O <sub>4</sub>	+	—	135.10	High	—	—
15NiAl	$\gamma$ -Al <sub>2.67</sub> O <sub>4</sub> , NiAl <sub>2</sub> O <sub>4</sub> + <sup>f</sup>	++	—	170.38	High	377	500
20NiAl	NiAl <sub>2</sub> O <sub>4</sub> ++	+++	—	124.04	High	361	500
5CoAl	$\gamma$ -Al <sub>2.67</sub> O <sub>4</sub> , CoAl <sub>2</sub> O <sub>4</sub> , $\alpha$ -Al <sub>2</sub> O <sub>3</sub> , Co <sub>3</sub> O <sub>4</sub>	++	—	10.53	High	431	—
10CoAl	$\gamma$ -Al <sub>2.67</sub> O <sub>4</sub> , CoAl <sub>2</sub> O <sub>4</sub>	+++	—	16.67	High	497	—
15CoAl	CoAl <sub>2</sub> O <sub>4</sub> , Co <sub>3</sub> O <sub>4</sub>	+	—	32.91	High	396	—
20CoAl	CoAl <sub>2</sub> O <sub>4</sub> , Co <sub>3</sub> O <sub>4</sub> +	++	—	90.88	High	294	356
5CuAl	$\alpha$ -Al <sub>2</sub> O <sub>3</sub> , CuO	+	15	5.84	High	180	267
10CuAl	$\alpha$ -Al <sub>2</sub> O <sub>3</sub> , CuO+	+	44	16.38	High	180	250
15CuAl	$\alpha$ -Al <sub>2</sub> O <sub>3</sub> , CuO++	++	46	23.46	Low	168	256
20CuAl	$\alpha$ -Al <sub>2</sub> O <sub>3</sub> , CuO+++	+++	51	10.33	Low	160	202

<sup>a</sup> XRD analyses.<sup>b</sup> N<sub>2</sub> adsorption-desorption isotherms.<sup>c</sup> SEM-EDX analyses.<sup>d</sup> Temperatures for the half conversion of CO into CO<sub>2</sub> (determined under transient conditions).<sup>e</sup> Temperatures for the full conversion of CO into CO<sub>2</sub> (determined under transient conditions).<sup>f</sup> Increasing phases' amounts.<sup>g</sup> Increasing crystallization behavior of the solids

## 4.2 Catalysts efficiency: Catalytic oxidation of CO over ternary oxides catalysts

The aim of the present section was to investigate the effect of the presence of a second metal oxide phase on the catalytic activity of alumina-based metal oxide catalysts and to achieve a systematic understanding of the factors that control the activity of ternary oxide catalysts. The catalytic performances of the 5M5MAI calcined catalysts with different metal compositions for CO oxidation were presented in **Figure 4.12**. To compare the activity of various samples, the light-off temperatures of 5M5MAI catalysts were determined and tabulated in **Table 4.11**.

The oxidation of CO over the 5Ni5CuAl and 5Co5CuAl catalysts began at 125 and 140 °C respectively. In contrast, 5Ni5CoAl catalyst started producing CO much later at 243 °C. The catalytic activity of the 5Ni5CuAl and 5Co5CuAl samples increased rapidly with rise of the temperature, in a similar manner to copper containing catalysts but remained lower than that of CuO/Al<sub>2</sub>O<sub>3</sub> catalyst studied previously, giving 50 % conversion at temperature approximately 208 and 268 °C, respectively, and a maximum conversion of 100 % at 400 °C. On the other hand, the activity of 5Ni5CoAl sample increased progressively, giving 50 % conversion at temperature approximately 500 °C; without reaching total conversion of CO. Among the three investigated catalysts, the 5Ni5CoAl catalyst sample seemed to be the least active for CO oxidation. The performance of 5Ni5CuAl catalyst was slightly greater than that of the 5Co5CuAl catalyst in the temperature range from 100 °C to 300 °C and almost similar conversion profile was obtained for both of them at temperature > 300 °C.

**Figure 4.12 (b)** compares the CO conversion for the three catalysts. As can be seen, CO oxidation activity for the 5Ni5CoAl catalyst is considerably weak at low and high temperature values, giving a CO conversion of approximately 20 % at 400 °C and a maximum value of 50 % at 500 °C. The 5Ni5CuAl catalyst showed better CO oxidation activity compared to 5Co5CuAl catalyst at 200 °C; the 5Ni5CuAl and 5Co5CuAl catalysts gave 41 % and 13 % of CO conversion respectively at 200 °C. The conversion value of CO from both 5Ni5CuAl and 5Co5CuAl catalysts are approximately the same at 300, 400 and 500 °C. The comparison of the CO oxidation activity of the ternary oxide catalysts proved that copper-based samples provided higher CO conversions and also, the best catalytic activity was found in the 5Ni5CuAl catalyst sample.

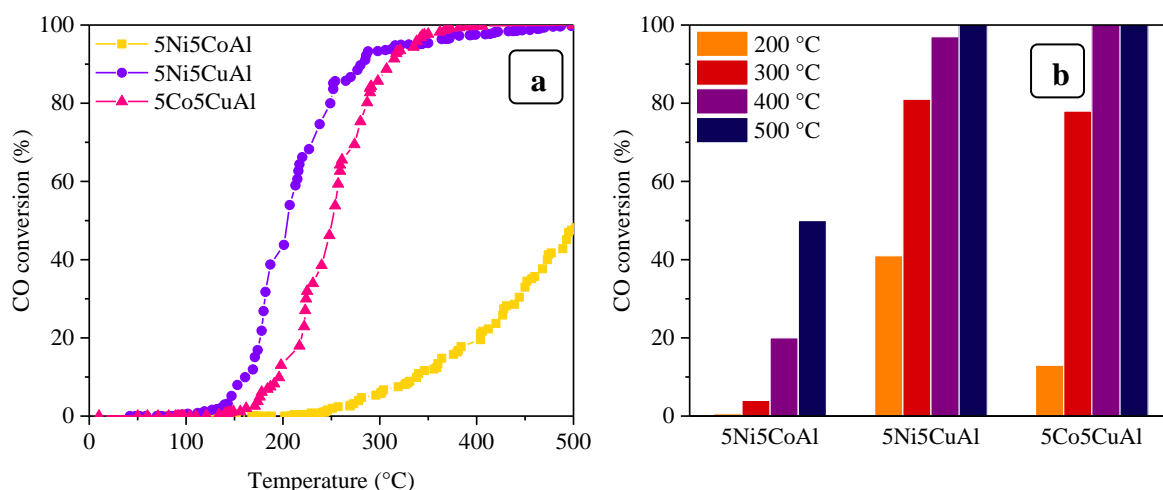


**Figure 4.12.** (a) CO conversion under transient and (b) steady state conditions over the 5M5MAI calcined catalysts.

**Table 4.11.** The light-off,  $T_{50}$  and  $T_{100}$  temperatures of 5M5MAI calcined catalysts.

Sample identity	$T_1$	$T_{50}$	$T_{100}$
5Ni5CoAl	243	500	—
5Ni5CuAl	125	208	475
5Co5CuAl	140	268	369

### Discussion

In the present investigation copper addition to nickel and cobalt-based catalysts has resulted in the enhancement of the catalytic activity for CO oxidation. It seemed that CuO acts as a catalyst promoter for nickel and cobalt containing catalysts; indeed the CuO promoted bimetallic catalysts showed 100 % CO conversion at a temperature close to 350 °C (see **Figure 4.12 (a)**). The observed increase in the catalytic activity of CuO containing catalysts could be attributed to the existence of bulk CuO over the catalysts' surface. However, the CuO-free catalyst sample (5Ni5CoAl) showed similar activity to 10CoAl–1.0 catalyst. The poor CO oxidation activity of 5Ni5CoAl sample could be attributed to the low concentration of nickel and cobalt in the top surface layers of the catalyst as well as to the known formation of both  $\text{NiAl}_2\text{O}_4$  and  $\text{CoAl}_2\text{O}_4$  phases.

The combined results of both characterizations and catalytic activity studies are presented in **Table 4.12** in order to search for correlations between the structure and performance of catalysts. **Table 4.12** reveals that the CO oxidation activity of 5M5MAI catalysts could be correlated to the degree of crystallization of CuO crystallites and to the surface concentration of copper oxide. It is seen that 5Ni5CuAl catalyst consists of well-crystallized CuO and  $\text{NiAl}_2\text{O}_4$  phases, together with  $\gamma\text{-Al}_{2.67}\text{O}_4$  phase, while the 5Co5CuAl catalyst consists of very

poorly crystallized CuO, CoAl<sub>2</sub>O<sub>4</sub> and  $\gamma$ -Al<sub>2.67</sub>O<sub>4</sub> phases. Moreover, the concentration of copper on the upper surface layers of the 5Ni5CuAl catalyst is higher than that of 5Co5CuAl catalyst. It should be noted that the obtained trend of the catalytic activity is not in agreement with the investigated analysis such as TEM-EDX and BET. On the other hand, the observed decrease in the activity of copper aluminum mixed oxide catalysts (CuO–Al<sub>2</sub>O<sub>3</sub> systems) due to nickel or cobalt addition might be discussed in terms of: (a) Decrease in the surface concentration of CuO crystallites via a corresponding decrease in their degree of dispersion on the surface of Al<sub>2</sub>O<sub>3</sub>. In other words, the excessive heating of the catalyst sample in presence of nickel or cobalt species might promote thermal diffusion of some of the copper species from the outermost surface layers of the catalyst to its bulk, (b) Presence of cobalt and nickel aluminates which exhibit poor catalytic properties towards CO oxidation.

**Table 4. 12.** *Main data of the characterization and catalytic activity tests over 5M5MAI calcined catalysts.*

Sample identity	Phase detected <sup>a</sup>	Degree of crystallinity <sup>a</sup>	BET surface area <sup>b</sup> (m <sup>2</sup> g <sup>-1</sup> )	Cu element dispersion <sup>c</sup>	Surface chemical composition <sup>d</sup>	Surface atomic ratio <sup>d</sup>	CO oxidation activity	
							T <sub>50</sub> <sup>e</sup> (°C)	T <sub>100</sub> <sup>f</sup> (°C)
5Ni5CoAl	$\gamma$ -Al <sub>2.67</sub> O <sub>4</sub> CoAl <sub>2</sub> O <sub>4</sub> NiAl <sub>2</sub> O <sub>4</sub>	++ <sup>g</sup>	25.0	—	NiAl <sub>2</sub> O <sub>4</sub> CoAl <sub>2</sub> O <sub>4</sub>	Ni/Al = 0.035 Co/Al = 0.033	500	—
5Ni5CuAl	$\gamma$ -Al <sub>2.67</sub> O <sub>4</sub> NiAl <sub>2</sub> O <sub>4</sub> CuO	++	22.8	+ <sup>h</sup>	NiAl <sub>2</sub> O <sub>4</sub> CuO	Ni/Al = 0.032 Cu/Al = 0.136	208	465
5Co5CuAl	$\gamma$ -Al <sub>2.67</sub> O <sub>4</sub> CuO CoAl <sub>2</sub> O <sub>4</sub>	+	31.2	++	CoAl <sub>2</sub> O <sub>4</sub> CuO	Co/Al = 0.038 Cu/Al = 0.076	268	369

<sup>a</sup> XRD analyses.<sup>b</sup> N<sub>2</sub> adsorption-desorption isotherms.<sup>c</sup> TEM-EDX analyses.<sup>d</sup> XPS analyses.<sup>e</sup> Temperatures for the half conversion of CO into CO<sub>2</sub> (determined under transient conditions).<sup>f</sup> Temperatures for the full conversion of CO into CO<sub>2</sub> (determined under transient conditions).<sup>g</sup> Increasing crystallization of the solids.<sup>h</sup> Increasing Cu element dispersion.

### 4.3 Comparison with the literature

Copper and cobalt-based catalysts have mostly been used in CO oxidation reactions, but few studies have been devoted to nickel-based catalysts for this reaction.

Many studies have been carried out on supported copper oxide catalysts [97-103, 182-187]. Most of these oxide catalysts were made by traditional synthesis methods. Pierron et al. [98] and Luo et al. [99] obtained a CO conversion of 50 % at around 270 °C (reaction conditions: 4.8 vol% CO in air) and 250 °C (reaction conditions: 2.4 vol % CO and 1.2 vol % O<sub>2</sub> in N<sub>2</sub>), using 10 wt % Cu–Al<sub>2</sub>O<sub>3</sub> catalysts prepared by wet impregnation. Renuka et al. [182] used wet impregnation method to prepare 11 wt % Cu supported mesoporous alumina catalyst. Their results showed that the conversion of CO reached 100 % at around 300 °C. The presence of reduced cationic species of Cu and metallic copper atoms induces a beneficial effect on CO oxidation. Huang et al. [100, 101] prepared 7 wt% Cu catalysts supported on Al<sub>2</sub>O<sub>3</sub> using impregnation method. The 7 wt% Cu–Al<sub>2</sub>O<sub>3</sub> catalyst showed a CO conversion of 70 % at 210 °C (reaction conditions: 2 vol% CO and 1.9 vol% O<sub>2</sub> in N<sub>2</sub>) [100]. Severino et al. [183] reported a study of the effect of copper concentration (2–30 wt %) on the CO oxidation activity at 400 °C for 3h (reaction conditions: 5 vol% CO in air), using impregnation method. It is seen that the activity of the catalysts increases with increasing metal loading from 2 to 10 wt% with a maximum CO conversion of about 85 %, but the activity decreases at higher concentrations (> 10 wt%). Alumina-supported copper catalyst, prepared by impregnation method, was also studied by Jiang et al. [187]. 12 wt % CuO/Al<sub>2</sub>O<sub>3</sub> catalyst showed a CO conversion (reaction conditions: 4 vol% CO, 17 vol% O<sub>2</sub> and 79% N<sub>2</sub>) of 50 % and 99 % at around 200 °C and 260 °C, respectively [187].

Oxidation of CO over cobalt-based catalysts has been the subject of many studies [86-95, 188, 189]. Thormahlen et al. [188, 189] reported a high catalytic activity of CoO<sub>x</sub>/Al<sub>2</sub>O<sub>3</sub> system using impregnation method and different oxidizing and reducing pretreatments prior to reaction. Pre-reduced cobalt oxide/alumina catalyst with 20 wt% CoO<sub>x</sub> showed a CO conversion of 50 % at 157 °C (reaction conditions: 1 vol% CO and 0.6 vol% O<sub>2</sub> in N<sub>2</sub>) [188]. Later, Jansson et al. [89, 91] clearly demonstrated the high activity of the pretreated CoO<sub>x</sub>/Al<sub>2</sub>O<sub>3</sub> system for CO oxidation. They reported a T<sub>50</sub> of 150 °C for pre-reduced CoO<sub>x</sub>/Al<sub>2</sub>O<sub>3</sub> catalyst compared to 80 °C for the pre-oxidised catalyst. Full conversion is reached at about 265 °C for the pre-reduced catalyst (reaction conditions: 2 vol% CO and 1.17 vol% O<sub>2</sub> in N<sub>2</sub>) [89]. Wang et al. [93] prepared supported cobalt catalyst on Al<sub>2</sub>O<sub>3</sub> (5 wt% as

metal Co loading) by incipient wetness impregnation. A full conversion of CO is obtained at 300 °C (reaction conditions: 10 vol% O<sub>2</sub> and 4 vol% CO in He). Yao [86] compared the catalytic activity of Co<sub>3</sub>O<sub>4</sub>/Al<sub>2</sub>O<sub>3</sub> catalyst using different modes of preparation; physical mixing and impregnation method. The results showed that the catalysts formed with physical mixing have a higher activity than the impregnated catalysts. For the impregnated catalysts, the close contact between the support surface and Co species facilitates the formation of CoAl<sub>2</sub>O<sub>4</sub> and deactivates the catalyst. Based on the above studies, it is clear that Co<sub>3</sub>O<sub>4</sub>/Al<sub>2</sub>O<sub>3</sub> is a very active catalyst for CO oxidation at low temperature. However, most studies have found that a deactivation always occurs, when the reaction is carried out at low temperature, due to the strong adsorption of CO on cobalt oxide and to the formation of surface carbonates [17].

In comparison to copper and cobalt based catalysts, few references can be found, dealing with the activity of nickel-based catalysts for the CO oxidation reaction. This is essentially due to its low activity in CO oxidation. Nickel-based catalysts were studied by El-shobaky et al. [65, 66, 190] and Chen et al. [96]. The study of El-shobaky et al. was mainly focused on the physicochemical properties of NiO-Al<sub>2</sub>O<sub>3</sub> systems, prepared by co-precipitation and impregnation. In their studies [66, 190], they did not observe the formation of the spinel phase at temperatures below 850 °C. Higher activation temperatures (above 850 °C) resulted in the formation of the nickel aluminates phase. Chen et al. [96] clearly demonstrated the low activity of nickel-based catalysts for CO oxidation. Indeed, reduced 15 wt% Ni/Al<sub>2</sub>O<sub>3</sub> catalyst showed full conversion of CO at around 500 °C.

In comparison to these different studies, the copper based catalysts prepared in the present work showed better performances for CO oxidation than similar catalysts prepared by the impregnation method. On the other hand, the low activity of the Ni and Co containing catalysts obtained in this study can be attributed to the formation of low active CoAl<sub>2</sub>O<sub>4</sub> and NiAl<sub>2</sub>O<sub>4</sub> “surface spinels”.

## Conclusions

The CO oxidation activity of alumina-based mixed oxide catalysts synthesized via microwave assisted solution combustion method seemed to be sensitive to RV/OV ratio and their synthesis should be conducted at 1.0 as the optimum RV/OV ratio.

The metal oxide-alumina interaction effect is responsible for the low activity of nickel and cobalt-based catalysts and this effect is pronounced by the high RV/OV ratio. In fact, high

RV/OV ratio seems to induce stronger metal oxide-alumina surface interactions and produces more surface spinels which cause a dramatic reduction in CO oxidation activity.

Copper based catalysts presented a high catalytic activity for the CO oxidation at low temperatures, while nickel and cobalt-based catalysts showed relatively low activity at low temperatures. This can be related to the existence of free copper oxides on the surface of copper-based catalysts, favoring the redox properties of the catalyst and enhancing its catalytic activity.

On the basis of the activity results, we propose that the catalyst activity derives primarily from the extent of the interaction between the metal oxide and alumina. The interaction of metal oxide with alumina affects the bulk and surface chemical composition, structural properties, and active sites dispersion which further affect the catalytic performances. Meanwhile, the presence of free bulk metal oxide is mandatory for the CO oxidation activity.

The three investigated catalyst series with different metal loadings proved that their activities depend more on the metal phase nature than on the metal sites dispersion. Indeed, copper-based catalyst with different metal loadings exhibited the best catalytic performances for CO oxidation compared to nickel and cobalt-based catalysts, which is attributed to bulk CuO.

For ternary oxide catalysts, alumina-based mixed oxide catalysts containing copper in the top surface layers of the catalyst are more active, especially at low temperature, than those without copper, indicating that copper improves the catalytic activity of these catalysts. Nevertheless, the presence of crystalline nature of the catalyst and the interaction between the metal oxide and alumina were also considered.

It worth noting that all the studied catalysts were able to maintain stable conversion of CO after 30 min time-on-stream at the different constant temperatures, indicating a satisfying resistance to deactivation. However, these results are not conclusive and further studies on deactivation phenomena of the studied catalysts for CO oxidation are needed.

After the catalytic tests, XRD characterizations were carried out on the working catalysts. XRD patterns of the spent and the fresh catalysts are given in **Figures B.1** and **B.2** (See **Annex B**). The results showed that there were no significant differences between each both samples (spent and fresh), also there are any diffraction peaks belonged to carbon. Further analysis, to check the variations of microstructure and carbon deposition, by TEM and TG-DTG characterizations are needed.

## Résumé en Français du chapitre 4

Le chapitre 4 présente les principaux résultats de l'étude de l'influence de la stoechiométrie, la teneur en métal de transition, et l'effet de synergie sur les performances catalytiques des oxydes binaires et ternaires.

L'étude de l'influence de la stoechiométrie sur les performances catalytiques a montré que l'activité catalytique des trois séries de catalyseurs étudiés avec différents ratio RV/OV, en régime transitoire et en régime stationnaire, a été sensible à la stoechiométrie, et l'activité optimale a été établie pour les catalyseurs synthétisés avec un ratio RV/OV=1.0.

Les catalyseurs à base de cuivre ont montré l'activité d'oxydation de CO la plus élevée, avec un taux de conversion de 100 % de CO atteinte dès 225 °C, par rapport aux catalyseurs à base de nickel et de cobalt. La différence d'activité catalytique de ces catalyseurs est liée principalement à leurs différentes propriétés de surface; En effet, l'existence des cristallites d'oxydes de cuivre libres en surface, favorise les propriétés redox du catalyseur et améliore son activité catalytique. De plus, les catalyseurs à base de cuivre sont généralement connus pour présenter des activités intrinsèques élevées pour la réaction d'oxydation du CO.

A l'opposé des oxydes à base de cuivre, les oxydes à base de Ni et Co ont présenté des structures «spinelles de surface» d'aluminates. Ces structures particulières sont connues pour présenter des activités intrinsèques faibles pour la réaction d'oxydation du CO, car elles ont tendance à baisser la teneur en sites actifs en surface, suite à l'incorporation du métal de transition dans la structure de l'alumine, et également à affecter la mobilité d'oxygène, et réduit par conséquent les performances du catalyseur.

L'étude de l'influence de la teneur en métal de transition sur les performances catalytiques a montré que l'activité catalytique, s'est considérablement améliorée avec l'augmentation de la teneur en métal, et l'activité optimale a été établie pour les catalyseurs synthétisés avec une teneur de 20 % massique en métal.

La tendance de variation de l'activité catalytique avec l'augmentation de la teneur en métal a été expliquée, en considérant la tendance d'évolution des propriétés structurales des catalyseurs en fonction de la teneur en métal: pour les catalyseurs à base de nickel et de cobalt, l'étendue de l'interaction entre les espèces de Ni ou Co et l'alumine semblait avoir un effet prononcé sur l'activité du catalyseur. Sur la base des résultats de caractérisation XRD, les faibles concentrations en métaux ont conduit à la formation d'aluminates de surface plus au moins

amorphes. Ces espèces instables, qui ont une interaction moyenne avec l'alumine, ne semblent pas présenter de bonnes performances dans la réaction d'oxydation du CO. En augmentant la charge métallique, l'interaction entre les oxydes métalliques et l'alumine s'est améliorée et des spinelles aluminates mieux cristallisées sont formées, conduisant à une activité d'oxydation du CO plus élevée. Les teneurs métalliques plus élevées, en particulier pour les catalyseurs à base de cobalt, ont entraîné la formation des oxydes de cobalt, qui ont amélioré considérablement l'activité des catalyseurs.

Dans le cas des catalyseurs à base de cuivre, l'activité catalytique a été légèrement augmentée avec l'augmentation de la teneur en Cu. Sur la base des résultats considérés, il a été confirmé que l'activité d'oxydation du CO augmente avec l'augmentation de la charge en métal. Ce résultat était prévisible, en effet, il est généralement connu que l'activité catalytique augmente avec l'augmentation de la teneur en métal dans le catalyseur, car l'interaction des molécules gazeuses avec les surfaces d'oxyde s'est améliorée avec une plus grande teneur en sites actifs en surface.

Pour les oxydes ternaires, les catalyseurs contenant du cuivre ont été plus actifs, que ceux sans cuivre, ce qui confirme l'effet positif du cuivre pour l'amélioration de l'activité catalytique des oxydes à base de Ni ou Co. D'autre part, la diminution de l'activité observés sur ces oxydes ternaires par rapports à celles des oxydes binaires (contenant le cuivre seul) pourrait être expliqué en termes de: (a) diminution des sites actifs en surface via la diminution de la teneur en Cu, (b) diminution des sites actifs en surface via la diffusion du cuivre des couches superficielles au volume intérieur du catalyseur, favorisé par la présence des espèces de nickel ou de cobalt, et (c) présence d'aluminates de cobalt et de nickel qui sont connus pour leurs faibles activités catalytiques vis-à-vis de l'oxydation du CO.

Il convient de noter que les tendances observées de l'activité d'oxydation du CO, avec la variation de la stœchiométrie, de la teneur en métal et la composition des oxydes, n'étaient pas corrélées avec la surface spécifique des catalyseurs.

Sur la base des résultats de l'activité des oxydes métalliques synthétisés, il a été proposé que l'activité de ces catalyseurs dérive principalement de la nature du métal de transition et de l'étendue de l'interaction entre l'oxyde de métal de transition et l'alumine.

## CONCLUSIONS AND PERSPECTIVES

---

## Conclusions

The objective of this project was to develop an original synthesis approach for the preparation of active catalytic materials for carbon monoxide oxidation. For this, binary and ternary metal oxide catalysts were synthesized, characterized and tested for CO oxidation reaction. Metal oxides based-catalysts were obtained in a very short time (less than 10 min) under microwave irradiation from the combustion of an aqueous solution of metal nitrates (oxidizing agent) and urea (reducing agent). The combustion reactions, corresponding to the different catalytic systems, were estimated by applying the thermochemical concepts of propellant chemistry. Several experimental factors such as the metal precursor, the stoichiometry of the reactants (RV/OV ratio), and the metal loading were varied and tested. The different characterization techniques, such as X-ray fluorescence spectrometry, X-ray diffraction, N<sub>2</sub> adsorption-desorption analysis, scanning electron microscopy, transmission electron microscopy and X-ray photoelectron spectroscopy, were employed specifically to follow the physicochemical properties of the combustion-synthesized mixed oxide catalysts. These complementary techniques allowed, on the one hand, a better understanding of the correlation between the different characterization results and on the other, a deep understanding of the correlation between the physicochemical properties of the catalysts and their catalytic activities for CO oxidation. Through the results of this study, it was found that microwave-assisted solution combustion method is a successful route to synthesize compositionally homogeneous alumina-based binary and ternary metal oxide materials. However, controlling the synthesis of desirable phases and micro/nanostructure of these mixed oxides via microwave-assisted solution combustion route remains a challenge.

From the experimental point of view, it is worth noting that the microwave-assisted solution combustion method is an extremely simple and fast synthesis approach to prepare binary and ternary metal oxide catalysts. This method may be easily extended to other mixed oxides.

In the light of the bulk and surface characterization results, it is clear that the microwave-assisted solution combustion method using urea is suitable for obtaining “bulk-like” copper oxide phases, but not suitable for obtaining “bulk-like” NiO or Co<sub>x</sub>O<sub>y</sub> separated phases. Indeed, nickel and cobalt oxides interact strongly with alumina and result in the formation of well-dispersed “surface spinels” and bulk metal aluminates (MA<sub>2</sub>O<sub>4</sub>) phases.

The presence of these phases was detected by XRD, XPS and TEM. The degree of interaction between alumina and nickel or cobalt oxides is directly proportional to the stoichiometry of the reactants (RV/OV ratio) and metal (Ni or Co) loadings. In an attempt to prevent the interaction between alumina and NiO or  $\text{Co}_x\text{O}_y$  phases, introduction of copper into the Ni-Al or Co-Al combustion systems was adopted. However, this approach had not proved fruitful, since copper oxides were not effective in inhibiting the formation of  $\text{NiAl}_2\text{O}_4$  and  $\text{CoAl}_2\text{O}_4$  spinels.

Although the combustion-synthesized mixed oxides did not show sufficiently high surface areas in comparison to those prepared by the conventional methods, this method showed great results on the chemical homogeneity, high purity, and unique properties of mixed oxide products.

The low surface area found for most of the obtained catalysts had a direct correlation to the phase transformation in alumina, as an important factor for determining the textural properties of the catalyst. The major detected phases for the nickel and cobalt-based catalysts were the metal aluminates ( $\text{MAl}_2\text{O}_4$ ), while, in copper-based catalysts, alumina existed in the crystalline phase  $\alpha\text{-Al}_2\text{O}_3$ . According to the literature, the surface areas of the combustion-synthesized metal aluminates ( $\text{MAl}_2\text{O}_4$ ) and  $\alpha\text{-Al}_2\text{O}_3$  structures are generally low and thus have resulted in a low surface area of the synthesized catalysts.

For the microstructural aspects of the combustion-synthesized mixed oxide catalysts, the agglomerates were characterized by a foamy and “flaky-like” morphology, consisting of hexagonal platelet particles. These morphologies are quite common among metal oxide-based solution combustion method. Variation in surface features was found between the different mixed oxide catalysts. Nickel and cobalt-based catalysts presented soft surface area, while quasi-spherical nanoparticles were dispersed on the surface of the copper-based catalysts. These observations were associated to the well-known interaction between alumina and metal oxides. Incorporated nickel and cobalt oxides developed two-dimensional (2D) nanostructures, forming well-dispersed  $\text{CoAl}_2\text{O}_4$  and  $\text{NiAl}_2\text{O}_4$  “surface spinels”. On the other hand, copper oxides that do not interact with alumina developed three dimensional (3D) crystallites. The size of these nanostructures lies in the nanometer range, around 5–95 nm. The size, dispersion and aggregation behavior of copper oxide nanoparticles were controlled by the stoichiometry of the reactants (RV/OV ratio) and Cu loading.

In this study, variation of the stoichiometry of the reactants (RV/OV ratio) has demonstrated a well-settled approach for controlling the properties of the combustion-synthesized mixed oxides catalysts. Indeed, it has been found that the stoichiometry can play a critical role in controlling the phase composition, surface area, micro/nanostructure characteristics, and surface chemical composition (surface M/Al atomic ratio). Based on the different characterizations, improvements in the properties of the combustion-synthesized can be achieved by proper estimation of the mixture RV/OV ratio.

It has been shown in this thesis report that the final physiochemical properties affect the catalytic properties of alumina-based mixed oxide catalysts and the nature of active metal oxides on the alumina surface was of primary importance. Copper containing catalysts, prepared by the microwave-assisted solution combustion method, have an excellent activity for CO oxidation at low reaction temperature. These combustion-synthesized catalysts were more active than similar catalysts, reported in the literature, prepared by conventional methods and tested under similar reaction conditions. Both the highly dispersed CuO and bulk CuO species were responsible for the high CO oxidation activity.

Although the results obtained with cobalt and nickel-based catalysts were not completely satisfactory, a clarification on the origins of their low activity has been achieved. Alumina-Ni/Co chemical interaction is unfavorable for the CO oxidation; the conversion of Ni or Co oxides into metal aluminates via the solid-solid interaction with alumina resulted in the formation of the low active  $\text{CoAl}_2\text{O}_4$  and  $\text{NiAl}_2\text{O}_4$  “surface spinels”.

The comparison study between the catalytic activities of the different combustion-synthesized binary and ternary oxide catalysts has demonstrated that copper containing catalysts were the highly active, at low temperature, and the order of activity for binary oxide catalysts was the following: copper-based catalysts > cobalt-based catalysts > nickel-based catalysts, while for ternary oxide catalysts, it was the following: nickel-copper-based catalyst > cobalt-copper-based catalyst > nickel-cobalt-based catalyst.

The activity of the catalyst was found proportional to the reaction temperature. As a general behavior, the increase of temperature accelerates the rate of CO oxidation reaction (under transient conditions) and significantly improves the catalytic activity (under steady state). It is assumed that reaction temperature affects the interaction of adsorbed molecules

(CO and O<sub>2</sub>) with the metal oxide surfaces (O<sub>2</sub> adsorption is inhibited by CO at low temperature).

The examination of the influence of RV/OV ratio on catalytic activity of the binary oxide catalysts revealed a linear relationship between their final physicochemical properties and catalytic properties. Optimal physicochemical properties and best catalytic activities were achieved when the redox system is stoichiometrically balanced (RV/OV=1).

## Perspectives

More research needs to be done on crystal growth and nucleation of Ni-Al, Co-Al and Cu-Al combustion systems. Specifically, it would be of interest to understand why Ni-Al or Co-Al combustion systems favor the formation of CoAl<sub>2</sub>O<sub>4</sub> and NiAl<sub>2</sub>O<sub>4</sub> phases with least priority given to free nickel and cobalt oxides, while Cu-Al combustion system led to the formation of CuO and  $\alpha$ -Al<sub>2</sub>O<sub>3</sub> separated phases.

Calculations based on thermodynamic considerations have to be carried out to predict the theoretical adiabatic flame temperature of combustion reaction for the Ni-Al, Co-Al and Cu-Al combustion systems and so that there can be a full understanding of the alumina-metal oxides interactions. It would also be a good idea to study the effect of a different RV/OV stoichiometry or metal loading on flame temperature. Understanding how physicochemical properties of these mixed oxide systems vary with combustion reaction temperature would be worth studying in the future. Such understanding will definitely lead to better control of product properties.

It would be important to perform more studies on Ni-Al and Co-Al combustion systems and find new ways of inhibiting the interaction between alumina and NiO or Co<sub>x</sub>O<sub>y</sub> phases without having to lose product homogeneity.

Fundamental understanding of the chemical mechanisms of solution combustion reactions is critical for controlling the properties of the combustion-synthesized mixed oxide materials. Further works are needed to establish a detailed description of solution combustion mechanisms and address the exact formation mechanisms responsible for the various properties.

As far as we are concerned, the next step would be characterizing the combustion-synthesized mixed oxides, after their use during CO oxidation, to examine the deactivation phenomena. TEM, XRD, XPS, Temperature-programmed oxidation (TPO), Fourier-transform infrared spectroscopy (FTIR) or X-ray absorption near-edge structure (XANES) measurements, might be envisaged in this regard.

We hope that this thesis report has brought a clear understanding of the solution combustion chemistry and great insight into the physicochemical properties of the combustion-synthesized alumina-based binary and ternary metal oxide materials. We hope also that this study will inspire further efforts to develop more advanced mixed metal oxide catalytic materials via microwave-assisted solution combustion synthesis.

## Résumé en Français de la conclusion générale

À la lumière des résultats de caractérisation structurales, il est clair que la combustion assistée par micro-ondes des solutions nitrate-urée contenant les métaux Al et Ni ou Al et Co donne des structures d'aluminates métalliques et de  $\gamma$ -alumine. D'autre part, la combustion des solutions nitrate-urée contenant Al et Cu donne in situ et en une seule étape des nanoparticules de CuO et de  $\alpha$ -alumine. La formation des aluminates de Ni ou Co est associée à l'interaction entre l'alumine et les oxydes de nickel ou de cobalt. Le degré d'interaction entre l'alumine et les oxydes de nickel ou de cobalt est directement proportionnel à la stoechiométrie des réactifs (ratio RV/OV) et des charges métalliques (cas du Ni ou Co). Afin d'empêcher l'interaction entre l'alumine et des oxydes de Ni ou Co, l'introduction de cuivre dans les systèmes de combustion Ni-Al et Co-Al a été adoptée. Cependant, cette approche n'a pas permis d'inhiber la formation des phases aluminates.

Les oxydes mixtes synthétisés par combustion n'ont pas montré de surfaces spécifiques suffisamment élevées par rapport à celles préparées par les méthodes conventionnelles. La faible surface spécifique trouvée pour la plupart des catalyseurs obtenus avait une corrélation directe avec l'évolution de la phase d'alumine au sein de ces oxydes, comme facteur important pour déterminer les propriétés texturales de ces derniers. Les principales phases détectées pour les catalyseurs à base de nickel et de cobalt étaient les aluminates métalliques ( $\text{MAl}_2\text{O}_4$ ), tandis que, dans les catalyseurs à base de cuivre, l'alumine existait dans la phase cristalline  $\alpha$ - $\text{Al}_2\text{O}_3$ . Selon la littérature, les surfaces des aluminates métalliques ( $\text{MAl}_2\text{O}_4$ ) et  $\alpha$ - $\text{Al}_2\text{O}_3$  synthétisés par combustion sont généralement faibles.

Pour les aspects microstructuraux des oxydes mixtes synthétisés par combustion, les agglomérats étaient caractérisés par une morphologie mousseuse et plaquettaire. Une variation des caractéristiques de surface a été trouvée entre les différents catalyseurs, en fonction de la nature du métal de transition. Les catalyseurs à base de nickel et de cobalt présentaient une surface lisse, tandis que des nanoparticules quasi sphériques étaient dispersées à la surface des à base de cuivre. Ces observations étaient associées à l'interaction entre l'alumine et les oxydes métalliques. Les oxydes de nickel et de cobalt incorporés ont développé des nanostructures bidimensionnelles (2D), formant des «spinelles de surface»  $\text{CoAl}_2\text{O}_4$  et  $\text{NiAl}_2\text{O}_4$  bien dispersés. D'autre part, les oxydes de cuivre qui n'interagissent pas avec l'alumine ont développé des nanostructures tridimensionnelles (3D). La taille de ces nanostructures se situe dans la gamme des nanomètres, autour de 5–95 nm. La taille et la

dispersion de ces nanostructures ont été contrôlées par la stœchiométrie des réactifs (rapport RV/OV) et la teneur en Cu.

Dans cette étude, la variation de la stœchiométrie était une approche intéressante pour contrôler les propriétés des catalyseurs d'oxydes mixtes synthétisés par combustion. En effet, il a été constaté que la stœchiométrie peut jouer un rôle critique dans le contrôle de la composition de phase, de la surface, des caractéristiques de la micro/nanostructure et de la composition chimique de la surface (rapport atomique M/Al en surface). Sur la base des différentes caractérisations, des améliorations des propriétés de la combustion synthétisée peuvent être obtenues en choisissant un ratio RV/OV égale à 1.0.

Il a été démontré dans ce rapport de thèse que les catalyseurs contenant du cuivre ont une excellente activité pour l'oxydation du CO à basse température de réaction. Ces catalyseurs synthétisés par combustion étaient plus actifs que des catalyseurs similaires, rapportés dans la littérature, préparés par des méthodes conventionnelles et testés dans des conditions de réaction similaires. Bien que les résultats obtenus avec les catalyseurs à base de cobalt et de nickel ne soient pas entièrement satisfaisants, une clarification sur les origines de leur faible activité a été obtenue. La formation des aluminates métalliques via l'interaction solide-solide entre l'alumine et les oxydes de Ni/Co est défavorable à l'oxydation du CO.

Des études supplémentaires doivent être effectuées sur les mécanismes de la nucléation et de la croissance cristalline des systèmes de combustion Ni-Al, Co-Al et Cu-Al. Plus précisément, il serait intéressant de comprendre pourquoi les systèmes de combustion Ni-Al ou Co-Al favorisent la formation de phases  $\text{CoAl}_2\text{O}_4$  et  $\text{NiAl}_2\text{O}_4$ , tandis que le système de combustion Cu-Al a conduit à la formation des phases CuO et  $\alpha\text{-Al}_2\text{O}_3$ . Aussi, il serait important de trouver des nouvelles façons d'inhiber l'interaction entre l'alumine et les oxydes de Ni/Co, sans avoir perdre l'homogénéité du produit.

Une étude thermodynamique doit être effectuée pour prédire la température théorique de la flamme adiabatique de la réaction de combustion pour les systèmes de combustion Ni-Al, Co-Al et Cu-Al, et également pour corrélérer les propriétés physicochimiques avec les données thermodynamiques de la réaction de combustion. Comprendre comment les propriétés physicochimiques de ces systèmes d'oxydes mixtes varient avec la température de réaction de combustion mériterait d'être étudié à l'avenir. Une telle compréhension conduira certainement à un meilleur contrôle des propriétés du produit.

## REFERENCES

---

- 
- [1] J. Wisniak, "The history of catalysis. From the beginning to nobel prizes," *Educ. Química*, vol. 21, no. 1, pp. 60–69, 2010.
- [2] A. J. B. Robertson, "The early history of catalysis," *Platin. Met. Rev.*, vol. 19, no. 2, p. 69, 1975.
- [3] L. Lloyd, *Handbook of industrial catalysts*, 1st ed. New York, USA: Springer Science+Business Media, 2011.
- [4] W. J. Thomas and J. M. Thomas, *Principles and practice of heterogeneous catalysis*, 2nd ed. Weinheim, Germany: Wiley-VCH Verlag GmbH & Co. KGaA, 2015.
- [5] G. Chinchin, P. Davies, and R. J. Sampson, "The historical development of catalytic oxidation processes," in *Catalysis - Science and Technology*, 1st ed., Heidelberg, Germany: Springer-Verlag, 1987, p. 61.
- [6] J. C. Védrine, "Fundamentals of heterogeneous catalysis," in *Metal Oxides in Heterogeneous Catalysis*, Amsterdam, Netherlands: Elsevier, 2018.
- [7] K. J. Laidler, "A glossary of terms used in chemical kinetics, including reaction dynamics (IUPAC recommendations 1996)," *Pure Appl. Chem.*, vol. 68, no. 1, pp. 149–192, 1996.
- [8] J. C. Védrine, "Heterogeneous catalysis on metal oxides," *Catalysts*, vol. 7, no. 11, 2017.
- [9] B. M. Reddy, "Redox properties of metal oxides," in *Metal Oxides: Chemistry and Applications*, New York, USA: Taylor & Francis Group, 2005.
- [10] K. Shibata, T. Kiyoura, J. Kitagawa, T. Sumiyoshi, and K. Tanabe, "Acidic properties of binary metal oxides," *Bull. Chem. Soc. Jpn.*, vol. 46, no. 10, pp. 2985–2988, 1973.
- [11] R. N. Spitz, J. E. Barton, M. A. Barteau, R. H. Staley, and A. W. Sleight, "Characterization of the surface acid-base properties of metal oxides by titration/displacement reactions," *J. Phys. Chem.*, vol. 90, no. 17, pp. 4067–4075, 1986.
- [12] G. Busca, "Bases and basic materials in chemical and environmental processes. Liquid versus solid basicity," *Chem. Rev.*, vol. 110, no. 4, pp. 2217–2249, 2010.
- [13] G. Busca, "The surface acidity of solid oxides and its characterization by IR spectroscopic methods. An attempt at systematization," *Phys. Chem. Chem. Phys.*, vol. 1, no. 5, pp. 723–736, 1999.
- [14] N. Bion, F. Can, X. Courtois, and D. Duprez, "Transition metal oxides for combustion and depollution processes," in *Metal Oxides in Heterogeneous Catalysis*, Amsterdam, Netherlands: Elsevier, 2018, pp. 287–353.
- [15] H. H. Kung, *Transition metal oxides: Surface chemistry and catalysis*, 1st ed. Amsterdam, Netherlands: Elsevier Science, 1989.
- [16] P. Anthony, *Transition metal oxides. An introduction to their electronic structure and properties*, 1st ed. Oxford, UK: Oxford University Press, 1992.
- [17] S. Royer and D. Duprez, "Catalytic oxidation of carbon monoxide over transition metal oxides," *ChemCatChem*, vol. 3, no. 1, pp. 24–65, 2011.
- [18] S. S. Batsanov, "Van der Waals radii of elements," *Inorg. Mater.*, vol. 37, no. 9, pp. 871–885, 2001.
- [19] L. Qiao and M. T. Swihart, "Solution-phase synthesis of transition metal oxide

- nanocrystals: Morphologies, formulae, and mechanisms,” *Adv. Colloid Interface Sci.*, vol. 244, pp. 199–266, 2017.
- [20] R. L. Parker, “Crystal growth mechanisms: energetics, kinetics, and transport,” *Solid State Phys.*, vol. 25, pp. 151–299, 1970.
- [21] X. Liu and C. T. Prewitt, “High-temperature X-ray diffraction study of  $\text{Co}_3\text{O}_4$ : Transition from normal to disordered spinel,” *Phys. Chem. Miner.*, vol. 17, no. 2, pp. 168–172, 1990.
- [22] R. W. G. Wyckoff, *Crystal structures*, 1st ed. New York, USA: Interscience Publishers, 1963.
- [23] S. Åsbrink and L. J. Norrby, “A refinement of the crystal structure of copper(II) oxide with a discussion of some exceptional e.s.d.’s,” *Acta Crystallogr.*, vol. 26, no. 1, pp. 8–15, 1970.
- [24] M. C. Neuburger, “Präzisionsmessung der Gitterkonstante von Cuprooxyd  $\text{Cu}_2\text{O}$ ,” vol. 67, pp. 845–850, 1931.
- [25] P. Sabatier, “Hydrogenations et deshydrogenations par catalyse,” *Berichte der Dtsch. Chem. Gesellschaft*, vol. 44, no. 3, pp. 1984–2001, 1911.
- [26] P. Sabatier, “How i have been led to the direct hydrogenation method by metallic catalysts,” *Ind. Eng. Chem.*, vol. 18, no. 10, pp. 1005–1008, 1926.
- [27] M. Guisnet and C. Naccache, “Catalyse hétérogène - mode d’action des catalyseurs,” in *Techniques de l’Ingénieur*, Paris, France, 2004, p. 13.
- [28] P. Sabatier, *Catalysis in organic chemistry*, 1st ed. New York, USA: D. Van Nostrand Company, 1922.
- [29] H. Yang and H. Chen, “Biomass gasification for synthetic liquid fuel production,” in *Gasification for Synthetic Fuel Production: Fundamentals, Processes and Applications*, Amsterdam, Netherlands: Elsevier, 2015, pp. 241–275.
- [30] J. Zhang, “Research and development of nickel based catalysts for carbon dioxide reforming of methane,” in *Thesis: Chemical engineering*, Saskatchewan, Canada, 2008, pp. XIII–195.
- [31] C. Kordulis, K. Bourikas, M. Gousi, E. Kordouli, and A. Lycourghiotis, “Development of nickel based catalysts for the transformation of natural triglycerides and related compounds into green diesel: A critical review,” *Appl. Catal. B Environ.*, vol. 181, pp. 156–196, 2016.
- [32] F. L. Chan and A. Tanksale, “Review of recent developments in Ni-based catalysts for biomass gasification,” *Renew. Sustain. Energy Rev.*, vol. 38, pp. 428–438, 2014.
- [33] Z. Bian, S. Das, M. H. Wai, P. Hongmanorom, and S. Kawi, “A review on bimetallic nickel-based catalysts for  $\text{CO}_2$  reforming of methane,” *ChemPhysChem*, vol. 18, no. 22, pp. 3117–3134, 2017.
- [34] P. Frontera, A. Macario, M. Ferraro, and P. Antonucci, “Supported catalysts for  $\text{CO}_2$  methanation: A review,” *Catalysts*, vol. 7, no. 59, pp. 1–28, 2017.
- [35] V. P. Ananikov, “Nickel: The ‘spirited horse’ of transition metal catalysis,” *ACS Catal.*, vol. 5, no. 3, pp. 1964–1971, Mar. 2015.
- [36] J. L. Dubois, “Main industrial processes using metal oxides as catalysts or support and future trends in heterogeneous catalysis,” in *Metal Oxides in Heterogeneous Catalysis*,

- Amsterdam, Netherlands: Elsevier, 2018, pp. 401–549.
- [37] A. W. Budiman, S. H. Song, T. S. Chang, C. H. Shin, and M. J. Choi, “Dry reforming of methane over cobalt catalysts: A literature review of catalyst development,” *Catal. Surv. from Asia*, vol. 16, no. 4, pp. 183–197, Dec. 2012.
- [38] H. Song and U. S. Ozkan, “Ethanol steam reforming over Co-based catalysts: Role of oxygen mobility,” *J. Catal.*, vol. 261, no. 1, pp. 66–74, 2009.
- [39] F. Diehl and A. Y. Khodakov, “Promotion of cobalt fischer-tropsch catalysts with noble metals: A review,” *Oil Gas Sci. Technol.*, vol. 63, no. 1, pp. 9–19, 2008.
- [40] X. Xie, Y. Li, Z. Q. Liu, M. Haruta, and W. Shen, “Low-temperature oxidation of CO catalysed by Co<sub>3</sub>O<sub>4</sub> nanorods,” *Nature*, vol. 458, no. 7239, pp. 746–749, 2009.
- [41] H. Lin, H. Chiu, H. Tsai, S. Chien, and C. Wang, “Synthesis, characterization and catalytic oxidation of carbon monoxide over cobalt oxide,” *Catal. Letters*, vol. 88, pp. 169–174, 2003.
- [42] Q. Yan, X. Li, Q. Zhao, and G. Chen, “Shape-controlled fabrication of the porous Co<sub>3</sub>O<sub>4</sub> nanoflower clusters for efficient catalytic oxidation of gaseous toluene,” *J. Hazard. Mater.*, vol. 209–210, pp. 385–391, Mar. 2012.
- [43] Y. Xia, H. Dai, H. Jiang, and L. Zhang, “Three-dimensional ordered mesoporous cobalt oxides: Highly active catalysts for the oxidation of toluene and methanol,” *Catal. Commun.*, vol. 11, no. 15, pp. 1171–1175, Sep. 2010.
- [44] M. S. Kamal, S. A. Razzak, and M. M. Hossain, “Catalytic oxidation of volatile organic compounds (VOCs) – A review,” *Atmos. Environ.*, vol. 140, pp. 117–134, Sep. 2016.
- [45] P. W. Park and J. S. Ledford, “The influence of surface structure on the catalytic activity of alumina supported copper oxide catalysts. Oxidation of carbon monoxide and methane,” *Appl. Catal. B Environ.*, vol. 15, no. 3–4, pp. 221–231, Feb. 1998.
- [46] Z. Zhang, Z. Jiang, and W. Shangguan, “Low-temperature catalysis for VOCs removal in technology and application: A state-of-the-art review,” *Catal. Today*, vol. 264, pp. 270–278, 2016.
- [47] T. J. Huang and D. H. Tsai, “CO oxidation behavior of copper and copper oxides,” *Catal. Letters*, vol. 87, no. 3–4, pp. 173–178, 2003.
- [48] E. M. Cordi, P. J. O’Neill, and J. L. Falconer, “Transient oxidation of volatile organic compounds on a CuO/Al<sub>2</sub>O<sub>3</sub> catalyst,” *Appl. Catal. B Environ.*, vol. 14, no. 1–2, pp. 23–36, Dec. 1997.
- [49] P. Burtin, “Transformation des alumines de transition en alumine alpha. Influence d’éléments étrangers sur la stabilité des alumines,” in *Thesis: Chemical engineering*, Saint-Etienne, France, 1985, p. 179.
- [50] R. S. Zhou and R. L. Snyder, “Structures and transformation mechanisms of the  $\eta$ ,  $\gamma$  and  $\theta$  transition aluminas,” *Acta Crystallogr. Sect. B Struct. Sci.*, vol. 47, no. 5, pp. 617–630, Oct. 1991.
- [51] I. Levin and D. Brandon, “Metastable alumina polymorphs: crystal structures and transition sequences,” *J. Am. Ceram. Soc.*, vol. 81, no. 8, pp. 1995–2012, Jan. 2005.
- [52] F. W. Dynys and J. W. Halloran, “Alpha alumina formation in alum-derived gamma alumina,” *J. Am. Ceram. Soc.*, vol. 65, no. 9, pp. 442–448, Sep. 1982.

- [53] S. Takashi, W. Hideo, M. Fuji, and T. Minoru, "Structural properties and surface characteristics on aluminum oxide powders," *Annu. Rep. Res. Cent. Ceram. Eng.*, vol. 9, pp. 23–31, 2009.
- [54] M. Trueba and S. P. Trasatti, " $\gamma$ -Alumina as a support for catalysts: A review of fundamental aspects," *Eur. J. Inorg. Chem.*, no. 17, pp. 3393–3403, Sep. 2005.
- [55] A. R. Ferreira *et al.*, "Direct comparison between two structural models by DFT calculations," *J. Solid State Chem.*, vol. 184, no. 5, pp. 1105–1111, May 2011.
- [56] Y. Lei and G. Wang, "Linking diffusion kinetics to defect electronic structure in metal oxides: Charge-dependent vacancy diffusion in alumina," *Scr. Mater.*, vol. 101, pp. 20–23, May 2015.
- [57] A. M. Turek and I. E. Wachs, "Acidic properties of supported niobium oxide catalysts: An infrared spectroscopy investigation," *J. Phys. Chem.*, vol. 96, no. 12, pp. 5000–5007, May 1992.
- [58] J. Čejka, "Organized mesoporous alumina: synthesis, structure and potential in catalysis," *Appl. Catal. A Gen.*, vol. 254, no. 2, pp. 327–338, Nov. 2003.
- [59] D. L. Trimm and A. Stanislaus, "The control of pore size in alumina catalyst supports: A review," *Appl. Catal.*, vol. 21, pp. 215–238, 1986. [60] D. L. Cocke, E. D. Johnson, and R. P. Merrill, "Planar models for alumina-based catalysts," *Catal. Rev.*, vol. 26, no. 2, pp. 163–231, Jun. 1984.
- [61] R. J. Farrauto and K. E. Voss, "Monolithic diesel oxidation catalysts," *Appl. Catal. B Environ.*, vol. 10, no. 1–3, pp. 29–51, 1996.
- [62] M. V. Twigg, "Rôles of catalytic oxidation in control of vehicle exhaust emissions," *Catal. Today*, vol. 117, no. 4, pp. 407–418, 2006.
- [63] M. V. Twigg, "Progress and future challenges in controlling automotive exhaust gas emissions," *Appl. Catal. B Environ.*, vol. 70, no. 1–4, pp. 2–15, Jan. 2007.
- [64] M. V. Glazoff, S. T. Pantelides, S. N. Rashkeev, K. Sohlberg, J. Novak, and S. J. Pennycook, "Transition metal atoms on different alumina phases: The role of subsurface sites on catalytic activity," *Phys. Rev. B - Condens. Matter Mater. Phys.*, vol. 67, 2003.
- [65] G. A. El-Shobaky, T. El nabarawy, I. M. Morsi, and N. M. Ghoneim, "Physicochemical properties of NiO-Al<sub>2</sub>O<sub>3</sub> mixed oxides and their relationship with thermal treatment and chemical composition," *Surf. Technol.*, vol. 19, pp. 109–118, 1983.
- [66] G. A. El Shobaky and A. N. Al Noaimi, "Surface properties of Ni-Al mixed oxide catalysts," *Surf. Technol.*, vol. 26, pp. 235–244, 1985.
- [67] J. M. Rynkowski, T. Paryjczak, and M. Lenik, "On the nature of oxidic nickel phases in NiO/ $\gamma$ -Al<sub>2</sub>O<sub>3</sub> catalysts," *Appl. Catal. A Gen.*, vol. 106, no. 1, pp. 73–82, Nov. 1993.
- [68] M. Zangouei, A. Z. Moghaddam, and M. Arasteh, "The influence of nickel loading on reducibility of NiO/Al<sub>2</sub>O<sub>3</sub> catalysts synthesized by sol-gel method," *Chem. Eng. Res. Bull.*, vol. 14, no. 2, pp. 97–102, 2010.
- [69] L. Smoláková, M. Kout, E. Koudelková, and L. Čapek, "Effect of calcination temperature on the structure and catalytic performance of the Ni/Al<sub>2</sub>O<sub>3</sub> and Ni-Ce/Al<sub>2</sub>O<sub>3</sub> catalysts in oxidative dehydrogenation of ethane," *Ind. Eng. Chem. Res.*, vol. 54, no. 51, pp. 12730–12740, Dec. 2015.

- [70] K. Y. Koo, H. S. Roh, Y. T. Seo, D. J. Seo, W. L. Yoon, and S. Bin Park, "Coke study on MgO-promoted Ni/Al<sub>2</sub>O<sub>3</sub> catalyst in combined H<sub>2</sub>O and CO<sub>2</sub> reforming of methane for gas to liquid (GTL) process," *Appl. Catal. A Gen.*, vol. 340, no. 2, pp. 183–190, 2008.
- [71] J. T. Richardson and L. W. Vernon, "The magnetic properties of the cobalt oxides and the system cobalt-alumina," *J. Phys. Chem.*, vol. 62, no. 10, pp. 1153–1158, 1958.
- [72] W. J. Wang and Y. W. Chen, "Influence of metal loading on the reducibility and hydrogenation activity of cobalt/alumina catalysts," *Appl. Catal.*, vol. 77, no. 2, pp. 223–233, 1991.
- [73] R. L. Chin and D. M. Hercules, "Surface spectroscopic characterization of cobalt-alumina catalysts," *J. Phys. Chem.*, vol. 86, no. 3, pp. 360–367, 1982.
- [74] J. Lindsey and S. Klettlinger, *Fischer-Tropsch cobalt catalyst improvements with the presence of TiO<sub>2</sub>, La<sub>2</sub>O<sub>3</sub>, and ZrO<sub>2</sub> on an alumina support*. Ohio, USA, 2012.
- [75] N. K. Renuka, A. V. Shijina, A. K. Praveen, and C. U. Aniz, "Redox properties and catalytic activity of CuO/ $\gamma$ -Al<sub>2</sub>O<sub>3</sub> meso phase," *J. Colloid Interface Sci.*, vol. 434, pp. 195–200, Nov. 2014.
- [76] K. E. Sickafus, J. M. Wills, and N. W. Grimes, "Structure of Spinel," *J. Am. Ceram. Soc.*, vol. 82, no. 12, pp. 3279–3292, Dec. 2004.
- [77] I. E. Achouri, "Ingénierie d'un catalyseur spinelle Ni-Al pour le reformage à la vapeur du diesel: Analyse et Optimisation," in *Thesis: Chemical engineering*, Québec, Canada, 2015, pp. X–129.
- [78] R. Armistead, "Managing carbon monoxide pollution in meteorological and topographical problem areas," in *National Research Council 2003*, Washington, USA: National Academies Press, 2003.
- [79] M. D. Armin Ernst and M. D. Joseph D Zibrak, "Carbon monoxide poisoning," *N. Engl. J. Med.*, vol. 339, no. 22, pp. 1603–1608, 1998.
- [80] R. J. Farrauto and R. M. Heck, "Environmental catalysis into the 21st century," *Catal. Today*, vol. 55, no. 1–2, pp. 179–187, 2000.
- [81] I. Fechete, Y. Wang, and J. C. Védrine, "The past, present and future of heterogeneous catalysis," *Catal. Today*, vol. 189, no. 1, pp. 2–27, 2012.
- [82] M. V. Twigg, "Catalytic control of emissions from cars," *Catal. Today*, vol. 163, no. 1, pp. 33–41, 2011.
- [83] H. S. Gandhi, G. W. Graham, and R. W. McCabe, "Automotive exhaust catalysis," *J. Catal.*, vol. 216, no. 1–2, pp. 433–442, 2003.
- [84] R. M. Heck, R. K. Farrauto, and S. T. Gulati, "Catalytic air pollution control: Commercial technology, 3rd edition," *Platin. Met. Rev.*, vol. 54, no. 3, pp. 180–183, 2010.
- [85] J. E. Mcevoy, "Catalysts for the control of automotive pollutants," *Adv. Chem. Ser.*, 1975.
- [86] Y. F. Y. Yao, "The oxidation of hydrocarbons and CO over metal oxides," *J. Catal.*, vol. 33, no. 4, pp. 108–122, 1974.
- [87] Y. Yu, T. Takei, H. Ohashi, H. He, X. Zhang, and M. Haruta, "Pretreatments of Co<sub>3</sub>O<sub>4</sub> at moderate temperature for CO oxidation at –80°C," *J. Catal.*, vol. 267, no. 2, pp.

- 121–128, Oct. 2009.
- [88] Y. Z. Wang, Y. X. Zhao, C. G. Gao, and D. S. Liu, “Preparation and catalytic performance of  $\text{Co}_3\text{O}_4$  catalysts for low-temperature CO oxidation,” *Catal. Letters*, vol. 116, no. 3–4, pp. 136–142, 2007.
- [89] J. Jansson, “Low-temperature CO oxidation over  $\text{Co}_3\text{O}_4/\text{Al}_2\text{O}_3$ ,” *J. Catal.*, vol. 194, no. 1, pp. 55–60, 2000.
- [90] Y. Z. Wang, Y. X. Zhao, C. G. Gao, and D. S. Liu, “Origin of the high activity and stability of  $\text{Co}_3\text{O}_4$  in low-temperature CO oxidation,” *Catal. Letters*, vol. 125, no. 1–2, pp. 134–138, Sep. 2008.
- [91] J. Jansson *et al.*, “On the catalytic activity of  $\text{Co}_3\text{O}_4$  in low-temperature CO oxidation,” *J. Catal.*, vol. 211, no. 2, pp. 387–397, 2002.
- [92] M. Kang, M. W. Song, and C. H. Lee, “Catalytic carbon monoxide oxidation over  $\text{CoO}_x/\text{CeO}_2$  composite catalysts,” *Appl. Catal. A Gen.*, vol. 251, no. 1, pp. 143–156, 2003.
- [93] C. Bin Wang, C. W. Tang, H. C. Tsai, M. C. Kuo, and S. H. Chien, “In situ FT-IR spectroscopic studies on the mechanism of the catalytic oxidation of carbon monoxide over supported cobalt catalysts,” *Catal. Letters*, vol. 107, no. 1–2, pp. 31–37, 2006.
- [94] C. Bin Wang, C. W. Tang, H. C. Tsai, and S. H. Chien, “Characterization and catalytic oxidation of carbon monoxide over supported cobalt catalysts,” *Catal. Letters*, vol. 107, no. 3–4, pp. 223–230, 2006.
- [95] Y. F. Yu Yao and J. T. Kummer, “A study of high temperature treated supported metal oxide catalysts,” *J. Catal.*, vol. 46, no. 3, pp. 388–401, 1977.
- [96] C. S. Chen, J. H. You, J. H. Lin, C. R. Chen, and K. M. Lin, “The effect of a nickel promoter on the reducibility of a commercial  $\text{Cu}/\text{ZnO}/\text{Al}_2\text{O}_3$  catalyst for CO oxidation,” *Catal. Commun.*, vol. 9, no. 6, pp. 1230–1234, 2008.
- [97] G. Centi and S. Perathoner, “Nature of active species in copper-based catalysts and their chemistry of transformation of nitrogen oxides,” *Appl. Catal. A Gen.*, vol. 132, no. 2, pp. 179–259, Nov. 1995.
- [98] E. D. Pierron, J. A. Rashkin, and J. F. Roth, “Copper oxide on alumina. I. XRD studies of catalyst composition during air oxidation of carbon monoxide,” *J. Catal.*, vol. 9, no. 1, pp. 38–44, 1967.
- [99] M. F. Luo, P. Fang, M. He, and Y. L. Xie, “In situ XRD, Raman, and TPR studies of  $\text{CuO}/\text{Al}_2\text{O}_3$  catalysts for CO oxidation,” *J. Mol. Catal. A Chem.*, vol. 239, no. 1–2, pp. 243–248, 2005.
- [100] T. J. Huang, T. C. Yu, and S. H. Chang, “Effect of calcination atmosphere on  $\text{CuO}/\gamma\text{-Al}_2\text{O}_3$  catalyst for carbon monoxide oxidation,” *Appl. Catal.*, vol. 52, no. 1, pp. 157–163, 1989.
- [101] T. J. Huang and T. C. Yu, “Calcination conditions on copper/alumina catalysts for carbon monoxide oxidation and nitric oxide reduction,” *Appl. Catal.*, vol. 71, no. 2, pp. 275–282, 1991.
- [102] J. Laine and F. Severino, “Changes in alumina-supported copper and copper-chromite catalysts by the introduction of water during carbon monoxide oxidation,” *Appl. Catal.*, vol. 65, no. 2, pp. 253–258, 1990.

- [103] A. L. Agudo, J. M. Palacios, J. L. G. Fierro, J. Laine, and F. Severino, "Activity and structural changes of alumina-supported CuO and CuCr<sub>2</sub>O<sub>4</sub> catalysts during carbon monoxide oxidation in the presence of water," *Appl. Catal. A, Gen.*, vol. 91, no. 1, pp. 43–55, 1992.
- [104] J. A. Schwarz, C. Contescu, and A. Contescu, "Methods for preparation of catalytic materials," *Chem. Rev.*, vol. 95, no. 3, pp. 477–510, 1995.
- [105] M. Campanati, G. Fornasari, and A. Vaccari, "Fundamentals in the preparation of heterogeneous catalysts," *Catal. Today*, vol. 77, no. 4, pp. 299–314, 2003.
- [106] C. N. R. Rao and K. Biswas, *Essentials of inorganic materials synthesis*, 1st ed. New Jersey, USA: John Wiley & Sons, 2015.
- [107] D. W. Lee and B. R. Yoo, "Advanced metal oxide (supported) catalysts: Synthesis and applications," *J. Ind. Eng. Chem.*, vol. 20, no. 6, 2014.
- [108] X. Carrier, S. Royer, and E. Marceau, "Synthesis of metal oxide catalysts," in *Metal Oxides in Heterogeneous Catalysis*, Amsterdam, Netherlands: Elsevier, 2018, pp. 43–103.
- [109] M. B. Schütz, L. Xiao, T. Lehn, T. Fischer, and S. Mathur, "Microwave-assisted synthesis of nanocrystalline binary and ternary metal oxides," *Int. Mater. Rev.*, vol. 63, no. 6, pp. 341–374, Aug. 2017.
- [110] B. L. Hayes, *Microwave synthesis: chemistry at the speed of light*, 1st ed. Matthews, USA: CEM Publishing, 2002.
- [111] T. Cablewski, A. F. Faux, and C. R. Strauss, "Development and application of a continuous microwave reactor for organic synthesis," *J. Org. Chem.*, vol. 59, pp. 3408–3412, 1994.
- [112] Y. J. Zhu and F. Chen, "Microwave-assisted preparation of inorganic nanostructures in liquid phase," *Chem. Rev.*, vol. 114, no. 12, pp. 6462–6555, Jun. 2014.
- [113] M. B. Gawande, S. N. Shelke, R. Zboril, and R. S. Varma, "Microwave-assisted chemistry: Synthetic applications for rapid assembly of nanomaterials and organics," *Acc. Chem. Res.*, vol. 47, no. 4, pp. 1338–1348, 2014.
- [114] I. Bilecka and M. Niederberger, "Microwave chemistry for inorganic nanomaterials synthesis," *Nanoscale*, vol. 2, no. 8, pp. 1358–1374, 2010.
- [115] M. Bhattacharya and T. Basak, "A review on the susceptor assisted microwave processing of materials," *Energy*, vol. 97, pp. 306–338, 2016.
- [116] S. Singh, D. Gupta, V. Jain, and A. K. Sharma, "Microwave processing of materials and applications in manufacturing industries: A Review," *Mater. Manuf. Process.*, vol. 30, no. 1, pp. 1–29, 2015.
- [117] E. T. Thostenson and T. W. Chou, "Microwave processing: fundamentals and applications," *Compos. Part A Appl. Sci. Manuf.*, vol. 30, no. 9, pp. 1055–1071, 1999.
- [118] D. M. P. Mingos, "The applications of microwaves in chemical syntheses," *Res. Chem. Intermed.*, vol. 20, no. 1, pp. 85–91, 1994.
- [119] L. Y. Meng, B. Wang, M. G. Ma, and K. L. Lin, "The progress of microwave-assisted hydrothermal method in the synthesis of functional nanomaterials," *Mater. Today Chem.*, vol. 1–2, pp. 63–83, 2016.
- [120] J. J. Moore and H. J. Feng, "Combustion synthesis of advanced materials: Part I.

- Reaction parameters,” *Prog. Mater. Sci.*, vol. 39, no. 4–5, pp. 243–273, 1995.
- [121] K. C. Patil, M. S. Hegde, T. Rattan, and S. T. Aruna, *Chemistry of Nanocrystalline Oxide Materials*. Singapore: World Scientific Publishing, 2008.
- [122] S. T. Aruna and A. S. Mukasyan, “Combustion synthesis and nanomaterials,” *Curr. Opin. Solid State Mater. Sci.*, vol. 12, no. 3–4, pp. 44–50, 2008.
- [123] K. C. Patil, S. T. Aruna, and T. Mimani, “Combustion synthesis: An update,” *Curr. Opin. Solid State Mater. Sci.*, vol. 6, no. 6, pp. 507–512, 2002.
- [124] J. J. Kingsley and K. C. Patil, “A novel combustion process for the synthesis of fine particle  $\alpha$ -alumina and related oxide materials,” *Mater. Lett.*, vol. 6, no. 11–12, pp. 427–432, 1988.
- [125] A. Varma, A. S. Mukasyan, A. S. Rogachev, and K. V. Manukyan, “Solution combustion synthesis of nanoscale materials,” *Chem. Rev.*, vol. 116, no. 23, pp. 14493–14586, 2016.
- [126] M. S. Hegde, G. Madras, and K. C. Patil, “Noble metal ionic catalysts,” *Acc. Chem. Res.*, vol. 42, no. 6, pp. 704–712, 2009.
- [127] S. R. Jain, K. C. Adiga, and V. R. Pai Verneker, “A new approach to thermochemical calculations of condensed fuel-oxidizer mixtures,” *Combust. Flame*, vol. 40, pp. 71–79, Jan. 1981.
- [128] S. L. González-Cortés and F. E. Imbert, “Fundamentals, properties and applications of solid catalysts prepared by solution combustion synthesis (SCS),” *Appl. Catal. A Gen.*, vol. 452, pp. 117–131, 2013.
- [129] E. E. Wolf, A. Kumar, and A. S. Mukasyan, “Combustion synthesis: A novel method of catalyst preparation,” *Catalysis*, vol. 31, pp. 297–346, 2019.
- [130] R. Ianoş, I. Lazău, C. Păcurariu, and P. Barvinschi, “Fuel mixture approach for solution combustion synthesis of  $\text{Ca}_3\text{Al}_2\text{O}_6$  powders,” *Cem. Concr. Res.*, vol. 39, no. 7, pp. 566–572, Jul. 2009.
- [131] A. Kumar, A. S. Mukasyan, and E. E. Wolf, “Combustion synthesis of Ni, Fe and Cu multi-component catalysts for hydrogen production from ethanol reforming,” *Appl. Catal. A Gen.*, vol. 401, no. 1–2, pp. 20–28, 2011.
- [132] R. Rosa, C. Ponzoni, and C. Leonelli, “Direct energy supply to the reaction mixture during microwave-assisted hydrothermal and combustion synthesis of inorganic materials,” *Inorganics*, vol. 2, no. 2, pp. 191–210, 2014.
- [133] R. Rosa, P. Veronesi, and C. Leonelli, “A review on combustion synthesis intensification by means of microwave energy,” *Chem. Eng. Process. Process Intensif.*, 2013.
- [134] N. L. Freitas, E. Fagury-Neto, H. L. Lira, L. Gama, R. H. G. A. Kiminami, and A. C. F. M. Costa, “Combustion synthesis of  $\alpha$ - $\text{Al}_2\text{O}_3$  powders,” *Mater. Sci. Forum*, vol. 530–531, pp. 631–636, 2006.
- [135] K. Laishram, R. Mann, and N. Malhan, “A novel microwave combustion approach for single step synthesis of  $\alpha$ - $\text{Al}_2\text{O}_3$  nanopowders,” *Ceram. Int.*, vol. 38, no. 2, pp. 1703–1706, Mar. 2012.
- [136] A. Sharma, O. P. Modi, and G. K. Guptab, “Effect of fuel to oxidizer ratio on synthesis of Alumina powder using Solution Combustion Technique-Aluminium Nitrate &

- Glycine combination,” *Adv. Appl. Sci. Res.*, vol. 3, no. 4, pp. 2151–2158, 2012.
- [137] J. Li, Y. Wu, Y. Pan, W. Liu, Y. Zhu, and J. Guo, “Agglomeration of  $\alpha$ -Al<sub>2</sub>O<sub>3</sub> powders prepared by gel combustion,” *Ceram. Int.*, vol. 34, no. 6, pp. 1539–1542, Aug. 2008.
- [138] W. Wen and J. M. Wu, “Eruption combustion synthesis of NiO/Ni nanocomposites with enhanced properties for dye-absorption and lithium storage,” *ACS Appl. Mater. Interfaces*, vol. 3, no. 10, pp. 4112–4119, Oct. 2011.
- [139] W. Wen, J. M. Wu, and M. H. Cao, “Rapid one-step synthesis and electrochemical performance of NiO/Ni with tunable macroporous architectures,” *Nano Energy*, 2013.
- [140] L. J. Groven, T. L. Pfeil, and T. L. Pourpoint, “Solution combustion synthesized cobalt oxide catalyst precursor for NaBH<sub>4</sub> hydrolysis,” *Int. J. Hydrogen Energy*, vol. 38, no. 15, pp. 6377–6380, 2013.
- [141] T. L. Pfeil, T. L. Pourpoint, and L. J. Groven, “Effects of crystallinity and morphology of solution combustion synthesized Co<sub>3</sub>O<sub>4</sub> as a catalyst precursor in hydrolysis of sodium borohydride,” *Int. J. Hydrogen Energy*, vol. 39, no. 5, pp. 2149–2159, 2014.
- [142] W. Wen, J. M. Wu, and M. H. Cao, “Facile synthesis of a mesoporous Co<sub>3</sub>O<sub>4</sub> network for Li-storage via thermal decomposition of an amorphous metal complex,” *Nanoscale*, vol. 6, no. 21, pp. 12476–12481, 2014.
- [143] P. Sahoo, H. Djieutedjeu, and P. F. P. Poudeu, “Co<sub>3</sub>O<sub>4</sub> nanostructures: the effect of synthesis conditions on particles size, magnetism and transport properties,” *J. Mater. Chem. A*, vol. 1, no. 47, p. 15022, 2013.
- [144] S. Bazgir and S. Farhadi, “Microwave-assisted rapid synthesis of Co<sub>3</sub>O<sub>4</sub> nanorods from CoC<sub>2</sub>O<sub>4</sub>·2H<sub>2</sub>O nanorods and its application in photocatalytic degradation of methylene blue under visible light irradiation,” *Int. J. Nano Dimens.*, vol. 8, no. 4, pp. 284–297, 2017.
- [145] M. Rashad, M. Rüsing, G. Berth, K. Lischka, and A. Pawlis, “CuO and Co<sub>3</sub>O<sub>4</sub> nanoparticles: synthesis, characterizations, and raman spectroscopy,” *J. Nanomater.*, 2013.
- [146] M. Umadevi and A. Jegatha Christy, “Synthesis, characterization and photocatalytic activity of CuO nanoflowers,” *Spectrochim. Acta - Part A Mol. Biomol. Spectrosc.*, vol. 109, pp. 133–137, 2013.
- [147] A. J. Christy, L. C. Nehru, and M. Umadevi, “A novel combustion method to prepare CuO nanorods and its antimicrobial and photocatalytic activities,” *Powder Technol.*, vol. 235, no. 3, pp. 783–786, 2013.
- [148] D. Suresh *et al.*, “Chironji mediated facile green synthesis of ZnO nanoparticles and their photoluminescence, photodegradative, antimicrobial and antioxidant activities,” *Mater. Sci. Semicond. Process.*, vol. 40, pp. 759–765, 2015.
- [149] J. K. Sharma, M. S. Akhtar, S. Ameen, P. Srivastava, and G. Singh, “Green synthesis of CuO nanoparticles with leaf extract of *Calotropis gigantea* and its dye-sensitized solar cells applications,” *J. Alloys Compd.*, vol. 632, pp. 321–325, 2015.
- [150] H. Nasiri, E. Bahrami Motlagh, J. Vahdati Khaki, and S. M. Zebajad, “Role of fuel/oxidizer ratio on the synthesis conditions of Cu-Al<sub>2</sub>O<sub>3</sub> nanocomposite prepared through solution combustion synthesis,” *Mater. Res. Bull.*, vol. 47, no. 11, pp. 3676–3680, 2012.

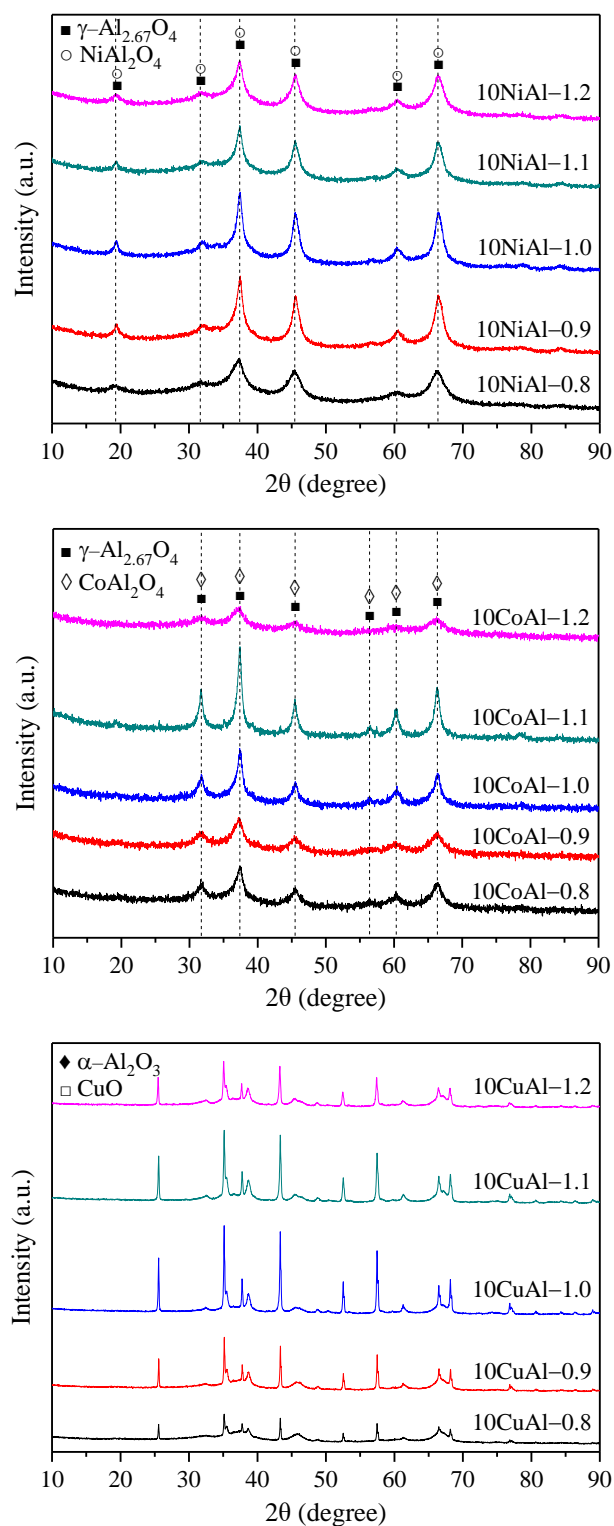
- [151] J. Y. Park, S. J. Oh, C. H. Jung, G. W. Hong, and I. H. Kuk, "Al<sub>2</sub>O<sub>3</sub>-dispersed Cu prepared by the combustion synthesized powder," *J. Mater. Sci. Lett.*, vol. 18, pp. 67–70, 1999.
- [152] B. Roy, U. Martinez, K. Loganathan, A. K. Datye, and C. A. Leclerc, "Effect of preparation methods on the performance of Ni/Al<sub>2</sub>O<sub>3</sub> catalysts for aqueous-phase reforming of ethanol: Part I-catalytic activity," *Int. J. Hydrogen Energy*, vol. 37, no. 10, pp. 8143–8153, May 2012.
- [153] B. Roy, K. Loganathan, H. N. Pham, A. K. Datye, and C. A. Leclerc, "Surface modification of solution combustion synthesized Ni/Al<sub>2</sub>O<sub>3</sub> catalyst for aqueous-phase reforming of ethanol," *Int. J. Hydrogen Energy*, vol. 35, no. 21, pp. 11700–11708, Nov. 2010.
- [154] A. Cross, A. Kumar, E. E. Wolf, and A. S. Mukasyan, "Combustion synthesis of a nickel supported catalyst: Effect of metal distribution on the activity during ethanol decomposition," *Ind. Eng. Chem. Res.*, vol. 51, no. 37, pp. 12004–12008, 2012.
- [155] A. Zhao, W. Ying, H. Zhang, H. Ma, and D. Fang, "Ni-Al<sub>2</sub>O<sub>3</sub> catalysts prepared by solution combustion method for syngas methanation," *Catal. Commun.*, vol. 17, pp. 34–38, 2012.
- [156] Y. Zeng, H. Ma, H. Zhang, W. Ying, and D. Fang, "Highly efficient NiAl<sub>2</sub>O<sub>4</sub>-free Ni/ $\gamma$ -Al<sub>2</sub>O<sub>3</sub> catalysts prepared by solution combustion method for CO methanation," *Fuel*, vol. 137, pp. 155–163, Dec. 2014.
- [157] Y. Gao, F. Meng, K. Ji, Y. Song, and Z. Li, "Slurry phase methanation of carbon monoxide over nanosized Ni-Al<sub>2</sub>O<sub>3</sub> catalysts prepared by microwave-assisted solution combustion," *Appl. Catal. A Gen.*, vol. 510, pp. 74–83, 2016.
- [158] Y. Gao, F. Meng, X. Li, J. Z. Wen, and Z. Li, "Factors controlling nanosized Ni-Al<sub>2</sub>O<sub>3</sub> catalysts synthesized by solution combustion for slurry-phase CO methanation: the ratio of reducing valences to oxidizing valences in redox systems," *Catal. Sci. Technol.*, vol. 6, no. 21, pp. 7800–7811, 2016.
- [159] Y. Gao, F. Meng, Y. Cheng, and Z. Li, "Influence of fuel additives in the urea-nitrates solution combustion synthesis of Ni-Al<sub>2</sub>O<sub>3</sub> catalyst for slurry phase CO methanation," *Appl. Catal. A Gen.*, vol. 534, pp. 12–21, 2017.
- [160] U. Zavyalova, P. Scholz, and B. Ondruschka, "Influence of cobalt precursor and fuels on the performance of combustion synthesized Co<sub>3</sub>O<sub>4</sub>/ $\gamma$ -Al<sub>2</sub>O<sub>3</sub> catalysts for total oxidation of methane," *Appl. Catal. A Gen.*, vol. 323, pp. 226–233, 2007.
- [161] H. Liang, Y. Y. Ting, H. Sun, H. M. Ang, M. O. Tadé, and S. Wang, "Solution combustion synthesis of Co oxide-based catalysts for phenol degradation in aqueous solution," *J. Colloid Interface Sci.*, vol. 372, no. 1, pp. 58–62, 2012.
- [162] J. I. Langford and A. J. C. Wilson, "Seherrer after Sixty Years: A Survey and Some New Results in the Determination of Crystallite Size," *J. Appl. Crystallogr.*, pp. 102–113, 1978.
- [163] K. S. W. Sing *et al.*, "Reporting physisorption data for gas/solid systems," *Pure Appl. Chem.*, vol. 57, pp. 603–619, 1985.
- [164] M. Thommes *et al.*, "Physisorption of gases, with special reference to the evaluation of surface area and pore size distribution (IUPAC Technical Report)," *Pure Appl. Chem.*, vol. 87, no. 9–10, pp. 1051–1069, 2015.

- [165] S. Brunauer, P. H. Emmett, and E. Teller, "Adsorption of gases in multimolecular layers," *J. Am. Chem. Soc.*, vol. 60, no. 2, pp. 309–319, 1938.
- [166] E. P. Barrett, L. G. Joyner, and P. P. Halenda, "The determination of pore volume and area distributions in porous substances. I. Computations from nitrogen isotherms," *J. Am. Chem. Soc.*, vol. 73, no. 1, pp. 373–380, 1951.
- [167] G. Li, L. Hu, and J. M. Hill, "Comparison of reducibility and stability of alumina-supported Ni catalysts prepared by impregnation and co-precipitation," *Appl. Catal. A Gen.*, vol. 301, no. 1, pp. 16–24, 2006.
- [168] E. Kiš *et al.*, "Structural and textural properties of the NiO-Al<sub>2</sub>O<sub>3</sub> catalyst," *Polyhedron*, vol. 17, no. 1, pp. 27–34, 1998.
- [169] J. L. Ewbank, L. Kovarik, F. Z. Diallo, and C. Sievers, "Effect of metal-support interactions in Ni/Al<sub>2</sub>O<sub>3</sub> catalysts with low metal loading for methane dry reforming," *Appl. Catal. A Gen.*, vol. 494, pp. 57–67, 2015.
- [170] M. C. Biesinger, B. P. Payne, A. P. Grosvenor, L. W. M. Lau, A. R. Gerson, and R. S. C. Smart, "Resolving surface chemical states in XPS analysis of first row transition metals, oxides and hydroxides: Cr, Mn, Fe, Co and Ni," *Appl. Surf. Sci.*, vol. 257, no. 7, pp. 2717–2730, 2011.
- [171] M. C. Biesinger, B. P. Payne, L. W. M. Lau, A. Gerson, and R. S. C. Smart, "X-ray photoelectron spectroscopic chemical state Quantification of mixed nickel metal, oxide and hydroxide systems," *Surf. Interface Anal.*, vol. 41, no. 4, pp. 324–332, 2009.
- [172] B. P. Payne, M. C. Biesinger, and N. S. McIntyre, "Use of oxygen/nickel ratios in the XPS characterisation of oxide phases on nickel metal and nickel alloy surfaces," *J. Electron Spectros. Relat. Phenomena*, vol. 185, no. 5–7, pp. 159–166, 2012.
- [173] A. P. Grosvenor, M. C. Biesinger, R. S. C. Smart, and N. S. McIntyre, "New interpretations of XPS spectra of nickel metal and oxides," *Surf. Sci.*, vol. 600, no. 9, pp. 1771–1779, 2006.
- [174] X. Duan, M. Pan, F. Yu, and D. Yuan, "Synthesis, structure and optical properties of CoAl<sub>2</sub>O<sub>4</sub> spinel nanocrystals," *J. Alloys Compd.*, vol. 509, no. 3, pp. 1079–1083, 2011.
- [175] J. K. Han, L. T. Jia, B. Hou, D. B. Li, Y. Liu, and Y. C. Liu, "Catalytic properties of CoAl<sub>2</sub>O<sub>4</sub>/Al<sub>2</sub>O<sub>3</sub> supported cobalt catalysts for Fischer-Tropsch synthesis," *J. Fuel Chem. Technol.*, vol. 43, no. 7, pp. 846–851, 2015.
- [176] M. C. Biesinger, L. W. M. Lau, A. R. Gerson, and R. S. C. Smart, "Resolving surface chemical states in XPS analysis of first row transition metals, oxides and hydroxides: Sc, Ti, V, Cu and Zn," *Appl. Surf. Sci.*, vol. 257, no. 3, pp. 887–898, 2010.
- [177] L. Fu and H. Yang, "Tailoring the electronic structure of mesoporous spinel  $\gamma$ -Al<sub>2</sub>O<sub>3</sub> at atomic level: Cu-doped case," *J. Phys. Chem. C*, vol. 118, no. 26, pp. 14299–14315, 2014.
- [178] S. Bennici, A. Auroux, C. Guimon, and A. Gervasini, "Supported binary oxide catalysts containing CuO coupled with Ga<sub>2</sub>O<sub>3</sub> and SnO<sub>2</sub>," *Chem. Mater.*, vol. 18, no. 16, pp. 3641–3650, 2006.
- [179] M. C. Biesinger, "Advanced analysis of copper X-ray photoelectron spectra," *Surf. Interface Anal.*, vol. 49, no. 13, pp. 1325–1334, 2017.
- [180] S. Thirumalairajan, V. R. Mastelaro, and C. A. Escanhoela, "In-depth understanding of

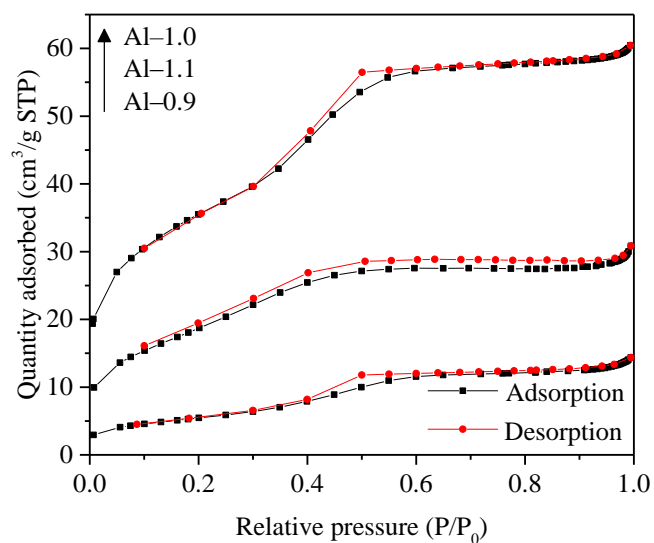
- the relation between CuAlO<sub>2</sub> particle size and morphology for ozone gas sensor detection at a nanoscale level,” *ACS Appl. Mater. Interfaces*, vol. 6, no. 23, pp. 21739–21749, 2014.
- [181] D. Xiong *et al.*, “Synthesis and characterization of CuAlO<sub>2</sub> and AgAlO<sub>2</sub> delafossite oxides through low-temperature hydrothermal methods,” *Inorg. Chem.*, vol. 53, no. 8, pp. 4106–4116, 2014.
- [182] N. K. Renuka, A. V. Shijina, and A. K. Praveen, “Synthesis, characterisation, and CO oxidation activity of M/Al<sub>2</sub>O<sub>3</sub> meso phase catalysts (M=Ce, V, Cu),” *Mater. Lett.*, vol. 113, pp. 96–99, 2013.
- [183] F. Severino, J. Brito, O. Carías, and J. Laine, “Comparative study of alumina-supported CuO and CuCr<sub>2</sub>O<sub>4</sub> as catalysts for CO oxidation,” *J. Catal.*, vol. 102, no. 1, pp. 172–179, 1986.
- [184] G. A. El-Shobaky, G. A. Fagal, and N. H. Amin, “Thermal solid-solid interaction between CuO and pure Al<sub>2</sub>O<sub>3</sub> solids,” *Thermochim. Acta*, vol. 141, pp. 205–216, 1989.
- [185] K. CHOI and M. VANNICE, “CO oxidation over Pd and Cu catalysts,” *J. Catal.*, vol. 131, no. 1, pp. 36–50, 1991.
- [186] M. Ferrandon *et al.*, “Copper oxide–platinum/alumina catalysts for volatile organic compound and carbon monoxide oxidation: Synergetic effect of cerium and lanthanum,” *J. Catal.*, vol. 202, no. 2, pp. 354–366, 2001.
- [187] X. Y. Jiang, R. X. Zhou, P. Pan, B. Zhu, X. X. Yuan, and X. M. Zheng, “Effect of the addition of La<sub>2</sub>O<sub>3</sub> on TPR and TPD of CuO/ $\gamma$ -Al<sub>2</sub>O<sub>3</sub> catalysts,” *Appl. Catal. A Gen.*, vol. 150, no. 1, pp. 131–141, 1997.
- [188] P. Thormählen, M. Skoglundh, E. Fridell, and B. Andersson, “Low-temperature CO oxidation over platinum and cobalt oxide catalysts,” *J. Catal.*, vol. 188, pp. 300–310, 1999.
- [189] A. Törncrena, M. Skoglundh, P. Thormählen, E. Fridell, and E. Jobson, “Low temperature catalytic activity of cobalt oxide and ceria promoted Pt and Pd: -influence of pretreatment and gas composition,” *Appl. Catal. B Environ.*, vol. 14, no. 1–2, pp. 131–145, 1997.
- [190] G. A. El-Shobaky and A. N. Al-Noaimi, “Catalytic oxidation of CO on sodium-treated NiO/Al<sub>2</sub>O<sub>3</sub> solid,” *Appl. Catal.*, vol. 29, no. 2, pp. 235–242, 1987.

## ANNEX A

---



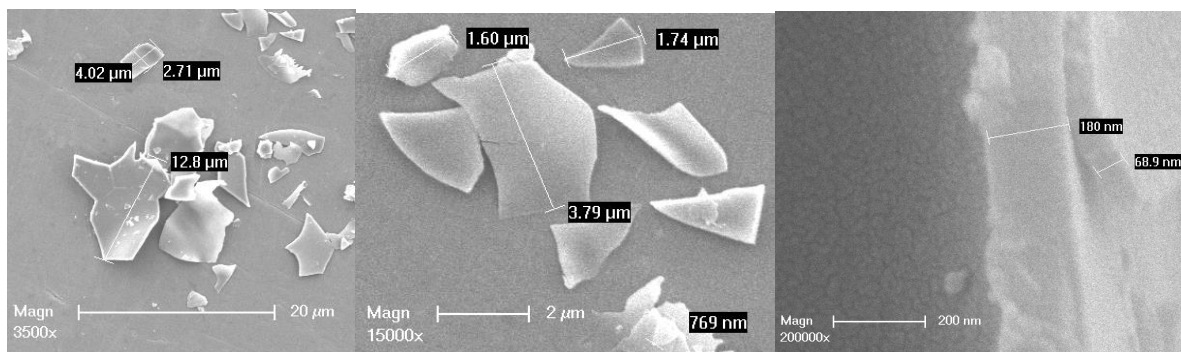
**Figure A. 1.** XRD patterns of 10MAl-*x* calcined catalysts obtained with different RV/OV ratios.



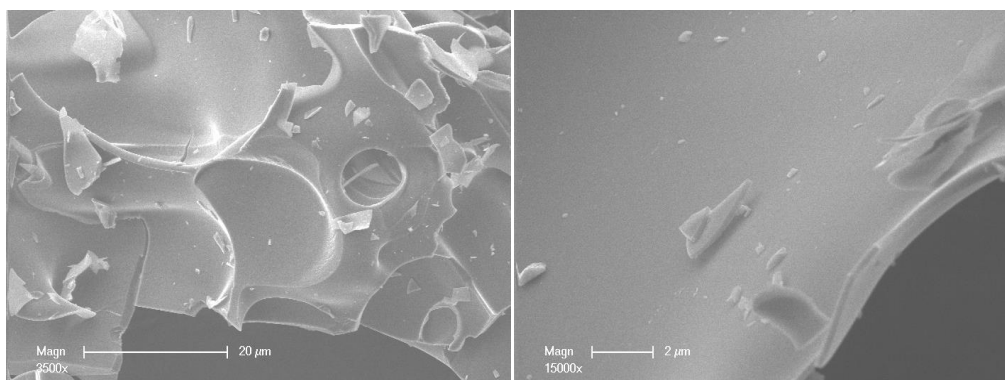
**Figure A. 2.** Nitrogen adsorption/desorption isotherms of Al- $x$  calcined samples obtained with different RV/OV ratios.

**Table A. 1.** Textural properties of Al- $x$  calcined samples.

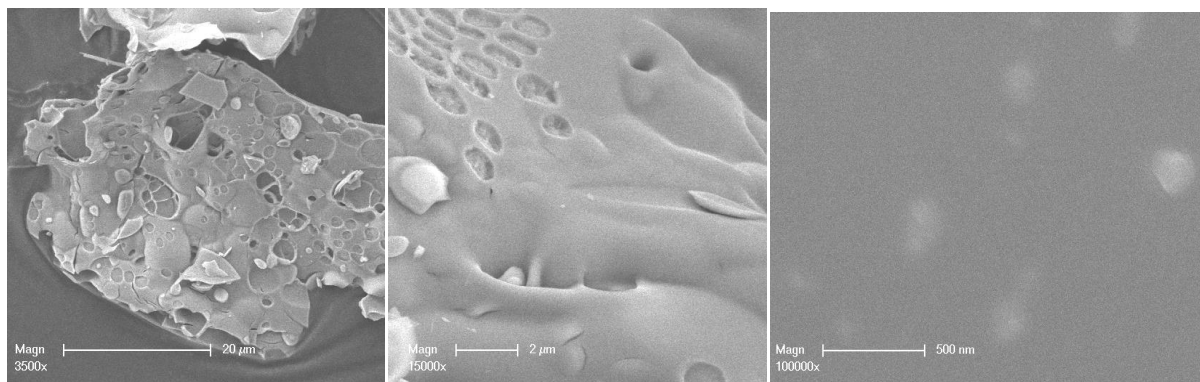
Sample	BET surface area ( $\text{m}^2\text{g}^{-1}$ )	BJH desorption	
		Pore volume ( $\text{cm}^3\text{g}^{-1}$ )	Pore diameter (nm)
Al-0.9	20.0	0.02	3.8
Al-1.0	125.4	0.08	2.9
Al-1.1	69.8	0.04	2.6



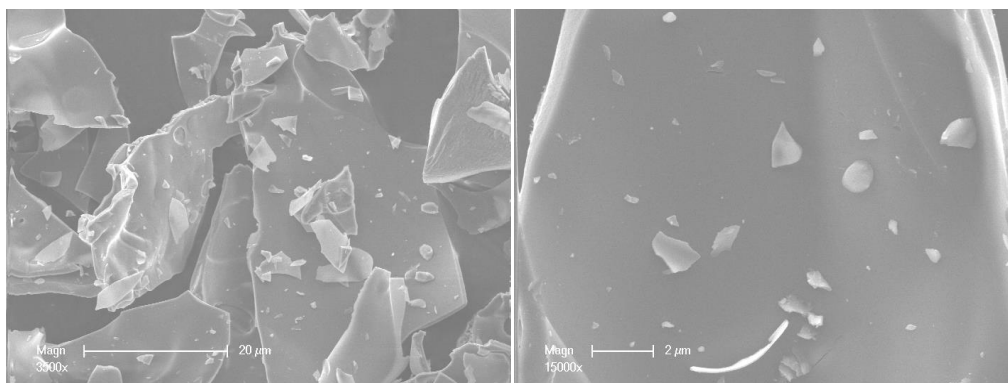
**Figure A. 3.** SEM images of Al-1.0 calcined sample.



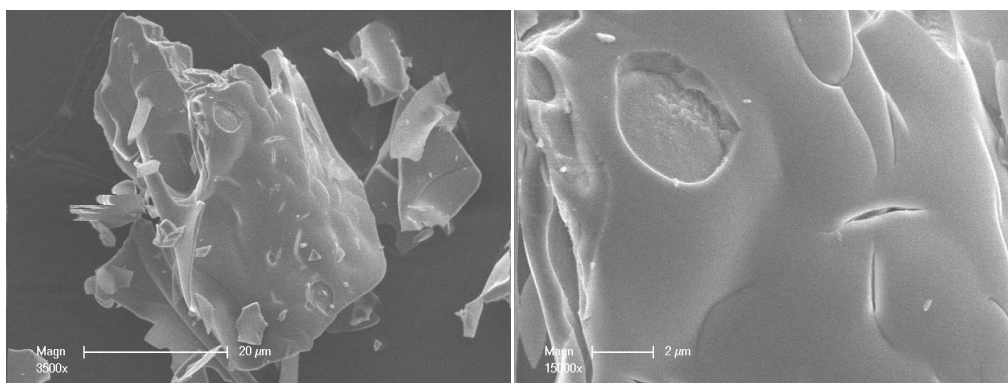
**Figure A. 4.** SEM images of 10NiAl-0.8 calcined sample.



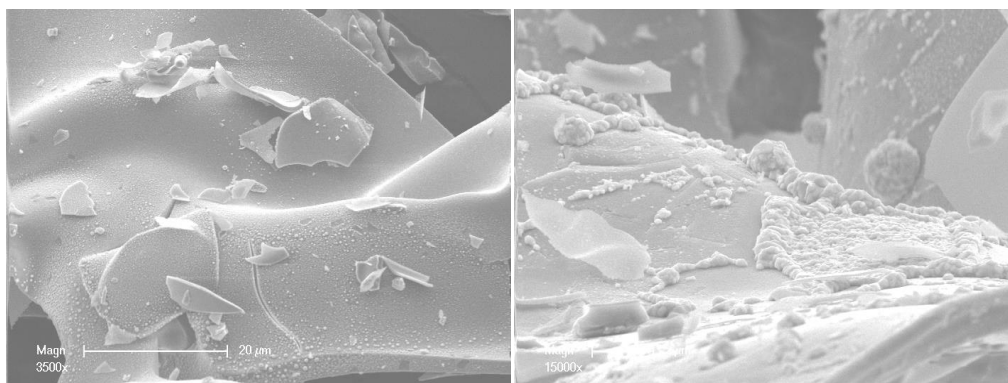
**Figure A. 5.** SEM images of 10NiAl-1.2 calcined sample.



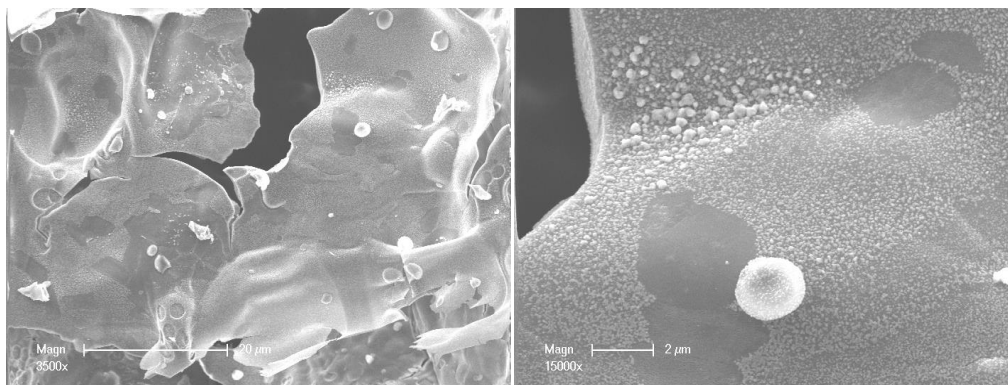
**Figure A. 6.** SEM images of 10CoAl-0.8 calcined sample.



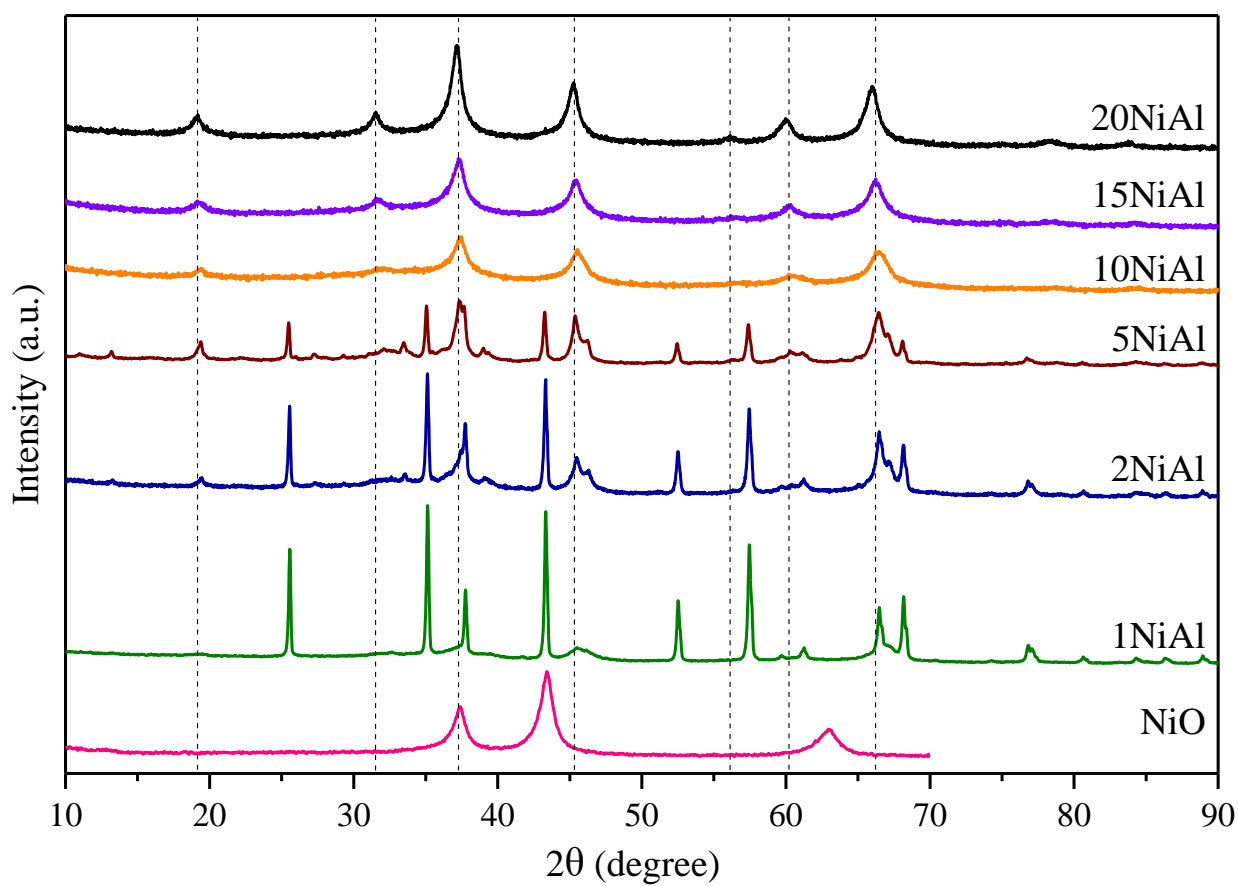
**Figure A. 7.** SEM images of 10CoAl-1.2 calcined sample.



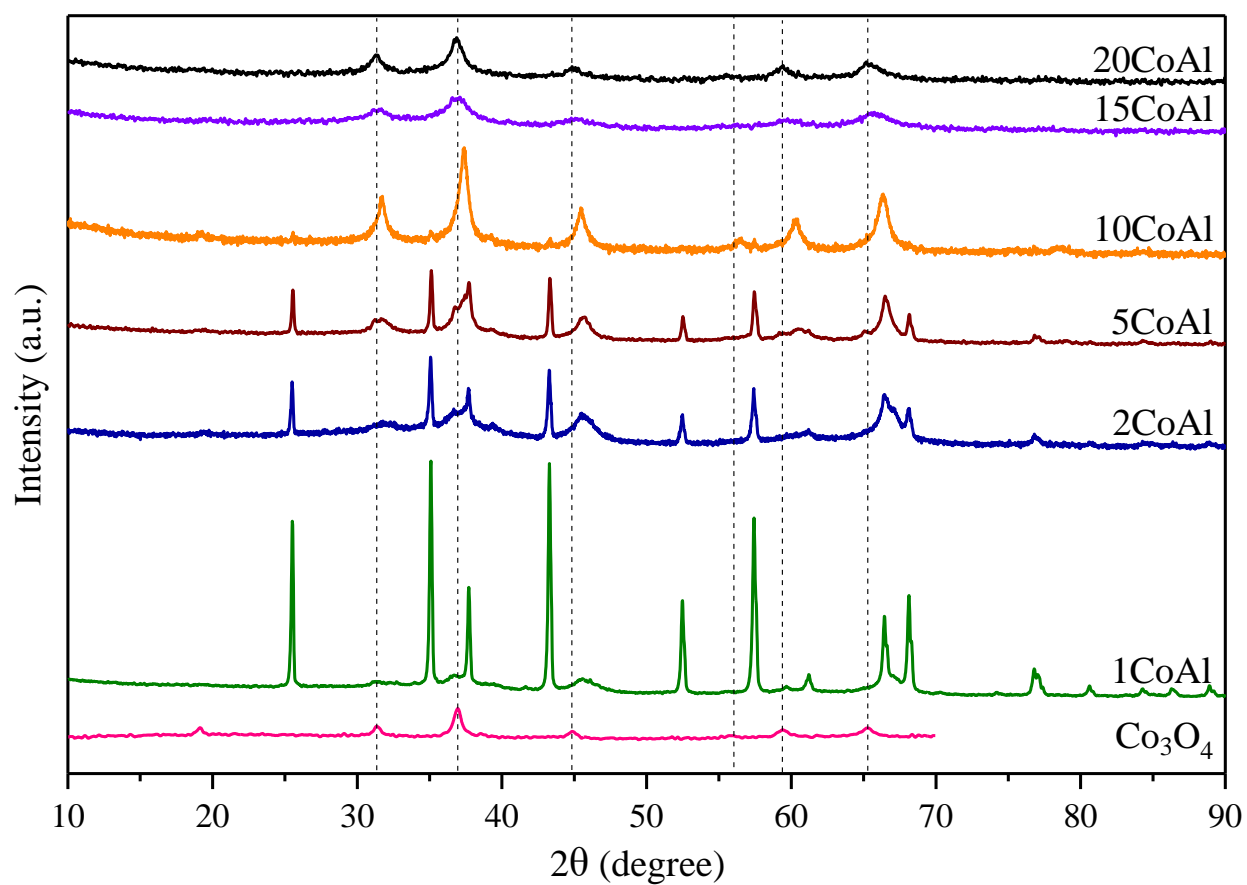
**Figure A. 8.** SEM images of 10CuAl-0.8 calcined sample.



**Figure A. 9.** SEM images of 10CuAl-1.2 calcined sample.



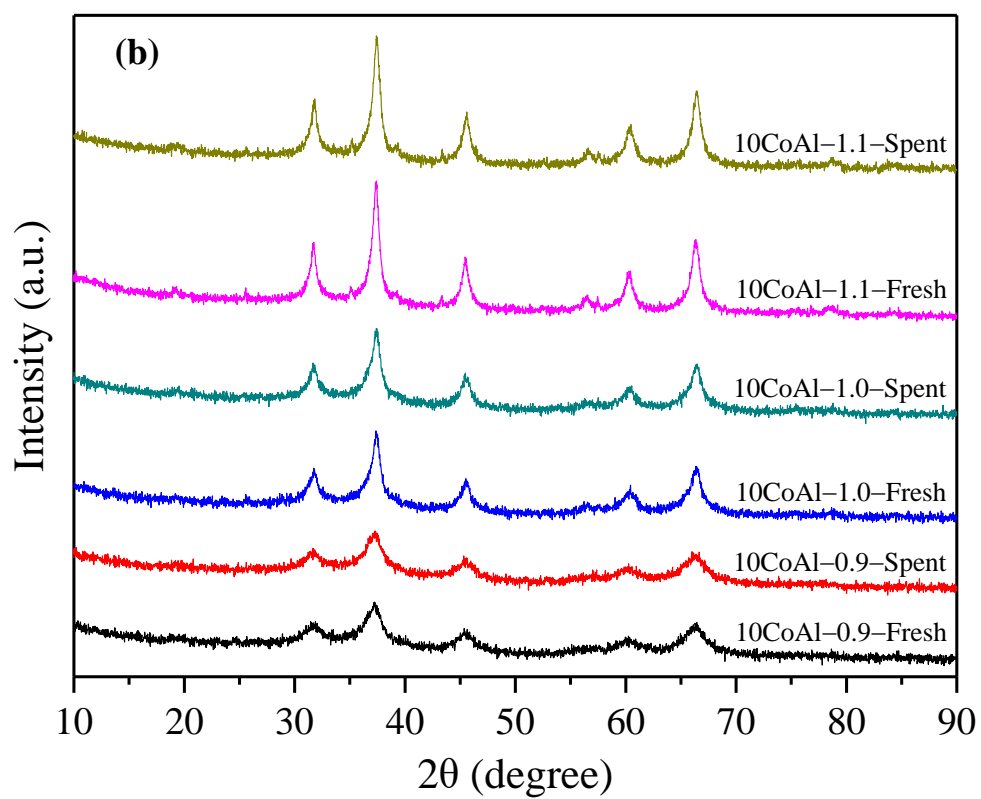
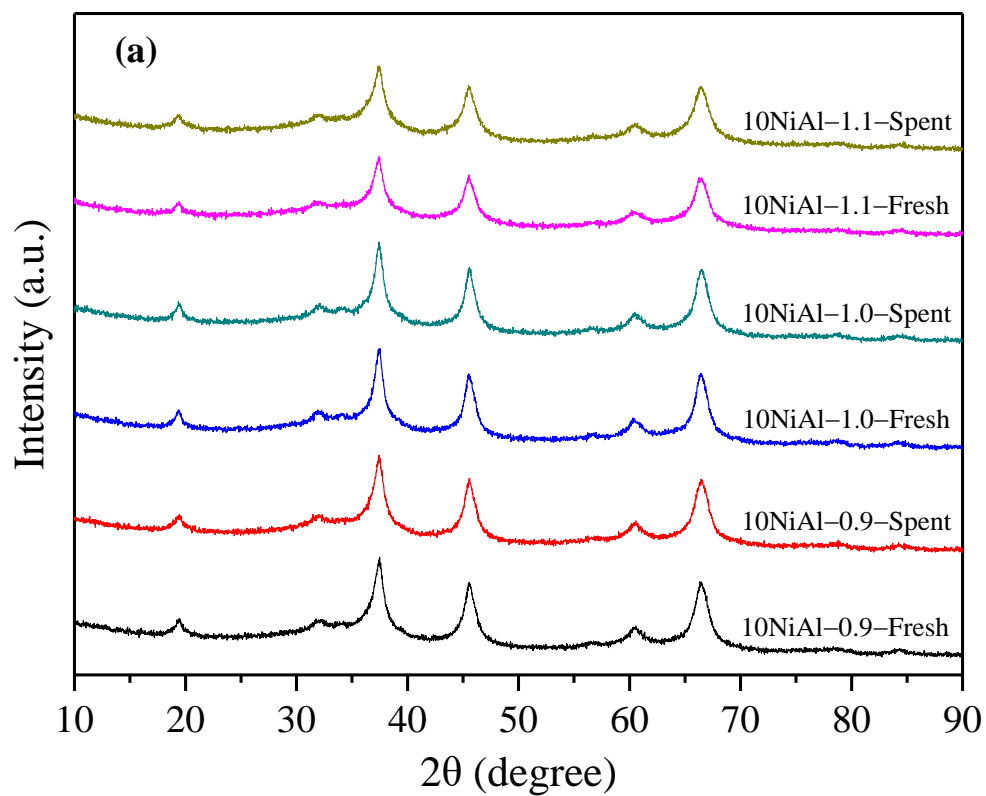
**Figure A. 10.** XRD patterns of XNiAl calcined catalysts obtained with different metal loadings

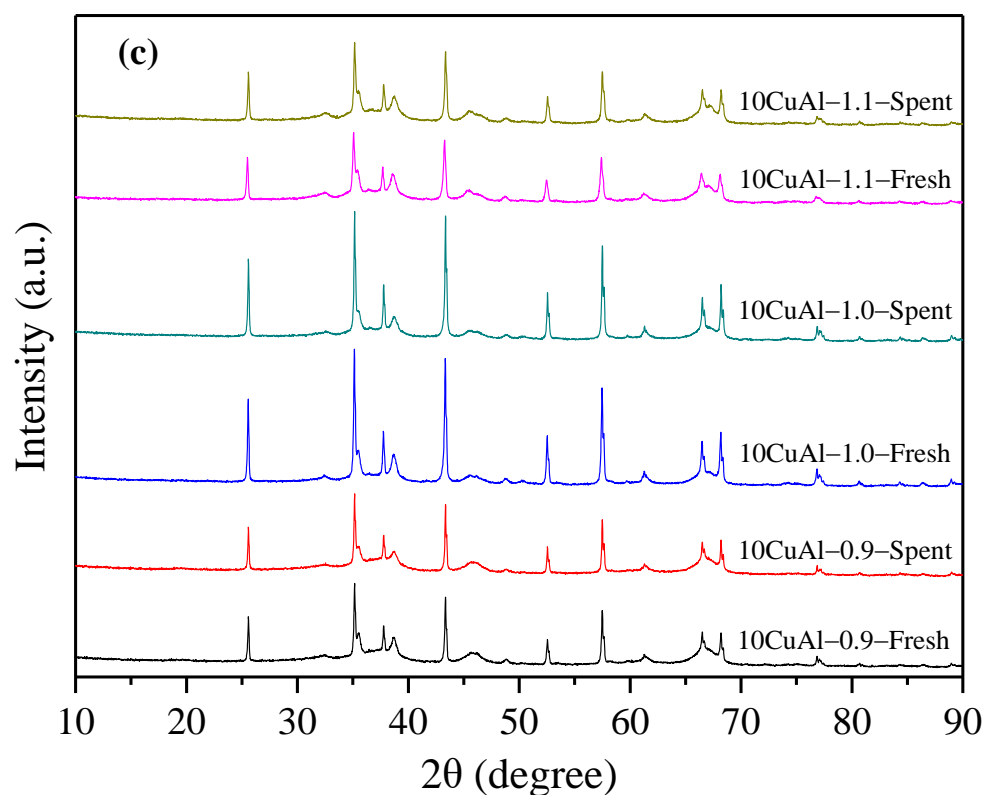


**Figure A. 11.** XRD patterns of XCoAl calcined catalysts obtained with different metal loadings

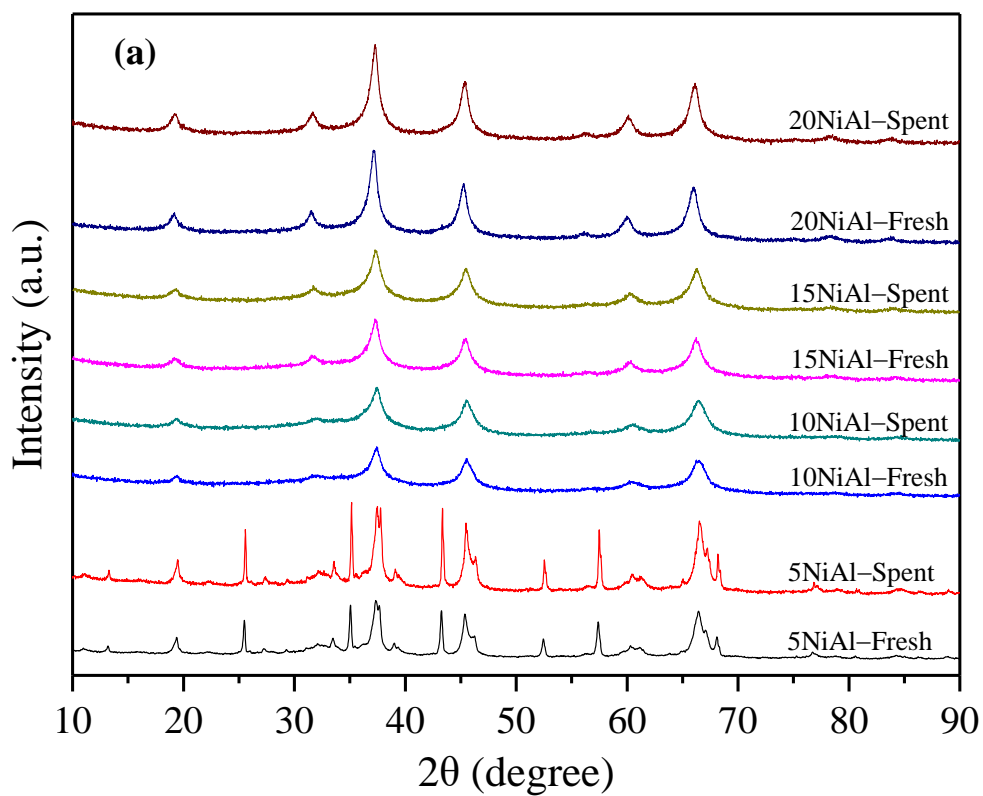
## ANNEX B

---





**Figure B. 1.** XRD patterns of (a) 10NiAl-*x*, (b) 10CoAl-*x* and (c) 10CuAl-*x* catalyst samples before and after their use in CO oxidation.



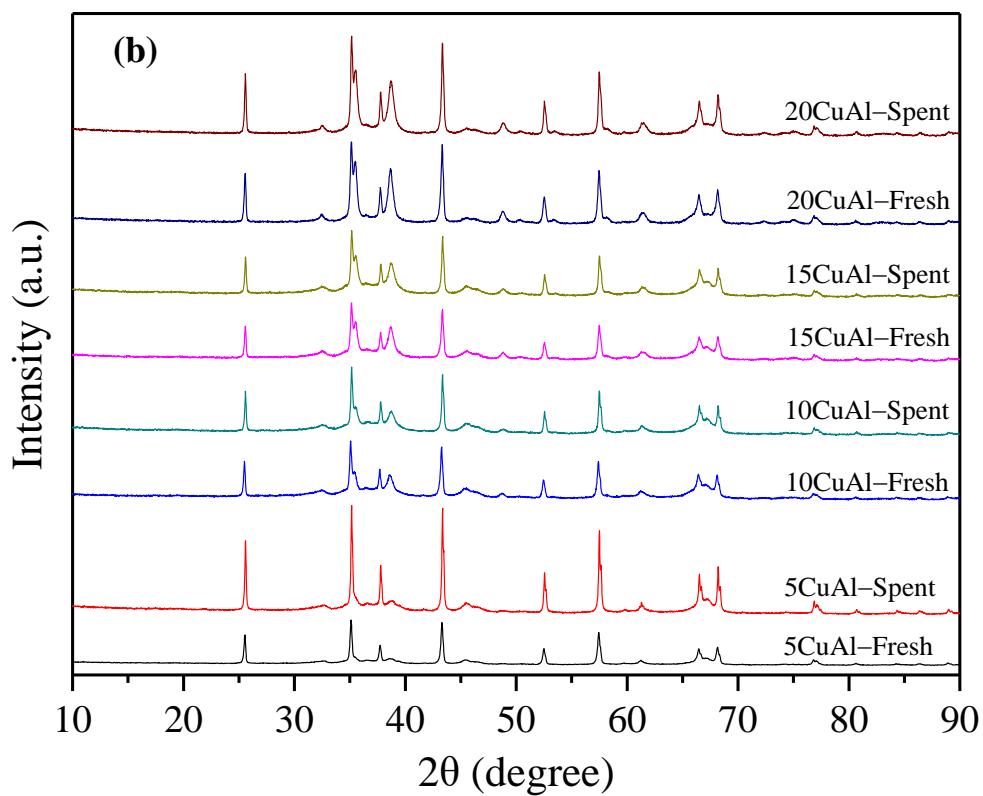


**Figure B. 2.** XRD patterns of (a) XNiAl and (b) XCuAl catalyst samples before and after their use in CO oxidation.

## **Synthesis of metal oxide-based catalysts by microwave-assisted solution combustion method**

Microwave assisted combustion synthesis (MACS) has emerged as one of the most promising routes that being a simple and fast synthesis approach. This thesis project aims to prepare metal oxide-based catalysts by MACS method for carbon monoxide (CO) removal. In this study, binary and ternary metal oxide catalysts were prepared in a very short time under microwave irradiation from the combustion of an aqueous solution of metal nitrates and urea. Several experimental factors such as the metal precursor, the stoichiometry of the reactants, and the metal loading were varied and studied. A set of multi-scale characterizations were performed in order to identify the correlation between the physico-chemical properties of the catalysts and their catalytic activities for CO oxidation. Cobalt aluminates and nickel aluminates were the mainly phases formed in Ni or Co containing catalysts while, CuO and  $\alpha$ -Al<sub>2</sub>O<sub>3</sub> separated phases were detected in copper containing catalysts. The stoichiometry and metal loading can play a critical role in controlling the phase composition and surface chemical composition. Copper containing catalysts presented a high catalytic activity for the CO oxidation at low temperatures, while nickel and cobalt containing catalysts showed relatively low activity at low temperatures. The extent of the interaction between the metal oxide and alumina affects the bulk and surface chemical composition, structural properties, and active sites dispersion which further affect the catalytic activity.

**Keywords:** Metal oxide-based catalysts; Microwave assisted combustion synthesis; CO oxidation; Physico-chemical properties; Catalytic activity.

## **Synthèse de catalyseurs d'oxydes métalliques par la méthode de combustion en solution assistée par micro-ondes**

La synthèse par combustion assistée par micro-ondes s'est récemment montrée comme l'une des voies de synthèse les plus prometteuses étant une approche simple et rapide. Ce projet de thèse s'intéresse à préparer des catalyseurs à base d'oxyde métallique par la méthode de combustion en solution assistée par micro-ondes pour l'élimination du monoxyde de carbone. Dans cette étude, des catalyseurs à base d'oxyde binaire et ternaire ont été préparés en un temps de réaction très court sous irradiation micro-ondes à partir de la combustion d'une solution aqueuse de nitrates métalliques et d'urée. Plusieurs facteurs expérimentaux tels que le précurseur métallique, la stœchiométrie des réactifs et la charge métallique ont été variés et étudiés. Une séquence de caractérisations multi-échelle a été réalisée afin d'identifier la corrélation entre les propriétés physico-chimiques des catalyseurs et leurs activités catalytiques pour l'oxydation du CO. Les aluminates de cobalt et les aluminates de nickel étaient principalement les phases formées dans les catalyseurs contenant du Ni ou du Co, tandis que les phases CuO et  $\alpha$ -Al<sub>2</sub>O<sub>3</sub> ont été détectées dans les catalyseurs contenant du cuivre. La stœchiométrie et la charge métallique peuvent jouer un rôle critique dans le contrôle de la composition de phase et de la composition chimique de surface. Les catalyseurs contenant du cuivre présentaient une activité catalytique élevée à basse température pour l'oxydation du CO, tandis que les catalyseurs contenant du nickel et du cobalt montraient une activité relativement faible à basse température. Le degré d'interaction entre l'oxyde métallique et l'alumine affecte la composition chimique de la masse et de la surface, les propriétés structurales et la dispersion des sites actifs, qui, à leur tour, affectent l'activité catalytique.

**Mots clés:** Oxydes métalliques; Combustion en solution assistée par micro-ondes; Oxydation du CO; propriétés physico-chimiques; Activité catalytique.